NUMERICAL STUDY OF HEAT TRANSFER AND ENTROPY GENERATION IN NANOFLUID FILLED ENCLOSURE

Ph.D. THESIS

by

SUMIT MALIK

DEPARTMENT OF MATHEMATICS
INDIAN INSTITUTE OF TECHNOLOGY ROORKEE
ROORKEE-247667 (INDIA)
NOVEMBER, 2017

NUMERICAL STUDY OF HEAT TRANSFER AND ENTROPY GENERATION IN NANOFLUID FILLED ENCLOSURE

A THESIS

Submitted in partial fulfilment of the requirements for the award of the degree

of

DOCTOR OF PHILOSOPHY

in

MATHEMATICS

by

SUMIT MALIK

DEPARTMENT OF MATHEMATICS
INDIAN INSTITUTE OF TECHNOLOGY ROORKEE
ROORKEE-247667 (INDIA)
NOVEMBER, 2017

INDIAN INSTITUTE OF TECHNOLOGY ROORKEE
ROORKEE

CANDIDATE'S DECLARATION

I hereby certify that the work which is being presented in the thesis entitled "**NUMERICAL STUDY OF HEAT TRANSFER AND ENTROPY GENERATION IN NANOFLUID FILLED ENCLOSURE**" in partial fulfilment of the requirements for the award of the degree of **Doctor of Philosophy** and submitted in the Department of Mathematics, Indian Institute Of Technology Roorkee is an authentic record of my own work carried out during a period from July, 2013 to November, 2017 under the supervision of Dr. Ameeya Kumar Nayak, Associate Professor, Department of Mathematics, Indian Institute Of Technology Roorkee.

The matter presented in this thesis has not been submitted by me for the award of any other degree of this or any other institute.

(SUMIT MALIK)

This is to certify that the above statement made by the candidate is correct to the best of our knowledge.

Date: **(Ameeya Kumar Nayak)**

Supervisor

The Ph.D. Viva-Voce Examination of **Mr. Sumit Malik,** Research Scholar, has been held on……

Chairman, SRC Signature of External Examiner

This is to certify that the student has made all the corrections in the thesis.

Signature of Supervisor Head of the Department/Chairman, ODC

Abstract

In today's world the need and dependency of human being on mechanical system is increasing day by day. With the increasing demand, the advancement in the performance of mechanical system is one of the most important factor for energy optimization. The improvement in the performance of any mechanical system means the increase in the life of mechanical system and improvement in the working efficiency in the sense of time as well as production at optimal cost.

This thesis presents a detailed numerical studies for the analysis of various aspects of fluid flow, heat transfer and entropy generation within an enclosure equipped with different types of thermal boundary conditions for fluid and porous media with and without induced magnetic field effects. Comparative studies are conducted over clear fluid as well as nanofluid with increasing nanoparticle volume fraction to obtain the most suitable fraction of nanoparticles in the base fluid in order to improve the thermal performance of mechanical systems. Method of entropy generation minimization is used for the modeling and optimization of energy systems related to heat exchangers in aircraft engines, cooling devices for cars and nuclear power plants. The total entropy generation in such systems can be minimized under some physical and geometric arrangements and some optimal configuration can provide the minimum energy loss.

The numerical solution of set of non-linear coupled partial differential equations governing the fluid flow, temperature distribution and entropy generation is attained by finite volume based approach. The numerical simulation has been presented in the form of streamlines, isotherms, energy flux vectors and entropy generation in various flow conditions of industrial importance. The heat transfer rates are obtained in terms of local and average Nusselt number. Chapter-1 deals with various definitions of flow governing parameters and solution methods used in flow governing equations. The analysis of heat

and mass transfer, entropy generation with their measuring and controlling parameters such as Nusselt number, entropy generation, Bejan number is made in terms of various flow governing parameters such as Reynolds number, Rayleigh number, Richardson number and Darcy number etc.

In **Chapter-2**, we have studied the mixed convection heat transfer effects in a lid-driven enclosure filled with copper-water nanofluid due to a heated wall mounted block of constant heat flux attached along the vertical wall. A detailed analysis of flow and heat transfer properties are discussed by placing the heated mounted block on left and right vertical walls. The flow governing equations are solved numerically using streamfunction-vorticity formulation approach using finite volume method.

Chapter-3 deals with the study of copper-water nanofluid flow in a two-sided lid-driven rectangular enclosure in which the vertical walls move in different directions. Three different configurations have been considered on the basis of direction of movement of vertical walls to study the fluid flow and heat transfer effects to find an optimum configuration in order to obtain maximum heat transfer.

In **Chapter-4** we have presented a numerical study of hydromagnetic mixed convection flow inside a cubical enclosure filled with porous mixture. A sinusoidal time dependent discrete temperature gradient along the boundaries is considered. A time history analysis is made for flow and thermal stratification. The fluid flow and heat transfer analysis is made with the variation of Grashof number, Hartmann number, Darcy number and Prandtl number to obtain the average Nusselt number and bulk average temperature.

Chapter-5 consists of the same configuration as that of chapter-3 and a detailed analysis of entropy generation in combination with heat transfer effects is considered. The energy efficiency is discussed on the basis of performance evaluation criteria based on heat transfer and entropy generation.

In **Chapter-6** a similar configuration as that of chapter-4 is used to study the heat transfer and entropy generation of a magnetohydrodynamic nanofluid flow. The flow is influenced by time periodic discrete heat sources. A detailed study of fluid flow, heat transfer and entropy generation is used to study the performance of the system. Based on the proposed performance evaluation criteria an optimum configuration is suggessted to obtain maximum heat transfer on the cost of minimum entropy generation.

Bibliography is the last section of the thesis. All the computations are made by writing our own codes in MATLAB and FORTRAN, rather then using existing toolboxes. TECPLOT and MATLAB are used for plotting of simulated data.

List of Publications

1. Sumit Malik, A. K. Nayak, MHD convection and entropy generation of nanofluid in a porous enclosure with sinusoidal heating, ***International Journal of Heat and Mass Transfer*** *(Elsevier)*, Volume 111, August 2017, Pages 329-345, ISSN 0017-9310.

2. Sumit Malik, A. K. Nayak, Effect of moving walls on heat transfer and entropy generation in a nanofluid-filled enclosure, ***Journal of Engineering Mathematics, Springer*** *(Springer)*, October 2017, Pages 1-19, ISSN 1573-2703.

3. A. K. Nayak, Sumit Malik, K. Venkateshwarlu, P. K. Jena, Magneto-convection and its effect on partially active thermal zones in a porous square domain, ***International Journal of Heat and Mass Transfer*** *(Elsevier)*, Volume 95, April 2016, Pages 913-926, ISSN 0017-9310.

4. Sumit Malik, A. K. Nayak, Comparative study of nanofluid mixed convection and its effect on partially active thermal zones in two sided lid-driven cavity, ***Engineering Science and Technology, an International Journal*** *(Elsevier)*, Volume 19, September 2016, Pages 12831298, ISSN 2215-0986.

5. Sumit Malik, A. K. Nayak, Buoyancy Driven heat transfer in nanofluids due to wall mounted heat source, ***Alexandria Engineering Journal*** *(Elsevier)*, Volume 55, June 2016, Pages 797810, ISSN 1110-0168.

6. Neha Gupta, A. K. Nayak, Sumit Malik, Conjugate heat and species transport in an air filled ventilated enclosure with a thermo-contaminated block, ***International Journal of Heat and Mass Transfer*** *(Elsevier)*, Volume 117, February 2018, Pages 388-411, ISSN 0017-9310.

7. K. Venkateshwarlu, A. K. Nayak, Bhupinder Singh, V. K. Katiyar, Sumit Malik, Heat transfer effect in an air cooled ventilated enclosure, ***Journal of Thermophysics and Heat Transfer*** *(AIAA)*, Volume 30, 2016, Pages- 318-333, ISSN-0887-8722.

Acknowledgements

Through this thanks giving note, at the first place, I express my deepest gratitude to God Almighty for providing me this golden opportunity to pursue higher studies under the supervision of Dr. A. K. Nayak, Department of Mathematics, IIT Roorkee. No words are enough to express my regards and gratitude to my supervisor for his valuable guidance, encouragement and constant support throughout my research work. His presence has made this time significant yet relishable. I shall always remain obligated to him for pertinent and well-timed comments rendered by him at various demanding phases during this entire course of study. His foreknowledge and thoughtfulness has made me learn a lot not only in Ph.D. programme but also in strenuous situations of my life. Most importantly his technical solidarity along with the programming skills and amazingly wonderful social behavior make him a man of substance and an inspiring teacher.

My sincere gratitude to Prof. V. K. Katiyar, as Head, Department of Mathematics, IIT Roorkee for his valuable direction, constant support and for providing all the necessary facilities for carrying out research work. I also thank Prof. Tanuja Srivastava, DRC Chairman, Prof Rama Bhargava, SRC Chairman, all the members of Student Research Committee and faculty members of the department for their unstinted support and encouragement at all levels.

My deepest regards to Dr. Kaushik Pal, Department of Mechanical Engineering, for providing me necessary advice and discussions as and when required. His valuable comments has made me overcome the flaws and demerits of this work.

Last, but not the least, my candid thanks to my friends Amit, Vikram, Bimal, Indira, Rangoli, Ruchi, Alka, Kalu Ram, Abhishek, Ainul, Neha, Renu and Dr. Sandeep Mogha for their whole-hearted help and assistance.

I wish to put on records that whatever I have achieved in my life is due to the blessings

and unconditional support of my father Sh. Dhyan Singh Malik, mother Smt. Savita and brother Dr. Amit Malik. No words to express my thanks to my wife Sumita, whose unconditional love, patience and kindness has made me achieve whatever I deserve.

I can not wrap it here without expressing my gratitude to the Ministry of Human Resource and Development, India, for the financial support provided by them in the form of JRF and SRF.

Thanks is also due to all those who helped me directly or indirectly for completion of this work.

Roorkee (Sumit Malik)

15 October, 2017

Table of Contents

List of Tables

List of Figures

Nomenclature

Notation	Description
C_p	Specific heat capacity (J/kgK)
g	Gravitational acceleration (m/s^2)
B_0	Magnetic field (Amp/m)
K	Permeability of the porous medium (m^2)
H	Height of cavity (m)
W	Width of cavity (m)
L	Length of cavity (m)
x^*, y^*, z^*	Cartesian coordinates (m)
x, y, z	Dimensionless cartesian coordinates
k	Thermal conductivity (W/m K)
Gr	Grashof number $(\beta g L^3 \Delta T/\nu^2)$
Pr	Prandtl number (ν/α)
Ra	Rayleigh number $(\beta g L^3 \Delta T/(\nu\alpha))$
Re	Reynolds number $(\rho U_0 H/\mu)$
Ri	Richardson number $(\beta g L \Delta T/v^2)$
Da	Darcy number (K/L^2)
Ha	Hartmann number $(B_0 L^2 \sigma_e/\mu)$
A	Amplitude factor (L)
T^*	Temperature (K)
T	Dimensionless temperature
u^*, v^*, w^*	Components of velocity (m/s)
u, v, w	Dimensionless velocity components

U_0	Reference horizontal velocity (m/s)
V	Volume of the enclosure (L^3)
$\mathbf{V}$	Velocity vector
p^*	Pressure (N/m^2)
p	Dimensionless pressure
t^*	Time (s)
t	Dimensionless time
S^*	Entropy $(Wm^{-3}K^{-1})$
S	Dimensionless entropy
H'	Heatfunction
E	Energy flux vector
q	Heat flux (Wm^{-2})
Be	Bejan number
Nu	Nusselt number
Greek Letters	
Ψ	Stream function (m^2/s)
ψ	Dimensionless stream function (Ψ/α_f)
Ω	Vorticity (s^{-1})
ω	Dimensionless vorticity $(\Omega H^2/\alpha_f)$
σ	Ratio of heat capacity $([\epsilon(\rho C_p)_f + (1-\epsilon)(\rho C_p)_s]/(\rho C_p)_f)$
σ_e	Electrical conductivity of the medium
$\hat{\omega}$	Period
δ	Dimensionless period
α	Thermal diffusivity $(k/(\rho C_p))$ (m^2/s)
β	Coefficient of thermal expansion (K^{-1})
ϕ	Solid volume fraction
μ	Dynamic viscosity(Pa s)
ν	Kinematic viscosity (m^2/s)
ρ	Density (kg/m^3)
Subscripts	
$_f$	Fluid
$_m$	Average

nf	Nanofluid
o	Reference state
s	Solid
w	Wall
c	Cold
h	Hot
ff	Fluid flow
ht	Heat transfer
mf	Magnetic field
gen	Total
l	Left wall
r	Right wall

Chapter 1

Introduction

1.1 Motivation

Human life is getting changed in every span of time in today's world and the need to control and speed up the processes (either for quick response or for stability purposes) is one of the most fundamental requirements of present generation. The work efficiency and performance of electrical as well as mechanical equipments in industrial processes is based on their thermal management. In many industrial processes involving electronic devices, heat exchangers, transportation vehicles, nuclear reactors, glass production and indoor cooling systems in industries, the requirement of high heat transfer rate is very essential. Fluids are used very frequently as the heat transfer carriers for these purposes. High heat transfer rate is utmost important in context of measuring the performance in both heating as well as cooling. However, the traditional fluids like water, ethylene glycol, kerosene, engine oil etc. have inherently low thermal conductivity, which limits the heat transfer efficiency in equipments. To overcome this drawback, the idea of utilizing nano-sized metallic and non-metallic particles in a solution form came into existence.

The thermal properties of the fluid can be improved by suspending nano-sized particles of higher thermal conductivity into the base fluid. The term 'nanofluid', coined by S.U.S. Choi [52] is characterized by enrichment of base fluid like water, ethylene glycol or oil with nanoparticles in various types of metals, oxides, carbides and carbon. Afterwards, a lot of applications of nanofluids came into existence such as solar absorption [253], nuclear systems cooling [249], space and defence technology [237] [58], electronic cooling components [216], friction reduction [239], magnetic sealing [251], energy storage [41],

antibacterial activity [225], nano-drug delivery [201], power generation in nuclear reactors [200], energy storage [174] and more specifically in any heat removal process involved in industrial applications.

The ongoing research have extended the utilization of various class of nanoparticles over base cooling fluids to characterize the heat removal process. Most Commonly used nanoparticles are Cu, CuO, Al_2O_3, TiO_2, Fe, Au and the base fluids consists of water, oil, ethylene glycol, toluene etc. The diameter of nanoparticles used in the formation of nanofluids lies mostly in the range of $1 - 100$nm [202]. Nanoparticles are easily fluidized into the base fluid and are sufficiently small in size because of which the problem of blockage in channels and erosion of walls does not appear. Nanofluids satisfies the basic need of improving the thermal conductivity of traditional fluids by suspending nanoparticles of relatively higher heat transfer rate.

The heat transfer characteristics and energy efficiency can be improved by minimizing the loss of energy inside the system. The loss of available energy in the separation systems due to irreversible processes of heat and mass transfer and thermal mixing is directly proportional to the entropy generation inside the system. Hence, energy efficiency in any thermal system requires the basic understanding of entropy generation which is based on second law of thermodynamics. According to second law of thermodynamics, the entropy in any cyclic process is always non-decreasing. Thus, in order to obtain a better performance of the system, the system should be designed in such a fashion that it generates minimum entropy.

1.2 Fluid flow and heat transfer

The motion of fluid due to various forces and stresses is termed as fluid flow. This can be observed during the pouring of water or can be felt when the motion of air caused due to the rotation of fan inside the room. However, a clear understanding of fluid flow pattern can provide us the important information regarding energy saving, optimum output of products from any process and better mixing of fluids in industrial applications. The performance of mixing of fluid inside any domain depends on various parameters effecting the flow pattern e.g., velocity, flow direction, presence of obstacles in the flow etc. A

balanced and favorable use of these parameters may lead to a quick and stable response of machines which are the fundamental requirement of many modern industrial processes. Another application of fluid flow and heat transfer can be found in our daily life for maintaining the indoor air comfort while using air-conditioner inside the room. The cooling efficiency of air-conditioner is highly dependent on the location/positioning inside the room, to obtain the best output at low energy consumption.

Energy exchange in the form of heat between two different regions of the considered medium or in between individual elements is termed as heat transfer. It can be simply observed, when the movement of heat energy occurs among two systems resulting from the temperature difference and it moves from regions of higher temperature to regions of lower temperature. Heat transfer in fluid flow are usually classified into three different modes i.e. a) radiation b) conduction and c) convection.

The interplay of energy generated during the exchange of thermal radiations between two or more bodies is termed as radiation. The radiative transfer occur through electromagnetic waves, when heat released by one body travels through a medium or through space and is absorbed by another body. There does not require any medium between the two bodies for heat transfer via radiation whereas both convection and conduction requires a medium for general heat transfer. Moreover, the energy exchange takes place without any medium even in its presence. The perfect example elaborating this phenomenon is the sun's heat, which travels to earth as radiations traveling through the vacuum of space. Here, the photons play the key role of intermediaries that travel at the speed of light.

Conduction is the process of heat transfer via molecules when there exists a direct contact between the substances. The heating of the substance leads to vibration in the molecules due to energy gain. The vibrating molecules transfer a part of their energy as they bump into the nearby particles. Thus, conduction is the exchange of heat energy due to molecular transport of energy. Motion of particles in a conducting medium is not necessary for energy transfer and this process of energy transfer from higher levels to lower levels continues till an equilibrium stage is reached. This phenomenon can be described well by using a steel rod. If one end of the rod is heated by putting it on a stove, the other portion soon becomes hot and the energy in the form of heat from

the stove causes an increase in the rate of vibration on the end which is held up on the stove. These vibration leads to the molecules bump into nearby particles and transferring a share of their energy into the adjacent molecules resulting an increase of temperature throughout the rod. Thermal conductivity is that property of the substance which decides how rapidly the exchange of thermal energy occurs within the substance.

Convection is the exchange of thermal energy from one place to another place due to the bulk movement of fluids such as liquids and gases. This exchange of thermal energy occurs due to the motion of non-isothermal fluids causing a heat transfer difference. Heat transfer by convection is always followed up by another property of fluids called as conduction. There are two types of convection that occur in the system: a) Forced convection and b) Natural convection. Forced convection refers to the phenomena, when an external source is involved to generate the motion inside the system, i.e., the induction of convection current artificially inside the system by pumping, stirring, vibration etc.

If we non-dimensionalize the governing equations for fluid flow due to forced convection, several non-dimensional parameters come into picture. One of them is the Reynolds number (Re). Reynolds number is named after Osborne Reynolds (1883) that quantifies the relative importance of inertial forces and viscous forces. Reynolds number can be written as

$$Re = \frac{\text{inertial forces}}{\text{frictional forces}} = \frac{\rho u \frac{\partial u}{\partial x}}{\mu \frac{\partial^2 u}{\partial y^2}} \sim \frac{\rho U.(U/L)}{\mu(U/L^2)} \sim \frac{\rho U L}{\mu}$$

where U and L are characteristic velocity and length, respectively. Two flows are said to be mechanically similar if the Reynolds number is equal for both the flows.

Natural convection refers to the flow pattern which arises due to density difference either by temperature or mass variation in the presence of gravity. It is also called buoyancy induced convection process. In natural convection, the fluid surrounding a heat or concentration source gets heated and rises against the gravity due to buoyancy force. It is replaced by colder fluid that moves downward and again gets heated. This process repeats itself thus forming natural convection current and transferring heat or solutal energy from bottom to top. It can be noted that the absence of natural convection lead to lower heat transfer rate as heat transfer would be by conduction. At a constant pressure, buoyancy force is proportional to density difference which in turn is proportional

to temperature difference. Therefore, it can be stated that for a larger temperature difference between fluid surrounding the heat source and fluid away from it, the buoyancy force would be larger, thus resulting in stronger natural convection currents and higher heat transfer rate.

Natural convection can be well described with boiling water. If a pan filled with water is kept on stove, the water adjacent to bottom surface gets heated and its density is reduced, which moves to the top and the cold water replaces it in the bottom. This transfer of heat from the bottom of the pan to the top of the pan is termed as natural convection heat transfer. In natural convection, the fluid motion is caused by buoyancy forces due to density variation of fluid in contact with heated boundaries. The flow velocities are basically developed by temperature differences and the boundary layers are of same order irrespective of Prandtl number, which is defined as,

$$Pr = \frac{\nu}{\alpha}.$$

The heat flux at a wall is given by

$$q_{T_w} = -k \left(\frac{\partial T}{\partial y} \right)_w$$

where T_w is the surface temperature and $\left(\frac{\partial T}{\partial y}\right)_w$ is the gradient of fluid temperature at the body surface. Also, from Newton's law of cooling, the heat flux can be written in terms of heat transfer coefficient h as,

$$q_{T_w} = h(T_w - T_0) \quad \text{or} \quad h = -\frac{k \left(\frac{\partial T}{\partial y}\right)_w}{(T_w - T_0)}.$$

The heat transfer is measured in terms of the non-dimensional quantity called as Nusselt number and defined by

$$Nu = \frac{hL}{k}$$

Here, L denotes the characteristic length of the body. The non-dimensional parameter involving the coefficient of thermal expansion is

$$Gr_T = \frac{g\beta_T(T_w - T_0)L^3}{\nu^2}$$

where, Gr_T may be interpreted in physical term as representing the ratio of buoyancy force to viscous force. This plays same role in natural convection as the Reynolds number in forced convection.

Mixed convection refers to the convection process due to both forced and natural convection to serve the energy transfer. This form of convection can be visualized in the case of heat removal from a hollow plain channel heated from downwards by using any mechanical device at the inlet or exhaust on the outlet of the channel. Nowadays, a study of mixed convection and heat transfer in enclosures is invariably encountered in many industrial heating or cooling applications including cooling of electronic devices, solar collectors, float glass production, drying technologies, chemical processing equipments, etc. and is of great interest for researchers. This type of fluid flow and heat transfer represents a complicated flow phenomena due to the movement of one or more walls which involves forced convection and the temperature difference causing secondary buoyancy driven flow.

1.3 Introduction to fluid mechanics

Fluid mechanics deals with the study of transportation of fluid and forces acting on it. The movement and characterization of fluid flows are described either by using Eulerian or Lagrangian approach. In Eulerian approach, a certain control volume is fixed in space through which the fluid flows. The motion of fluid is demonstrated by the mechanical properties of fluid such as velocity and pressure at fixed locations of an allusion frame in space with variation of time. Lagrangian approach represents the fluid motion by considering individual fluid particles which are tracked in terms of their positions and velocities. These approaches can be imagined with the observation of a moving car as; if the observer is fixed at a point of frame and observing the movement of car at one fixed point then this represents the Eulerian approach but if the observer is sitting in the car and observing the motion of car then this represents the Lagrangian approach. The fluid flow and mechanical properties used in this thesis are based on Eulerian approach.

1.3.1 Basic flow governing equations

The flow phenomenon and characteristics of fluid motion are based on three well known fundamental conservation laws; i.e., conservation of mass, conservation of momentum and conservation of energy. The basic flow governing equations are derived by using Eulerian

system and the material derivative used in the formulation are,

$$\frac{D}{Dt} = \frac{\partial}{\partial t} + \mathbf{V}.\nabla$$

where,

$$\nabla = \mathbf{i}\frac{\partial}{\partial x} + \mathbf{j}\frac{\partial}{\partial y} + \mathbf{k}\frac{\partial}{\partial z}.$$

Conservation of mass: *The continuity equation*

The equation of continuity is based on the principle of conservation of mass, i.e., mass of a system can neither be created nor destroyed. Hence, in an isolated system having no source and sink, the mathematical expression of the law of conservation of mass is defined as: Net mass outflow (inflow) in a control volume through surface S = The time rate of decrease (increase) of mass inside control volume.

The equation of continuity is given by:

$$\frac{D\rho}{Dt} + \rho\nabla.\mathbf{V} = 0$$

where ρ and $\mathbf{V}$ are density and velocity fields of fluid respectively.

When the density of the fluid changes significantly due to pressure and temperature, then the fluid is called compressible, otherwise incompressible. The work of this thesis is restricted to only incompressible fluid. The density variation assumes the Boussinesq approximation and hence the continuity equation satisfies,

$$\nabla.\mathbf{V} = 0.$$

In cartesian coordinates, the above equation can be written as:

$$\frac{\partial u^*}{\partial x^*} + \frac{\partial v^*}{\partial y^*} + \frac{\partial w^*}{\partial z^*} = 0$$

where u^*, v^* and w^* denotes the dimensional velocity components in the direction of x^*, y^* and z^* axis respectively. The non-dimensional form of continuity equation can be obtained by using the following dimensionless variables,

$$x = \frac{x^*}{L},\ y = \frac{y^*}{L},\ z = \frac{z^*}{L},\ u = \frac{u^*L}{\alpha},\ v = \frac{v^*L}{\alpha},\ w = \frac{w^*L}{\alpha} \tag{1.1}$$

where, α denotes the thermal diffusivity.

Finally, the non-dimensional form of continuity equation is given by,

$$\frac{\partial u}{\partial x} + \frac{\partial v}{\partial y} + \frac{\partial w}{\partial z} = 0. \tag{1.2}$$

Conservation of momentum: *The Navier − Stokes equations*

Momentum equations are based on the *Newton's second law of motion*, which satisfies the proportionality relation between applied force and resulting acceleration of a particle with mass m and is given by:

$$\mathbf{F} = m\mathbf{a}$$

The momentum equations for incompressible fluid takes the form

$$\frac{D\mathbf{V}}{Dt} = -\frac{1}{\rho}\nabla p + \nu\nabla^2\mathbf{V}$$

where, p is the pressure, $\nu(= \mu/\rho)$ is the kinematic viscosity and μ is the fluid viscosity respectively. In cartesian coordinates, the above equation is given by

$u - momentum\ equation$

$$u^*\frac{\partial u^*}{\partial x^*} + v^*\frac{\partial u^*}{\partial y^*} + w^*\frac{\partial u^*}{\partial z^*} = -\frac{1}{\rho}\frac{\partial p^*}{\partial x^*} + \nu\left(\frac{\partial^2 u^*}{\partial x^{*^2}} + \frac{\partial^2 u^*}{\partial y^{*^2}} + \frac{\partial^2 u^*}{\partial z^{*^2}}\right),$$

$v - momentum\ equation$

$$u^*\frac{\partial v^*}{\partial x^*} + v^*\frac{\partial v^*}{\partial y^*} + w^*\frac{\partial v^*}{\partial z^*} = -\frac{1}{\rho}\frac{\partial p^*}{\partial y^*} + \nu\left(\frac{\partial^2 v^*}{\partial x^{*^2}} + \frac{\partial^2 v^*}{\partial y^{*^2}} + \frac{\partial^2 v^*}{\partial z^{*^2}}\right) + g\beta(T^* - T_c)$$

and $w - momentum\ equation$

$$u^*\frac{\partial w^*}{\partial x^*} + v^*\frac{\partial w^*}{\partial y^*} + w^*\frac{\partial w^*}{\partial z^*} = -\frac{1}{\rho}\frac{\partial p^*}{\partial z^*} + \nu\left(\frac{\partial^2 w^*}{\partial x^{*^2}} + \frac{\partial^2 w^*}{\partial y^{*^2}} + \frac{\partial^2 w^*}{\partial z^{*^2}}\right).$$

The non-dimensional form of the above mentioned governing equations can be obtained by using the variables defined in eq. (1.1) and

$$p = \frac{p^* L^2}{\rho\alpha^2} \text{ and } T = \frac{T^* - T_c}{T_h - T_c}$$

as, $u - momentum\ equation$

$$u\frac{\partial u}{\partial x} + v\frac{\partial u}{\partial y} + w\frac{\partial u}{\partial z} = -\frac{\partial p}{\partial x} + Pr\left(\frac{\partial^2 u}{\partial x^2} + \frac{\partial^2 u}{\partial y^2} + \frac{\partial^2 u}{\partial z^2}\right), \tag{1.3}$$

$v-$ *momentum equation*

$$u\frac{\partial v}{\partial x}+v\frac{\partial v}{\partial y}+w\frac{\partial v}{\partial z}=-\frac{\partial p}{\partial y}+Pr\left(\frac{\partial^2 v}{\partial x^2}+\frac{\partial^2 v}{\partial y^2}+\frac{\partial^2 v}{\partial z^2}\right)+RaPrT \tag{1.4}$$

and $w-$ *momentum equation*

$$u\frac{\partial w}{\partial x}+v\frac{\partial w}{\partial y}+w\frac{\partial w}{\partial z}=-\frac{\partial p}{\partial z}+Pr\left(\frac{\partial^2 w}{\partial x^2}+\frac{\partial^2 w}{\partial y^2}+\frac{\partial^2 w}{\partial z^2}\right) \tag{1.5}$$

where, $Pr=\nu/\alpha$ and $Ra=g\beta(T_h-T_c)L^3/(\nu\alpha)$ are the Prandtl number and Rayleigh number respectively.

Conservation of energy: *The energy equation*

The equation of conservation of energy is based on the first law of thermodynamics, which states that the energy can neither be created nor be destroyed. Let us consider that heat dQ is added with the volume ΔV during time Δt and resulting an increment in internal energy dE_T to carry out the work done dW, then according to the first law of thermodynamics,

$$dQ=dE_T+dW$$
$$\Rightarrow \frac{dQ}{dt}=\frac{dE_T}{dt}+\frac{dW}{dt}$$

i.e., rate of heat transfer into the system=rate of increase of internal energy of the system + rate of work done by surface force (combined force due to pressure and shear effect) on the surrounding.

The resulting energy equation for a viscous incompressible fluid is,

$$u^*\frac{\partial T^*}{\partial x^*}+v^*\frac{\partial T^*}{\partial y^*}+w^*\frac{\partial T^*}{\partial z^*}=\alpha\left(\frac{\partial^2 T^*}{\partial x^{*^2}}+\frac{\partial^2 T^*}{\partial y^{*^2}}+\frac{\partial^2 T^*}{\partial z^{*^2}}\right)+\phi$$

where, ϕ is the dissipation function given by

$$\phi=2\frac{\mu}{\rho C_p}\left[\left(\frac{\partial u^*}{\partial x^*}\right)^2+\left(\frac{\partial v^*}{\partial y^*}\right)^2+\left(\frac{\partial w^*}{\partial z^*}\right)^2\right]+\frac{\mu}{\rho C_p}\left[\left(\frac{\partial u^*}{\partial y^*}+\frac{\partial v^*}{\partial x^*}\right)^2+\left(\frac{\partial u^*}{\partial z^*}+\frac{\partial w^*}{\partial x^*}\right)^2+\left(\frac{\partial v^*}{\partial z^*}+\frac{\partial w^*}{\partial y^*}\right)^2\right]$$

where, C_p is the heat capacity at constant pressure per unit mass.

Finally, the non-dimensional form of energy equation with negligible viscous dissipation can be expressed as,

$$u\frac{\partial T}{\partial x}+v\frac{\partial T}{\partial y}+w\frac{\partial T}{\partial z}=\frac{\partial^2 T}{\partial x^2}+\frac{\partial^2 T}{\partial y^2}+\frac{\partial^2 T}{\partial z^2}.$$

1.4 Entropy generation

The efficiency of any mechanical system is based on the total energy available to the system and depends on the usefulness of the output. Every real process is irreversible in nature i.e., during any mechanical process some of the available energy (called as exergy) is always lost, which effects the efficiency of the system. Entropy generation; a never decreasing quantity, is the measure of effect of irreversibilities during a process. The performance of any mechanical system can be improved by minimizing the energy loss within the system. According to Gouy-Stodola principle, the exergy loss in the system during the irreversible process of heat and mass transfer and thermal mixing is directly proportional to the entropy generation. Thus, a better understanding of entropy generation inside the system is needed for the efficient designing of real systems. Naturally, the minimization of entropy generation is not an easy task in real design applications due to various factors such as the complexity of the model, complicated boundary conditions and the operating point with time. The application procedure is divided into two types; (i) methods based on deterministic approach, (ii) methods based on heuristic approach. Majority of applications for heat transfer problems belongs to first category.

A complete study on reduction of entropy generation for various physical and geometrical combinations may enable the user to obtain most efficient system for minimization of entropy generation inside the system. The entropy generation minimization method has a large scale of applications in energy exchangers of heat engines, air conditioners, nuclear reactors, power plants, refrigerators etc. There are various factors responsible for entropy generation in a system depending on the flow conditions and flow domain such as irreversibility due to fluid friction, heat transfer, magnetic field, porosity etc. The entropy generation inside the closed domain due to fluid friction occurs mostly near the boundaries of the domain and the corners of the flow domain. However, the entropy generation due to heat transfer is mostly found near the heat source locations of the system. The overall contribution of entropy generation with respect to each local factor varies with the flow conditions and the heat transfer properties. The concept of entropy generation is combined with the principles of fluid mechanics to acquire the information about the influence of irreversibilities observed inside the system.

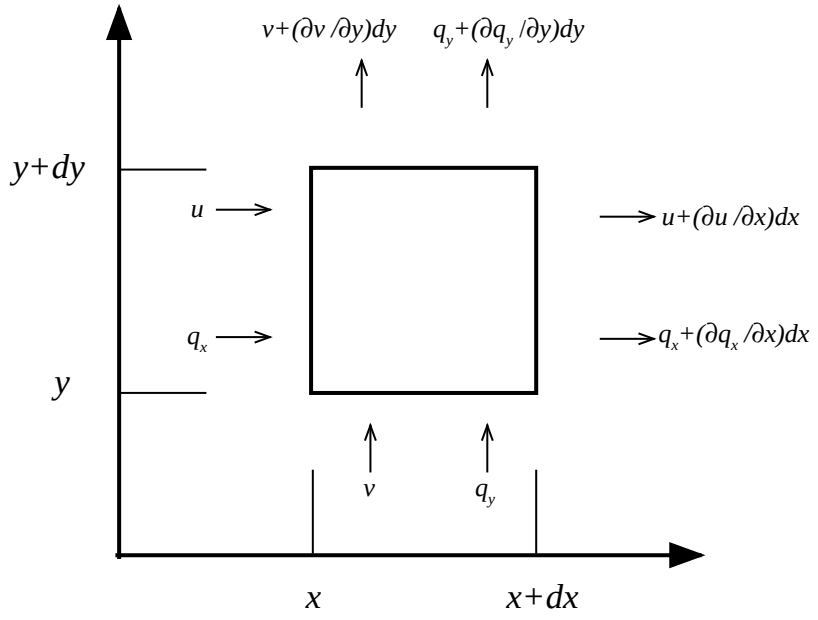

Figure 1.1: Analysis of second law of thermodynamics

1.4.1 Mathematical approach for entropy generation

Let us consider an open thermodynamical system subjected to mass flux, energy transfer and entropy generation interactions that penetrate the fixed control surface formed by the elementary rectangle of sides dx and dy surrounding the point (x, y) in a fluid engaged in convective heat transfer as shown in Fig.1.1. The size of element is considered to be sufficiently small so that the thermodynamic state of fluid inside the fluid element can be regarded as independent of its position. The state of fluid element in $dxdy$ may get changed with time. The entropy generation rate S^*_{gen} per unit volume may be estimated by using second law of thermodynamics for $dxdy$ as an open system.

The total entropy generation inside the system is the sum of entropy associated with heat transfer, entropy convected into and out of the system and the time rate of entropy

accumulation in the $dxdy$ control volume. In mathematical form it can be expressed as,

$$\begin{aligned} S^*_{gen}dx^*dy^* = &\frac{q_x + \frac{\partial q_x}{\partial x^*}dx^*}{T^* + \frac{\partial T^*}{\partial x^*}dx^*}dy^* + \frac{q_y + \frac{\partial q_y}{\partial y^*}dy^*}{T^* + \frac{\partial T^*}{\partial y^*}dy^*}dx^* - \frac{q_x}{T^*}dy^* - \frac{q_y}{T^*}dx^* \\ &+\left(s^* + \frac{\partial s^*}{\partial x^*}dx^*\right)\left(u^* + \frac{\partial u^*}{\partial x^*}dx^*\right)\left(\rho^* + \frac{\partial \rho^*}{\partial x^*}dx^*\right)dy^* \\ &+\left(s^* + \frac{\partial s^*}{\partial y^*}dy^*\right)\left(v^* + \frac{\partial v^*}{\partial y^*}dy^*\right)\left(\rho^* + \frac{\partial \rho^*}{\partial y^*}dy^*\right)dx^* \\ &-s^*u^*\rho^*dy^* - s^*v^*\rho^*dx^* + \frac{\partial(\rho^* s^*)}{\partial t^*}dx^*dy^* \end{aligned}$$

$$\begin{aligned} \Rightarrow S^*_{gen} = &\frac{1}{T^*}\left(\frac{\partial q_x}{\partial x^*} + \frac{\partial q_y}{\partial y^*}\right) - \frac{1}{T^{*2}}\left(q_x\frac{\partial T^*}{\partial x^*} + q_y\frac{\partial T^*}{\partial y^*}\right) + \rho^*\left(\frac{\partial s^*}{\partial t^*} + u^*\frac{\partial s^*}{\partial x^*} + v^*\frac{\partial s^*}{\partial y^*}\right) \\ &+s\left(\frac{\partial \rho^*}{\partial t^*} + u^*\frac{\partial \rho^*}{\partial x^*} + v^*\frac{\partial \rho^*}{\partial y^*}\right) + s\rho^*\left(\frac{\partial u^*}{\partial x^*} + \frac{\partial v^*}{\partial y^*}\right). \end{aligned} \quad (1.6)$$

But according to mass conservation principle we have,

$$\frac{\partial \rho^*}{\partial t^*} + u^*\frac{\partial \rho^*}{\partial x^*} + v^*\frac{\partial \rho^*}{\partial y^*} + \rho^*\left(\frac{\partial u^*}{\partial x^*} + \frac{\partial v^*}{\partial y^*}\right) = 0. \quad (1.7)$$

Using the above relation in eq. (1.6) we have,

$$S^*_{gen} = \frac{1}{T^*}\left(\frac{\partial q_x}{\partial x^*} + \frac{\partial q_y}{\partial y^*}\right) - \frac{1}{T^{*2}}\left(q_x\frac{\partial T^*}{\partial x^*} + q_y\frac{\partial T^*}{\partial y^*}\right) + \rho^*\left(\frac{\partial s^*}{\partial t^*} + u^*\frac{\partial s^*}{\partial x^*} + v^*\frac{\partial s^*}{\partial y^*}\right). \quad (1.8)$$

The vectorial representation of the above equation is given by,

$$S^*_{gen} = \frac{1}{T^*}\nabla.\mathbf{q} - \frac{1}{T^{*2}}\mathbf{q}.\nabla T^* + \rho^*\frac{Ds^*}{Dt}. \quad (1.9)$$

Now, according to the first law of thermodynamics the rate of change of internal energy per unit volume is the sum of total rate of heat transfer by conduction, rate of work done due to compression and the rate of work done per unit volume associated with viscous dissipation. Therefore, in convective medium, the first law of thermodynamics for Newtonian fluid at a point can be written as,

$$\rho^*\frac{Du^*}{Dt^*} = -\nabla.\mathbf{q} - P^*(\nabla.v) + \mu\Phi$$

where μ and Φ are the viscosity and viscous dissipation function respectively. Furthermore, by using substantial derivative notation, the canonical relation given by

$$du^* = T^*ds^* - P^*d(1/\rho^*)$$

can be written as

$$\rho^* \frac{Ds^*}{Dt^*} = \frac{\rho^*}{T^*}\frac{Du^*}{Dt^*} - \frac{P^*}{\rho^* T^*}\frac{D\rho^*}{Dt^*}.$$

Substituting this in eq. (1.9) we obtain:

$$S^*_{gen} = -\frac{1}{T^{*2}}\mathbf{q}.\nabla T + \frac{\mu}{T^*}\Phi$$

now, if we consider Fourier law of heat conduction for an isotropic medium then,

$$\mathbf{q} = -k\nabla T^*$$

and hence,

$$S^*_{gen} = \frac{k}{T^{*2}}(\nabla T)^2 + \frac{\mu}{T^*}\Phi.$$

The representation of above equation in two dimensional cartesian coordinates is given by:

$$S^*_{gen} = \frac{k}{T^{*2}}\left[\left(\frac{\partial T^*}{\partial x^*}\right)^2 + \left(\frac{\partial T^*}{\partial y^*}\right)^2\right] + \frac{\mu}{T^*}\left\{2\left[\left(\frac{\partial u^*}{\partial x^*}\right)^2 + \left(\frac{\partial v^*}{\partial y^*}\right)^2\right] + \left(\frac{\partial u^*}{\partial y^*} + \frac{\partial v^*}{\partial x^*}\right)^2\right\}.$$

On introducing the non-dimensional variables, the above equation becomes,

$$S'_{gen} = \frac{k}{T_0^2}\left(\frac{\Delta T^2}{L^2}\right)\left[\left(\frac{\partial T}{\partial x}\right)^2 + \left(\frac{\partial T}{\partial y}\right)^2\right] + \frac{\mu\alpha^2}{T_0 L^4}\left\{2\left[\left(\frac{\partial u}{\partial x}\right)^2 + \left(\frac{\partial v}{\partial y}\right)^2\right] + \left(\frac{\partial u}{\partial y} + \frac{\partial v}{\partial x}\right)^2\right\} \tag{1.10}$$

$$\Rightarrow \frac{S'_{gen}}{\frac{k(\Delta T)^2}{L^2 T_0^2}} = \left[\left(\frac{\partial T}{\partial x}\right)^2 + \left(\frac{\partial T}{\partial y}\right)^2\right] + \frac{\mu\alpha^2 T_0}{L^2 k(\Delta T)^2}\left\{2\left[\left(\frac{\partial u}{\partial x}\right)^2 + \left(\frac{\partial v}{\partial y}\right)^2\right] + \left(\frac{\partial u}{\partial y} + \frac{\partial v}{\partial x}\right)^2\right\} \tag{1.11}$$

Hence, the total entropy generation (S_{gen}) can be written as,

$$S_{gen} = \left[\left(\frac{\partial T}{\partial x}\right)^2 + \left(\frac{\partial T}{\partial y}\right)^2\right] + \chi\left\{2\left[\left(\frac{\partial u}{\partial x}\right)^2 + \left(\frac{\partial v}{\partial y}\right)^2\right] + \left(\frac{\partial u}{\partial y} + \frac{\partial v}{\partial x}\right)^2\right\} \tag{1.12}$$

i.e.,

$$S_{gen} = S_{ht} + S_{ff}$$

where, $\chi = \frac{\mu\alpha^2 T_0}{k(\Delta T)^2 L^2}$, S_{ht} is entropy generation due to heat transfer and S_{ff} is entropy generation due to fluid friction.

1.5 Vorticity vector

The measure of rotation or circulation of a fluid particle is termed as vorticity vector and is defined by

$$\overrightarrow{\Omega} = \overrightarrow{\nabla} \times \overrightarrow{q}. \tag{1.13}$$

The vorticity components for irrotational flow are zero. The curve drawn on which the tangent to it at every point is in the direction of the vorticity vector is known as vortex line. The general equation of vortex line can be written as,

$$\overrightarrow{\Omega} \times d\overrightarrow{s} = \overrightarrow{0}. \tag{1.14}$$

For the cartesian co-ordinates [Ω_x, Ω_y, Ω_z] of $\overrightarrow{\Omega}$, the equation of vortex lines is given by,

$$\frac{dx}{\Omega_x} = \frac{dy}{\Omega_y} = \frac{dz}{\Omega_z}. \tag{1.15}$$

1.6 Stream function

The velocity components of an incompressible plain flow can be represented by using the derivatives of stream functions. The concept of stream function has originated from the principle of continuity. Considering a two-dimensional incompressible flow field in rectangular cartesian coordinates, the velocity components can be defined as,

$$u = u(x, y, t),\ v = v(x, y, t) \text{ and } w = 0.$$

The continuity equation corresponding to the steady two dimensional incompressible flow is given by,

$$\frac{\partial u}{\partial x} + \frac{\partial v}{\partial y} = 0. \tag{1.16}$$

Let us define a function $\psi(x, y, t)$ as

$$\frac{\partial \psi}{\partial y} = u,\ \frac{\partial \psi}{\partial x} = -v. \tag{1.17}$$

The function ψ as defined by eq. (1.17) satisfy eq. (1.16) is known as stream function. For a two-dimensional irrotational flow, we have,

$$\frac{\partial v}{\partial x} - \frac{\partial u}{\partial y} = 0. \tag{1.18}$$

Substituting the values of u and v from eq. (1.17) we get,

$$\frac{\partial}{\partial x}\left(-\frac{\partial \psi}{\partial x}\right)-\frac{\partial}{\partial y}\left(\frac{\partial \psi}{\partial y}\right)=0 \tag{1.19}$$

or

$$\frac{\partial^2 \psi}{\partial x^2}+\frac{\partial^2 \psi}{\partial y^2}=0, \tag{1.20}$$

in notation form this can be written as

$$\nabla^2 \psi = 0$$

where,

$$\nabla^2 = \frac{\partial^2}{\partial x^2}+\frac{\partial^2}{\partial y^2}.$$

Thus, the stream function satisfies the Laplace's equation for an irrotational flow.

Being a point function, ψ has a value at every point in the flow domain. Therefore, for a small variation in ψ we have,

$$d\psi = \frac{\partial \psi}{\partial x}dx+\frac{\partial \psi}{\partial y}dy \tag{1.21}$$

$$= -vdx+udy. \tag{1.22}$$

Moreover, the equation of streamline is,

$$\frac{u}{dx}=\frac{v}{dy}$$

or

$$udy-vdx=0. \tag{1.23}$$

On combining eqs. (1.21) and (1.23) we can obtain, $d\psi$=0 on the streamline. Hence, ψ is constant along the streamline. Once the value of ψ is known, the streamline can be drawn by joining the same values of ψ in the flow field.

1.7 Solution of Navier-Stokes equations

A large amount of complicated flow phenomenon can be modeled by Navier-Stokes equations and it is well known that the solution of Navier-stokes equations enable to obtain a complete description of the properties of fluid flow problems. But, due to the presence of

highly non-linear terms inside the flow governing equations it is very difficult to obtain the solution in exact form, only the weak solutions are available. As a consequence, it is natural to adopt numerical techniques to find solutions. In numerical approaches, the linear derivative terms are approximated by Taylor series expansion with neglecting the higher order terms, known as truncation error and the non-linear terms are approximated by suitable linearization techniques. Hence, in place of solving the complex differential equations, an equivalent system of difference equations is to be solved.

A proper numerical technique for the solution of Navier-Stokes equations together with appropriate initial and boundary conditions leads to an approximate solution of the physical flow problem. A proper choice of numerical method for a solution process need to satisfy three basic necessities; consistency, stability and convergence.

(i) **Consistency**: A finite difference approximation is said to be consistent if on reducing the mesh size and time step, the solution corresponding to this approximation approaches the exact solution of the partial differential equation, i.e., the truncation error of the difference scheme approaches to zero.

(ii) **Stability**: A finite difference approximation is said to be stable if the error of approximation is non-increasing from one step to next step of computation.

(iii) **Convergence**: A finite difference approximation is said to be convergent if the numerical solution approaches to the true solution of partial differential equation as the mesh and time step size approaches to zero.

The accuracy of numerical results for the fluid flow problems is highly dependent on the choice of numerical schemes. Hence, it is very important to choose the best suitable numerical methods for the solution of particular set of equations. Generally, the Navier-Stokes equations comprises of four terms namely, the temporal term, convective term, diffusive terms and source term. Each term can be approximated through various schemes depending on the accuracy of the solution. A comprehensive description about various schemes together with their applications and implementation is provided by many authors such as Anderson et al. [13], Fletcher [72], Anderson [14], Ferzigar and Peric [71], Peyret and Taylor. [182] and Lomax et al. [135].

1.7.1 Discretization schemes

To obtain the numerical solution of the Navier-Stokes equations, the governing equations needed to be discretized. The information contained in continuous form of original set of equations is provided to the set of discrete equations. The most common methods for discretization of flow governing equations are as follows:

(a) **Finite difference method**

(b) **Finite element method** and

(c) **Finite volume method**

(a) Finite difference method (FDM)

In FDM an equivalent finite difference expression is used at each grid point of the discretized domain for corresponding derivative term of unknown variables. One of the main advantage of using FDM compared to other methods is its ease of implementation. But, on the other hand this method has several drawbacks such as, low order accuracy in the derivative evaluation, difficulty in managing with irregular geometries and in implementation of unusual boundary conditions. The detailed description of FDM is made by Smith [223]. Admau and Sinha [2], Deresse and Sinha [59] and Sinha and Admau [218] presented a number of studies on differential equations where they have discussed various ways of approximating the derivatives in finite difference form.

(b) Finite element method (FEM)

FEM has been generalized and applied to solve a wide range of differential equations consisting of applications from fluid dynamics to structural dynamics. It provides a piecewise approximation to the differential equations. A variation of variable with the information on grid point is assumed and the solution is approximated by using interpolation functions between the grid points. As the assumed variables does not satisfy the differential equations in general, hence, a residual is obtained on substituting the assumed variable in the differential equation. The residual is then multiplied with a set of weight functions and an integration is performed over the considered domain. The most commonly used finite element approximations are least square method and Galerkin method. The most significant characteristics of FEM is the ability to handle the solution domains having

irregular geometry. In general it requires fewer grid points for a given accuracy of solution as compared to FDM. Some of the recent studies made using finite element method consists of [149, 150]. The main drawback of FEM is its complex algorithmic approach of solution and it continue to retain a low-order method. A complete discussion of FEM and its applications to the Navier-Stokes equations is made by Chung [54], Baker [19], Fletcher [72] and Oden [173] and detailed analysis is carried out with other methods.

(c) Finite volume method (FVM)

In FVM, the computational domain is divided into a number of non-overlapping control volumes in such a way that there is one control volume neighbouring each grid point and the governing differential equation is integrated over each control volume. FVM can be applied to any type of grids and hence, it is suitable in case of complex geometries also. The method is popular for dealing with various engineering applications because of its simple understanding and easy coding. Several commercial softwares such as FLUENT, STAR-CD, FLOW3D and PHOENICS employ FVM in their solution algorithm, since it involves easy coding as compared to other algorithms. Some of the recent studies made using finite volume method consists of [49, 80, 224, 252] A complete discussion with its application is made by Patankar [178], Anderson et al. [13] and several improvements are discussed by other authors such as Fletcher [72] and Versteeg and Malalashekera [240]. All the simulations performed in this thesis are based on FVM and hence a more detailed discussion of FVM is presented in the later part of the thesis.

1.7.2 Differencing schemes of Navier-Stokes equation

The Navier-Stokes equation comprises of various derivative terms namely, the temporal derivative, convective, diffusive and source terms which occur frequently in flow governing equations. For the solution purposes, all the four terms need to be approximated by various difference formula, which decides the level of accuracy of the solution. As far as the diffusion term is concerned, a discretization scheme for three-point central difference formula does not pose any problem in the solution. But, an extra care is required while selecting a difference scheme for convective terms. For example, a central differencing scheme for convective terms may lead to an intense non-physical oscillations, especially for the flows with higher Reynolds number. Generally, upwind schemes are used to overcome

this problem.

The difference scheme used for Marker and Cell (MAC) method are central difference schemes to approximate the derivatives. The stability of flow solution is achieved by discretising the convective term with two-point upwind difference scheme or a weighted average of upwind and central difference schemes [88]. On the other hand, the solutions are in accurate form if the local velocity vector is oblique to the local grid and the local velocity gradients are large. To attain more accurate solutions, a higher order upwind scheme can be used for convective terms.

Quadratic Upwind Interpolation for Convective Kinematics abbreviated as 'QUICK' scheme is one of the most attractive scheme used for higher order accuracy introduced by Leonard [133]. QUICK scheme is an attempt to achieve the accuracy of the central difference approximation and the stability inherent in upwinding by taking flow parameters in each direction separately to obtain quadratic upstream interpolation. This scheme can be interpreted as the pure upwind scheme augmented by gradient and curvature-type correction terms. Due to the one-dimensional form of interpolation, this scheme is suitable for steady or quasi-steady flows in which the cell Reynolds number is large. The scheme is modified and studied by many authors such as, Raithby et al. [187], Han et al. [84], Pollard and Siu [184], Shyy [212] and Hayase et al. [86].

1.7.3 Solution algorithm

The solution of Navier-Stokes equations may be attained in many ways. The common algorithms used for the solution methods are,

(a) **Explicit algorithm**

(b) **Implicit algorithm**

(c) **Semi-implicit algorithm**

(a) Explicit algorithm

Explicit algorithm uses the current state of system to calculate the later state of system. In other words, the value of unknown variable at next time level is represented in terms of variable at current time level which is already known. Hence, by using explicit algorithms,

the unknown variable at advanced state of time can be calculated in a very straight forward manner by using the current state of system. The explicit algorithms are famous and used because of their simple algorithm and easy implementation process. But, sometimes, to maintain the stability condition, it require very small time steps, which demand a huge number of iterations to find the converged solution, which leads to a significant increase in calculation time.

(b) Implicit algorithm

In implicit algorithm, the foremost variables are obtained by using both the current and later state of the system. In other words, the unknowns are represented in terms of known as well as unknown variables and the solution is achieved by solving simultaneous equations. The solution process may require some extra computations as compared to explicit algorithms but the implicit schemes have clear advantage for not being restricted by stability criteria. As a result, it easily handles the time steps and grid sizes used in the solution process, which enables to lower the computation time of solution.

(b) Semi-implicit algorithm

In semi-implicit algorithm, some variables are treated explicitly and some are treated implicitly. Particularly, for unsteady approaches the velocity components are updated to the new time level in a explicit manner while the pressure may be calculated implicitly by solving the pressure Poisson equation using successive over/under relaxation technique.

1.8 Solution approaches for incompressible Navier-Stokes equations

The solution of incompressible Navier-Stokes equations can be obtained by using either of the two ways:

(i) Vorticity-stream function formulation

(ii) Primitive variables approach.

1.8.1 Vorticity-stream function formulation

Vorticity-stream function formulation is one of the first unsteady, incompressible Navier-Stokes algorithm. Due to the lack of a separate equation for pressure term in Navier-Stokes

equation, it is difficult to deal with the conventional form of Navier-Stokes equation. Let us consider a two-dimensional incompressible flow, where the Navier-Stokes equations are given by,

$$\frac{\partial u^*}{\partial x^*} + \frac{\partial v^*}{\partial y^*}, \tag{1.24}$$

$$\frac{\partial u^*}{\partial t^*} + u\frac{\partial u^*}{\partial x^*} + v\frac{\partial u^*}{\partial y^*} = -\frac{1}{\rho}\frac{\partial p^*}{\partial x^*} + \left(\frac{\partial^2 u^*}{\partial x^{*2}} + \frac{\partial^2 u^*}{\partial y^{*2}}\right) \tag{1.25}$$

and

$$\frac{\partial v^*}{\partial t^*} + u\frac{\partial v^*}{\partial x^*} + v\frac{\partial v^*}{\partial y^*} = -\frac{1}{\rho}\frac{\partial p^*}{\partial y^*} + \left(\frac{\partial^2 v^*}{\partial x^{*2}} + \frac{\partial^2 v^*}{\partial y^{*2}}\right). \tag{1.26}$$

For the flow visualization and solution process, the conventional form of Navier-Stokes equations can be simplified by introducing two new dependent variables called as vorticity(Ω) and stream function (Ψ). The vorticity vector at any point can be defined as,

$$\overrightarrow{\Omega} = \nabla \times \overrightarrow{V}$$

and its two-dimensional form is given by,

$$\Omega_z = \overrightarrow{\Omega}.\hat{k} = \frac{\partial v^*}{\partial x^*} - \frac{\partial u^*}{\partial y^*}. \tag{1.27}$$

Now, introducing the stream function as

$$u^* = \frac{\partial \Psi}{\partial y^*}, \qquad v^* = -\frac{\partial \Psi}{\partial x^*} \tag{1.28}$$

which automatically satisfies the continuity equation [eq. (1.24)] of two-dimensional incompressible flows. On substituting these values of u^* and v^* in eq. (1.27) we get,

$$\frac{\partial^2 \Psi}{\partial x^{*2}} + \frac{\partial^2 \Psi}{\partial y^{*2}} = -\Omega \tag{1.29}$$

which is the kinematic equation relating to the vorticity and stream function known as the Poisson equation for Ψ.

Finally, on combining eqs. (1.25) and (1.26) using (1.29), a vorticity transport equation can be developed which is free from pressure term and is given by,

$$\frac{\partial \Omega}{\partial t^*} + u^*\frac{\partial \Omega}{\partial x^*} + v^*\frac{\partial \Omega}{\partial y^*} = \nu\left(\frac{\partial^2 \Omega}{\partial x^{*2}} + \frac{\partial^2 \Omega}{\partial y^{*2}}\right). \tag{1.30}$$

In this way, a set of three equations [eqs. (1.24), (1.25) and (1.26)] are replaced by a set of two coupled equations [eqs. (1.29) and (1.30)] known as streamline-vorticity formulation.

Moreover, the pressure can be obtained by solving the pressure Poisson equation, which can be obtained by using the momentum equations [eqs. (1.25) and (1.26)]. The pressure Poisson equation is given by,

$$\left(\frac{\partial^2 p^*}{\partial x^{*2}} + \frac{\partial^2 p^*}{\partial y^{*2}}\right) = 2\rho\left(\frac{\partial u^*}{\partial x^*}\frac{\partial v^*}{\partial y^*} - \frac{\partial v^*}{\partial x^*}\frac{\partial u^*}{\partial y^*}\right) \tag{1.31}$$

using relation established by eq. (1.17), the pressure Poisson equation in terms of stream function is give by,

$$\left(\frac{\partial^2 p^*}{\partial x^{*2}} + \frac{\partial^2 p^*}{\partial y^{*2}}\right) = 2\rho\left[\frac{\partial^2 \Psi}{\partial x^{*2}}\frac{\partial^2 \Psi}{\partial y^{*2}} - \left(\frac{\partial^2 \Psi}{\partial x^* \partial y^*}\right)\right]. \tag{1.32}$$

Although, the vorticity-stream function is comparatively easy to implement then the primitive variable approach, but it has drawbacks due to the lack of boundary conditions for vorticity and stream function. Also, the primitive variable approach can also be theoretically extendable to the three-dimensional problems in a straight forward manner.

1.8.2 Primitive variable approach

(a) Variable arrangement

The first and foremost issue regarding the discretization of the flow governing equations is to decide the domain discretization method. As the values of flow governing variables are to be calculated at the grid points of discretized domain hence, a proper and most suitable grid arrangement needs to be defined. The most comfortable choice is to consider same control volumes for each of the variables by storing all the variables at the same set of grid points. The process of such a grid arrangement is called *collocated grid* arrangement. The collocated grid arrangement in cartesian coordinates are represented in Fig. 1.2 in which all the flow governing variables $u,\ v,\ P$ are shown to be placed at the same location. The collocated arrangement of grids are preferred due to its simple and straight forward implementation process. This grid arrangement has a major advantage over the complicated flow domains, especially in the case when boundaries have slope discontinuities or the boundary conditions are discontinuous. A set of control volumes can be designed to fit the boundary including the discontinuity. The collocated grid arrangement is not much useful for the incompressible flow computations due to the difficulties with pressure-velocity coupling and the occurrence of oscillations in the pressure. Moreover, for

some of the problems it is possible to show that the collocated grid arrangement comes up with some physically unrealistic values of velocity and pressure as solutions. A detailed discussion regarding these difficulties is made by Patankar [178].

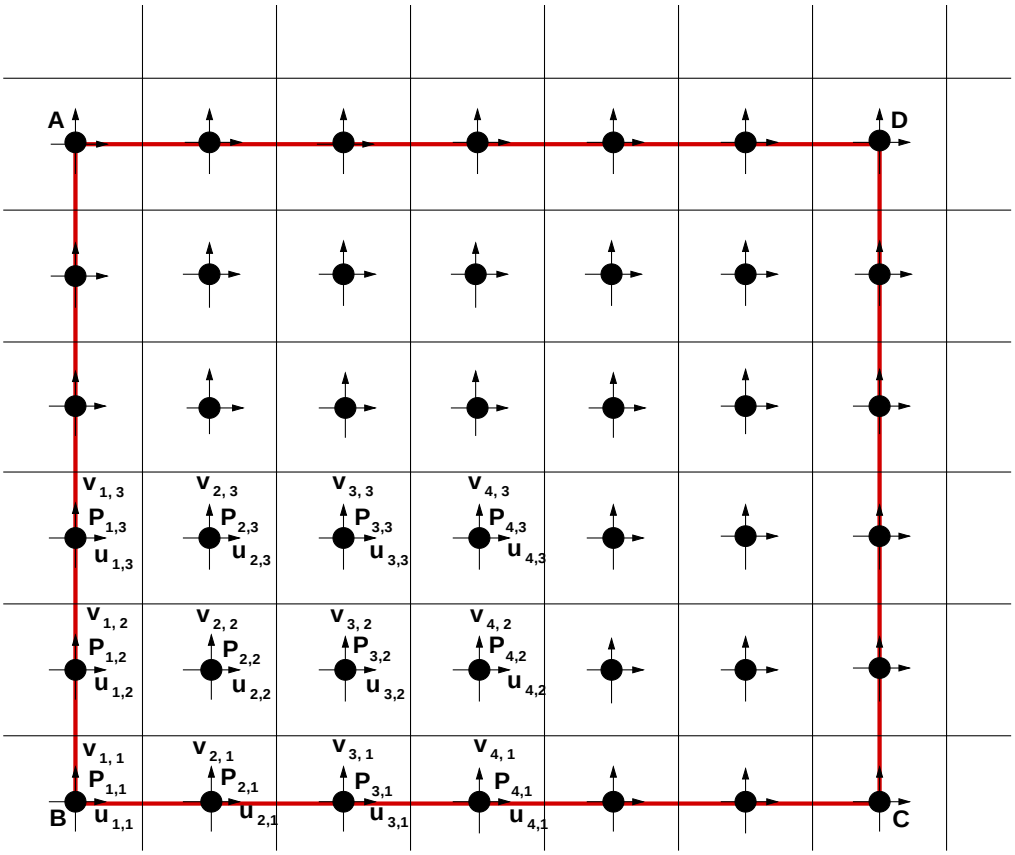

Figure 1.2: Collocated Grid

To overcome these complications of collocated grid, the *staggered grid* approach is developed. The staggered grid arrangement of variables is shown in Fig. 1.3 in which the physical components are stored at different places of control volume. The velocity components are located at the center of control volume faces whereas pressure and other components are considered at the grid points shown by dots. The arrows on the faces of control volume show the location and direction of velocity components. The main reason of using staggered grid over collocated grid is to overcome the problem of possible

decoupling of the pressure and velocity.

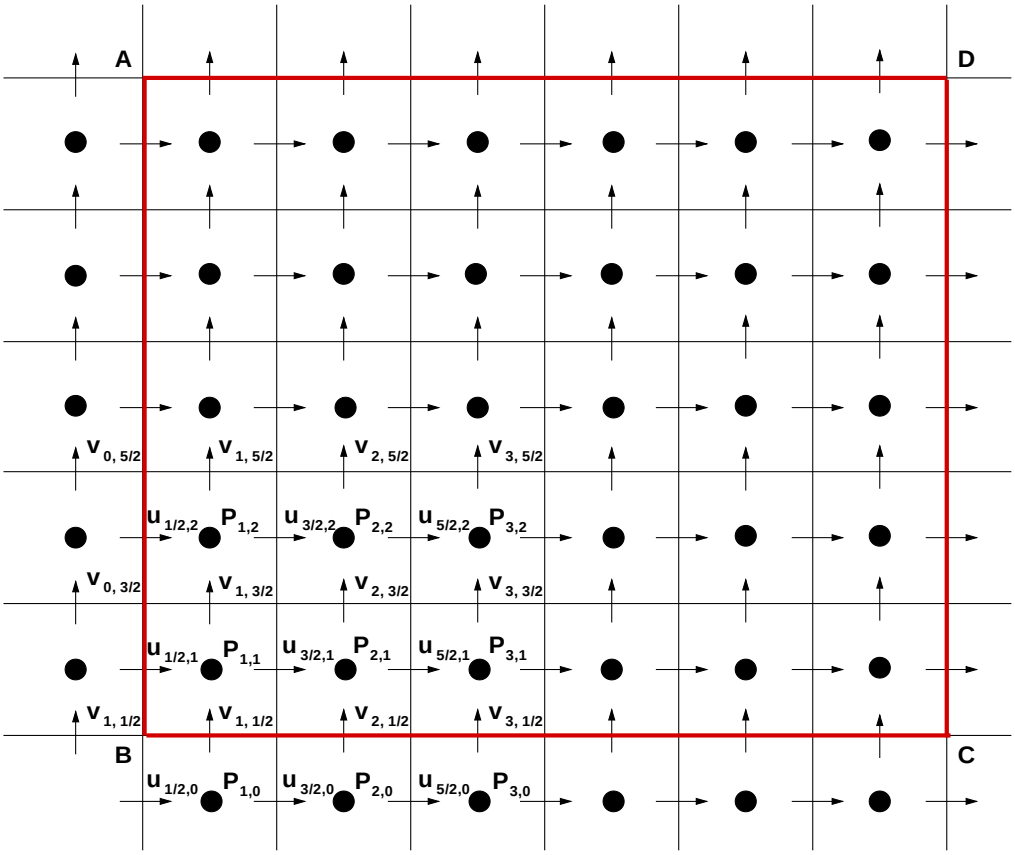

Figure 1.3: Staggered Grid

The most frequently used method for the solution of Navier-Stokes equations is to deal with the pressure Poisson equation for pressure computation and momentum equation for velocity computation using a staggered grid arrangement. The marker-and-cell (MAC) method developed by Harlow and Welch [85] is a prototype of such a method. Initially, the MAC method was derived for the problems dealing with free surfaces, but it can be applicable to any incompressible fluid flow problem. Following the similar methodology of using staggered grid and pressure Poisson equation the MAC method has been improved by several researchers. In Simplified-MAC (SMAC) method introduced by Amsden and Harlow [11], a second Poisson equation for an auxiliary velocity

potential is solved to satisfy the continuity equation directly. Similar to MAC method, SOLA(SOLution Algorithm) is another powerful method which is introduced by Hirt et al. [88]. Moreover, Patankar and Spalding [179] introduced another powerful method known as Semi Implicit Method for Pressure Linked Equations (SIMPLE). The SIMPLE method is one of the most used methods among the similar and modified versions of it and found to be suitable by many authors for the solution of the set of flow governing Navier-Stokes equations ([31, 75, 169]). The SIMPLE method is further modified by several authors for convergence acceleration such as SIMPLE-Revised (SIMPLER) and SIMPLE-Consistent (SIMPLEC). A detailed description and applications are studied by Fletcher [72] and Anderson [14].

1.9 Implementation of boundary conditions

Considering the staggered grid arrangement in a rectangular domain, the grid is arranged in such a fashion that the pressure point is placed at the mid point of elementary volume and the velocity points lie on the boundary of control volume. In particular, the horizontal velocity points are placed on the right and left vertical boundaries whereas the vertical velocity points are placed on the upper and lower boundaries as shown in Fig. 1.3. The fictitious boundaries are used to define the flow variables on the fictitious cells wherever necessary. The aim of fictitious cells are useful for defining the flow variables which are not present on the boundary walls but are used in the calculation process to satisfy the flow impacts. Another benefit of using fictitious cells is that the difference equations used in the interior mesh can also be used at the boundaries. Considering the flow domain where the vertical boundary AB is assumed to be inflow boundary with horizontal velocity $u = u_0$ and vertical velocity $v = v_0$ and BC is assumed to be a solid wall, the boundary conditions may be defined as follows:

On AB,

$$u_{1/2,j} = \alpha, \quad v_{0,j+1/2} = 2\beta - v_{1,j+1/2} \quad \text{for} \quad j = 0, 1, 2, 3, ... \quad \text{and}$$

on BC,

$$v_{i,1/2} = 0, \quad u_{i+1/2,0} = u_{i+1/2,1} \quad \text{or} \quad -u_{i+1/2,1} \quad \text{for} \quad i = 0, 1, 2, 3, ...$$

according to the free-slip or no-slip condition along the wall.

The pressure evaluation inside the domain using pressure Poisson equation requires the values of pressure outside the domain. Along the boundary walls the pressure can be calculated using the following relation,

$$\frac{\partial p}{\partial y} = \frac{1}{Re}\frac{\partial^2 v}{\partial y^2}.$$

In SIMPLE approach, the pressure corrections can be obtained by using similar approach. Also, the value of pressure correction p' at the boundary with no normal flow will be zero.

1.9.1 Finite volume method

In finite volume method, whole computational domain is divided into a number of small non-overlapping control volumes and the flow governing differential equations are integrated over each control volume. The staggered grid is used to utilize its advantages in discretizing the pressure gradients in combination with the continuity equation.

For more clear understanding of finite volume method, let us consider a two-dimensional convection-diffusion equation for a generic variable φ,

$$\frac{\partial \varphi}{\partial t} + \nabla.\overrightarrow{F} = S_\varphi \tag{1.33}$$

where, $\overrightarrow{F}$ denotes the flux vector consisting of convection and diffusion part and S_φ denoted the source term. Integrating eq.1.33 over the finite volume around the grid point (j,k) with volume $V_{j,k}$

$$\int_{V_{j,k}} \frac{\partial \varphi}{\partial t} dV + \int_{V_{j,k}} \nabla.\overrightarrow{F}\, dV = \int_{V_{j,k}} S_\varphi dV.$$

On applying Gauss divergence theorem and rewriting the term $\nabla.\overrightarrow{F}$ as fluxes through the sides of control volume $V_{j,k}$, we get,

$$\int_{V_{j,k}} \frac{\partial \varphi}{\partial t} dxdy + \int_{side} (F_e - F_w)dy + \int_{side} (F_n - F_s)dx = \int_{V_{j,k}} S_\varphi dxdy$$

the subscripts $e,\ w,\ n$ and s refers to the east, west, north and south sides of the control volume $V_{j,k}$ respectively. Finally, the integrals are approximated as,

$$\left(\frac{\partial \varphi}{\partial t}\right)_{j,k} \Delta x\Delta y + (F_{j+1/2,k} - F_{j-1/2,k})\Delta y + (F_{j,k+1/2} - F_{j,k-1/2})\Delta x$$
$$= (S_\varphi)_{j,k}\Delta x\Delta y + \Delta x\Delta y \mathbf{O}(\Delta x^2, \Delta y^2).$$

The unsteady term, the fluxes and the source term are further discretized with finite differences.

1.9.2 Pressure computation

The absence of an independent equation for pressure makes it difficult to solve the Navier-Stokes equations, since the gradient of pressure term is a part of each of momentum equation. Moreover, in incompressible flow, the continuity equation does not have a dominant variable. To overcome this difficulty, a pressure field can be constructed so as to satisfy the continuity equation. Harlow and Welch [85] was the first to introduce the primitive variable approach for incompressible flow using pressure projection after which a number of alternative solutions have been developed.

The following three different approaches are generally preferred to calculate the pressure in incompressible flow:

(a) **Artificial compressibility approach**

(b) **Pressure Poisson approach**

(c) **Pressure correction approach**

(a) Artificial compressibility approach

The artificial compressibility approach due to Chorin [53] was among the earliest technique of solving incompressible Navier-Stokes equations in primitive variable approaches. In this method, an artificial compressibility term is added to the continuity equation which vanishes as soon as the steady state solution is attained. The continuity equation becomes an evolution equation for pressure. The introduction of compressibility term in incompressible form enables the use of compressible flow solvers which enhances the convergence characteristics of the solution. Peyret and Taylor [183] recommended the staggered grid arrangement and showed that by using explicit time differencing pseudo-transient artificial compressibility construction can be interpreted as an iterative procedure for the solution of discrete Poisson equation for the pressure. Ramshaw and Mousseau [189] and Ramshaw and Mesina [188] used this approach for the coputation of incompressible flows.

(b) Pressure Poisson approach

The most common way of pressure calculation is to formulate the pressure equation by combining the continuity equation with the momentum equation. The mathematical description of pressure equation is as follows:

Taking divergence of the momentum equation we get,

$$\nabla.(\nabla p) = -\nabla.\left[\nabla.(\rho\overrightarrow{q}\,\overrightarrow{q} - S) - \rho b + \frac{\partial}{\partial t}(\rho\overrightarrow{q})\right].$$

In cartesian coordinates above equation can be written as

$$\frac{\partial}{\partial x_i}\left(\frac{\partial p}{\partial x_i}\right) = -\frac{\partial}{\partial x_i}\left[\frac{\partial}{\partial x_j}(\rho u_i u_j - \tau_{ij})\right] + \frac{\partial}{\partial x_i}(\rho b_i) + \frac{\partial^2\Omega}{\partial t^2},$$

for the steady incompressible flow with constant viscosity, the unsteady and viscous terms disappear and by virtue of continuity equation we have,

$$\frac{\partial}{\partial x_i}\left(\frac{\partial p}{\partial x_i}\right) = -\frac{\partial}{\partial x_i}\left(\frac{\partial}{\partial x_j}(\rho u_i u_j)\right).$$

The solution of above mentioned pressure equation can be obtained by using any numerical method for elliptic equation. This kind of pressure equation can be used to calculate the pressure in both explicit and implicit solution methods.

(c) Pressure correction approach

A number of numerical methods including SOLA, PISO (Pressure Implicit with Splitting of Operator), SIMPLE are developed on the basis of pressure correction approach.

In SOLA, developed by Hirt et al. [88], a combined form of central and second order upwinding formulation is used for the discretization of convective terms. The PISO algorithm is developed by Issa [100] where the starting velocity field is calculated from momentum equation by using an assumed pressure field and the calculated velocity is then used to compute the new pressure field using the pressure equation. Finally, pressure is used for the correction of the velocity field to provide a second correction for both pressure and velocity fields.

SIMPLE algorithm was first introduced by Patankar and Spalding [179] which includes a finite volume discretization based on staggered grid arrangement. SIMPLE algorithm provides the solution for discretized equations. In this method, a pressure equation is derived by using continuity equation together with momentum equations. In numerical computations a pressure field is guessed initially and is used to obtain the velocity

fields after solving the momentum equations, which may not satisfy the continuity equation. Hence, the pressure and velocity fields are corrected so as to satisfy the continuity equation. A brief discussion about SIMPLE algorithm is provided in the next section.

1.10 SIMPLE algorithm

The term SIMPLE stands for Semi-Implicit Method for Pressure Linked Equations and is developed by Patankar and Spalding [179] in 1972. It is an iterative method of solving the discretized form of Navier-Stokes equations. The main difficulty in finding the solutions of Navier-Stokes equations arises due to the absence of a separate equation for pressure field. To overcome this difficulty, the concept of using the continuity equation for pressure field calculation came into existence in which the pressure field is indirectly specified via continuity equation.

The main advantage of SIMPLE method lies in its iterative approach, which is used to solve the whole set of discretized equations, so that they may be applied to single dependent variable or even to a single point. It is very difficult to find a direct solution methodology for the solution of entire set of velocity and pressure components. Another advantage of SIMPLE method is that it can be applicable to both incompressible and compressible flow problems. In compressible flows, the pressure can be obtained from the density and temperature by using the equation of state where density is regarded as dependent variable of continuity equation as discussed in Versteeg and Malalasekera [240].

In this thesis we are dealing with incompressible flow problems, i.e., the density is constant with respect to pressure. There exist a coupling between the pressure and velocity fields which introduces a variation on the solution of flow field. If the correct pressure field is provided in the momentum equations, the resulting velocity field satisfies the continuity equation, else some correction is sought in the values of pressure as well as velocity values.

1.10.1 Numerical methodology

Flow governing equations

Considering a two-dimensional incompressible laminar fluid flow problem; the governing

equations in their primitive variables are given by,

$$\frac{\partial u}{\partial x} + \frac{\partial v}{\partial y} = 0, \tag{1.34}$$

$$\frac{\partial u}{\partial t} + \frac{\partial u^2}{\partial x} + \frac{\partial uv}{\partial y} = -\frac{\partial p}{\partial x} + \frac{1}{Re}\left(\frac{\partial^2 u}{\partial x^2} + \frac{\partial^2 u}{\partial y^2}\right), \tag{1.35}$$

$$\frac{\partial v}{\partial t} + \frac{\partial uv}{\partial x} + \frac{\partial v^2}{\partial y} = -\frac{\partial p}{\partial y} + \frac{1}{Re}\left(\frac{\partial^2 v}{\partial x^2} + \frac{\partial^2 v}{\partial y^2}\right). \tag{1.36}$$

Eqs. (1.35) and (1.36), consists of unsteady and convective terms on the left hand side of equation, and the pressure gradient and diffusion term on the right hand side.

Discretization process

The very first step in the solution process of above mentioned flow governing equations is the discretization of these equations. To obtain the numerical solution of these equations, the finite volume method is applied. Following the finite volume methodology, the continuity and momentum equations are integrated over the control volume on a uniform staggered grid (shown in Fig. 1.3). All the scalar variables (p in present case) are stored in the cell center and the velocity components are stored at the cell faces. In particular, the u-velocity components, represented by horizontal arrows ($\rightarrow$), stored at east and west cell faces and the v-velocity, represented by vertical arrows ($\uparrow$), stored at north and south cell faces.

Now, integrating the continuity equation [eq. (1.34)] over the $(j,k)^{th}$ scalar control volume as shown in Fig. 1.4 at $(n+1)^{th}$ time level, we obtain,

$$(u_{j,k}^{n+1} - u_{j-1,k}^{n+1})\Delta y + (v_{j,k}^{n+1} - v_{j,k-1}^{n+1})\Delta x = 0. \tag{1.37}$$

On integrating the x-momentum equation [eq. (1.35)] at $(n+1)^{th}$ time step over the $(j,k)^{th}$ control volume for u as shown in Fig. 1.5, we get,

$$\left(\frac{\partial u}{\partial t}\right)_{j,k} \Delta x\Delta y + (F_{j+1/2,k}^{u} - F_{j-1/2,k}^{u})\Delta y + (G_{j,k+1/2}^{u} - G_{j,k-1/2}^{u})\Delta x + \left(\frac{\partial p}{\partial x}\right)_{j+1/2,k} \Delta x\Delta y + \Delta x\Delta y\mathbf{O}(\Delta x^2, \Delta y^2) = 0 \tag{1.38}$$

where,

$$F^u = u^2 - \frac{1}{Re}\frac{\partial u}{\partial x}, \quad \text{and} \quad G^u = uv - \frac{1}{Re}\frac{\partial v}{\partial y}.$$

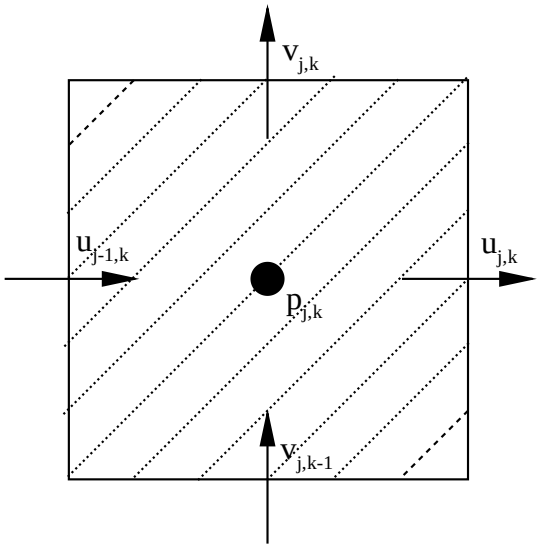

Figure 1.4: Scalar control volume

Moreover, using first order finite difference scheme for the discretization of unsteady term, fluxes (F^u and G^u) and pressure gradient at $(n+1)^{th}$ time level, we obtain,

$$\left(\frac{\partial u}{\partial t}\right)_{j,k} = \frac{u_{j,k}^{n+1} - u_{j,k}^{n}}{\Delta t} + \mathbf{O}(\Delta t),$$

$$F_{j+1/2,k}^{u} = \frac{1}{4}(u_{j,k}^{n+1} + u_{j+1,k}^{n+1})(u_{j,k}^{n} + u_{j+1,k}^{n}) - \frac{1}{Re}\left(\frac{u_{j+1,k}^{n+1} - u_{j,k}^{n+1}}{\Delta x}\right) + \mathbf{O}(\Delta x),$$

$$G_{j,k+1/2}^{u} = \frac{1}{4}(u_{j,k}^{n+1} + u_{j,k+1}^{n+1})(v_{j,k}^{n} + v_{j+1,k}^{n}) - \frac{1}{Re}\left(\frac{u_{j,k+1}^{n+1} - u_{j,k}^{n+1}}{\Delta y}\right) + \mathbf{O}(\Delta y).$$

It is worth mentioning that, in the discretization of unsteady term, fluxes and pressure gradient terms, the local truncation error are of first order but the global truncation error is of second order.

Now, on substituting the above discretized forms in eq. (1.38) we get,

$$\left(\frac{\Delta x \Delta y}{\Delta t} + a_{j,k}^{u}\right) u_{j,k}^{n+1} + \sum a_{nb}^{u} u_{nb}^{n+1} = \frac{\Delta x \Delta y}{\Delta t} u_{j,k}^{n} - \Delta y (p_{j+1,k}^{n+1} - p_{j,k}^{n+1}) \tag{1.39}$$

where,

$$\begin{aligned} a_{j,k}^{u} = \frac{2}{Re}\left(\frac{\Delta y}{\Delta x} + \frac{\Delta x}{\Delta y}\right) + \frac{1}{4}(u_{j+1,k}^{n} - u_{j-1,k}^{n})\Delta y \\ + \frac{1}{4}(v_{j,k}^{n} + v_{j+1,k}^{n} - v_{j,k-1}^{n} - v_{j+1,k-1}^{n})\Delta x \end{aligned} \tag{1.40}$$

and $\sum a_{nb}^{u} u_{nb}^{n+1}$ represents the contribution of neighboring nodes $(j-1,k)$, $(j+1,k)$, $(j,k-1)$ and $(j,k+1)$ in the form of convection and diffusion. In a similar fashion, the

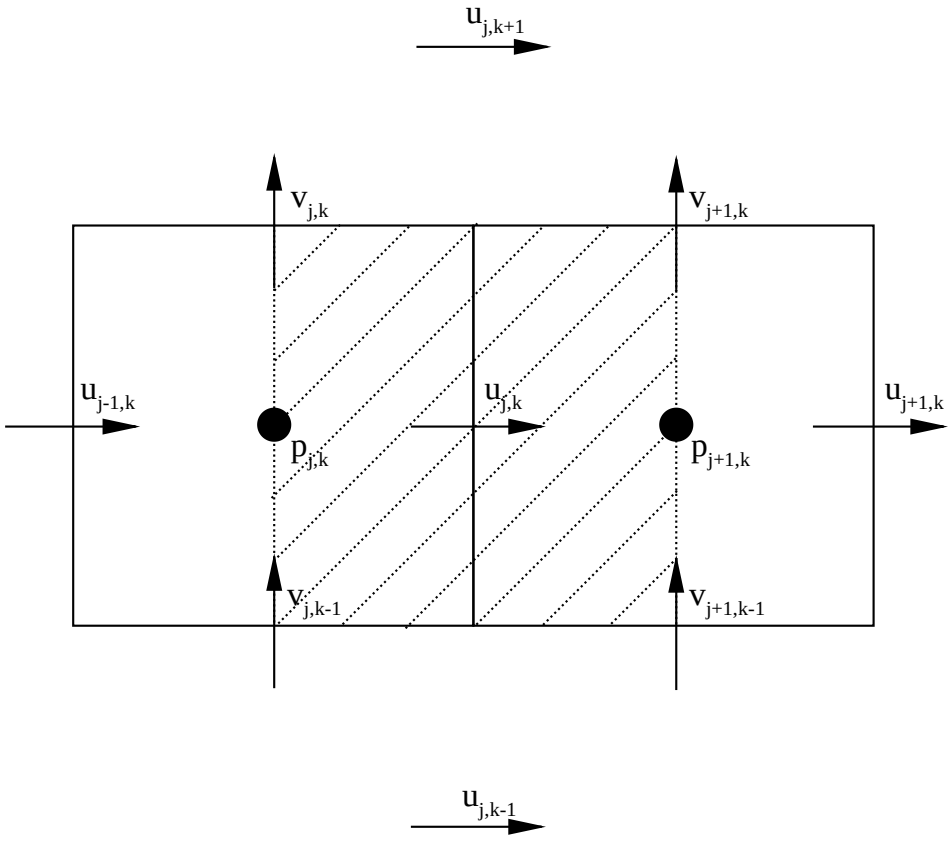

Figure 1.5: u-control volume

y-momentum equation [eq. (1.36)] over $(j,k)^{th}$ control volume for v shown in Fig. 1.6 at $(n+1)^{th}$ time step reduced to the following difference equation,

$$\left(\frac{\Delta x \Delta y}{\Delta t} + a^v_{j,k}\right) v^{n+1}_{j,k} + \sum a^v_{nb} v^{n+1}_{nb} = \frac{\Delta x \Delta y}{\Delta t} v^n_{j,k} - \Delta x (p^{n+1}_{j,k+1} - p^{n+1}_{j,k}) \tag{1.41}$$

where,

$$\begin{aligned} a^v_{j,k} = \frac{2}{Re}\left(\frac{\Delta y}{\Delta x} + \frac{\Delta x}{\Delta y}\right) + \frac{1}{4}(v^n_{j,k+1} - v^n_{j,k-1})\Delta x \\ \frac{1}{4}(u^n_{j,k} + u^n_{j,k+1} - u^n_{j-1,k+1} - u^n_{j-1,k})\Delta x \end{aligned} \tag{1.42}$$

and $\sum a^v_{nb} v^{n+1}_{nb}$ represents the contribution of neighboring nodes $(j-1,k)$, $(j+1,k)$, $(j,k-1)$ and $(j,k+1)$ in the form of convection and diffusion.

SIMPLE algorithm: The solution process

The aim of SIMPLE algorithm is to establish the pressure link between continuity and

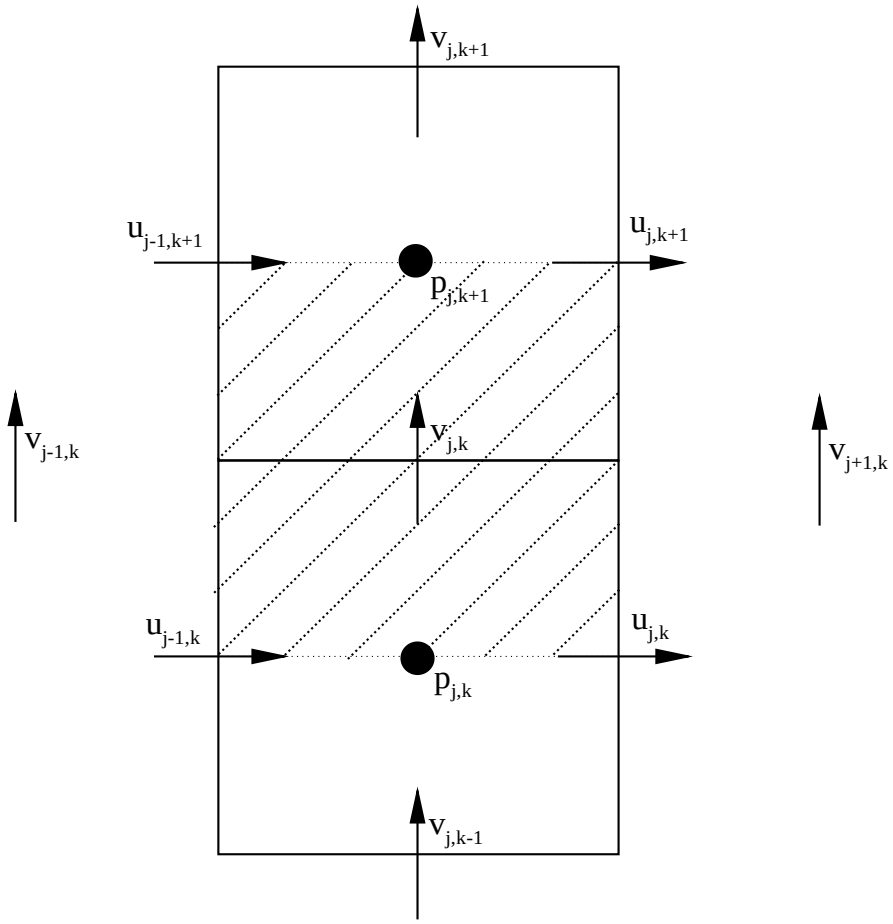

Figure 1.6: v-control volume

momentum equations by transforming the continuity equation to pressure Poisson equation. The Poisson equation implements a pressure correction for a divergent free velocity field.

SIMPLE is an iterative procedure which calculates the solution at a next time level using the values at a previous time level. First, the discretized momentum equations [eq. (1.39) and (1.41)] are solved using current guessed pressure field $p^*_{j,k}$ ($=p^n_{j,k}$; the pressure obtained at previous time step of solution) to yield the intermediate velocity fields $u^*_{j,k}$ and $v^*_{j,k}$. Hence, $u^*_{j,k}$ and $v^*_{j,k}$ satisfy the equations,

$$\left(\frac{\Delta x \Delta y}{\Delta t} + a^u_{j,k}\right) u^{n+1}_{j,k} + \sum a^u_{nb} u^{n+1}_{nb} = \frac{\Delta x \Delta y}{\Delta t} u^n_{j,k} - \Delta y (p^*_{j+1,k} - p^*_{j,k}) \tag{1.43}$$

and

$$\left(\frac{\Delta x \Delta y}{\Delta t} + a^v_{j,k}\right) v^{n+1}_{j,k} + \sum a^v_{nb} v^{n+1}_{nb} = \frac{\Delta x \Delta y}{\Delta t} v^n_{j,k} - \Delta x (p^*_{j,k+1} - p^*_{j,k}), \tag{1.44}$$

but, $u^*_{j,k}$ and $v^*_{j,k}$ may not satisfy the continuity equation [eq. (1.37)]. Therefore, a correction is sought in the velocity and pressure fields so as to satisfy the continuity equation [eq. (1.37)]. Hence, if $p^c_{j,k}$ is pressure correction and $u^c_{j,k}$ and $v^c_{j,k}$ are velocity corrections, then the modified pressure and velocity fields are given by,

$$p^{n+1}_{j,k} = p^*_{j,k} + p^c_{j,k}, \tag{1.45}$$

$$u^{n+1}_{j,k} = u^*_{j,k} + u^c_{j,k}, \tag{1.46}$$

$$v^{n+1}_{j,k} = v^*_{j,k} + v^c_{j,k} \tag{1.47}$$

where, the new velocity fields $u^{n+1}_{j,k}$ and $v^{n+1}_{j,k}$ satisfy the continuity equation [eq. (1.37)]. Subtracting eq. (1.43) from eq. (1.39) and eq. (1.44) from eq. (1.41), we obtain,

$$\left(\frac{\Delta x\Delta y}{\Delta t} + a^u_{j,k}\right)u^c_{j,k} + \sum a^u_{nb}u^c_{nb} = -\Delta y(p^c_{j+1,k} - p^c_{j,k}), \tag{1.48}$$

$$\left(\frac{\Delta x\Delta y}{\Delta t} + a^v_{j,k}\right)v^c_{j,k} + \sum a^v_{nb}v^c_{nb} = -\Delta x(p^c_{j,k+1} - p^c_{j,k}), \tag{1.49}$$

ignoring the small correction terms of neighborhood $\sum a^u_{nb}u^c_{nb}$ and $\sum a^v_{nb}v^c_{nb}$ we obtain,

$$u^c_{j,k} = -\alpha_{u_{j,k}}\frac{\Delta t}{\Delta x}(p^c_{j+1,k} - p^c_{j,k}), \tag{1.50}$$

$$v^c_{j,k} = -\alpha_{v_{j,k}}\frac{\Delta t}{\Delta x}(p^c_{j,k+1} - p^c_{j,k}) \tag{1.51}$$

where,

$$\alpha_{u_{j,k}} = \frac{\Delta x\Delta y}{\Delta x\Delta y + a^u_{j,k}\Delta t} \quad \text{and} \quad \alpha_{v_{j,k}} = \frac{\Delta x\Delta y}{\Delta x\Delta y + a^v_{j,k}\Delta t}.$$

Hence, to obtain the corrected velocity fields, substitute these values of $u^c_{j,k}$ and $v^c_{j,k}$ to the corrected velocity fields given by eqs. (1.46) and (1.47) we get,

$$u^{n+1}_{j,k} = u^*_{j,k} - \alpha_{u_{j,k}}\frac{\Delta t}{\Delta x}(p^c_{j+1,k} - p^c_{j,k}), \tag{1.52}$$

$$v^{n+1}_{j,k} = v^*_{j,k} - \alpha_{v_{j,k}}\frac{\Delta t}{\Delta x}(p^c_{j,k+1} - p^c_{j,k}). \tag{1.53}$$

Finally, substitute these corrected velocity fields to the discretized continuity equation [eq. (1.37)] we get,

$$2\left[\alpha_{u_{j,k}}\left(\frac{\Delta t\Delta y}{\Delta x}\right) + \alpha_{v_{j,k}}\left(\frac{\Delta t\Delta x}{\Delta y}\right)\right]p^c_{j,k} = -div$$
$$+\alpha_{u_{j,k}}\frac{\Delta t\Delta y}{\Delta x}(p^c_{j+1,k} + p^c_{j-1,k}) + \alpha_{v_{j,k}}\frac{\Delta t\Delta y}{\Delta x}(p^c_{j,k+1} + p^c_{j,k-1}) \tag{1.54}$$

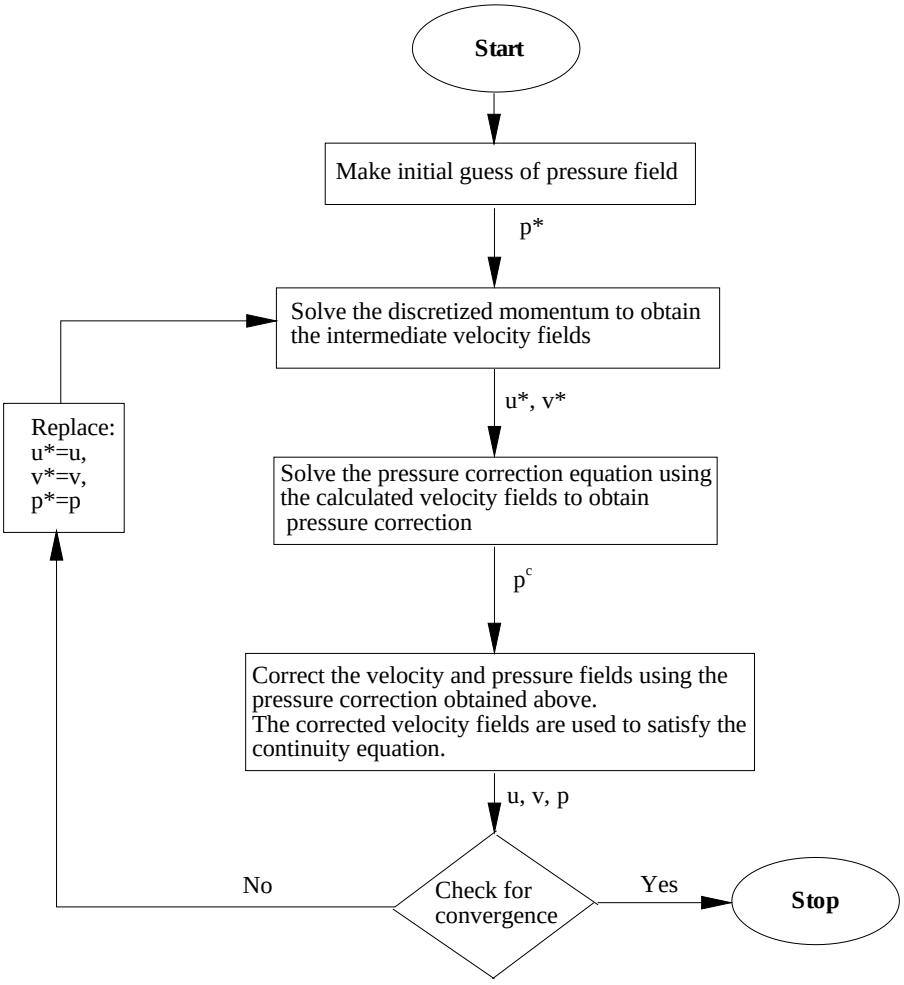

Figure 1.7: Flow chart of SIMPLE algorithm

where,

$$div = (u^*_{j,k} - u^*_{j-1,k})\Delta y + (v^*_{j,k} - v^*_{j,k-1})\Delta x.$$

The derived corrected form of pressure term given in eq. (1.45) sometimes lead to a divergence in the solution, hence, a relaxation factor is used as follows

$$p^{n+1}_{j,k} = \alpha_p p^*_{j,k} + p^c_{j,k}.$$

The SIMPLE algorithm contains three relaxation parameters α_p, $\alpha_{u_{j,k}}$ and $\alpha_{v_{j,k}}$. In our problem, a faster convergence is observed for $\alpha_p = 0.8$ or 0.975 and $\alpha_{u_{j,k}} = \alpha_{v_{j,k}} = \frac{2}{3}$. The flow chart for SIMPLE algorithm is presented in Fig. 1.7.

SIMPLE algorithm is one of the most popular algorithm for the solution of incompressible flow problems using simpler grids, but it suffers with a limitation of using

the relaxation parameter to overcome the divergence of pressure correction equation [eq. (1.54)]. An under relaxation parameter can be used for the faster convergence of the method.

SIMPLE method is modified by several authors to achieve the faster convergence rate. Patankar [178], introduced a revised SIMPLE algorithm, known as SIMPLER, to improve the convergence. The SIMPLER method uses two pressure correction and two momentum steps in each iteration cycle and the method suggested to use the assumed velocity at the initial stage of computation. The new velocity can be computed directly from the momentum equations by omitting the pressure term with the initial guess. These new velocity fields are used to calculate the pressure term using pressure correction technique. The updated pressure is now used to calculate the new velocity from the original momentum equations, which includes the pressure term. This final form of velocity is implemented in the pressure equation to evaluate the pressure at the current time level. This completes one iteration cycle. The SIMPLER algorithm is obviously more expensive per iteration as compared to the SIMPLE but the convergence is achieved in sufficiently few iterations. Consistent SIMPLE or SIMPLEC algorithm is developed by Doormal and Raithby [60], where the change in cell pressure causes increment in the number of iterations, which is required for early convergence. They made a closure approximation to the velocity correction and gained a significant improvement in convergence rate.

Implementation of original form of SIMPLE algorithm to the problems indicates that the relaxation in cell pressure is an effective method for velocity field adjustment, but suffers a lesser speed of convergence of pressure field. Anjorin and Barton, [15] further proposed an improved version of SIMPLE algorithm known as SIMPLE-Vincent or SIMPLEV in which they suggested the removal of under-relaxation and temporal terms from pressure correction equation. The SIMPLE and SIMPLEV methods were applied for comparison to steady state laminar flow (i) over a backward facing step and (ii) around a square cylinder. The simulated results indicate that SIMPLEV algorithm converges more rapidly than the SIMPLE algorithm but it is also computationally more expensive.

1.11 Nanofluid flow

Now a days, heat transfer enhancement is one of the most fundamental and essential requirement of various industrial processes for manufacture, design or process management. Every industry is interested in reducing the processing time, energy saving, long lasting life of equipments but the poor heat transfer rate and uncontrolled heating may effect the overall working performance of equipments. In order to achieve higher heat transfer rate, the concept of nanofluid came into existence. Nanofluids are the engineered colloidal suspensions of nanometer sized particles in the base fluid. However, it is well known that, metals in solid form have higher thermal conductivity as compared to fluids. Hence, the fluid with suspended metallic particles is expected to have a comparatively higher thermal conductivity then its base fluid. Table 1.1 shows the thermal conductivity of various materials at room temperature (300K).

Table 1.1: Thermal conductivity of various materials at room temperature.

Class	Material	Thermal Conductivity($Wm^{-1}K^{-1}$)
Non-metallic liquids	Water	0.6
	Ethylene glycol	0.253
	Engine oil	0.145
Metallic liquids	Sodium(at 644K)	72.3
Non-Metallic solids	Alumina (Al_2O_3)	40
	Silicon	148
	Carbon nanotubes	3000
	Diamond	3300
Metallic solids	Copper(Cu)	400
	Silver	429
	Aluminium	237

1.11.1 Mathematical models of nanofluid flow

In the recent days, the nanofluids have attracted enormous interest from researchers due to their wide range applications in thermodynamic processes where higher order of heat transmission is required. Many researchers are working for analyzing and improving the flow properties of nanofluids and hence a large number of experimental, theoretical and numerical studies are going on. Mostly, two approaches are used for the development of nanofluid flow model,

(a) Single-phase model

(b) Two-phase model

(a) Single-phase model

In single phase model, both the base fluid and nanoparticles are assumed to be in thermal equilibrium and are flowing with the same local velocity. The classical theory of single phase fluids can be applied, where the physical properties of nanofluids are taken as a function of both concentration and their constituents. The basic thermophysical properties of nanofluids such as viscosity, thermal conductivity, density etc. are mostly used on the basis of experimental correlations. Moreover, single phase models can be sub-categorized into two classes; homogeneous model and dispersion model. The homogeneous models use the classical balance equations of regular fluids and the transport coefficients are replaced by effective transport properties. The dispersion model assumes convective heat transfer enhancement in nanofluids as a result of higher thermal conductivity and dispersion of nanofluids.

(b) Two-phase model

The modeling of nanofluid flow in a two-phase model uses two-component non-homogeneous equilibrium model for transport phenomena. This model is based on seven slip mechanisms introduced by Bongiorno [40] namely, inertia, Brownian diffusion, thermophoresis, diffusiophoresis, Magnus effect, fluid drainage and gravity. Out of these, only Brownian motion and thermophoresis are considered as important parameters in nanofluid flow. Mostly, the work in this thesis are based on the study of water based nanofluids. But, according to Buongiorno [40], the value of Brownian diffusion coefficient for water based nanofluids lies in the range of 4×10^{-10} to 4×10^{-12} $m^2 s^{-1}$ which is very small and can be neglected. Similarly, the range of thermal diffusion coefficient based on these parameters is found to be very small and hence the dependence of these parameters does not show any major contribution to the flow distribution. Moreover, the nanoparticles discussed in this thesis are assumed to be of uniform spherical shape and considered to be of diameter $100nm$ and hence, the nanoparticles inside the fluid behaves almost like a fluid [130]. One of the recent study by Garoosi et al. [74] shows the validity of single-phase model with the experimental observations. They concluded that the single-phase models are valid for the study of all types of nanofluids for low Richardson number and high Rayleigh number.

Hence, we have used single-phase model for fluid flow and heat transfer in nanofluid in this thesis. A more detailed analysis of single-phase modeling is made in the next section.

1.11.2 Single-phase model

The single-phase model assumes no-slip condition and thermal equilibrium between the nanoparticles and base fluid due to which the nanofluids can be treated as the base fluids. Thus, all the conservation laws can be directly extended to the nanofluids with some modifications in their thermophysical properties. The effect of dispersion of nanoparticles in the base fluid is found to make considerable change in viscosity, thermal conductivity, density and heat capacity. Thus, the governing equations for steady, viscous and incompressible nanofluid flow and heat transfer can be written as,

Conservation of mass (*Continuity equation*)**:**

$$\frac{\partial u}{\partial x}+\frac{\partial v}{\partial y}+\frac{\partial w}{\partial z}=0.$$

Conservation of momentum (*Momentum equations*)**:**

$u-$*momentum equation*:

$$\rho_{nf}\left(u\frac{\partial u}{\partial x}+v\frac{\partial u}{\partial y}+w\frac{\partial u}{\partial z}\right)=-\frac{\partial p}{\partial x}+\mu_{nf}\left(\frac{\partial^2 u}{\partial x^2}+\frac{\partial^2 u}{\partial y^2}+\frac{\partial^2 u}{\partial z^2}\right)+S_x,$$

$v-$*momentum equation*:

$$\rho_{nf}\left(u\frac{\partial v}{\partial x}+v\frac{\partial v}{\partial y}+w\frac{\partial v}{\partial z}\right)=-\frac{\partial p}{\partial y}+\mu_{nf}\left(\frac{\partial^2 v}{\partial x^2}+\frac{\partial^2 v}{\partial y^2}+\frac{\partial^2 v}{\partial z^2}\right)+S_y,$$

$w-$*momentum equation*:

$$\rho_{nf}\left(u\frac{\partial w}{\partial x}+v\frac{\partial w}{\partial y}+w\frac{\partial w}{\partial z}\right)=-\frac{\partial p}{\partial z}+\mu_{nf}\left(\frac{\partial^2 w}{\partial x^2}+\frac{\partial^2 w}{\partial y^2}+\frac{\partial^2 w}{\partial z^2}\right)+S_z.$$

Conservation of energy (*Energy equation*)**:**

$$(\rho C_p)_{nf}\left(u\frac{\partial T}{\partial x}+v\frac{\partial T}{\partial y}+w\frac{\partial T}{\partial z}\right)=k_{nf}\left(\frac{\partial^2 T}{\partial x^2}+\frac{\partial^2 T}{\partial y^2}+\frac{\partial^2 T}{\partial z^2}\right).$$

The above flow governing equations are used for the nanofluid flow where the thermophysical parameters are modified based on nanofluids and are quite different from base fluid. These parameters can be estimated on the basis of physical principle of mixture rule and can be verified with the existing experimentally observed data. For the suspension

of nanoparticles in base fluid, the density and heat capacity expression can be derived as [18],

$$\rho_{nf} = \left(\frac{M}{V}\right)_{nf} = \frac{M_f + M_s}{V_f + V_s} = \frac{\rho_f V_f + \rho_s V_s}{V_f + V_s} = (1-\phi)\rho_f + \phi\rho_s$$

where, M represents the mass, V is the volume, $\phi = V_s/V$ and the subscripts f and s represents the fluid and nanoparticle phases respectively. Similarly,

$$\begin{aligned}(\rho C_p)_{nf} = \rho_{nf}\left(\frac{Q}{M\Delta T}\right)_{nf} &= \rho_{nf}\frac{Q_f + Q_s}{M_f\Delta T + M_s\Delta T} = \rho_{nf}\frac{(MC_p)_f\Delta T + (MC_p)_s\Delta T}{(M_f + M_s)\Delta T} \\ &= \rho_{nf}\frac{(\rho C_p)_f V_f + (\rho C_p)_s V_s}{\rho_f V_f + \rho_s V_s} = (1-\phi)(\rho C_p)_f + \phi(\rho C_p)_s\end{aligned}$$

where Q represents the heat flow.

A considerable change in the fluid viscosity and thermal conductivity is expected when the nanoparticles are dispersed into the base fluid. On the basis of experimental studies many researchers have tried to establish most appropriate formula for finding the thermal conductivity of nanofluids. Einstein [62] introduced the first model for the effective viscosity of spherical solid suspension in the base fluid. The model was based on the assumption that disturbance caused in the flow pattern of matrix base fluid from one particle is independent of the disturbance of flow caused by another particle. The proposed model is given as,

$$\mu_{nf} = \mu_f(1 + 2.5\phi).$$

But, the proposed model is valid for low solid-volume fraction ($\phi < 0.05$). Later on, a large number of theoretical as well as experimental studies have been performed for constructing the viscosity models. Brinkman [39] proposed the model for higher solid-volume fraction as,

$$\mu_{nf} = \frac{\mu_f}{(1-\phi)^{2.5}}. \tag{1.55}$$

Throughout this thesis, we have used the model proposed by Brinkman [39] for calculating the viscosity of nanoparticles.

The effective thermal conductivity for uniformly distributed spherical shaped nanoparticles is proposed by Maxwell [151], where the thermal conductivity of nanofluids is expressed in terms of nanoparticle-volume fraction combined with thermal conductivity of nanoparticles as well as base fluid. The proposed model is given by,

$$\frac{k_{nf}}{k_f} = \frac{k_s + 2k_f - 2(k_f - k_s)\phi}{k_s + 2k_f + (k_f - k_s)\phi}. \tag{1.56}$$

and this model is used for calculation of the thermal conductivity of nanofluids throughout this thesis.

1.12 Literature survey

The improvement in the performance of mechanical systems is always an area of interest for researchers in industrial applications. The thermal performance of most of the mechanical systems is directly dependent on the internal heat generation of the systems. In many industrial processes, an uncontrolled heat generation can lead to a major loss in the working efficiency, production cost and quality of the product. Hence, the controlled heat transfer process is one of the main concern for the researchers, so that it can be increased or decreased rapidly according to the requirement.

The fluid flow and heat transfer in enclosures is frequently encountered in many industrial applications such as heating and/or cooling of machines, float glass production, drying technologies, solar collectors etc. [230]. An enormous amount of research is conducted in these fields and substantial efforts in the direction of experimental, theoretical and numerical studies have been made by several researchers ([35, 36]). Fluid flow and heat transfer in square and rectangular cavities due to shear and buoyancy driven effects is studied extensively, since it has large scale engineering applications in natural gas storage tanks, solidification process, solar ponds and crystal manufacturing [167]. The conventional fluid used for the heat transfer purposes does not fulfil the requirement of quick heat transfer response, due to which a suspension of metallic particles with higher thermal conductivity is suggested. A large number of studies have been conducted after the theoretical work of Maxwell [152] during 18^{th} century. But, for the century after Maxwell, the research for enhancement of heat transfer via metallic suspensions have been confined to milli- and micro-meter sized particles [52]. Dispersion of nano-sized solid particles to the base fluid started a new era for research in the direction of nanofluid flow. The term 'nanofluid' coined by Choi [52], refers to the fluid equipped with the suspension of nano-sized metallic particles of higher thermal conductivity in the base fluid.

In the last several years, extensive experimental as well as numerical studies focussing on the natural as well as mixed convection heat transfer in cavities filled with

nanofluid have been conducted. Out of these, the experimental investigation conducted by Lee et al. [134] to measure the thermal conductivity of Al_2O_3-water, CuO-water, Al_2O_3-ethylene glycol and CuO-ethylene glycol nanofluids using a transient hot wire method provide a complete idea about different class of nanofluids. The result shows a substantial increase in thermal conductivity of nanofluids as compared to clear fluids. Another experimental study was conducted by Mintsa et al. [155] using alumina-water and copper oxide-water nanofluids. The effective thermal conductivity is measured for the nanoparticle-volume fraction from 0% to as high as 18% and a considerable increase in the thermal conductivity with increase in volume fraction of nanoparticles is reported. Eastman et al. [61] conducted an experimental study to find the increment in thermal conductivity due to increment in Cu nanoparticles having mean diameter $< 10nm$ in ethylene glycol and observed the increment in thermal conductivity. Experimental study of natural convective heat transfer in square enclosures containing Al_2O_3-water nanofluid have been performed by Ho et al. [90] and a correlation analysis is made for thermophysical properties of nanofluid and concluded that only thermal conductivity of nanofluid favors the heat transfer due to natural convection across the enclosure. Recently, Ghodsinezhad et al. [78] studied the effect of nanoparticle-volume fraction on the natural convection heat transfer using Al_2O_3-water nanofluid for finding the optimum heat transfer coefficient. They concluded that addition of 0.1% of alumina nanoparticles to clear water results in the increment of heat transfer coefficient by 15% and further increase in volume fraction of nanoparticles lead to a decrement in heat transfer coefficient.

In many engineering applications including high temperature gas turbines, electronic equipments and heat exchangers, the convective heat transfer plays an important role [87]. Heat transfer via natural convection in enclosures is encountered in many engineering applications such as solar energy, electronic devices, heat exchanger design, cooling of continuous strips or filaments [38, 118], but, it is not always possible to go for experimental investigation for obtaining such results. The experimental investigation sometimes seems costly, time taking and even risky in many cases due to which the researchers are interested in obtaining numerical solutions (wherever analytical solutions are not possible) in place of experimental ones. The numerical study of fluid flow and heat transfer properties is dependent on the approximation of thermophysical properties

of nanofluids. The dispersion of nanoparticles in base fluid leads to a considerable change in viscosity as well as thermal conductivity of nanofluids.

A wide range of studies are performed for the calculation of these parameters and classical model is suggested for the viscosity of nanofluid and is given by [62],

$$\mu_{nf} = \mu_f(1 + 2.5\phi),$$

but this model finds a limitation when the nanofluids contains high nanoparticle concentration ($\phi > 0.05$). Mooney [158] introduced a model for higher nanoparticle-volume fraction as,

$$\mu_{nf} = \mu_f e^{\frac{2.5\phi}{1-k\phi}}$$

where, k is called the self-crowding factor and the value of k lies between $1.35 < k < 1.91$. Brinkman [39] extended the model of Einstein [62], which is valid for the nanofluids equipped with higher concentration of nanoparticles. The proposed model have gained considerable popularity and till date the researchers are using the same model for numerical simulations very frequently, i.e.,

$$\mu_{nf} = \frac{\mu_f}{(1-\phi)^{2.5}}$$

Several other models have also been introduced afterwards for viscosity calculation [22, 34, 51, 73, 79, 126].

The model developed by Maxwell [151] for approximating the thermal conductivity of solid suspensions in fluid with spherical shaped and comparatively large nanoparticle size, is extended for nanofluids. The model is used to evaluate the thermal conductivity of nanofluids based on the thermal conductivity of base fluid and nanoparticles together with nanoparticle volume fraction. The model is given by,

$$\frac{k_{nf}}{k_f} = \frac{k_s + 2k_f - 2(k_f - k_s)\phi}{k_s + 2k_f + (k_f - k_s)\phi}$$

This method is widely used by many authors for calculating the thermal conductivity of nanofluids containing uniformly distributed spherical shaped nanoparticles of size upto $100nm$. The method was extended by Hamilton and Crosser [83] for both spherical as well as rod shaped nanoparticles as,

$$\frac{k_{nf}}{k_f} = \frac{k_s + (n-1)k_f + (n-1)(k_f - k_s)\phi}{k_s + (n-1)k_f + (k_f - k_s)\phi}$$

where, n is empirical shape factor. Xuan and Li [247] validated the model of Hamilton and Crosser [83] experimentally. A lot of studies have been conducted and introduced the above mentioned models for approximating the thermal conductivity [29, 102, 125, 186, 219, 246, 248].

Khanafer et al. [122] numerically studied the dispersion effect of nanofluids due to natural convection in a differentially heated square cavity. The discussion was made among four models for estimation of the density, viscosity and thermal expansion coefficient, and the comparative results of heat transfer variation are presented based on the average Nusselt number. Oztop and Abu-Nada [175] studied the effect of buoyancy forces on heat transfer and fluid flow in a partially heated enclosure filled with nanofluid. The heat transfer enhancement is found to be more pronounced at low aspect ratio as compared to high aspect ratio. A three-dimensional numerical simulation of differentially heated cavity for the analysis of fluid flow and heat transfer is conducted by Ravnik et al. [191] using three different types of nanofluids. The results indicate that conduction dominated flow provides a larger heat transfer rate as compared to the convection dominated flows. In a numerical study of natural convective heat transfer inside a square enclosure with and without blocks Mahapatra et al. [137] observed that heat transfer rate increases with the increment in Ra only up to a certain block size but after that it starts decreasing.

Natural convection heat transfer sometimes fails to provide the sufficient rate of heat transfer, hence, some external force is needed to boost the heat transfer rate. Hence, the study of forced and mixed convection is required to analyze the flow and heat transfer behavior in such cases. One of the earliest study on the mixed convection is conducted by Torrance et al. [44]. The study is conducted over three different aspect ratios of a lid driven enclosure (i.e., height/width=1/2, 1 and 2) with moving upper wall. In their study the dominance of buoyancy is observed for all aspect ratios when $Gr = \pm 10^4$ at fixed $Re = 100$ and $Pr = 1$. Thereafter, a wide range of studies on mixed convection heat transfer have been made. The study of mixed convection in a upper lid-driven enclosure with a stable vertical temperature gradient has been conducted by Iwatsu et al. [101] using a finite difference numerical procedure, the flow is observed as forced convection dominated when $Gr/Re^2 \ll 1$ and buoyancy dominated when $Gr/Re^2 \gg 1$. The work of Iwatsu et al. [101] is extended by Khanafer and Chamkha [120] for fluid saturated porous

medium in presence of a heat generation medium using a finite volume technique. In their study, they established the dependency of average Nusselt number over Darcy number and Richardson number. The unsteady laminar mixed convection heat transfer in a moving lid enclosure is studied by Khanafer et al. [119]. The simulated results are obtained by finite element based Galerkin method of weighted residuals and found that the average Nusselt number increases with increase in Grashof number and decreases with increasing values of Reynolds number. Bhattacharyya and Singh [33] used the control volume approach for the numerical study of laminar vortex shedding and wake flow due to solid circular cylinder wrapped by a thin porous wrapper to control the vortex shedding and drag force around the cylinder.

Many researchers started working on the mixed convection heat transfer process using nanofluids due to the importance of nanofluids in the field of heat transfer enhancement. Fereidoon et al. [68] studied the effect of Al_2O_3 nanoparticle volume fraction and Richardson number on average Nusselt number and found a significant increment in average Nusselt number by increasing nanoparticle volume fraction and Richardson number. Sheikhzadeh et al. [82] considered a two sided lid-driven cavity filled with Cu-water nanofluid to show the increment of heat transfer rate by increasing the nanoparticle volume fraction in a base fluid. In a recent study, Chattopadhyay et al. [50] carried out a numerical investigation of two-sided lid-driven cavity having sinusoidal thermal boundary condition on the right wall and comparatively cold temperature on left wall. They concluded that the presence of porous medium strongly affects the flow features and the heat transfer rate increases with the increase in amplitude value.

A wide range of literature is available for the study of fluid flow and heat transfer in enclosures but the study of entropy generation is relatively newer. The analysis of entropy generation enables us to get information regarding the amount of energy that is unavailable to do work. Hence, the entropy generation minimization is an important factor to be considered while designing any mechanical equipments. The concept of entropy generation minimization was first reported by Bejan [25] which is based on the second law of thermodynamics. In his study, the thermal gradient and viscous effects are considered as the main effective factors responsible for increment in entropy generation. The effect of variable aspect ratio in rectangular cavities is investigated by Ilis et al. [98] and found

that the total entropy generation increased with increase in thermal Rayleigh number and the rate of increment depend on the aspect ratio of the cavity. Mukhopadhyay [160] investigated the entropy generation due to buoyancy effects considering the bottom wall heating using two isoflux heat sources. The heat transfer irreversibility is found to be the dominating factor over fluid friction irreversibility. Moreover, it is observed that the same configuration generates minimum peak temperature and also produces minimum entropy and vice versa. The analysis of entropy generation due to fluid friction and heat transfer within square tilted cavity with different angles considering isothermal and non-isothermal heating has been made by Singh et al. [215]. The study have been conducted for a wide range of Rayleigh number and Prandtl number and it has been observed that the maximum amount of entropy in case of isothermal heating is found at the corner regions of the lower wall and for non-isothermal case maximum entropy is observed at the central region of the lower wall of the cavity. In another similar study, Singh et al. [214] analyzed the role of tilted porous cavities for energy efficiency. In their study the maximum entropy generation is observed at lower corner regions.

The simulation of flow field and entropy generation due to natural convection in a square cavity consisting of Cu-water nanofluid is performed by Shahi et al. [199]. It has been observed that the minimum value of entropy generation and maximum value of average Nusselt number are obtained when the heat source is placed at the bottom wall. Recently, Bouchoucha et al. [63] conducted a numerical study of heat transfer and entropy generation due to natural convection in Al_2O_3-water nanofluid where the thick bottom wall of the enclosure is heated sinusoidally, the upper wall is maintained with comparatively cold temperature and both vertical walls are kept adiabatic. The simulated results are obtained by using a finite volume based technique and observed that entropy generation decreases with increase in wall thickness and increases with increase of Rayleigh number. Using the first and second law of thermodynamics, an effective configuration is expected to provide high heat transfer and minimum entropy generation rate. The steady state performance of a partially filled pipe with porous medium is evaluated by Mahdavi et al. [139] and reported that the losses caused due to increased pumping power cannot be compensated by enhanced heat transfer rate. Moreover, an increase in the total entropy generation is observed with increase in porous layer thickness and Darcy number. Torabi

et al. [231] conducted a numerical study of thermodynamic analysis of forced convection through porous medium using pore scale modeling. Examining the first and second law of thermodynamics, they concluded that the flow in high porosity medium provides a better heat transfer performance at higher Reynolds number and for low porosity, the better performance can be obtained with low Reynolds number.

1.13 Thesis overview

This thesis consists of six main chapters with three appendices. In the introduction section of each chapter, the problem definition and the brief survey of literature along with the motivation and applications are addressed. The mathematical description is then presented, followed by the numerical techniques used for the solution process. The computational flow visualization is included by solving the full Navier-Stokes equations with nanofluid viscous term and our model has the flexibility that it can handle any type of nanofluids. The accuracy of the present numerical methods are tested and verified with the existing numerical, analytical and experimental results available in the literature. The results are discussed with the help of relevant data and plots. At the end of each chapter, we have included the summery and conclusions.

Chapter-I is introductory. In this chapter we have discussed the general outlines of the use of Computational fluid dynamics (CFD) and its usage in industry and daily life. The governing equations of fluid flow, heat and mass transfer are described. We have considered the basic characteristics of nanofluid flows and the theoretical analysis of nanofluid based on different approaches and its limitations is explained in this section. Various computational methods used for solution of the flow governing non-linear partial differential equations for fluid flow and heat transfer are addressed. Different numerical estimations for discretization of convective and diffusive terms of nonlinear partial differential equations are carried out. Various classification of nanofluids are discussed based on their properties and characterization. Several flow phenomena such as stream function and vortex formulations, entropy generation etc. are introduced. The basic definitions of flow governing parameters such as Reynolds number, Rayleigh number, Grashof number etc. which are used in subsequent chapters are explained.

Chapter-II is focussed on the numerical modeling of mixed convection heat transfer effects in a lid-driven cavity filled with a copper-water nanofluid. A heated wall mounted block with constant heat flux is attached along the vertical wall. The left vertical wall is maintained at higher temperature as compared to the right vertical wall and the other (top and bottom) walls are considered to be insulated. A finite volume based numerical approach with QUICK scheme is used for the solution of nonlinear governing equations. A computational visualization technique is used to represent the two dimensional results of streamlines, isotherms, average Nusselt number and bulk-average temperature for a wide range of physical parameters, namely Reynolds number, Rayleigh number and solid volume fraction. The effective fluid flow and heat transfer variation is analyzed by placing the heated mounted block first along the left vertical wall (Case-I) and then along the right vertical wall (Case-II) to test the maximum heat transfer effects. The changes in main characteristics of the flow due to variation of Reynolds number and Rayleigh numbers are elaborated. The effect of various flow parameters on the thermal conductivity behavior for both cases are discussed on the basis of calculated average Nusselt number and bulk-average temperature. It is observed that case-I has higher heat transfer rate as compared to case-II, for higher $Re,\ Ra$ and ϕ.

In **Chapter-III**, mixed convection nanofluid flow in a two sided lid driven enclosure with discrete heat sources have been numerically investigated. The flow behavior is analyzed for three different cases, depending on the direction of the moving vertical walls with fixed upper and lower walls; In case-I, left vertical wall is moving downwards and the right one is moving upwards, in case-II, both the vertical walls are moving downwards and in case-III both walls are moving upwards. Two discrete heat sources of equal lengths are taken on the lower wall and the rest part of the wall is kept insulated. The other three walls are kept at constant low temperature. The effect of flow governing parameters such as Reynolds number $1 \leq Re \leq 100$, Richardson number $0.1 \leq Ri \leq 10$ and solid volume fraction $0.0 \leq \phi \leq 0.2$ with Prandtl number $Pr = 6.2$ is studied to understand the fluid flow pattern and the heat transfer effect using isotherms and average Nusselt number. We found that the heat transfer and fluid flow is sensitive to the direction of vertical walls. The average heat transfer rate is found to be highest in case-I.

In **Chapter-IV**, a numerical study of hydromagnetic mixed convective flow inside

a cubical enclosure filled with a porous mixture is presented. The flow enhancement is observed due to a sinusoidal time dependent discrete temperature gradient along the boundaries. A two dimensional computational visualization technique is used to find the detailed physical insights of the thermally activated porous flows subjected to the magnetic field effects. The time history analysis is made for flow and thermal stratification for a series of fluid parameters such as Grashof number, Hartmann number and Darcy number, porosity and oscillatory frequency. The total heat transfer effects are computed for both high convection (due to magnetic field) and diffusive forces (due to temperature). The local Nusselt number is increasing along the side walls for increase of Hartmann number. Bulk average temperature is found to be maximum due to the variation of Grashof number and oscillatory frequency.

In **Chapter-V**, a numerical investigation of mixed convection is carried out in a two-sided lid-driven enclosure filled with copper-water nanofluid. Three different cases(same as in chapter-III) have been discussed depending on the direction of moving vertical walls to analyze the performance evaluation criteria using a combined analysis of fluid flow, heat transfer and entropy generation. The buoyancy effects are incorporated using two discrete heat sources placed on the bottom wall maintaining a fixed distance from both the side walls. Rest part of the bottom wall is kept insulated while other walls are maintained at constant low temperature. The effect of higher nanoparticle volume fraction (upto 20%) with variation of Reynolds number and Richardson number is studied to find the effective heat transfer rate. The results are presented using streamlines, isotherms and energy flux vectors. The performance evaluation criteria of the system is analyzed through the Nusselt number and entropy generation. The result reveals that in case-I, both heat transfer and entropy generation rate are maximum. From the analysis of performance evaluation criteria, case-II is found to be the best as it provides maximum heat transfer on the cost of least entropy generation.

In **Chapter-VI**, the performance of heat transfer and entropy generation due to magneto-hydrodynamic (MHD) nanofluid flow inside an enclosure filled with a fluid saturated porous medium is presented. The flow is influenced by time periodic discrete heat sources along the short side walls. A detailed physical insights of time dependent flow and heat transfer is presented based on various flow governing parameters such as Grashof

number($10^4 - 10^6$), Hartmann number($1 - 50$), Darcy number($0.001 - 1$) and nanoparticle volume fraction ($0.0 - 0.20$) with a fixed Prandtl number (6.2). The resulting energy flux vectors are simulated to analyze the convection generated heat transfer ratio. Entropy generation and Bejan number are used to study the performance of the system. Based on the calculated performance evaluation criteria, the maximum heat transfer on the cost of least entropy generation for $Gr = 10^6$ and $Ha = 50$ is obtained when $Da = 0.001$ with $\phi = 0.2$.

1.14 Aims and objectives of thesis

The aim of this thesis is to investigate various flow conditions which helps to design an efficient mechanical system. The efficiency of the mechanical systems depends on various factors such as flow speed, flow direction, temperature on the boundaries, location of heat sources and entropy generation. Hence, the objectives of the present work is to simulate the flow problems and analyze the flow behavior, heat transfer and entropy generation for different configurations in order to obtain the best possible configuration in the sense of higher heat transfer rate with minimum loss of energy. It is well known that the metallic and nonmetallic nanoparticles are very much helpful for increasing the thermal conductivity of the fluid but it is not always a smart move to use maximum volume fraction of nanoparticles in clear fluid. A better understanding of exact proportion of nanoparticles in clear fluid is required to obtain the maximum efficiency from the system. Hence, another objective is to compare various volume fractions of nanoparticle and find the optimum volume fraction that needs to be added in the base fluid so as to obtain higher heat transfer rate with minimum entropy generation.

Chapter 2

Buoyancy Driven Heat Transfer in Nanofluids Due to Wall Mounted Heat Source [1]

2.1 Introduction

In recent years, nanofluids have attracted enormous interests from researchers due to their large scale of applications in industry, power plants and reactors for cooling processes. Normally, fluids like water, propylene glycol or ethylene glycol are used for cooling, but these compounds possesses very low thermal conductivity. The term nanofluid refers to the fluid in which nano-scale particles are suspended in the base fluid to utilize their suspension stability effectively [134]. Metallic nanoparticles with higher thermal conductivity leads to remarkable increase in effective thermal conductivity of these types of fluids. However, increase in thermal conductivity depends on shape and size of the solid nano-scale particles. The scalar transport properties can also be considerably enhanced by adding these particles to liquid flow.

The dependence of thermophysical properties in nanoparticles-fluid mixture is estimated by Xie et al.[245]. They found that nanoparticle fluid mixtures containing nano-sized particles have higher thermal conductivity compared to the same liquid without nanoparticles. Keblinski et al. [109] worked on the possible mechanisms of enhancing thermal conductivity and suggested that the size effect, the surface absorption and clustering of nanoparticles could be the major reasons for heat transfer enhancement.

[1]The contents of this chapter has been published in *Alexandria Engineering Journal, Elsevier, DOI:10.1016/j.aej.2016.01.030*

The model developed by Maxwell [153] has shown that effective thermal conductivity of suspensions containing spherical particles can be increased by increasing the solid volume fraction of the nanoparticles and the proposed model also depicted the dependence of thermal conductivity of nanofluid on the solid volume fraction ratio which is applicable to only micro sized particles with low dense mixtures. Consequently, Maxwell's model is improved by number of authors, e.g. Kumar et al. [129], Patel et al. [180], Yu and Choi [250] and Prasher et al. [185] by varying the particle size, solid volume fraction ratio and temperature to find the higher thermal conductivity.

In natural convection process, it is found that dynamic viscosity plays a vital role for heat transfer enhancement of the nanofluid. Xu [246] proposed a model for calculation of the thermal conductivity of nanofluids, due to Brownian motion of nanoparticles in the base fluid depending upon average size of nanoparticles, temperature, fractal dimensions and concentration of nanofluids. Sheremet and Pop [206] studied a steady natural convection heat transfer in a square porous enclosure filled with nanofluid using Buongiorno's model where the convective heat transfer is generated by heated left wall. Using Darcy's law for the flow in porous medium and Boussinesq approximation for the buoyancy effects, it is observed that high thermophoresis parameter, low Brownian motion parameter, low Lewis and Rayleigh numbers and high thermal conductivity ratio reflect essential non-homogeneous distribution of the nanoparticles inside the porous cavity.

Eastman et al. [61] experimentally observed that thermal conductivity can be increased upto 60% by using a water based nanofluid consisting of 5% CuO nanoparticles. In another experimental study Lee et al. [134] observed that thermal conductivity of nanofluids increases with the increase of solid volume fraction by considering both Al_2O_3-water and CuO-water mixture. Hwang et al. [95] carried out a theoretical investigation for the thermal characteristics of natural convection of an alumina-based nanofluid in a rectangular cavity heated from below using Jang and Choi's model [102] by predicting the effective thermal conductivity of nanofluids.

Khanafer et al. [122] investigated the problem of buoyancy-induced heat transfer of nanofluids in a two-dimensional enclosure due to a natural convection process where the vertical walls are differentially heated and other walls are insulated, non-conducting and impermeable to solute. Heat transfer performance is discussed on the basis of buoyancy

effects, solid particle dispersion and various flow controlling parameters. They found that for any Grashof number, heat transfer in the enclosure is increased by changing the volume fraction of copper nanoparticles in water. Ho et al. [89] numerically investigated the effects of uncertainties by implementing different formulas of effective thermal conductivity and dynamic viscosity of the Al_2O_3-water nanofluid in a vertical square enclosure. It is also found that by adding nanoparticles in pure water improves its cooling performance at low Rayleigh numbers.

Mixed convection flow in lid-driven cavity with a horizontal sliding wall is a subject of interest for many years, since this phenomenon is often encountered in thermal performance of the system. Tiwari and Das [230] investigated the heat transfer augmentation in a lid-driven cavity filled with a nanofluid numerically and found that the presence of nanoparticles in base fluid is capable of increasing the heat transfer capacity. Sheremet et al. [207] used the model suggested by Tiwari and Das, and discussed the natural convection heat transfer in a porous enclosure utilizing nanofluid subjected to thermal stratification. They have tried to find the effects of Rayleigh number, thermal stratification parameter, porosity of the porous medium, solid volume fraction parameter of nanoparticles, and the solid volume fraction for the local and average Nusselt numbers, streamlines and isotherms.

Mixed convective thermosolutal effects in a lid driven cavity is studied by Sheremet and Pop [207] where the movable upper and lower lids are maintained with higher and lower temperature to find the substantial effects on the flow and heat transfer characteristics due to variation of the Reynolds, Grashof, Prandtl and Lewis numbers along with the buoyancy-ratio. Study of laminar mixed convective flow and heat transfer of water with Al_2O_3 nanofluid in single and double lid-driven cavities is carried out by Chamkha and Abu-Nada [45] using streamline-vorticity function formulation. They reported about the heat transfer enhancement due to nanoparticles volume fraction for moderate and large Richardson numbers.

According to Nasrin et al. [166], Richardson number plays a vital role on the heat transfer characterization. The technique for improvement of thermal conductivity by using nanofluids in place of traditional fluids like water has been extensively used now a days. The most usage of mixed convection flow is to include the electronic cooling,

MEMS applications, food processing, nuclear reactors, drying technologies and lubrication technologies, etc [10, 226]. Despite a good number of theoretical and experimental works on nanofluid based buoyancy driven natural or mixed convection process are analyzed in the literature, still there are several information lacking regarding the heat transfer enhancement in enclosures.

The present chapter focusses on the effective heat transfer rate due to the localized heat source with constant heat flux embedded along the left and right vertical walls of the lid driven cavity filled with copper-water nanofluid. The left vertical wall is maintained at higher temperature compared to the right vertical wall and the top and bottom walls are kept insulated. A finite volume based numerical approach with QUICK scheme is used for the solution of nonlinear flow governing equations. The effective fluid flow and heat transfer variation is analyzed by mounting the heated block first along the left vertical wall (case-I) and then along the right vertical wall (case-II) to obtain the maximum heat transfer effects. The changes in main characteristics of the flow due to variation of nanoparticle volume fraction, Reynolds number and Rayleigh number are elaborated. The effect of various flow parameters on the thermal conductivity behavior for both cases are discussed on the basis of average Nusselt number and bulk-average temperature.

In the next section the physical configuration and mathematical formulation of the problem is derived.

2.2 Problem formulation

We consider the flow within a two-dimensional lid-driven square cavity of height H and width W filled with Cu-water nanofluid. The flow is assumed to be laminar and the nanofluid is assumed to be Newtonian and incompressible. The top and bottom walls are assumed to be non-conducting, insulated and impermeable to solute. The left vertical wall is kept at high temperature (T_h) and right vertical wall is maintained with low temperature (T_c). The copper nanoparticles are assumed to be of uniform shape (spherical) and size with diameter equal to 100nm.

Initially, the Cu-water nanofluid is considered to be at rest with uniform temperature T_c. A heated obstacle of the form of a rectangular block of length $W/2$ and width

$W/8$ is considered to be mounted along the middle of the left and right vertical wall maintained with temperature T_h. In case-I, the heat source with constant heat flux (T_h) is attached along the left vertical wall above the height $H/2$ (Fig. 2.1(a)) and in case-II, the heat source placed along the right vertical wall above the height $H/2$ (Fig. 2.1(b)).

It is assumed that the fluid phase and nanoparticles both are in thermal equilibrium state and have same velocity with no slip condition. The thermophysical properties of the nanofluid are assumed to be constant except for the density variation due to temperature which is determined by Boussinesq approximation [108] as,

$$\rho_f(T) = \rho_{f_0}[1 - \beta_T(T - T_C)] \tag{2.1}$$

where, ρ_{f_0} is the density of the undisturbed fluid, T_C is the uniform temperature of the fluid at rest and β_T (the volumetric coefficient of thermal expansion) is given by

$$\beta_T = -\frac{1}{\rho_f}\frac{\partial \rho_f}{\partial T} > 0. \tag{2.2}$$

The thermophysical properties of water and copper at the reference temperature are presented in Table 2.1 [142].

The two-dimensional flow governing Navier-Stokes equations along with heat transfer equation in stream function-vorticity formulation with Boussinesq-fluid assumption are given by,

Kinematics equation :

$$\frac{\partial^2 \Psi}{\partial x^{*^2}} + \frac{\partial^2 \Psi}{\partial y^{*^2}} = -\Omega. \tag{2.3}$$

Vorticity equation :

$$\frac{\partial \Omega}{\partial t^*} + u^*\frac{\partial \Omega}{\partial x^*} + v^*\frac{\partial \Omega}{\partial y^*} = \frac{\nu_{nf}}{\rho_{nf}}\left(\frac{\partial^2 \Omega}{\partial x^{*^2}} + \frac{\partial^2 \Omega}{\partial y^{*^2}}\right) + \left(\phi\beta_s + (1-\phi)\beta_f\right) g\left(\frac{\partial T^*}{\partial x^*}\right). \tag{2.4}$$

Energy equation :

$$\frac{\partial T^*}{\partial t^*} + u^*\frac{\partial T^*}{\partial x^*} + v^*\frac{\partial T^*}{\partial y^*} = \alpha_{nf}\left(\frac{\partial^2 T^*}{\partial x^{*^2}} + \frac{\partial^2 T^*}{\partial y^{*^2}}\right) \tag{2.5}$$

where, α_{nf} is the thermal diffusivity given by,

$$\alpha_{nf} = \frac{k_{nf}}{(\rho C_p)_{nf}}$$

and ρ_{nf} is the effective density given as,

$$\rho_{nf} = (1-\phi)\rho_f + \phi\rho_s$$

here, ϕ, ρ_{nf}, ρ_f, and ρ_s denotes the volume fraction of the nanoparticles, density of nanofluid, density of base fluid and density of nanoparticles respectively.

The heat capacitance of nanofluid can be written as

$$(\rho C_p)_{nf} = (1-\phi)(\rho C_p)_f + \phi(\rho C_p)_s.$$

The effective thermal conductivity of the nanofluid is approximated by the Maxwell self-consistent approximation model [153] and is given by,

$$\frac{k_{nf}}{k_f} = \frac{k_s + 2k_f - 2\phi(k_f - k_s)}{k_s + 2k_f + \phi(k_f - k_s)}.$$

The effective viscosity of nanofluid is calculated using Brinkman model [39] as,

$$\mu_{nf} = \frac{\mu_f}{(1-\phi)^{2.5}}.$$

The prescribed initial and boundary conditions are given by

$$u^* = v^* = T^* = 0 \qquad \text{for} \qquad t^* = 0;$$

for $t^* > 0$,

$$u^* = v^* = 0,\ T^* = T_H \qquad \text{at} \quad x^* = 0 \qquad 0 \le y^* \le H;$$

$$u^* = v^* = 0,\ T^* = T_C \qquad \text{at} \quad x^* = W \qquad 0 \le y^* \le H;$$

$$u^* = v^* = 0,\ \frac{\partial T^*}{\partial y^*} = 0 \qquad \text{at} \quad y^* = 0 \qquad 0 \le x^* \le W;$$

$$u^* = U_0, v^* = 0,\ \frac{\partial T^*}{\partial y^*} = 0 \qquad \text{at} \quad y^* = H \qquad 0 \le x^* \le W$$

and along the thermally activated surface; $u^* = v^* = 0$, $T^* = T_H$.

The above mentioned equations can be expressed in non-dimensional form by incorporating the following dimensionless variables,

$$x = \frac{x^*}{H};\ y = \frac{y^*}{H};\ u = \frac{u^*}{U_0};\ v = \frac{v^*}{U_0};\ T = \frac{T^* - T_C}{T_H - T_C}. \tag{2.6}$$

The governing equations in dimensionless form can be written as,

$$\frac{\partial^2 \psi}{\partial x^2} + \frac{\partial^2 \psi}{\partial y^2} = -\omega, \tag{2.7}$$

$$\frac{\partial \omega}{\partial t} + u\frac{\partial \omega}{\partial x} + v\frac{\partial \omega}{\partial y} = \frac{1}{Re}\frac{\rho_f}{\rho_{nf}}\frac{1}{(1-\phi)^{2.5}}\left(\frac{\partial^2 \omega}{\partial x^2} + \frac{\partial^2 \omega}{\partial y^2}\right) + \frac{Ra}{Re^2 Pr}\frac{\rho_f}{\rho_{nf}}\left(1 - \phi + \phi\frac{\rho_p \beta_p}{\rho_f \beta_f}\right)\frac{\partial T}{\partial x}, \tag{2.8}$$

$$\frac{\partial T}{\partial t} + u\frac{\partial T}{\partial x} + v\frac{\partial T}{\partial y} = \frac{1}{RePr}\frac{k_{nf}}{k_f}\frac{(\rho C_p)_f}{(\rho C_p)_{nf}}\left(\frac{\partial^2 T}{\partial x^2} + \frac{\partial^2 T}{\partial y^2}\right). \tag{2.9}$$

The initial conditions for $t = 0$ are given by,

$$u = v = 0,\ T = 0 \qquad \text{for} \quad 0 \le x \le 1, \quad 0 \le y \le 1; \tag{2.10}$$

and for $t > 0$,

$$\begin{aligned} u = v = 0,\ T = 1 \qquad &\text{at} \quad x = 0 \qquad 0 \le y \le 1; \\ u = v = T = 0 \qquad &\text{at} \quad x = 1 \qquad 0 \le y \le 1; \\ u = v = 0,\ \frac{\partial T}{\partial y} = 0 \qquad &\text{at} \quad y = 0 \qquad 0 \le x \le 1; \\ u = 1, v = \frac{\partial T}{\partial y} = 0 \qquad &\text{at} \quad y = 1 \qquad 0 \le x \le 1 \end{aligned} \tag{2.11}$$

and along the surface mounted block, the non-dimensional temperature is considered to be 1.

It can be seen from the equations that the flow and heat transfer are characterized by three dimensionless parameters (i) Rayleigh number (Ra), (ii) Reynolds number (Re) and (iii) Prandtl number (Pr) and are given by

$$Ra = \frac{g\beta_f L^3 \Delta t}{\nu_f \alpha_f}, \quad Re = \frac{\rho U_0 L}{\nu}, \quad Pr = \frac{\nu_f}{\alpha_f}. \tag{2.12}$$

In order to calculate the heat transfer enhancement, we have calculated Nu (Nusselt number) and Nu_m (average Nusselt number) along the heated surface as,

$$\begin{aligned} Nu(X) &= -\frac{k_{nf}}{k_f}\left(\frac{\partial T}{\partial x}\right)_{hot\ wall} \\ Nu_m &= \frac{\int_{hot\ wall} Nu(x)dx}{\int_{hot\ wall} dx}. \end{aligned} \tag{2.13}$$

The bulk average temperature [217] is defined as,

$$\kappa = \int \frac{TdV}{V} \tag{2.14}$$

where, V is the volume of enclosure.

2.3 Numerical method

In order to find the numerical solution of the governing fluid flow equations together with the specified boundary conditions a control volume approach is opted [178]. The numerical solutions are obtained by using uniform collocated grid system. The algebraic finite volume equations for vorticity and energy are solved through alternate direction implicit (ADI) scheme. When the flow is dominated by the convection effects, the numerical instability is achieved for higher Reynolds number. To overcome such instability a third order accurate quadratic upwind scheme (QUICK) is employed to discretize the convective terms [213]. In order to linearize the nonlinear system of partial differential equations, a quasi-linearization approximation has been employed.

At every time step, we approximate the nonlinear term as

$$\left(u\frac{\partial\omega}{\partial x}\right)^{n+1} = u^n\left(\frac{\partial\omega}{\partial x}\right)^{n+1} \tag{2.15}$$

with $n \geq 0$, the iteration index. The convective terms are discretized by third-order accurate upwind difference scheme as

$$u_{ij}\left(\frac{\partial\omega}{\partial x}\right)_{ij} = u_{ij}\frac{\omega_{i+2j} - 2\omega_{i+1j} + 9\omega_{ij} - 10\omega_{i-1j} + 2\omega_{i-2j}}{6\delta x} \tag{2.16}$$

for u_{ij} positive and,

$$u_{ij}\left(\frac{\partial\omega}{\partial x}\right)_{ij} = u_{ij}\frac{-2\omega_{i+2j} + 10\omega_{i+1j} - 9\omega_{ij} + 2\omega_{i-1j} - \omega_{i-2j}}{6\delta x} \tag{2.17}$$

for u_{ij} negative.

The truncation error of this scheme is given by $\frac{1}{4}(\delta x)^3(u_{ij}\partial^4\omega/\partial x^4)$.

The expression for ω, near the wall are obtained by a second order central difference scheme as,

$$u_{ij}\left(\frac{\partial\omega}{\partial x}\right)_{ij} = u_{ij}\frac{\omega_{i+1j} - \omega_{i-1j}}{2\delta x} + O(\delta x^2). \tag{2.18}$$

The diffusion terms are discretized through a second-order accurate central-difference scheme, which is conducive to a stable solution as,

$$\left(\frac{\partial^2\omega}{\partial x^2}\right)_{ij} = \frac{\omega_{i-1j} - 2\omega_{ij} + \omega_{i+1j}}{(\delta x)^2},$$

$$\left(\frac{\partial^2\omega}{\partial y^2}\right)_{ij} = \frac{\omega_{ij-1} - 2\omega_{ij} + \omega_{ij+1}}{(\delta y)^2}.$$

The boundary condition for vorticity on the solid boundary is unknown which can be evaluated by using the Poisson equation [eq. (2.7)] along the boundary. The boundary condition of wall vorticity on the lower flat surface is given by

$$\omega_{i1} = -\frac{8\psi_{i2} - \psi_{i3}}{2\delta y^2} + O[(\delta y)^2] \tag{2.19}$$

In a similar manner, boundary conditions for ω are obtained on the other walls.

We consider the grids (x_i, y_j),

$$x_i = (i-1)\delta x \qquad i = 1, ..., M+1 \tag{2.20}$$

$$y_j = (j-1)\delta y \qquad j = 1, ..., N+1 \tag{2.21}$$

where i and j are grid index in the x and y directions respectively. M and N are the number of grid points along x and y direction respectively. The increment along x axis is δx and along y axis is δy. The value of ψ and ω at $(i,j)^{th}$ cell is denoted by ψ_{ij} and ω_{ij} respectively.

An implicit calculation of the momentum and energy equations is performed. The discretization of the governing vorticity and heat transfer equations in horizontal direction results in a system of algebraic equations of the form

$$A_i\Phi_{i-1,j}^{n+1/2} + B_i\Phi_{i,j}^{n+1/2} + C_i\Phi_{i+1,j}^{n+1/2} = D_i \tag{2.22}$$

where Φ denotes ω and T and the coefficients for different cases are given by,

Case-I: When $u_{ij}^n > 0$, $v_{ij}^n > 0$:

$$A_i = -\frac{5}{3}\frac{u_{ij}^n}{\delta x} - \frac{\rho_f}{Re\rho_{nf}(1-\phi)^{2.5}(\delta x)^2},$$

$$B_i = \frac{2}{\delta t} + \frac{3}{2}\frac{u_{ij}^n}{\delta x} + \frac{2\rho_f}{Re\rho_{nf}(1-\phi)^{2.5}(\delta x)^2},$$

$$C_i = -\frac{1}{3}\frac{u_{ij}^n}{\delta x} - \frac{\rho_f}{Re\rho_{nf}(1-\phi)^{2.5}(\delta x)^2},$$

$$\begin{aligned} D_i =& \left(\frac{5}{3}\frac{v_{ij}^n}{\delta y} + \frac{\rho_f}{Re\rho_{nf}(1-\phi)^{2.5}(\delta y)^2}\right)\omega_{ij-1}^n \\ &+ \left(\frac{2}{\delta t} - \frac{3}{2}\frac{v_{ij}^n}{\delta y} - \frac{2\rho_f}{Re\rho_{nf}(1-\phi)^{2.5}(\delta y)^2}\right)\omega_{ij}^n \\ &+ \left(\frac{1}{3}\frac{v_{ij}^n}{\delta y} + \frac{\rho_f}{Re\rho_{nf}(1-\phi)^{2.5}(\delta y)^2}\right)\omega_{ij+1}^n \\ &- \frac{u_{ij}^n}{6\delta x}(\omega_{i+2j}^n + 2\omega_{i-2j}^n) - \frac{v_{ij}^n}{6\delta y}(\omega_{ij+2}^n + 2\omega_{ij-2}^n). \end{aligned}$$

Case-II: When $u_{ij}^n > 0$, $v_{ij}^n < 0$:

$$A_i = -\frac{5}{3}\frac{u_{ij}^n}{\delta x} - \frac{\rho_f}{Re\rho_{nf}(1-\phi)^{2.5}(\delta x)^2},$$

$$B_i = \frac{2}{\delta t} + \frac{3}{2}\frac{u_{ij}^n}{\delta x} + \frac{2\rho_f}{Re\rho_{nf}(1-\phi)^{2.5}(\delta x)^2},$$

$$C_i = -\frac{1}{3}\frac{u_{ij}^n}{\delta x} - \frac{\rho_f}{Re\rho_{nf}(1-\phi)^{2.5}(\delta x)^2},$$

$$\begin{aligned} D_i =& \left(-\frac{1}{3}\frac{v_{ij}^n}{\delta y} + \frac{\rho_f}{Re\rho_{nf}(1-\phi)^{2.5}(\delta y)^2} \right)\omega_{ij-1}^n \\ &+ \left(\frac{2}{\delta t} + \frac{3}{2}\frac{v_{ij}^n}{\delta y} - \frac{2\rho_f}{Re\rho_{nf}(1-\phi)^{2.5}(\delta y)^2} \right)\omega_{ij}^n \\ &+ \left(-\frac{5}{3}\frac{v_{ij}^n}{\delta y} + \frac{\rho_f}{Re\rho_{nf}(1-\phi)^{2.5}(\delta y)^2} \right)\omega_{ij+1}^n \\ &- \frac{u_{ij}^n}{6\delta x}(\omega_{i+2j}^n + 2\omega_{i-2j}^n) + \frac{v_{ij}^n}{6\delta y}(2\omega_{ij+2}^n + \omega_{ij-2}^n). \end{aligned}$$

Case-III: When $u_{ij}^n < 0$, $v_{ij}^n > 0$:

$$A_i = \frac{1}{3}\frac{u_{ij}^n}{\delta x} - \frac{\rho_f}{Re\rho_{nf}(1-\phi)^{2.5}(\delta x)^2},$$

$$B_i = \frac{2}{\delta t} - \frac{3}{2}\frac{u_{ij}^n}{\delta x} + \frac{2\rho_f}{Re\rho_{nf}(1-\phi)^{2.5}(\delta x)^2},$$

$$C_i = \frac{5}{3}\frac{u_{ij}^n}{\delta x} - \frac{\rho_f}{Re\rho_{nf}(1-\phi)^{2.5}(\delta x)^2},$$

$$\begin{aligned} D_i =& \left(\frac{5}{3}\frac{v_{ij}^n}{\delta y} + \frac{\rho_f}{Re\rho_{nf}(1-\phi)^{2.5}(\delta y)^2} \right)\omega_{ij-1}^n \\ &+ \left(\frac{2}{\delta t} - \frac{3}{2}\frac{v_{ij}^n}{\delta y} - \frac{2\rho_f}{Re\rho_{nf}(1-\phi)^{2.5}(\delta y)^2} \right)\omega_{ij}^n \\ &+ \left(\frac{1}{3}\frac{v_{ij}^n}{\delta y} + \frac{\rho_f}{Re\rho_{nf}(1-\phi)^{2.5}(\delta y)^2} \right)\omega_{ij+1}^n \\ &+ \frac{u_{ij}^n}{6\delta x}(2\omega_{i+2j}^n + \omega_{i-2j}^n) - \frac{v_{ij}^n}{6\delta y}(\omega_{ij+2}^n + 2\omega_{ij-2}^n). \end{aligned}$$

Case-IV: When $u_{ij}^n < 0$, $v_{ij}^n < 0$:

$$A_i = \frac{1}{3}\frac{u_{ij}^n}{\delta x} - \frac{\rho_f}{Re\rho_{nf}(1-\phi)^{2.5}(\delta x)^2},$$

$$B_i = \frac{2}{\delta t} - \frac{3}{2}\frac{u_{ij}^n}{\delta x} + \frac{2\rho_f}{Re\rho_{nf}(1-\phi)^{2.5}(\delta x)^2},$$

$$C_i = \frac{5}{3}\frac{u_{ij}^n}{\delta x} - \frac{\rho_f}{Re\rho_{nf}(1-\phi)^{2.5}(\delta x)^2},$$

$$\begin{aligned} D_i =& \left(-\frac{1}{3}\frac{v_{ij}^n}{\delta y} + \frac{\rho_f}{Re\rho_{nf}(1-\phi)^{2.5}(\delta y)^2}\right)\omega_{ij-1}^n \\ &+ \left(\frac{2}{\delta t} + \frac{3}{2}\frac{v_{ij}^n}{\delta y} - \frac{2\rho_f}{Re\rho_{nf}(1-\phi)^{2.5}(\delta y)^2}\right)\omega_{ij}^n \\ &+ \left(-\frac{5}{3}\frac{v_{ij}^n}{\delta y} + \frac{\rho_f}{Re\rho_{nf}(1-\phi)^{2.5}(\delta y)^2}\right)\omega_{ij+1}^n \\ &+ \frac{u_{ij}^n}{6\delta x}(2\omega_{i+2j}^n + \omega_{i-2j}^n) + \frac{v_{ij}^n}{6\delta y}(2\omega_{ij+2}^n + \omega_{ij-2}^n). \end{aligned}$$

and along the boundary, the coefficients are slightly different as the convective terms are discretized by central difference scheme. The coefficients are given by,

$$A_i = -\frac{1}{2}\frac{u_{ij}^n}{\delta x} - \frac{\rho_f}{Re\rho_{nf}(1-\phi)^{2.5}(\delta x)^2},$$

$$B_i = \frac{2}{\delta t} + \frac{2\rho_f}{Re\rho_{nf}(1-\phi)^{2.5}(\delta x)^2},$$

$$C_i = \frac{1}{2}\frac{u_{ij}^n}{\delta x} - \frac{\rho_f}{Re\rho_{nf}(1-\phi)^{2.5}(\delta x)^2},$$

$$\begin{aligned} D_i =& \left(\frac{1}{2}\frac{v_{ij}^n}{\delta y} + \frac{\rho_f}{Re\rho_{nf}(1-\phi)^{2.5}(\delta y)^2}\right)\omega_{ij-1}^n \\ &+ \left(\frac{2}{\delta t} - \frac{2\rho_f}{Re\rho_{nf}(1-\phi)^{2.5}(\delta y)^2}\right)\omega_{ij}^n \\ &+ \left(-\frac{1}{2}\frac{v_{ij}^n}{\delta y} + \frac{\rho_f}{Re\rho_{nf}(1-\phi)^{2.5}(\delta y)^2}\right)\omega_{ij+1}^n. \end{aligned}$$

The vertical direction scheme is developed in the similar fashion.

Second order Poisson equation for the stream function [eq. (2.7)], is discretized through an upwind spatial difference scheme. The resulting algebraic equations are solved using the successive over relaxation (SOR) method. The convergence criterion used for the calculation of temperature, vorticity and stream function are defined by the expression,

$$\epsilon = \left| \frac{\tau_{i,j}^{n+1} - \tau_{i,j}^n}{\tau_{i,j}^{n+1}} \right| \leq 10^{-5} \tag{2.23}$$

where, ϵ is the tolerance in any time level and τ represents the flow variables.

The velocity components u and v at every grid point are evaluated using central difference approximation. A time dependent numerical solution is achieved by obtaining

the flow field variables through a sequence of shorter time steps of duration 0.001. For the range of parameter values considered here, the flow field achieves a steady state after a transient state, and this steady state is independent of the initial conditions prescribed.

2.4 Code validation

To test the accuracy of our numerical algorithm, a two dimensional lid-driven cavity filled with Cu-water nanofluid is considered. For this structure non-dimensional governing equation involves Reynolds, Rayleigh and Prandtl number. The grid independence test is performed by varying the grid size between 61×61 to 121×121. Fig. 2.2(a) represents the grid size effect on the horizontal velocity component for $Re = 10,\ Ra = 1.47 \times 10^4$ with $\phi = 3\%$. The results are found to be grid independent for 81×81 size and more. Moreover, the comparison of our result with that of Talebi et al. [226] is found to be optimum for 81×81 grid size.

Fig. 2.2(b) represents the time step independence test using u-velocity profile for $Ri = 1,\ Ra = 100$ with $\phi = 2\%$. The velocity profile shows that any further decrement of dt value from 0.001 will not effect the results, hence, $dt = 0.001$ is chosen for calculation of numerical results.

A comparison of present result for streamlines with the result due to Amir et al. [141] is presented in Fig. 2.3(a), (b) with $Ra = 10^3$, $Re = 10$ and $\phi = 0\%$. Amir et al. [141] considered the natural convection in a square cavity filled with nanofluid, where a horizontal heat source is mounted along the left wall. The computed result is found to be in good agreement with those of Amir et al. [141].

In Fig. 2.4(a) we present a comparison of our result for average Nusselt number of nanofluid within a vertical square enclosure with the experimental result due to Ho et al. [90]. In their experimental observation nanofluid has been formulated by mixing water with different volumetric fractions of alumina (Al_2O_3) nanoparticles ranging from 0.1 vol% to 4 vol%. The enclosure is differentially heated along the two vertical walls, while the remaining walls are thermally insulated. In the present comparison, we have considered the particle fraction as 1%, and Ra is varied between, $6 \times 10^5 \leq Ra \leq 3.37 \times 10^6$. Our results are in excellent agreement with the results due to Ho et al. [90].

Fig. 2.4(b) presents the comparison of the present result with the results due to Davis [55], Manzari [148], Wan et al. [43], Muthtamilselvan et al. [162], for a clear fluid case with the variation of Rayleigh numbers between $10^3 \leq Ra \leq 10^6$ with $Pr = 1$. It can be observed that the computational code is in good agreement with the benchmark results. The results have been presented for the variation of average Nusselt number due to uniformly heated wall where the parameters are considered as $Pr = 6.2,\ Ri = 1,\ Re = 100$ and aspect ratio=1 with the variation of solid volume fraction $0 \leq \phi \leq 0.08$. Fig. 2.4(c) shows the average Nusselt number comparison with Muthtamilselvan et al. [162], which also found to be in good agreement with the present solution.

2.5 Results and discussion

In the present study pertaining to Cu-water nanofluid the numerical computations are performed for $10 \leq Re \leq 100$, $10^3 \leq Ra \leq 10^5$ and $0 \leq \phi \leq 5\%$ for a fixed Prandtl number, $Pr = 6.2$. Most of the studies in heat transfer process preferably uses the wall mounted block along the left and right vertical wall. In the present analysis, we have used the wall mounted blocks along the vertical walls to check the performance of heat transfer due to the moving lid. The flow is mainly governed by two mechanisms (i) shear force due to sliding of the top lid, (ii) Buoyancy force due to vertical temperature gradient from left wall along with heated wall mounted block.

In the first phase we have considered the block position on the left vertical hot wall (case-I). Fig. 2.5 and 2.6 displays the streamlines and isotherms for $Re = 10$ for different solid volume fractions and Rayleigh numbers. The fluid close to the heat source heated up quickly due to quick heat absorption. The fluid particles move upwards due to buoyancy force loosing their density and the cold fluid enters to this empty region moving from near region of the right cold wall. The hot fluid is moving towards the right wall through the lid movement. A large recirculating zone is formed filling the entire cavity. This confirms that for $Re \leq 10$, the flow in the cavity is defined due to the action of the moving lid and this is independent of the temperature and buoyancy variations in the cavity. With increase of Rayleigh number, the position of the center of vortex move towards the right vertical wall as depicted in Fig. 2.5. The presence of nanoparticles in the water increases

the intensity of the flow combined with the buoyancy and shear force. As the volume fraction of nanoparticles increases, the vortex move downwards.

Fig. 2.6 represents the effective thermal conductivity for small Reynolds number ($Re = 10$) with different Ra and ϕ values. For low Ra (10^3) values, it is observed that isotherms remain uniform in most part of cavity which signifies that heat transfer conductivity dominates. As Ra increases, the convective heat transfer effect increases and variation of temperature lying within the core of the cavity increases. At $Ra = 10^5$, it is found that the isotherms are almost parallel to the horizontal wall at the lower section of the cavity. From Fig. 2.6(g, h, i), it is observed that along downstream wall, the buoyancy is opposing the core flow and causes the down coming boundary layer to detach for the wall. It signifies that the temperature of the heated surface and adjacent fluid of the heat source is higher than other walls forming a large isothermal core. It is also clear from the figure that the value of isotherms increases with increase in solid volume fraction ratio as well as Rayleigh number and reaches its maximum value i.e., 0.9764 for $Ra = 10^5$ and $\phi = 5\%$.

The streamlines for $Re = 50$ and $Re = 100$ are presented in Fig. 2.7 and 2.9. As Re increases, for small Ra (10^3) the flow is dominated by buoyancy effects and the impact of shear mechanism generated by the moving top lid penetrates the hot fluid to a small distance towards the interior region of the cavity forming a primary eddy in the upper half of the enclosure. From Fig. 2.7 and 2.9, it is clearly observed that two small recirculation zones are created along the lower part of the cavity, since the temperature distribution does not influence the lower part of fluid which again demonstrates the insignificant contribution of buoyancy in the flow development.

For larger Re (100) values three eddies are generated at $Ra = 10^4$. It can also be observed from Fig. 2.9 that for $Ra = 10^3$, the lower right eddy is much larger as compared to the lower left eddy since flow is buoyancy dominated and as Ra increases the size gets reduced and finally vanished for $Ra = 10^5$ as the flow is dominated by shear effect. The hot fluid move towards the right vertical wall and the fluid in the origin mixed up for higher Reynolds number. At $Re = 100$ the fluid is well mixed and buoyancy force is dominated by shear force along the upper part of the cavity. The flow field shows a more significant contribution as Re increases.

A regular increase in effective thermal conductivity is observed from Fig. 2.8 and 2.10. The temperature is continuously increased with the increase in Ra as well as ϕ values. For the larger Re and smaller Ra values the isotherms in the upper portion of the cavity becomes parallel to the horizontal axis since the flow is shear dominated. However, in the lower section of the cavity, shear force is less effective and the heat transfer is mostly via convection in the boundary layers. As Ra increases, the convective heat transfer rate increases and the variation of temperature is occurring mostly in the core of the cavity, and the shear force dominates the flow. Thus, most of the isotherms become parallel to horizontal axis.

In the second case, we have kept the mounted heat source along the right vertical wall. Fig. 2.11 represents the streamlines for $Re = 10$ with $10^3 \leq Ra \leq 10^5$ and $0 \leq \phi \leq 5$ %. For low Re values, it is found that four separate eddies are formed inside the cavity for smaller Ra (10^3) values (Fig. 2.11(a, b, c)) and the fourth eddy vanishes with increase in Ra values. The upper eddy is formed due to the shear force created by the driven lid which tries the adjacent fluid to move forward. With increase in Ra values the upper eddy starts moving towards the right side of the cavity due to buoyancy effects from left wall. Middle eddy is formed because of the obstruction by mounted heat source, fractional loss and stagnation pressure but it vanishes with the increasing values of Ra. The lower upstream eddy formed for $Ra = 10^3$ is due to the combined buoyancy effects due to the left heated wall and the heat source, and got vanished for further increment in Ra. A lower downstream eddy is formed due to the opposing action of buoyancy and the heat transfer effects are mostly via convection in the boundary layers.

The buoyancy effects are significant only near the cavity wall however, the influence is less in the core of the cavity. With increase in Ra values, the lower downstream eddy gets enlarged and is divided into two parts due to the presence of secondary heat source along the middle of right wall. It can be observed that the solid volume fraction does not have any effect on the flow pattern but a significant difference is observed on the stream function values and the flow intensity is augmented with increase in the values of solid volume fraction. The flow fields indicate a variation for $Ra = 10^3$ with a 5% increase in solid volume fraction, i.e., flow line values changed from -0.0698 to -0.0669. Also, for smaller Ra values in Fig. 2.11(a, b, c) the primary eddy adheres to the walls of the cavity,

but moves away with increasing values of Ra as shown in Fig. 2.11(g, h, i), which shows that intensity of buoyancy increases with Ra. From Fig. 2.11, it is observed that the value of flow lines achieves higher values at higher values of Ra as compared to lower Ra values. It is also observed that due to increment of solid volume fraction the flow values are getting increased.

From Fig. 2.13 and 2.15, it is predicted that increase in Re result a significant change of the flow structure, i.e., the enlargement of lower upstream eddy and subsequently contraction of lower downstream eddy. But, at larger Re values with larger Ra the lower downstream eddy contracts and upper eddy expand towards lower right part of the cavity. We found a significant change of streamline values with increasing solid volume fraction ratio.

The heat transfer effect for case-II is presented in Fig. 2.12, 2.14 and 2.16 for Re=10, 50 and 100 respectively. The heat transfer for this case is due to conduction as well as convection effects resulting in a gradual variation of temperature in the cavity. Since, we have placed the heat source on the right wall, the heated fluid particles move upward region from the heat source and at the same time the opposing buoyancy effect takes place due to the heated left wall and the heat transfer rate increases in the whole domain. For increasing Re values, the isotherm lines becomes more and more parallel to the heat source due to the combined effect of buoyancy and shear force. The isotherm values are increased significantly with increase in Ra and solid volume fraction.

The variation of average Nusselt number against the Reynolds number ($10 \leq Re \leq 100$), Rayleigh number ($10^3 \leq Ra \leq 10^5$) and solid volume fraction ($0 \leq \phi \leq 5\%$) along the left vertical wall are presented in Fig. 2.17 and 2.18 for case-I and case-II respectively. In comparison to pure fluid, use of nanofluid increases the flow intensity, gives rise to the higher heat transfer rate resulting an increment in average Nusselt number (Fig. 2.17).

Increase in Re within the cavity leads to a forced convection dominated flow which results in the increment of average Nusselt number. For all Ra values, the increase of average Nusselt number seems to be linear and smooth. Increasing the value of Ra increases the average Nusselt number sharply. Also, the increase of solid volume fraction has a large impact on the heat transfer enhancement. The value of average Nusselt number corresponding to $Ra = 10^3$ with $\phi = 3\%$ is higher than the average Nusselt

number corresponding to $Ra = 10^4$ with $\phi = 0\%$. The same pattern can be observed if we compare average Nusselt number values for $Ra = 10^3$ at $\phi = 5\%$ with $Ra = 10^4$ at $\phi = 3\%$ or lower values of nanoparticle volume fraction. Hence, a higher heat transfer rate can be obtained at lower Ra values by increasing the nanoparticle volume fraction in fluid.

The average Nusselt number for case-II is presented in Fig. 2.18. In this case the average heat transfer rate is decreasing when Ra value is increasing at low Re values. Average Nusselt number values are increasing linearly with increase in Re values except for the value of $Ra = 10^5$. At Re=100, it is found that the highest average heat transfer rate is found for $Ra = 10^4$. The variation of average Nusselt number versus solid volume fraction found insignificant for lower Ra values. For $Ra = 10^5$, $Re \geq 50$, the average Nusselt number variation is found to be minimum. From both these cases, it can be observed that higher heat transfer rate is occurred in case-I compared to case-II. The use of heat source in case-I instead of case-II provides a relative increase of average Nusselt number and the relative increment is found to be 79.5% at $Ra = 10^5$, $Re = 10$ and ϕ=5% and 40.3% at $Ra = 10^5$, $Ra = 100$ and ϕ=5%.

Fig. 2.19 and 2.20 represents the bulk average nanofluid temperature for case-I and case-II respectively. The variation of bulk average temperature with Re is plotted and it has been observed that the bulk average temperature is decreasing when Re increases in both the cases. The bulk average temperature is found to be increasing with Ra values and a significant contribution is found at higher Re values in both cases. For all pertinent parameters case-II represents higher bulk average temperature than case-I. It can be clearly observed that bulk average temperature increases with increase of solid volume fraction except for higher Ra with higher ϕ values. For both the cases it is observed that higher values of Ra with $Re \geq 50$, the solid volume fraction shows negative impact on the heat transfer rate.

2.6 Conclusion

This chapter presents a numerical study of mixed convection flow of copper-water nanofluid in a lid driven cavity in which a heat source is mounted on the vertical wall of the cavity.

The mounted heat source is first placed on the left (hot) vertical wall and then to the right (cold) vertical wall. The left vertical wall is kept at higher temperature as compared to right vertical wall and the other two horizontal walls are kept insulated. The investigation is carried out for copper nanoparticles of size equal to 100nm with wide range of parameters Re and Ra and different values of solid volume fraction. In this study the effect of Re, Ra and ϕ on the flow pattern and heat transfer characteristics are investigated.

Based on the present analysis it is observed that for fixed value of Ra, the flow is dominated by the convection effects where the buoyancy-induced activities are appreciable, fluid is well mixed and temperature is well distributed in the bulk of cavity for low Re values. Under concurring thermal buoyancy forces with shear effect (i.e., when Re increases), stably-stratified region become wider along the lower part of the cavity and the vertical temperature gradients are increased. Heat conductivity is less when the heat source is mounted on the left side of the wall as compared to the right side. For a fixed Re, the solid volume fraction and Rayleigh number has a positive effect on heat transfer enhancement. Moreover, thermal conductivity increases with increasing Rayleigh number. The average Nusselt number is increasing with increase in Ra, Re and ϕ for both the cases, however, case-I shows higher heat transfer rate. Also, the effect of solid volume fraction is maximum in case-I as compared to case-II. In case-II, the solid volume fraction has a noticeable effect only for the larger Re and Ra values. The bulk average temperature is decreasing with increase in Re, and the bulk average temperature is higher in case-II as compared to case-I for all the considered parameters. The fluid mixing is found to be better in case-II as compared to case-I.

Tables and figures

Table 2.1: Thermophysical properties of water and copper.

Property	Water	Copper
C_p	4179	383
ρ	997.1	8954
k	0.6	400
β	2.1 $\times 10^{-4}$	1.67$\times 10^{-5}$

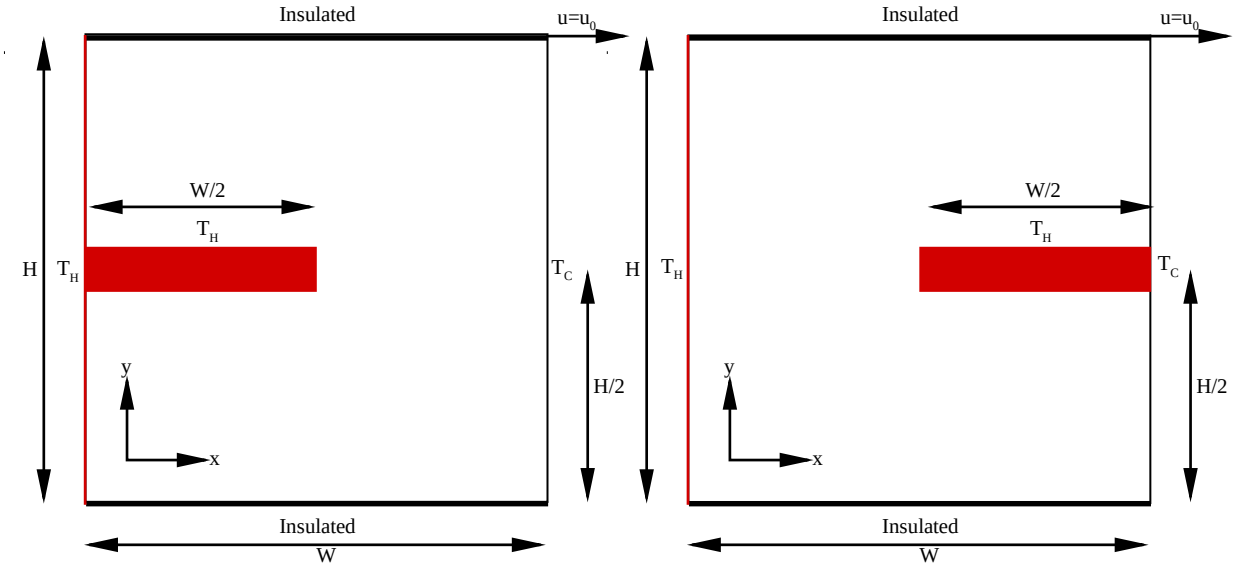

(a) case-I (b) case-II

Figure 2.1: A schematic diagram of the physical model.

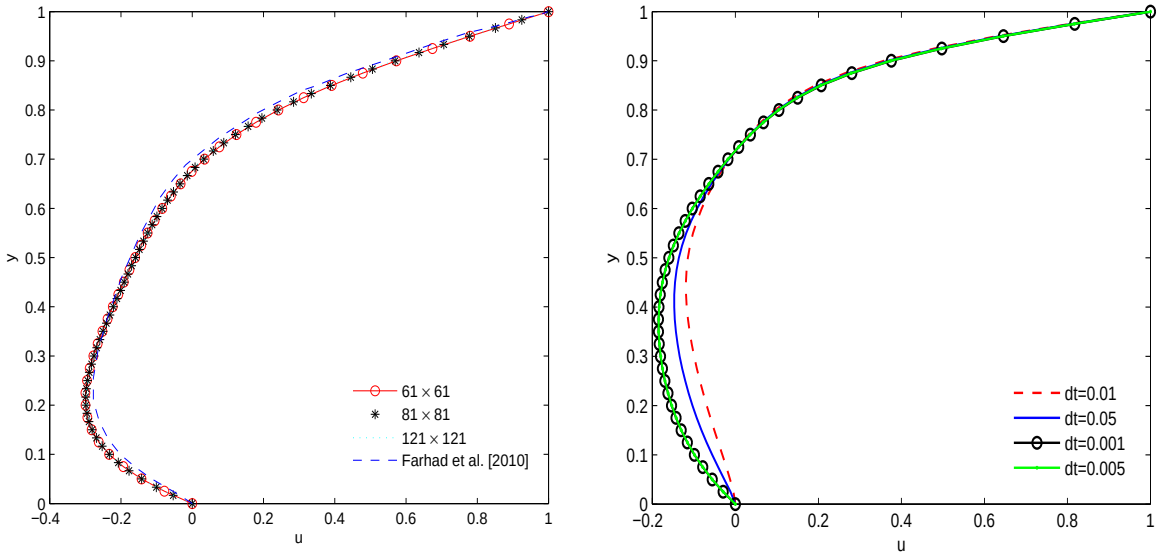

(a) (b)

Figure 2.2: Comparison of present results of (a) u-velocity with Farhad et al. [226], (b) time step independence test at $Re = 100$ and $Ra = 10^5$ for plain fluid.

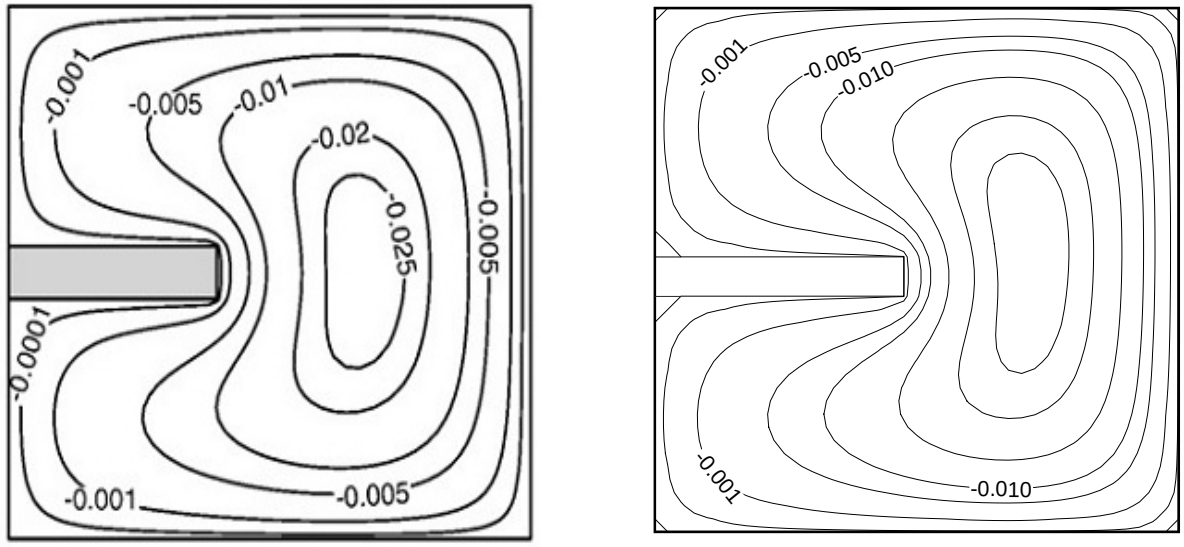

(a) (b)

Figure 2.3: Comparison of streamlines with Amir et al. [141]: (a) result due to Amir et al. [141], (b) present result where the flow parameters considered as $Ra = 10^3$, $Re = 10$ and $\phi = 0\%$.

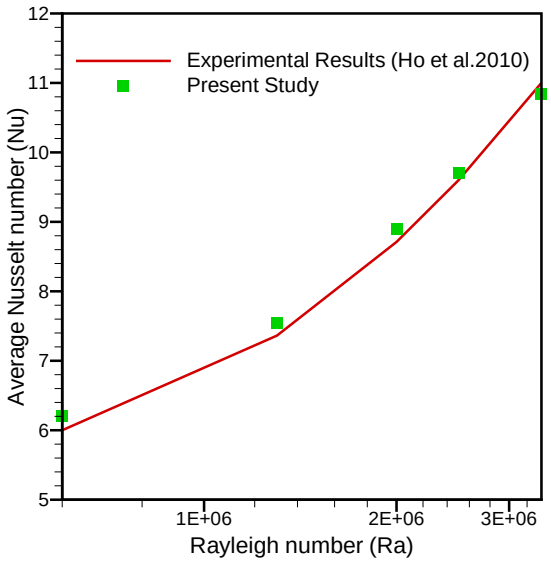

(a)

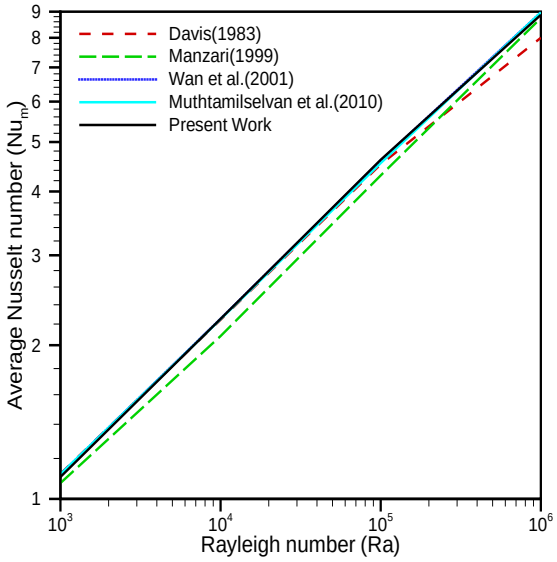

(b)

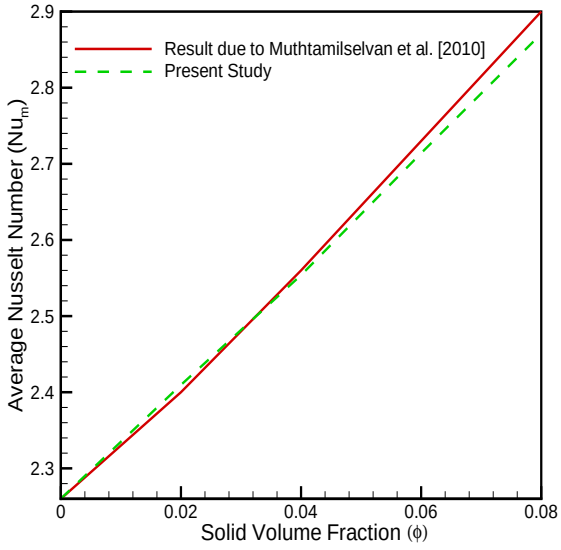

(c)

Figure 2.4: Average Nusselt number comparison with Rayleigh number(a, b) and solid volume fraction(c).

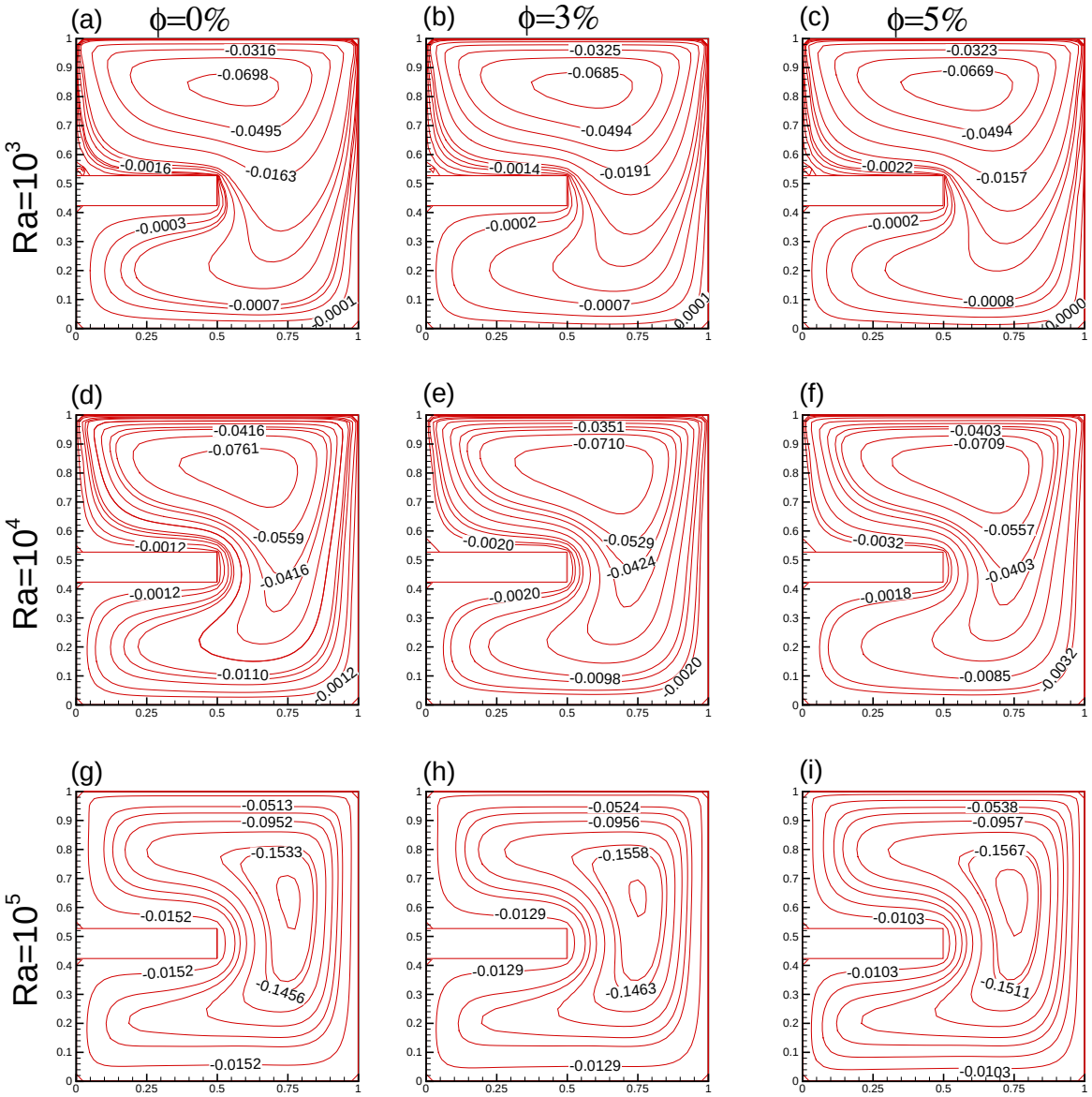

Figure 2.5: Solid volume fraction and Rayleigh number effects for $Re = 10$ on streamlines in case-I.

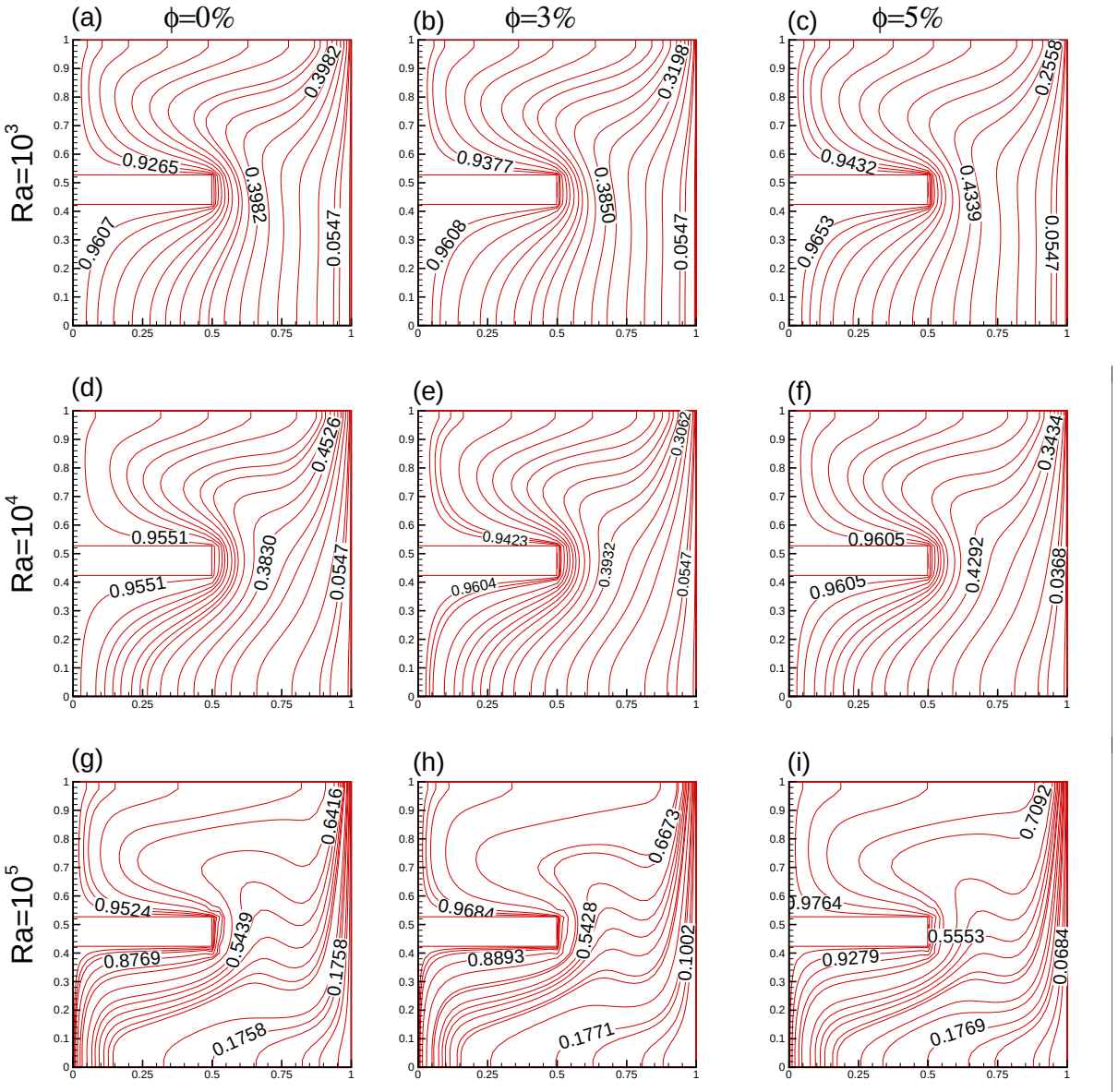

Figure 2.6: Solid volume fraction and Rayleigh number effects for $Re = 10$ on isotherms in case-I.

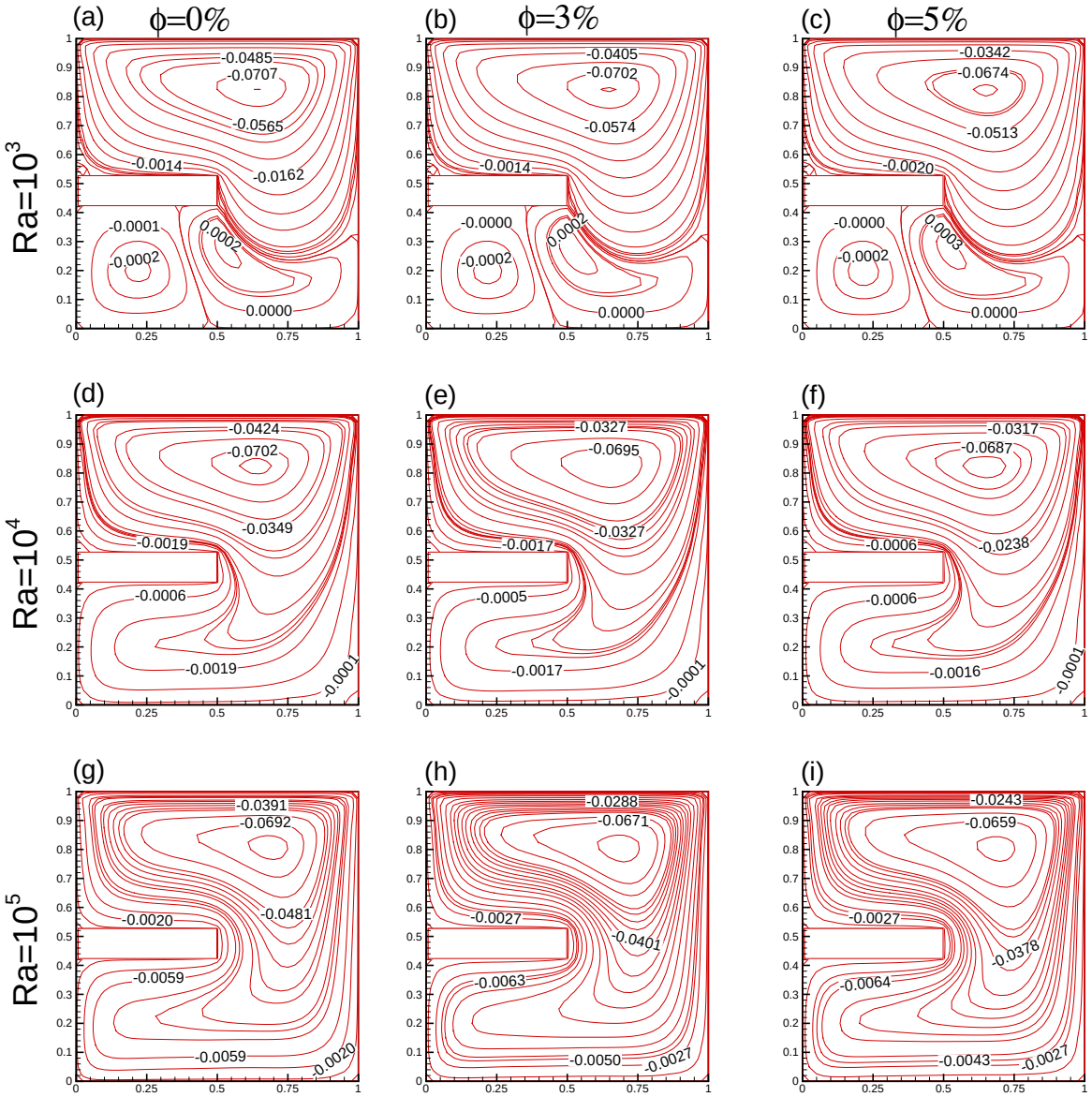

Figure 2.7: Solid volume fraction and Rayleigh number effects for $Re = 50$ on streamlines in case-I.

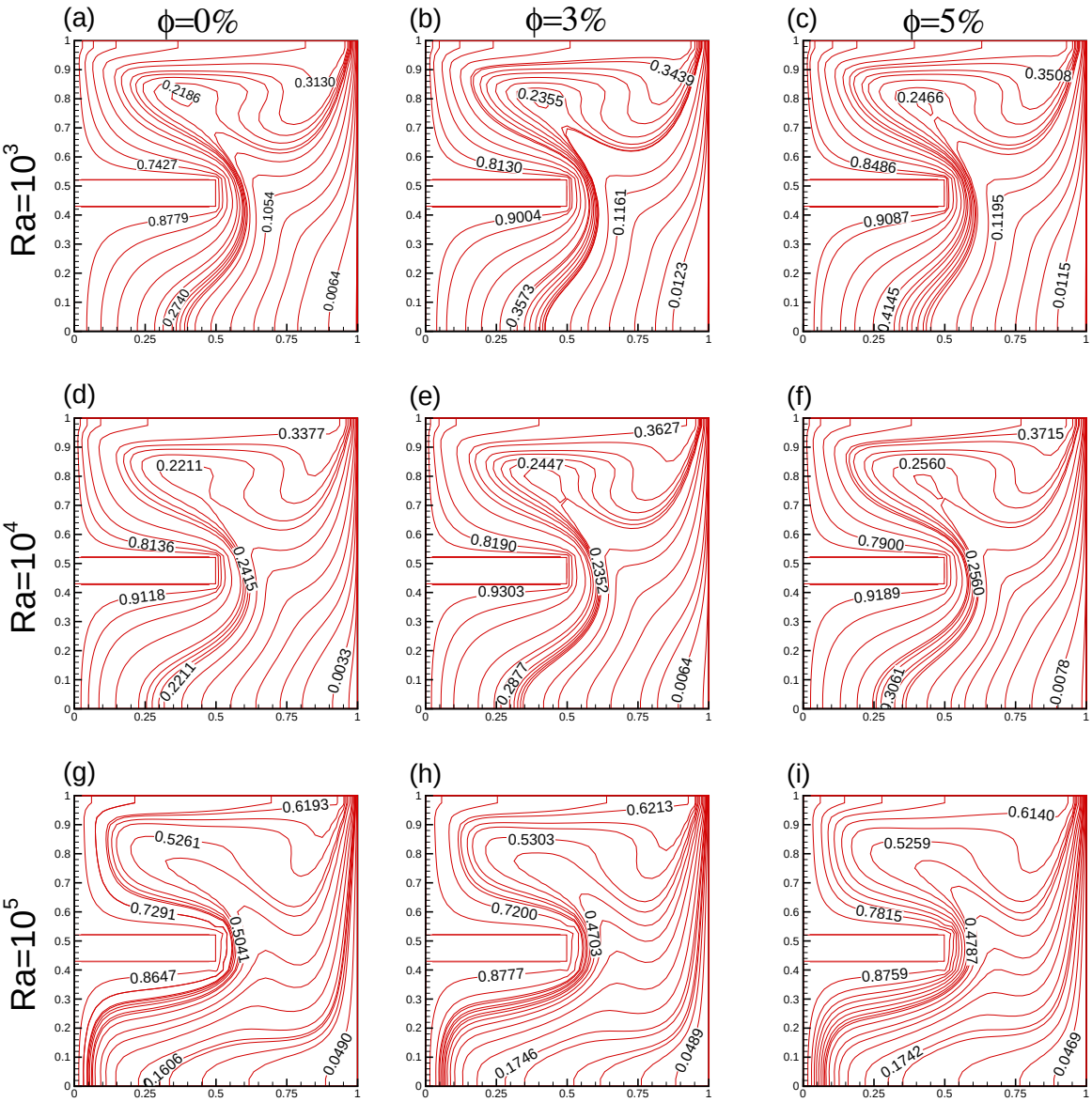

Figure 2.8: Solid volume fraction and Rayleigh number effects for $Re = 50$ on isotherms in case-I.

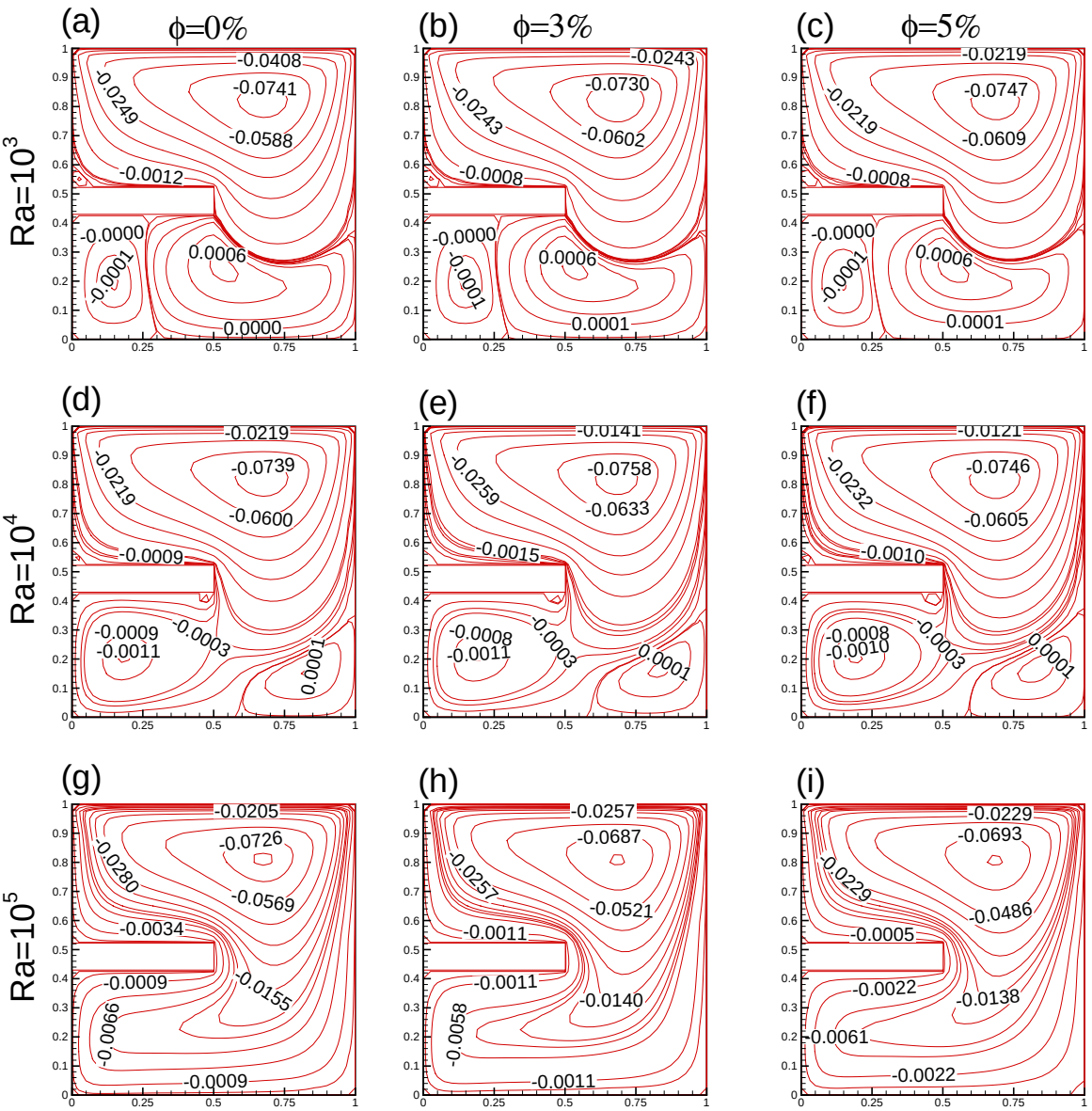

Figure 2.9: Solid volume fraction and Rayleigh number effects for $Re = 100$ on streamlines in case-I.

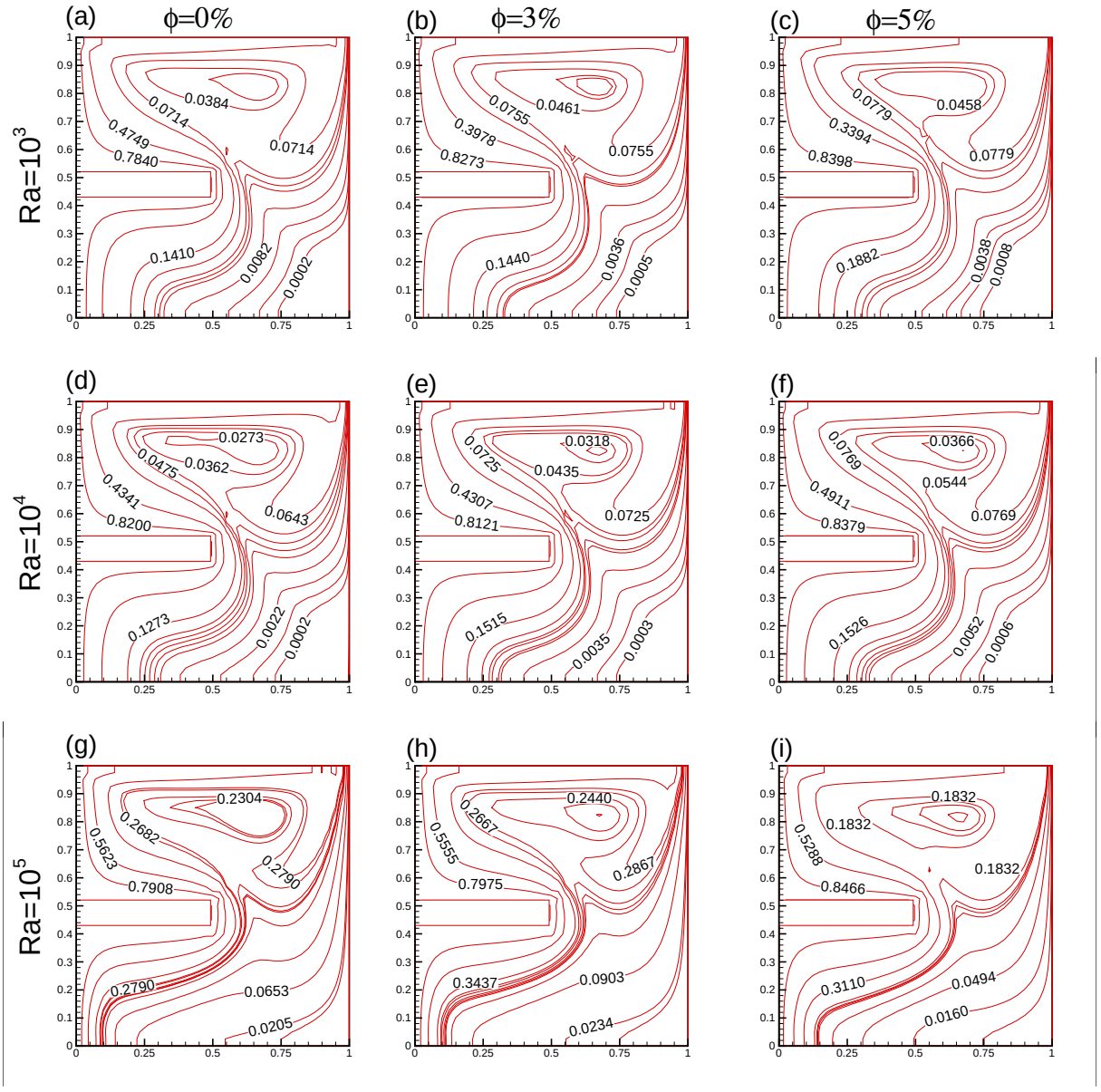

Figure 2.10: Solid volume fraction and Rayleigh number effects for $Re = 100$ on isotherms in case-I.

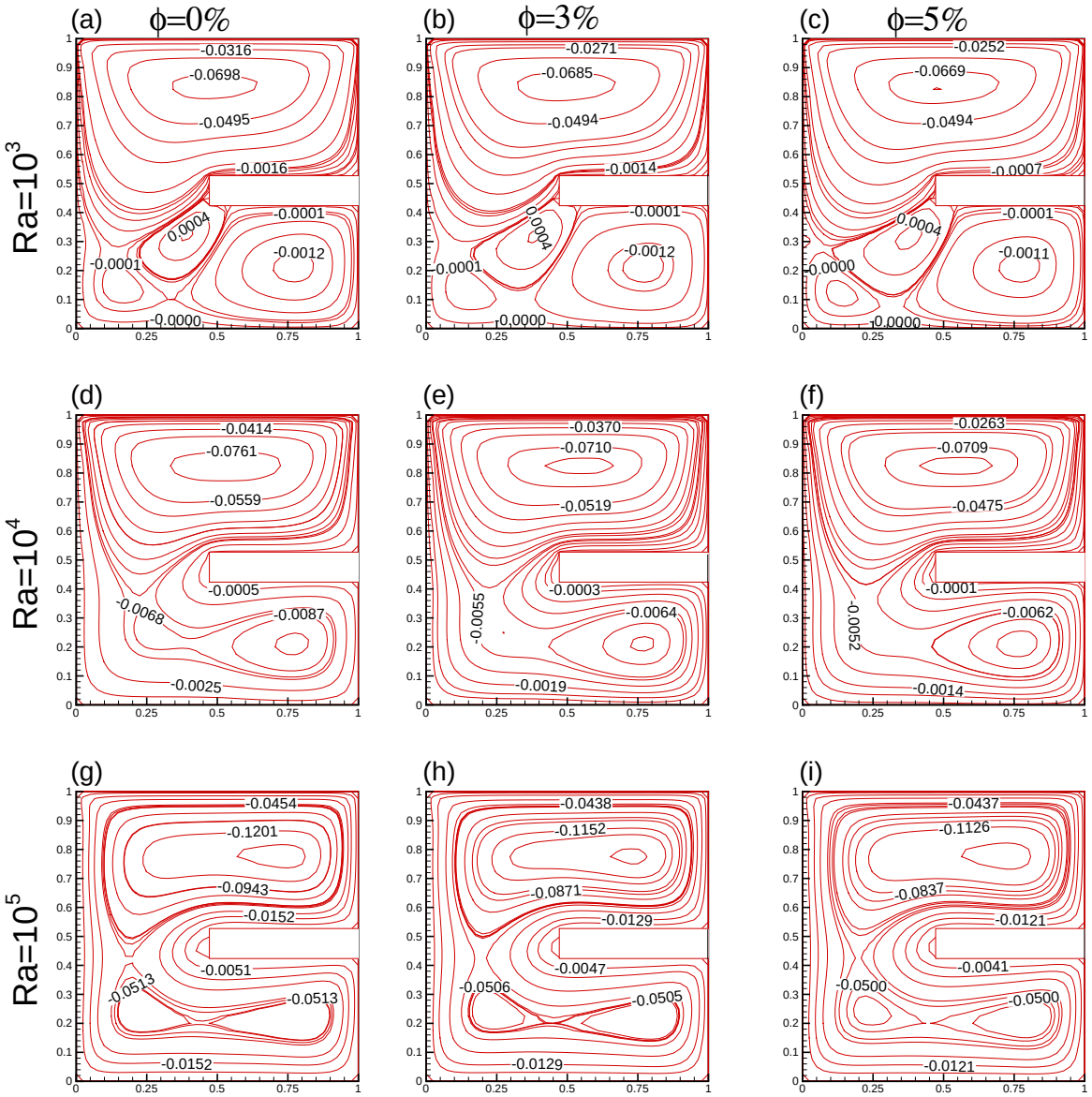

Figure 2.11: Solid volume fraction and Rayleigh number effects for Re=10 on streamlines in case-II.

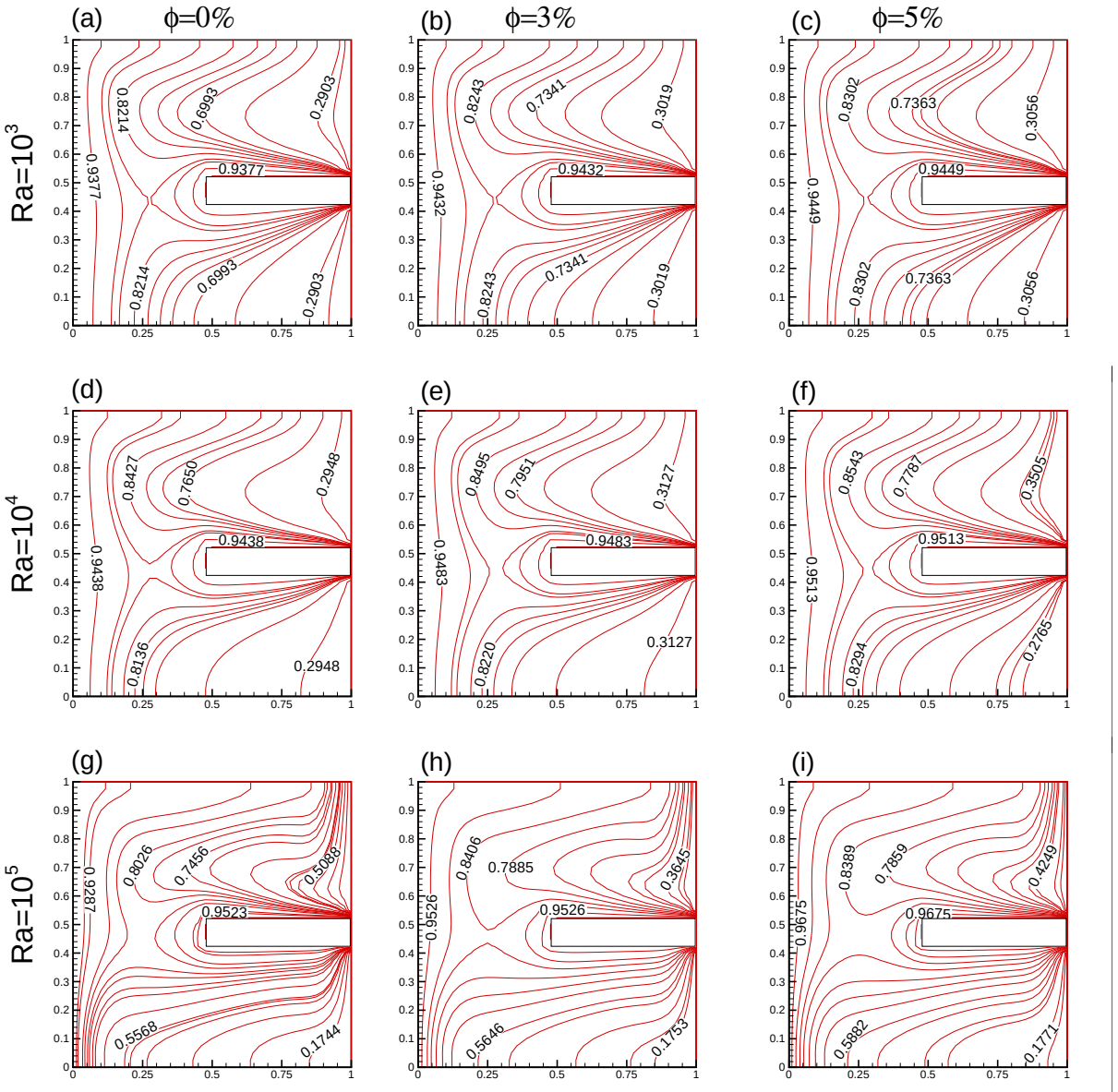

Figure 2.12: Solid volume fraction and Rayleigh number effects for Re=10 on isotherms in case-II.

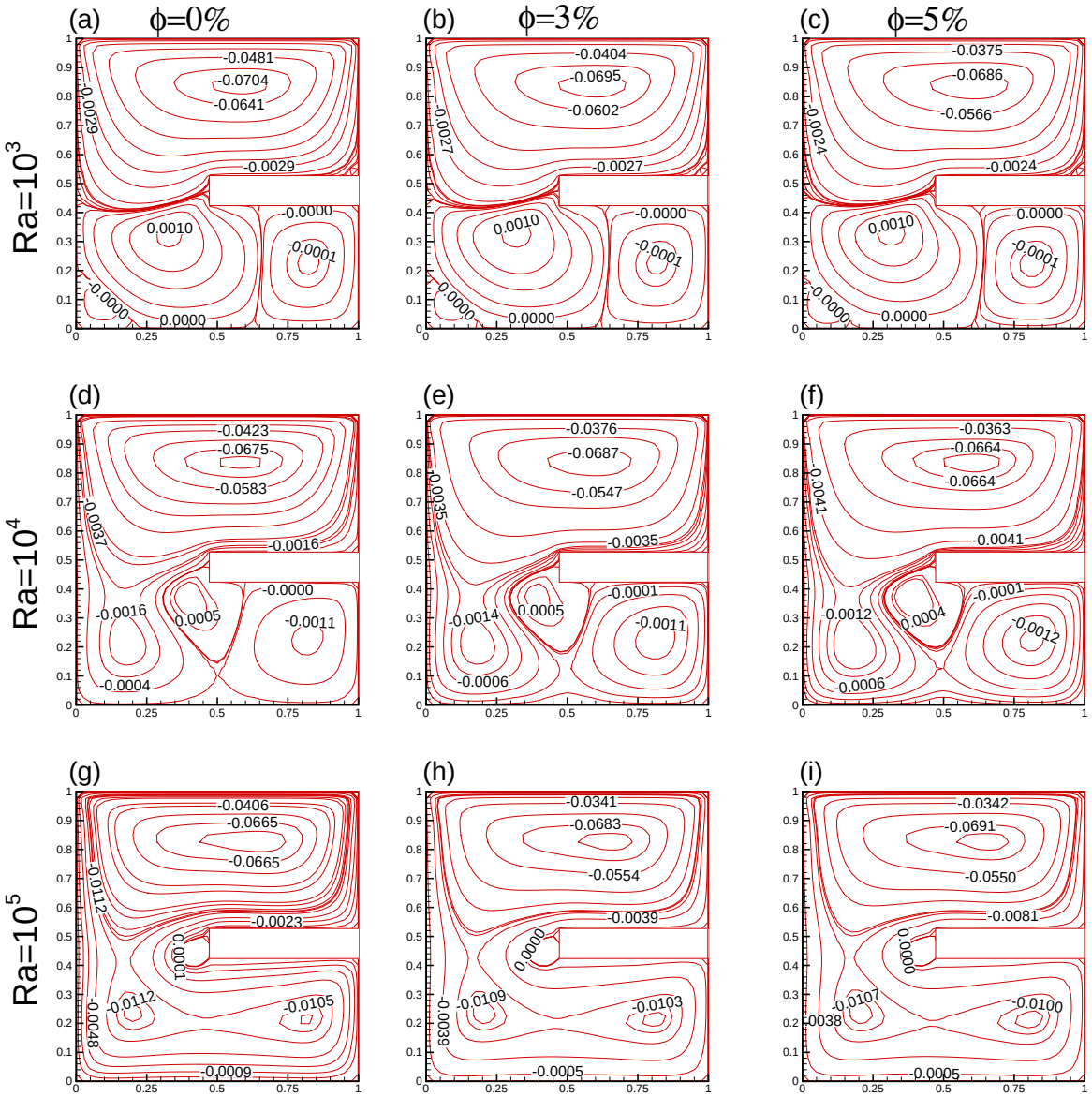

Figure 2.13: Solid volume fraction and Rayleigh number effects for $Re = 50$ on streamlines in case-II.

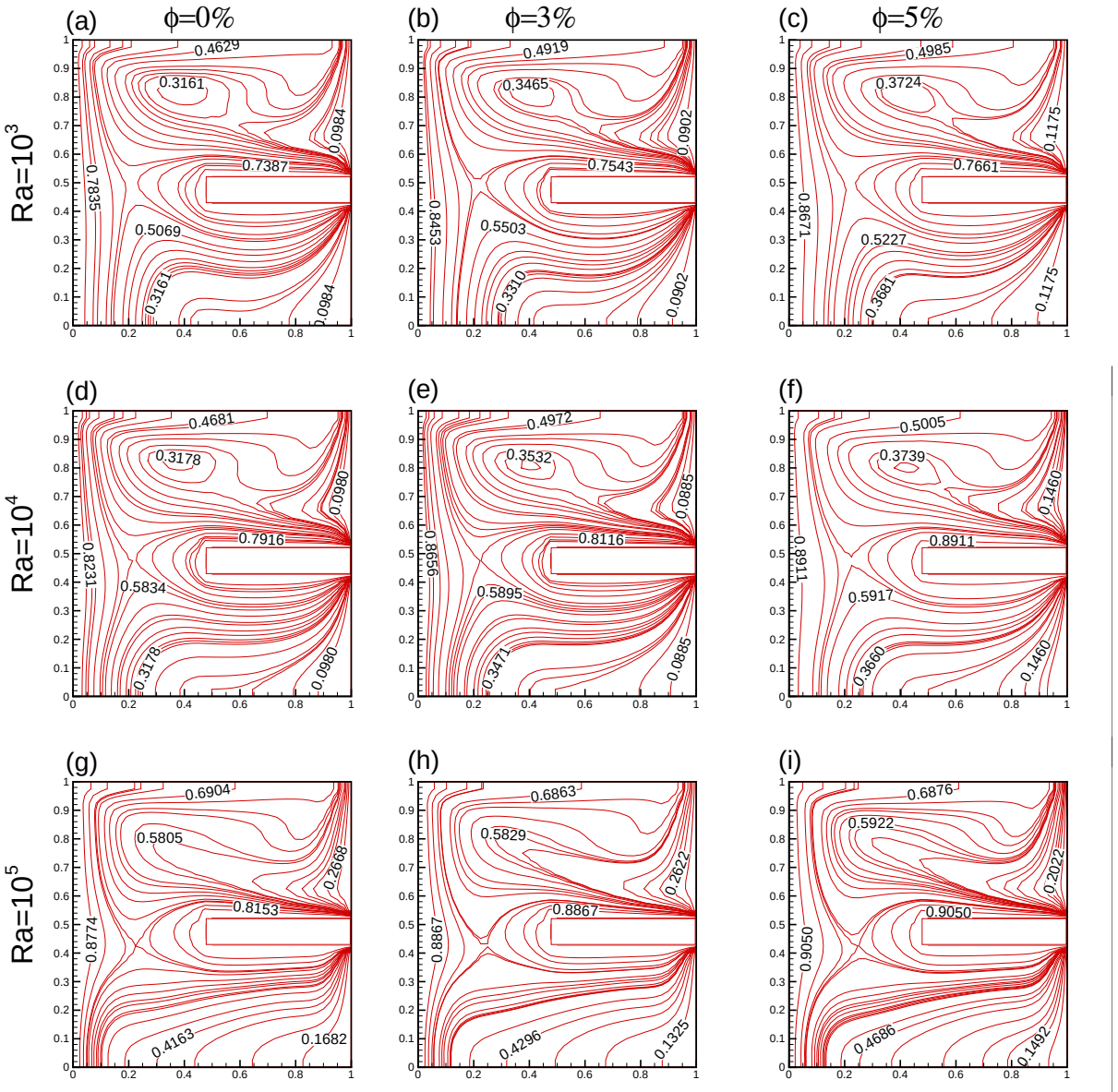

Figure 2.14: Solid volume fraction and Rayleigh number effects for $Re = 50$ on isotherms in case-II.

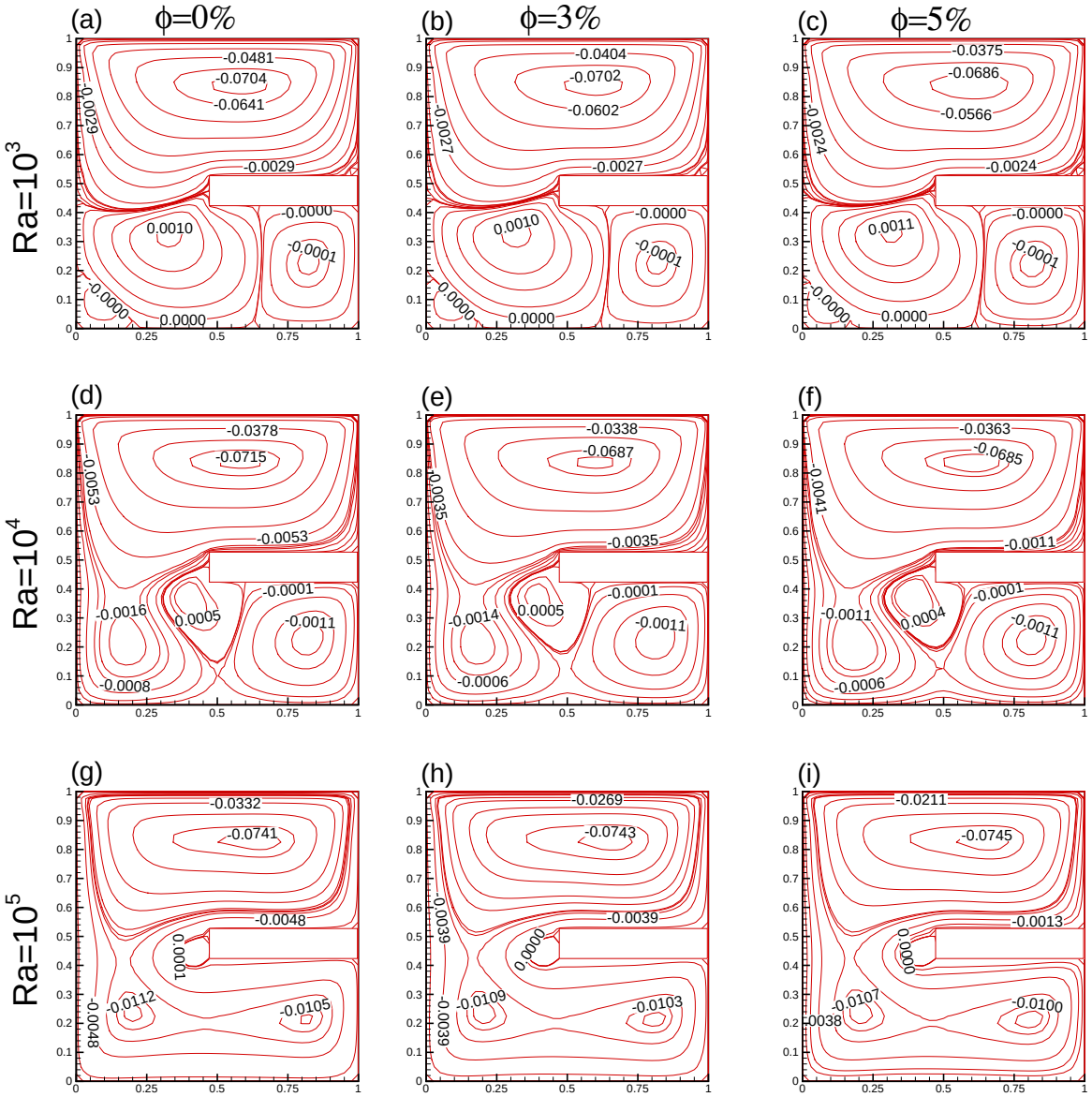

Figure 2.15: Solid volume fraction and Rayleigh number effects for $Re = 100$ on streamlines in case-II.

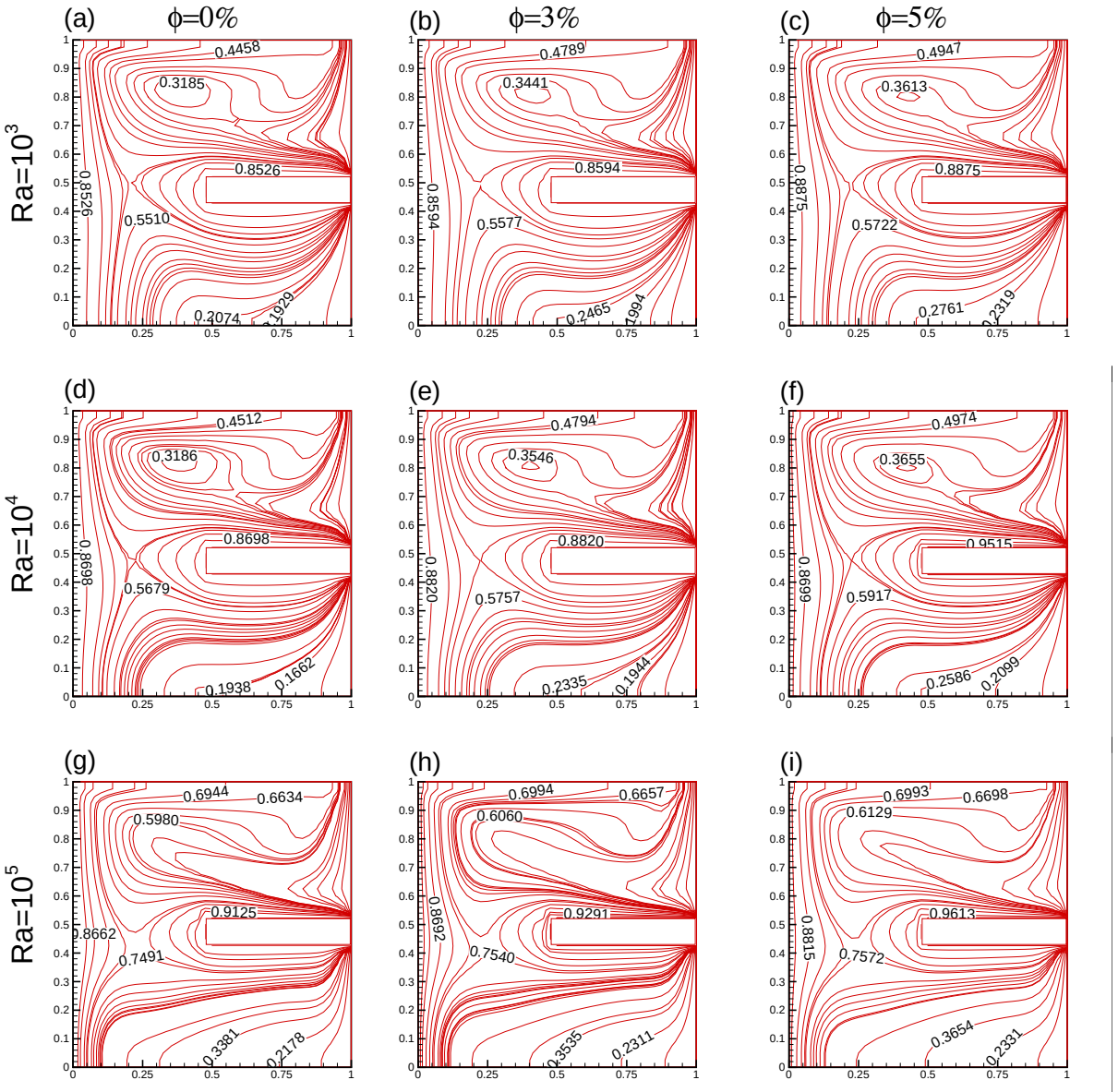

Figure 2.16: Solid volume fraction and Rayleigh number effects for $Re = 100$ on isotherms in case-II.

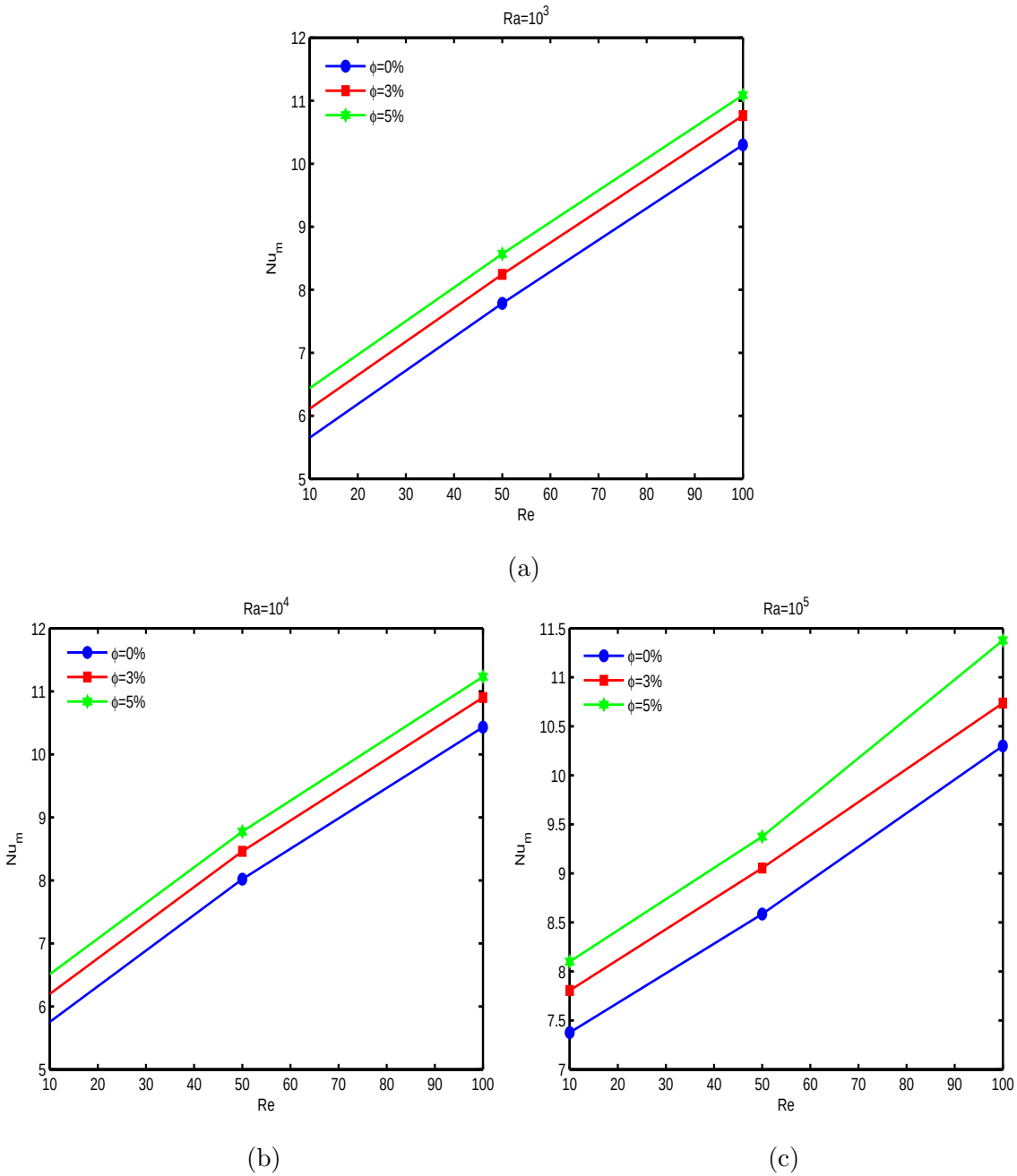

Figure 2.17: Average Nusselt number for various Re, Ra and ϕ for case-I.

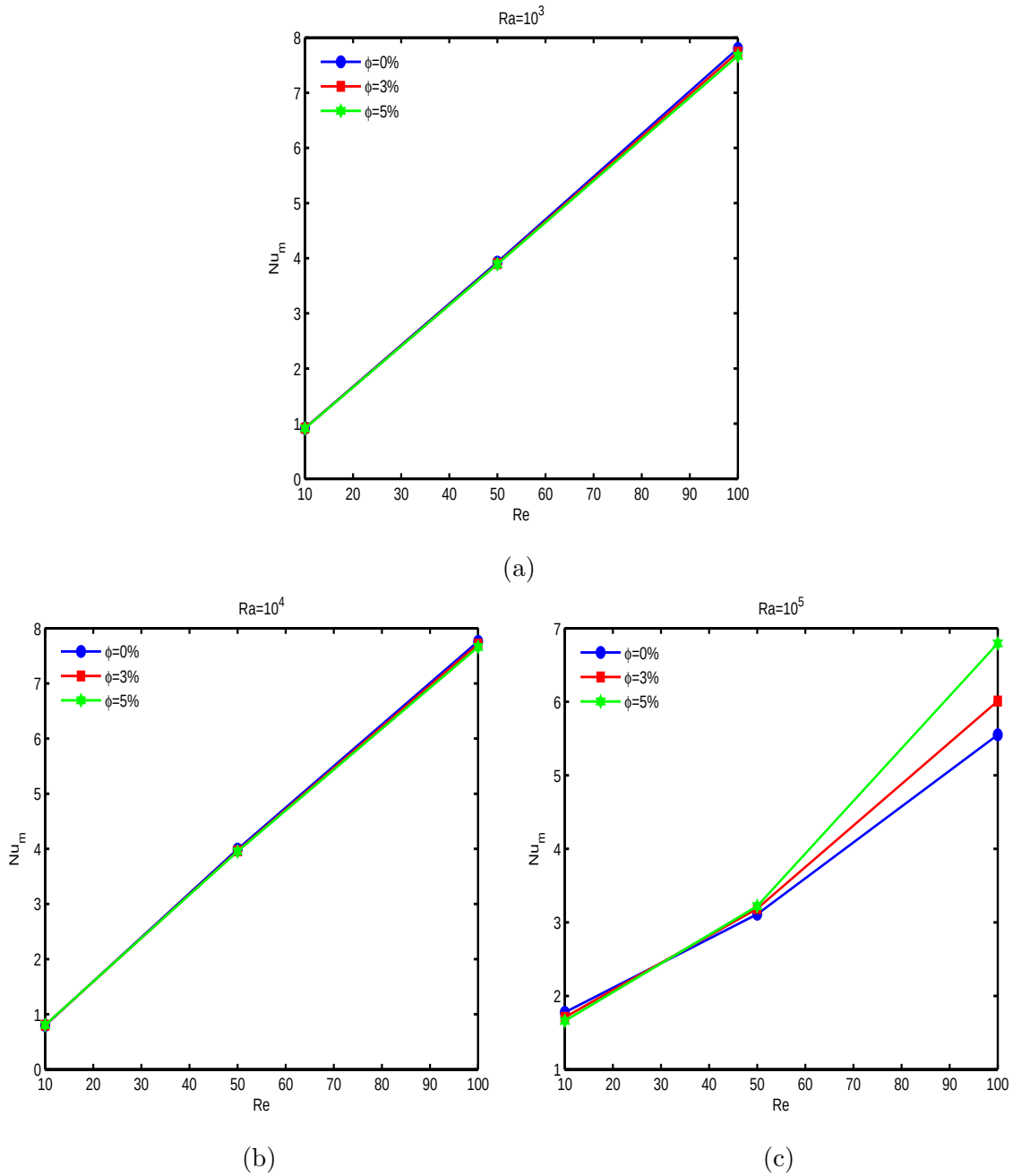

Figure 2.18: Average Nusselt number for various Re, Ra and ϕ for case-II.

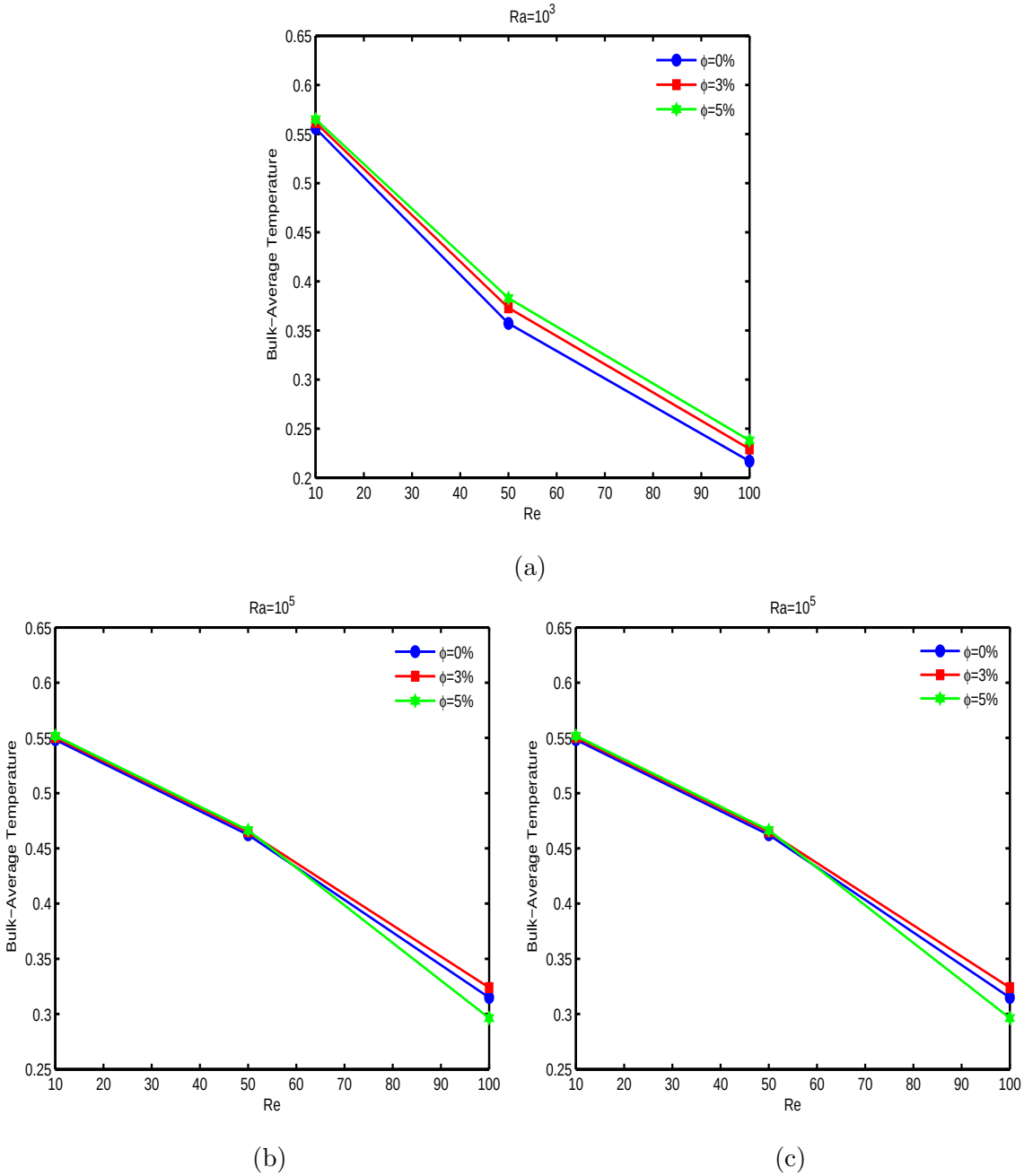

Figure 2.19: Bulk average temperature for various Re, Ra and ϕ for case-I.

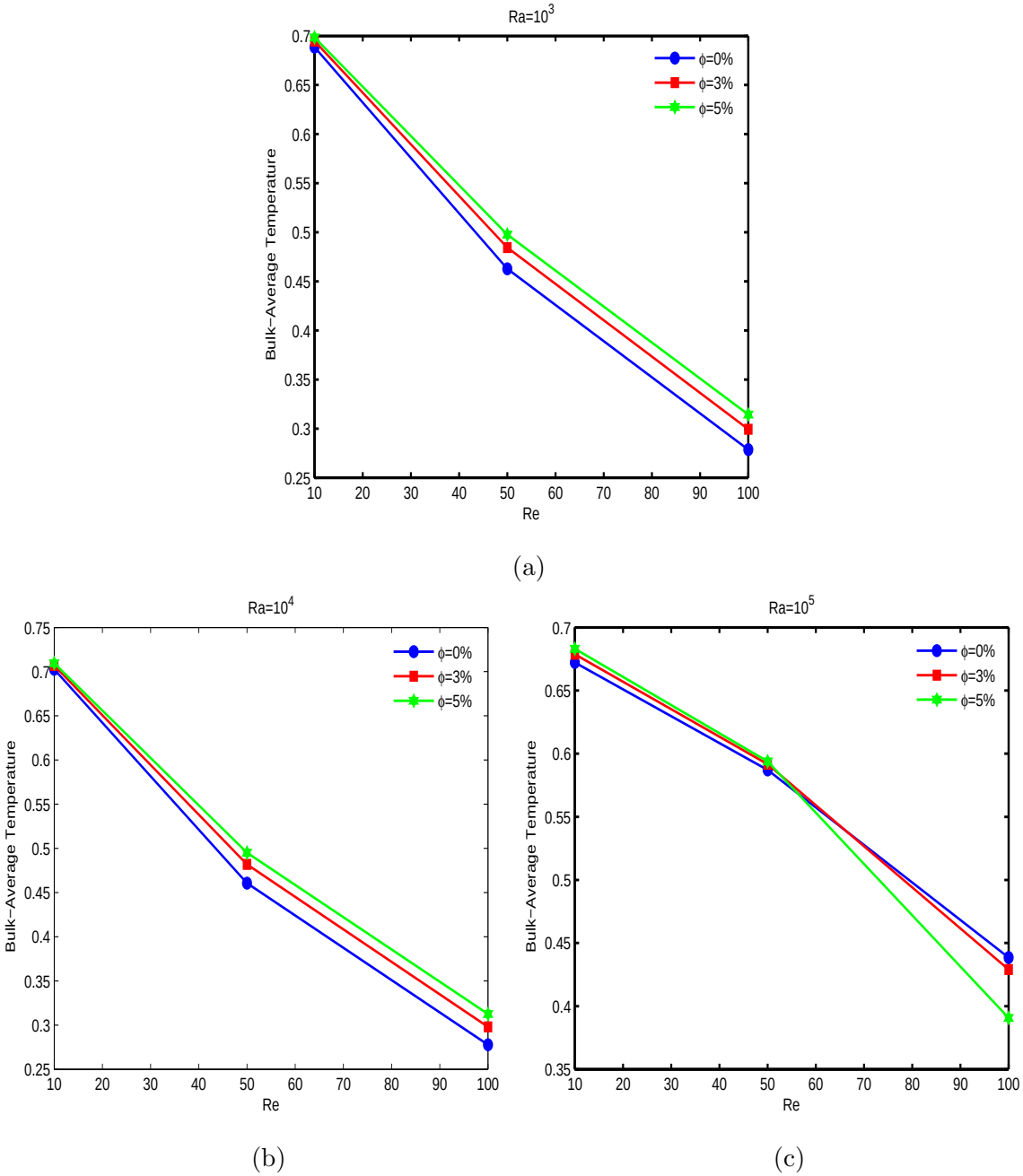

Figure 2.20: Bulk average temperature for various Re, Ra and ϕ for case-II.

Chapter 3

A Comparative Study of Mixed Convection and Its Effect on Partially Active Thermal Zones in a Two Sided Lid-driven Cavity Filled With Nanofluid [1]

3.1 Introduction

The study of mixed convection and heat transfer in enclosures is invariably encountered in many industrial heating as well as cooling applications; cooling of electronic devices, solar collectors, float glass production, drying technologies, chemical processing equipments, etc. and is of great interest for the researchers. This type of fluid flow and heat transfer represents complicated flow phenomena due to the movement of one or more walls which involves forced convection and the temperature difference causing secondary buoyancy driven flow. Fluid flow and heat transfer in square or rectangular cavities driven by shear and buoyancy effects have been studied extensively.

In the last several years, an extensive numerical, analytical and experimental study have been conducted on the problem of natural and mixed convection heat transfer in cavities filled with nanofluid. The natural convection problem in a differentially heated square cavity is first numerically studied by Khanafer et al. [122], with the consideration of dispersion effect and it is considered that a better model for nanofluids can be developed

[1] The contents of this chapter has been published in *Engineering Science and Technology, an International Journal, Elsevier, DOI:10.1016/j.jestch.2016.02.008*

by determining the dispersion coefficient. The effect of dispersion element in a nanofluid is discussed by Khaled and Vafai [116] where the volume fraction distribution is governed by the properties of dispersive elements combined with the flow parameters such as Reynolds number and Prandtl number for optimum heat transfer. In case of uniform flow the maximum Nusselt number distribution are found to be 21% higher than that of the dispersed distributed element flow.

Maiga et al. [143] numerically studied heat transfer effect of nanofluids in a uniformly heated tube for laminar and turbulent flow and tried to correlate the numerical results with the experimental data and observed that for increase of Reynolds number, the heat transfer effect is increasing due to the presence of nanoparticles and becomes more feasible in the case of turbulent flow. Tiwari and Das [230] numerically simulated the problem of mixed convection in a two sided lid-driven differentially heated square cavity filled with copper-water nanofluid. They observed that the average Nusselt number increased substantially with the increase of the volume fraction of the nanoparticles, for a fixed Richardson number.

The effect of nanoparticle concentration and viscosity are studied experimentally by Nguyen et al. [171] and Minsta et al. [155] for various temperature values. It is found that with the increment of concentration of the nanoparticles, the viscosity and temperature decreases sharply. Recently, Selimefendigil and Oztop [197] studied natural convection of nanofluid flow with different shaped obstacles including diamond, square and circular and discussed the effect of solid volume fraction and obstacle shapes on thermal flow patterns. In another study, Selimefendigil et al. [198] investigated the heat transfer and fluid flow in the presence of magnetic dipole in a partially heated cavity. They observed that the averaged heat transfer along the heat source is found to be minimum when magnetic dipole source is placed at the middle of the vertical wall.

Muthtamilselvan et al. [162] numerically investigated the mixed convection and heat transfer in a lid-driven enclosure filled with copper-water nanofluid, and observed that the heat transfer has a large effect on solid volume fraction and aspect ratio of the enclosure. Abu-Nada et al. [1] studied the heat transfer effect in a differentially heated enclosure using variable properties of CuO-water and Al_2O_3-water nanofluids due to natural convection. They found that for higher Rayleigh numbers variation of average

heat transfer is less sensitive in case of a thermal conductivity model than that of the viscosity model. Abbasian et al. [16] numerically studied the mixed convection effect of a $Cu-$water nanofluid in a lid-driven cavity, where the horizontal walls are kept insulated and vertical walls are heated sinusoidally. They observed that decrease in Richardson number and increase in volume fraction of nanoparticles results in increase in heat transfer. Also, it is found that for a constant Reynolds number, the rate of heat transfer increases with the increase of Richardson number.

Talebi et al. [226] numerically studied the problem of mixed convection flow of copper-water nanofluid in a lid-driven cavity with differentially heated vertical walls and shown the increment of average Nusselt number with solid volume fraction over constant Reynolds and Rayleigh numbers. Mahmoudi et al. [142] studied the problem of mixed convection in a vented square cavity filled with Cuwater nanofluid. It is observed that for higher Reynolds and Richardson number, the heat transfer performance due to the presence of nanoparticles is increasing.

A finite volume approach is used by Sebdani et al. [196] to investigate the fluid flow and heat transfer effect in a square cavity filled with Al_2O_3-water nanofluid with a bottom wall heated source. Both the vertical walls of the cavity are maintained at cold temperature and moving downwards with constant velocity whereas the horizontal walls are taken to be adiabatic and fixed. On addition of nanoparticles it is observed that heat transfer effect is enhanced with increase of Reynolds number, for a fixed Rayleigh number. Moumni et al. [159] studied the heat transfer characteristics of various water-based nanofluids in a two-sided square lid-driven cavity, using a pair of discrete heat sources with different locations along the bottom wall of the cavity. The heat transfer rate increases with increase in Reynolds number, Richardson number and solid volume fraction, and rate of heat transfer increment is found to be higher in case of Cu-water and Ag-water nanofluids as compared to Al_2O_3-water and TiO_2-water nanofluids.

Based on the above studies it is found that there is a lack of studies for the complete heat transfer effects based on mixed convection for differentially heated horizontal walls with moving vertical walls. It is also observed [176] that the heat transfer effects are mostly influenced by the movement of walls. The heat transfer rate is less when both vertical walls are moving upwards in comparison to the movement of vertical walls, in

the opposite direction. The present chapter deals with the comparative study of mixed convection flow of Cu-water nanofluid in a two-sided lid-driven cavity in which both the horizontal walls are kept fixed and the vertical walls are moving. Three different cases of study have been made on the basis of direction of moving walls with fixed location of two discrete heat sources on the bottom walls, keeping the other walls at comparatively lower temperature.

3.2 Problem formulation

Consider a nanofluid filled square enclosure equipped with partially heated bottom wall and moving side walls. Two equal portions of length L/4 of lower wall are maintained at higher temperature (T_h) and rest part of bottom wall is kept insulated. All other walls are maintained at relatively lower temperature (T_c). We have considered three different cases: In case-I, left vertical wall is moving downwards and the right one is moving upwards. In case-II, both the vertical walls are moving downwards and in case-III both the walls are moving upwards. The two-dimensional computational domain is presented in Fig. 3.1.

The nanofluid flow is assumed to be steady, laminar, and the fluid is assumed to be Newtonian, incompressible and is in thermal equilibrium with no slip condition between two phases. Except density, the thermophysical properties of the nanofluid are assumed to be constant. The density variation is based on Boussinesq approximation. Further, the shape and size of the nanoparticles are assumed to be uniform. The thermophysical properties of water and copper at the reference temperature are presented in Table 3.1.

The governing equations for an unsteady, two-dimensional laminar and incompressible flow are expressed as:

$$\frac{\partial u^*}{\partial x^*} + \frac{\partial v^*}{\partial y^*} = 0,$$

$$\frac{\partial u^*}{\partial t^*} + \frac{\partial (u^* u^*)}{\partial x^*} + \frac{\partial (u^* v^*)}{\partial y^*} = -\frac{1}{\rho_{nf}} \frac{\partial p^*}{\partial x^*} + \frac{\mu_{nf}}{\rho_{nf}} \Big(\frac{\partial^2 u^*}{\partial x^{*^2}} + \frac{\partial^2 u^*}{\partial y^{*^2}} \Big),$$

$$\frac{\partial v^*}{\partial t^*} + \frac{\partial (u^* v^*)}{\partial x^*} + \frac{\partial (v^* v^*)}{\partial y^*} = -\frac{1}{\rho_{nf}} \frac{\partial p^*}{\partial y^*} + \frac{\mu_{nf}}{\rho_{nf}} \Big(\frac{\partial^2 v^*}{\partial x^{*^2}} + \frac{\partial^2 v^*}{\partial y^{*^2}} \Big) + \frac{(\rho\beta)_{nf}}{\rho_{nf}} g(T^* - T_c),$$

$$\frac{\partial T^*}{\partial t^*} + \frac{\partial (u^* T^*)}{\partial x^*} + \frac{\partial (v^* T^*)}{\partial y^*} = \alpha_{nf}\Big(\frac{\partial^2 T^*}{\partial {x^*}^2} + \frac{\partial^2 T^*}{\partial {y^*}^2}\Big)$$

where, the thermal diffusivity α_{nf}, the effective density of nanofluid at reference temperature ρ_{nf} and the heat capacitance of nanofluid $(\rho C_p)_{nf}$ are given by [16],

$$\alpha_{nf} = k_{nf}/(\rho C_p)_{nf},$$

$$\rho_{nf} = (1-\phi)\rho_f + \phi\rho_s,$$

$$(\rho C_p)_{nf} = (1-\phi)(\rho C_p)_f + \phi(\rho C_p)_s,$$

$$(\rho\beta)_{nf} = (1-\phi)(\rho\beta)_f + \phi(\rho\beta)_s$$

where, ρ_f, ρ_s and ϕ are the density of base fluid, density of nanoparticle and volume fraction of the nanoparticles, respectively. The effective thermal conductivity of the nanofluid is approximated by the Maxwell self-consistent approximation model. For the two-component entity of spherical-particle suspension, the Maxwell model [153] given by,

$$\frac{k_{nf}}{k_f} = \frac{k_s + 2k_f - 2\phi(k_f - k_s)}{k_s + 2k_f + \phi(k_f - k_s)}.$$

The effective viscosity of nanofluid is given by Brinkmann [39] as,

$$\mu_{nf} = \frac{\mu_f}{(1-\phi)^{2.5}}.$$

The given formulation of the effective thermal conductivity and effective viscosity is found to be appropriate by various authors [16, 159, 162, 163, 230]. The above mentioned equations can be expressed in non-dimensional form by incorporating the following dimensionless variables,

$$x = \frac{x^*}{L};\ y = \frac{y^*}{L};\ u = \frac{u^*}{U_0};\ v = \frac{v^*}{U_0};\ T = \frac{T^* - T_c}{T_h - T_c};\ t = \frac{t^* U_0}{L};$$

$$p = \frac{p^*}{\rho_{nf} U_0^2};\ Re = \frac{U_0 L}{\nu_f};\ Pr = \frac{\nu_f}{\alpha_f};\ Ri = \frac{g\beta L(T_h - T_c)}{U_0^2}.$$

The governing equations in dimensionless form can be rewritten as,

$$\frac{\partial u}{\partial x} + \frac{\partial v}{\partial y} = 0,$$

$$\frac{\partial u}{\partial t}+\frac{\partial (uu)}{\partial x}+\frac{\partial (uv)}{\partial y}=-\frac{\partial p}{\partial x}+\frac{1}{Re}\frac{\rho_f}{\rho_{nf}}\frac{1}{(1-\phi)^{2.5}}\left(\frac{\partial^2 u}{\partial x^2}+\frac{\partial^2 u}{\partial y^2}\right),$$

$$\begin{aligned}\frac{\partial v}{\partial t}+\frac{\partial (uv)}{\partial x}+\frac{\partial (vv)}{\partial y}=&-\frac{\partial p}{\partial y}+\frac{1}{Re}\frac{\rho_f}{\rho_{nf}}\frac{1}{(1-\phi)^{2.5}}\left(\frac{\partial^2 v}{\partial x^2}+\frac{\partial^2 v}{\partial y^2}\right)\\&+Ri\frac{\rho_f}{\rho_{nf}}\left(1-\phi+\phi\frac{\rho_s\beta_s}{\rho_f\beta_f}\right)T,\end{aligned}$$

$$\frac{\partial T}{\partial t}+\frac{\partial uT}{\partial x}+\frac{\partial vT}{\partial y}=\frac{1}{RePr}\frac{k_{nf}}{k_f}\frac{(\rho C_p)_f}{(\rho C_p)_{nf}}\left(\frac{\partial^2 T}{\partial x^2}+\frac{\partial^2 T}{\partial y^2}\right).$$

The relevant boundary conditions are given by,

$$u=0,\ v=v_l,\ T=0 \quad \text{if} \quad x=0, \qquad y\in[0,1];$$

$$u=0,\ v=v_r,\ T=0 \quad \text{if} \quad x=1, \qquad y\in[0,1];$$

$$u=v=0,\ \begin{cases} T=1 & \text{if } x\in(1/8,3/8]\cup(5/8,7/8] \\ \frac{\partial T}{\partial y}=0 & \text{elsewhere}\end{cases},\ y=0$$

$$u=0,\ v=0,\ T=0 \qquad \text{if} \qquad x\in[0,1],\ y=1.$$

Three different cases are discussed according to the boundary conditions on the left and right wall, given as,

$$\text{Case-I: } v_l=-1,\ v_r=1,$$
$$\text{Case-II: } v_l=1,\ v_r=1,$$
$$\text{Case-III: } v_l=-1,\ v_r=-1.$$

In order to calculate the heat transfer enhancement, we have calculated Nu (Nusselt number) and Nu_m (average Nusselt number) along the heated surfaces as,

$$Nu(x)=-\frac{k_{nf}}{k_f}\left(\frac{\partial T}{\partial x}\right)_{hot\ wall},$$

$$Nu_{m_{s_i}}=\frac{\int_{hot\ wall}Nu(x)dx}{\int_{hot\ wall}dx}. \tag{3.1}$$

The overall surface average Nusselt number is the average of $Nu_{m_{s_1}}$ and $Nu_{m_{s_2}}$, where $Nu_{m_{s_1}}$ and $Nu_{m_{s_2}}$ represents the average Nusselt number along the two heated surfaces.

3.3 Numerical procedure

A finite volume approach [178] is used to solve the set of governing equations using the staggered grid algorithm with uniform grid arrangement. Semi-implicit method for pressure linked equations (SIMPLE) is used to couple the continuity equation with Navier-Stokes equations in their discretized form [145]. To solve the discretized system of momentum and energy equations, we have used the tridiagonal matrix algorithm (TDMA). When the flows are dominated by convection effects then the numerical instability occur for higher Reynolds number. In order to linearize the nonlinear system of partial differential equations, a quasi-linearization approximation has been employed.

At every time step, we approximate the nonlinear term as

$$\left(u\frac{\partial u}{\partial x}\right)^{n+1} = u^n\left(\frac{\partial u}{\partial x}\right)^{n+1},$$

with $n \geq 0$, is the iteration index. The discretization of non-linear flow governing equations is made in the similar fashion as discussed in section 2.3 (eq. 2.16 to 2.19). The second order Poisson equation is discretized through an upwind spatial difference scheme. The resulting algebraic equations are solved through Successive Over Relaxation (SOR) method. SOR method is used to combat the non-linear nature of governing equations. The convergence criterion used for the calculation of velocities, temperature and pressure correction is defined by the expression,

$$\epsilon = \left|\varepsilon_{i,j}^{n+1} - \varepsilon_{i,j}^{n}\right| \leq 10^{-5}$$

where, ϵ is the error of tolerance in any time level and ε represents the physical flow variables.

3.4 Grid independency test and code validation

A grid independency test is performed with the variation of grid sizes between 61×61 to 121×121. A comparison of various profiles is made with Muthtamilselvan et al. [162] with the variation of grid sizes and is presented in Fig. 3.2(a). A lid driven cavity filled with nanofluid is considered in which the upper lid is maintained at higher temperature, the lower lid with low temperature and all other walls are kept adiabatic. The results

for vertical v-velocity are compared for $Ri = 1,\ Ra = 100$ and $\phi = 2\%$ and for grid size 81×81, our results are found to be optimum and are in good agreement with the results due to Muthtamilselvan et al. [162].

Another grid independency test is performed for grid sizes varying from 61×61 to 121×121. The comparison of average Nusselt number for grid size effect is made with Moumni et al. [159] with $Pr = 6.2,\ \phi = 2\%,\ Re = 100$ and $1 \leq Ri \leq 10$ and is presented in Fig. 3.2(b). Our results for grid size 81×81 are found to be optimum and in good agreement with results due to Moumni et al. [159]. Hence, the grid size 81×81 is chosen for all the computations throughout this chapter. A comparison of average Nusselt number for different solid volume fraction is made with Moumni et al. [159]. A mixed convection flow with Cu-water nanofluid is considered in a two-sided lid-driven square cavity . Fig. 3.2(c) shows the variation of average Nusselt number with different solid volume fractions for $Ri = 10,\ Re = 100$ and $\phi = 0.2$. The maximum percentage difference of average Nusselt number from the result due to Moumni et al. [159] is 0.7%.

3.5 Results and discussion

Mixed convection flow and heat transfer of Cu-water nanofluid with discrete heating is numerically examined in a two-sided lid-driven enclosure, in which two discrete heat sources of length L/4 are placed along the bottom wall at a distance of L/8 and 7L/8 from the left wall respectively. The flow governing parameters are Richardson number, Rayleigh number and solid volume fraction ratio and varies in the range of $0.1 \leq Ri \leq 10,\ 1 \leq Re \leq 100,\ 0 \leq \phi \leq 0.2$. Three different configurations are chosen based on the direction of moving lids. In the figures of streamlines, dashed lines show the clockwise direction (i.e. negative stream function values) of fluid flow whereas the solid lines show the anticlockwise direction (i.e. positive stream function values) of fluid flow.

Case-I: In first case, we have considered that left lid is moving downwards and right lid is moving upwards. For the validation of our result, we have compared the results obtained by Oztop and Dagtekin [159] for a clear fluid case and it is found that our result has a very good agreement with them. Fig. 3.3 and 3.4 represents the streamlines (left) and isotherms (right) for $Ri = 0.1$, 10 respectively with the variation of $Re;\ 1 \leq Re \leq 100$

and $\phi = 0.0$ and 0.2. It is found that heat source along the lower boundary produces a symmetric profile along the vertical mid-line for low Reynolds number ($Re = 1$, Fig. 3.3(a), 3.4(a)) and it is dominated by natural convection. A conductive regime is formed with two inner cells at the center of the cavity. But increment in Reynolds number develops a forced convection effect which forces the fluid to move upwards from the right and downwards from the left side (Fig. 3.3(c, e), 3.4(c, e)). The effect can be easily seen at the core of cavity where the eddy is no more horizontal as observed for $Re = 1$.

As the Reynolds number increases, the flow develops a convective cell and the tiny inner cells vanishes. As Richardson number increases with $\phi = 0.2$, the eddy size increases due to buoyancy effect, represented in Fig. 3.4(a). From Fig. 3.3(b) and 3.4(b), it is observed that small clockwise rotating hot cells appear close to the bottom heating location and isotherms are parallel to the heat sources. The uniform distribution of isotherms indicates the conduction mode of heat transfer and represents a hyperbolic pattern. As Reynolds number increases, the clockwise rotating cells grow in size, move away from the boundary layer and forced convection dominates the heat transfer effect. Due to the movement of lids the cold fluid move towards the right wall and hot fluid is confined to the boundary layer entrained to the whole cavity.

From Fig. 3.3(c, e) and 3.4(c, e), it can be observed that the vortex length getting stronger as Reynolds number increases. From Fig. 3.3(c) it is observed that $|\psi_{centre}|$=0.118 at x=0.5 and y=0.45 and from Fig. 3.4(c) $|\psi_{centre}|$=0.150 at x=0.5 and y=0.45. From Fig. 3.3(c, e) and 3.4(c, e) it is also observed that for higher Reynolds number the stream function values increases. On increasing Ri values from 0.1 to 10 the flow lines are increased upto 25% and 21.02% respectively for $Re = 50$ and $Re = 100$. The flow is completely dominated by forced convection rather than natural convection.

The heat transfer lines changes their pattern at higher Reynolds number due to convection effect. The cold fluid adjacent to right vertical wall moves toward the top wall and return to the core section of the cavity due to the frictional effect of the left moving wall. As Reynolds number increases from 50 to 100, cold fluid remains centered at the middle position of the cavity and the heat transfer lines are almost circular in the middle of cavity as observed from Fig. 3.3(f) compared to Fig. 3.3(d), in which the isothermal lines are parallel to the top wall. The heat transfer due to forced convection effect is more

prominent as compared to the natural convection effect. Similar effect of flow and heat transfer is found as Richardson number is increasing from 0.1 to 10 for higher Reynolds number.

As Richardson number increases from 0.1 to 10 for Re=50, the vortex along the core tilted downwards and becomes more stronger compared to the case of Ri=0.1. The flow strength is increasing upto 2.7% as observed from Fig. 3.3(c) and 3.4(c). This signifies that buoyancy driven flow is more effective than forced and natural convection effects.

Case-II: In the second case we have considered both the vertical walls move downwards due to which the shear force is opposed by the buoyancy effects. Fig. 3.5 and 3.6 represents the streamlines (left) and isotherms (right) for Ri=0.1 and Ri=10 respectively with the variation of Reynolds number from $1 \leq Re \leq 100$. The streamline profiles (Fig. 3.5(a, c, e)) shows the development of Rayleigh-Bénard convection cell above each heat source. However, the increase in the Richardson number from Ri=0.1 to 10 resulting the increment in flow strength upto 23.56% in the core of the cavity for higher Reynolds number (Re=100) which reflects that flow is dominated by buoyancy effect.

Fig. 3.5(b, d, f)shows that the heat plums are developed above each heat source due to density loss in the fluid medium. Buoyancy forces drive the heated fluid towards the upper cold surface and the upper cold fluid move downwards. The temperature of cold fluid gets heated due to the heat source and move upwards which repeats the flow pattern resulting the circular region around the heat source. The closest layer of fluid makes a stable recirculation zone centered along the edges of each heat source forming a thermal boundary layer. In this case, it is clearly observed that buoyancy forces are opposing the shear forces. From Fig. 3.5(b), it is observed that the heat transfer lines are parallel to the heat sources but as Reynolds number increases, the lids drag the cold fluid towards the hot surface forming a sharp paraboloid profile. This reflects that hot fluid passes towards the center and upper region of the cavity only in the mid-section where the shear effect is minimum.

From Fig. 3.6, similar configurations of streamlines are observed for higher buoyancy forces $Ri = 10$. The flow variations produces two anticlockwise vortices as shown in Fig. 3.5 signifies the higher velocity due to forced convection effect. From Fig. 3.6(a, c, e), it is observed that flow velocity is increasing as Reynolds number is increasing but remains

stagnant after Re=50 and Re=100.

The heat transfer effect is found to be significant at higher Reynolds number for $Re = 100$ (Fig. 3.6(f)). At higher Reynolds number $Re = 50$ and $Re = 100$ (Fig. 3.6(d,f)) it is found that shear force is dominating the heat transfer rate and most of the cold fluid tries to store close to the lower left and right corner of the cavity. The heat transfer rate is found to be less as Re increases, since the heated fluid is suppressed by upper cold fluid. The heat transfer value i.e., isotherm lines value is 0.335 at axial position of (0.5, 0.42) for $Re = 50$ but this moves to the new position (0.5, 0.34) for Re=100.

Case-III: Streamlines and isotherm for case-III are presented in Fig. 3.7 and 3.8. In this case two vertical parallel lids are moving in the upward direction in which shear effect is supported by the buoyancy driven flow. Since two lids are moving in the same direction and effective velocities are influenced by the buoyancy effects. From 3.7(a, c, e), it is observed that for $Ri = 0.1$ as Re is increasing, the fluid circulated vortices are moving upwards supporting the shear effect as compared to buoyancy effects and magnitude of velocities are decreasing as compare to earlier case. An increment of 7.21% in stream function value at the center of the eddy is observed for $Re = 100$ on increasing Ri values from 0.1 to 10.

The heat transfer lines presented in Fig. 3.7(b, d, f), shows that at low Reynolds number the flow is dominated by buoyancy effect and found to have similar profile as obtained in earlier case. But as Re increases, the flow is dominated by forced convection effect and buoyancy has minimal effect. The cold fluid parallel to the moving boundaries forced to move to the core region of cavity and heated fluid moves towards the moving boundaries to fill the portion. Hence heat transfer is minimized at higher Reynolds number. The flow is completely forced dominated at larger Reynolds number.

From Fig. 3.7(d, f), it is found that the heat transfer values in the core is reduced from 0.0060 at (0.5, 0.4) to 0.0055 at (0.5, 0.4). Fig. 3.8 represents the flow and isothermal lines for Ri=10, where similar flow profiles are obtained as observed in Fig. 3.7. These figures are mirror images of earlier case (i.e., case-II) but the flow circulation are reversed in order to support the shear effect. Streamlines are symmetric about the right and left half of the cavity which is also same for case-III but the orientation is opposite. From Fig. 3.8(a, c, e) it is observed that vortex strength is increased with increase of Reynolds

number but shifts upwards.

The heat transfer lines presented in Fig. 3.8(d, f) shows that heat transfer rate is increasing due to the increase of Ri values. From Fig. 3.8(d, f) it is found that cold fluid forces to enter close to heat source for higher Reynolds number. For the higher Reynolds number as Ri is increased the isotherms are clustered close to the sliding wall and forming vortices along the upper section of the enclosure.

Overall flow and heat transfer: The flow and heat transfer in all three different considered configurations are found to be natural convection dominated when $Ri = 10$ and forced convection dominated when $Ri = 0.1$. The increment of Re shows the dominating effect of forced convection over natural convection. For case-I, the isotherm plot shows that heat transfer is mostly carried out by the moving lids in upward direction and the heated fluid is transported to the colder part and cold fluid comes down along the downward moving lid. In case-II and case-III, we can observe that heat transfer is reduced in comparison to case-I. This signifies that heat transfer is increasing when the lids are moving in opposite direction. In all the cases, it is found that heat transfer lines are almost similar for Re=1. This signifies that heat transfer is almost constant in lower Reynolds number for different Ri values and also independent of the direction of moving lids.

In the final form, the average Nusselt number for three different cases and varying solid volume fractions are calculated and presented in Fig. 3.9-3.11 using eq. (3.1). From Fig. 3.9, it is observed that the heat transfer efficiency is increasing with the increment of solid volume fraction (ϕ). A sudden variation of average Nusselt number is observed when Re is increased from 1 to 50 and 50 to 100. It is observed that average heat transfer at $Re = 50$ with high nanofluid concentration is higher than the heat transfer rate at $Re = 100$ with clear fluid. This shows that nanoparticles are very much responsible and capable to change the flow features.

For all the considered cases the average Nusselt number represented in Fig. 3.9-3.11 found to be increasing with Richardson number and solid volume fraction. It is also observed that average Nusselt number is almost constant when $Re = 1$ for all the Richardson number but with increase in Re the variation due to Richardson number is clearly visible except in case-III at $Re = 10$. The Nusselt number is found to be increasing

for all values of Richardson number and Reynolds number with increment in solid volume fraction.

From the above observations it can be concluded that average Nusselt number along the bottom of cavity is found to be highest in case-I compared to all other considered cases for all Ri and ϕ values. Increment of solid volume fraction increases the heat transfer rate of nanofluid very efficiently. In case-I, the heat transfer rate increment is found to be 47.73% for $Ri = 0.1$ and 40.65% for $Ri = 10$ in Cu-water nanofluid when the solid volume fraction is changing from 0.0 to 0.2. Similarly, in case-II the variation is about 49.82% for $Ri = 0.1$ and 39.12% for $Ri = 10$ and in case-III, the variation is 44.07% and 30.39% for $Ri = 0.1$ and 10 respectively. Hence, the solid volume fraction is found to be most effective in case-II for $Ri = 0.1$ as the increment in average Nusselt number is found to highest. But, when the overall heat transfer efficiency is considered, case-I is found to attain the maximum heat transfer rate, since, the maximum value of average Nusselt number in case-I to III are found to be 7.7599, 6.9914 and 6.1112 respectively at $Ri = 10$, $Re = 100$ for $\phi = 0.2$. Therefore oppositely moving lids give higher heat transfer rate as compared to same direction moving lids, as the average Nusselt number values are higher for all parameters in this case.

3.6 Conclusion

A comparative study of mixed convection flow in a two-dimensional lid-driven square cavity filled with Cu-water nanofluid is presented in this chapter. The cavity is partially heated from below, using two discrete heat sources. The effect of solid volume fraction, Reynolds number, Richardson number and the direction of lid movement on the fluid flow and heat transfer have been investigated numerically. From the above study, the conclusions are summarized as follows:

1. It is found that the heat transfer and fluid flow is sensitive to the solid volume fraction. Moreover, the solid volume fraction variation is an active factor for the average Nusselt number as variation in nanoparticle volume fraction changes the flow pattern.

2. The physical flow parameter Ri is mostly affecting the heat transfer rate. When

$Ri < 1$, the results predicted that the flow and heat transfer is dominated by forced convection effect and when $Ri > 1$, flow and heat transfer are dominated by natural convection.

3. In all the three cases for lower Re values, the average heat transfer is observed to be almost constant for different Ri values but found to be monotonically increasing with increasing solid volume fraction.

4. For a constant solid volume fraction with the increase of Re and Ri, it is found that heat transfer increases irrespective of the direction of moving walls. Out of the three considered cases, the maximum heat transfer is found in case-I. But, for $Ri < 0.1$ the result does not hold good.

5. The solid volume fraction is found to be most effective in case-II as the increment in average Nusselt number is found to be best when $Ri = 0.1$. But, still the maximum heat transfer is found in case-I, the average Nusselt number is maximum for all the flow parametric values.

6. The average heat transfer rate shows a sharp variation in case-III for large Ri and Re as the strength of the circulating eddy is decreasing by the opposing buoyancy forces.

Tables and figures

Table 3.1: Thermophysical properties of water and copper.

Property	Water	Copper
C_p	4179	383
ρ	997.1	8954
k	0.6	400
β	2.1 $\times 10^{-4}$	1.67$\times 10^{-5}$

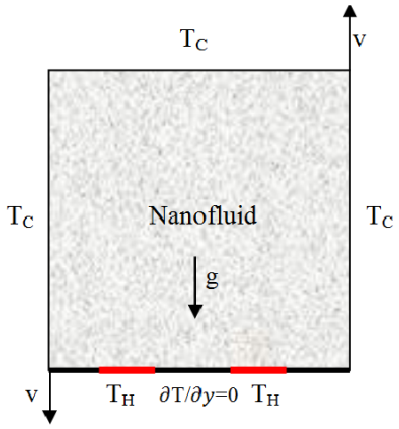

(a) case-I

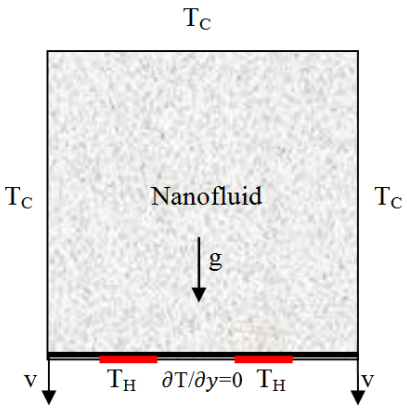

(b) case-II

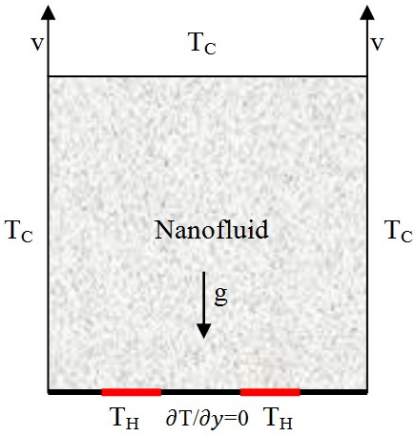

(c) case-III

Figure 3.1: Problem Geometry

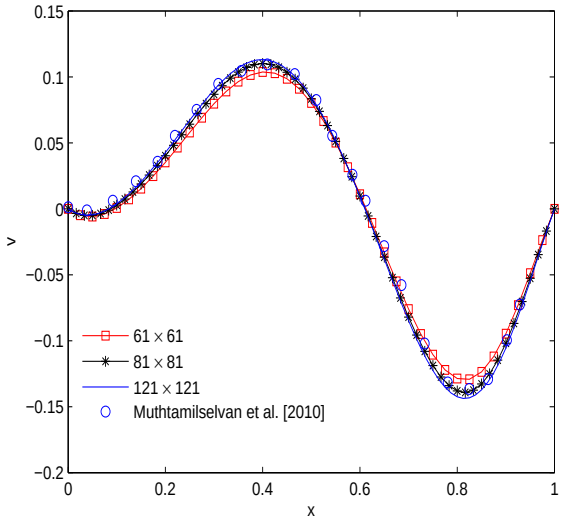

(a)

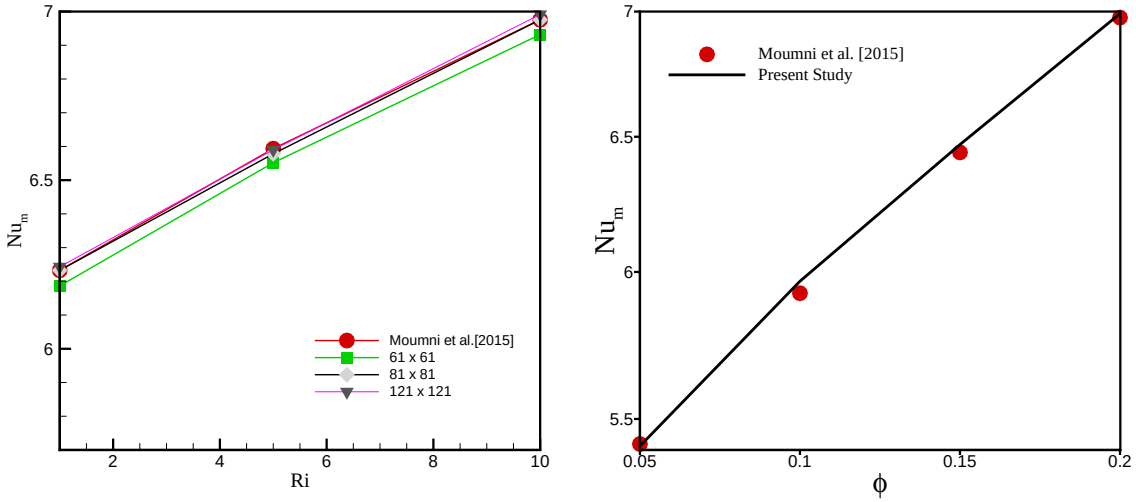

(b) (c)

Figure 3.2: Comparison of (a) vertical component of velocity at mid section of cavity due to Muthtamilselvan et al. [162] for $Ri = 1, Ra = 100, \phi = 2\%$, for various grid size from 61×61 to 121×121, (b) average Nusselt number with results due to [159] with $Pr = 6.2,\ \phi = 2\%,\ Re = 100$ and $1 \leq Ri \leq 10$ for various grid size from 61×61 to 121×121, (c) average Nusselt number with results due to [159] with $Pr = 6.2,\ Ri = 10,\ Re = 100$ and $0.05 \leq \phi \leq 0.2$.

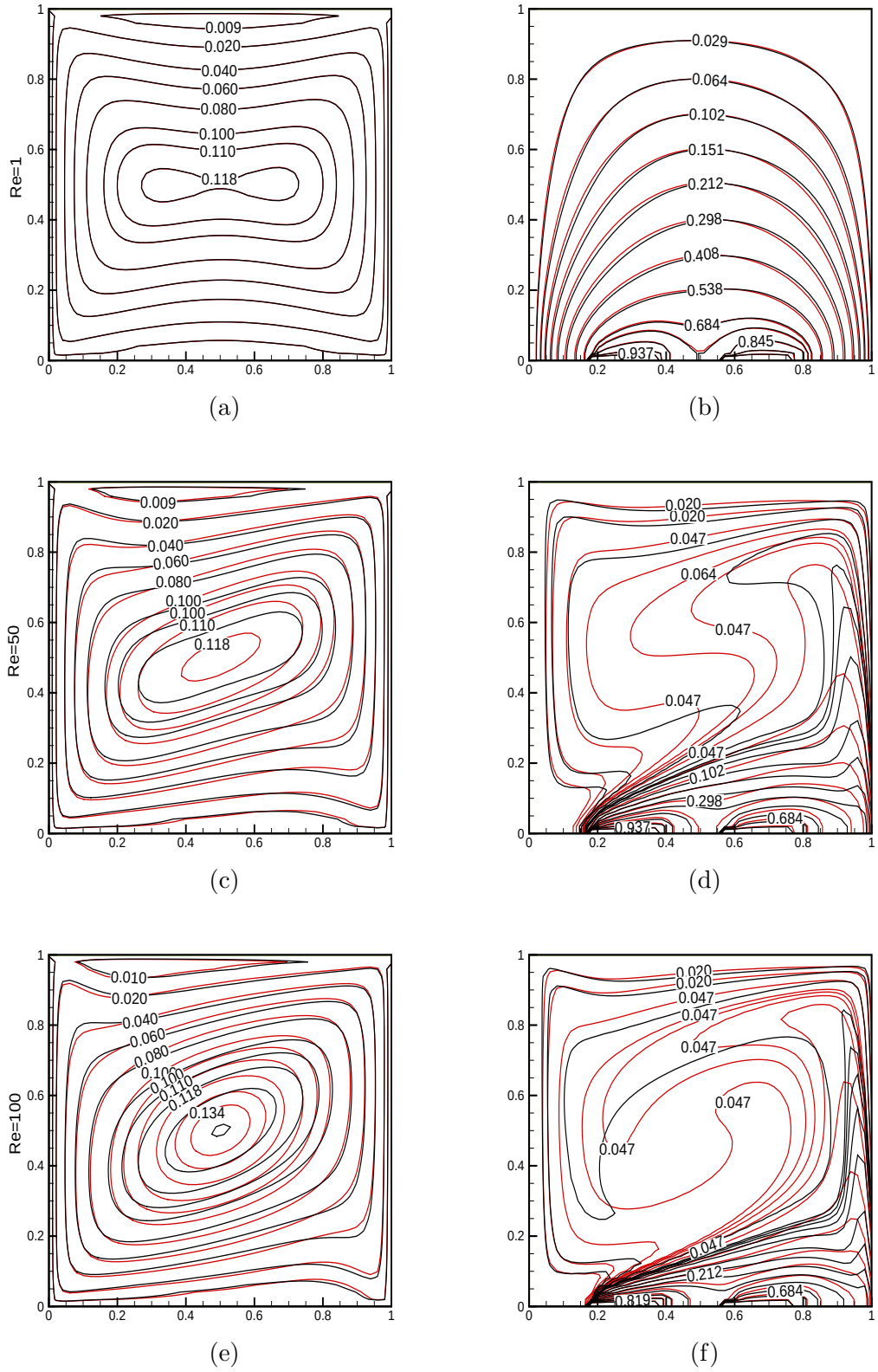

Figure 3.3: Streamlines and isotherm lines of clear fluid ($\phi = 0.0$, Black) and nanofluid ($\phi = 0.2$, Red) at Ri=0.1, $1 \leq Re \leq 100$ for case-I.

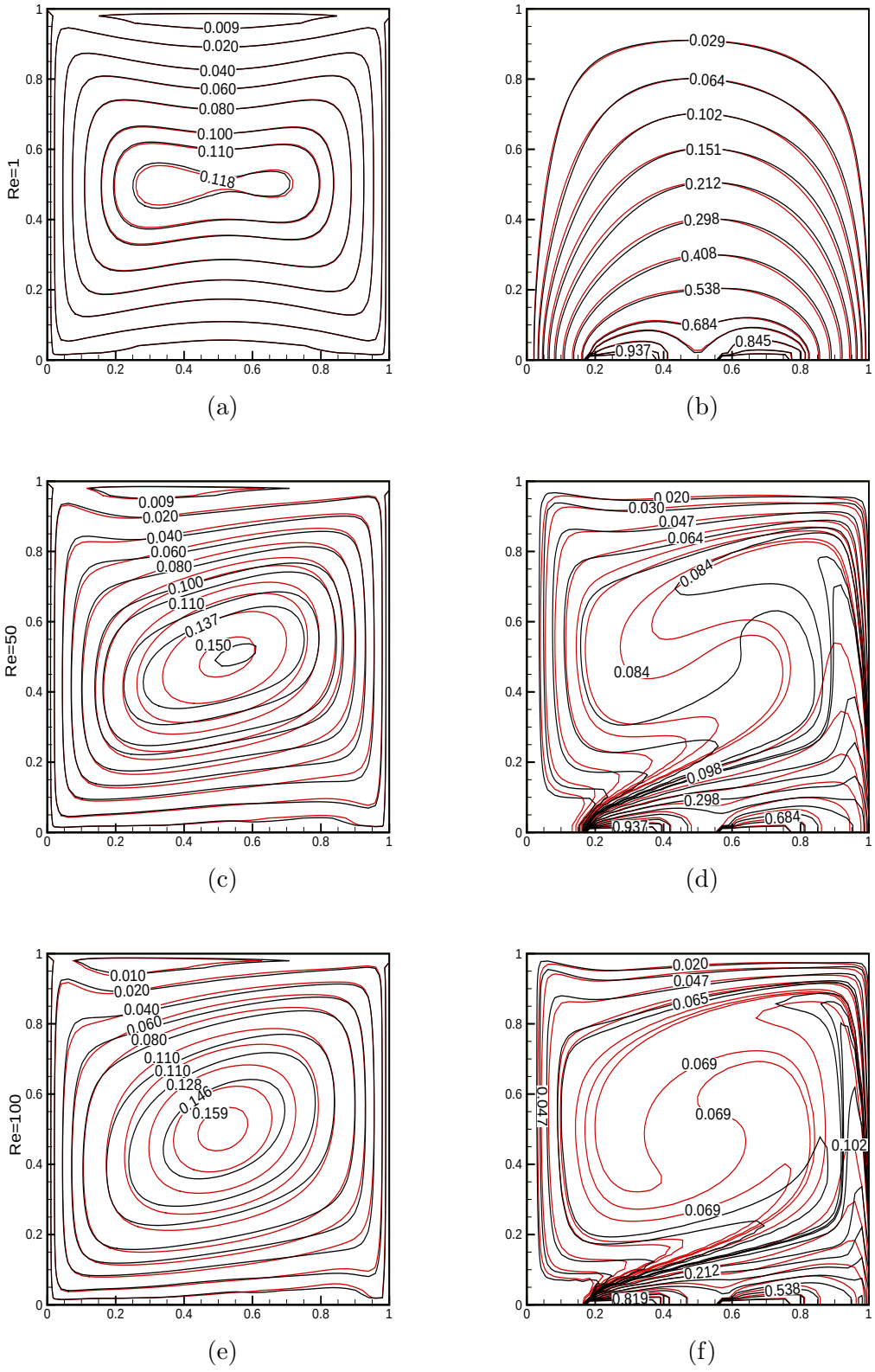

Figure 3.4: Streamlines and isotherm lines of clear fluid ($\phi = 0.0$, Black) and nanofluid ($\phi = 0.2$, Red) at Ri=10, $1 \leq Re \leq 100$ for case-I.

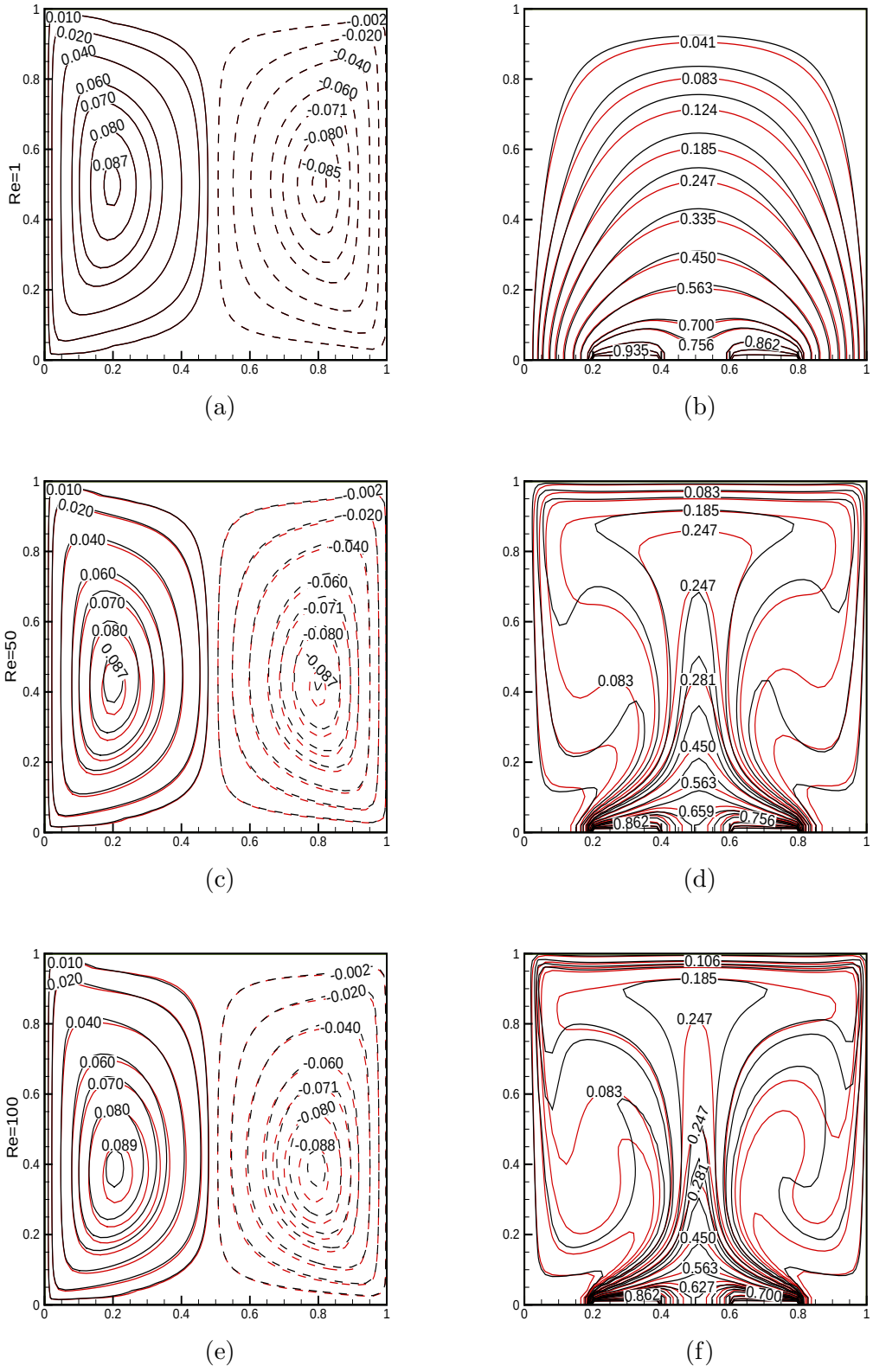

Figure 3.5: Streamlines and isotherm lines of clear fluid ($\phi = 0.0$, Black) and nanofluid ($\phi = 0.2$, Red) at Ri=0.1, $1 \leq Re \leq 100$ for case-II.

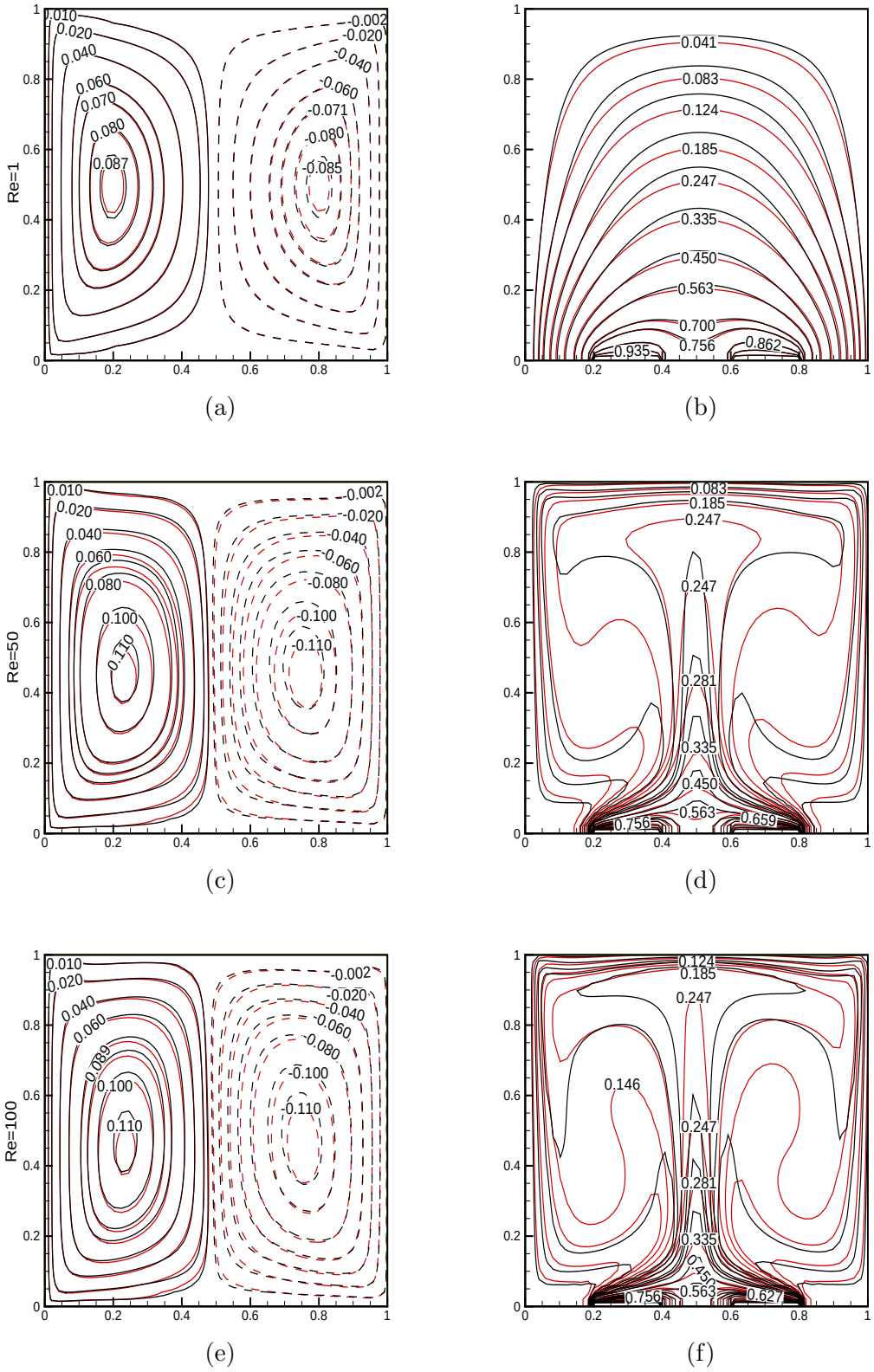

Figure 3.6: Streamlines and isotherm lines of clear fluid ($\phi = 0.0$, Black) and nanofluid ($\phi = 0.2$, Red) at Ri=10, $1 \leq Re \leq 100$ for case-II.

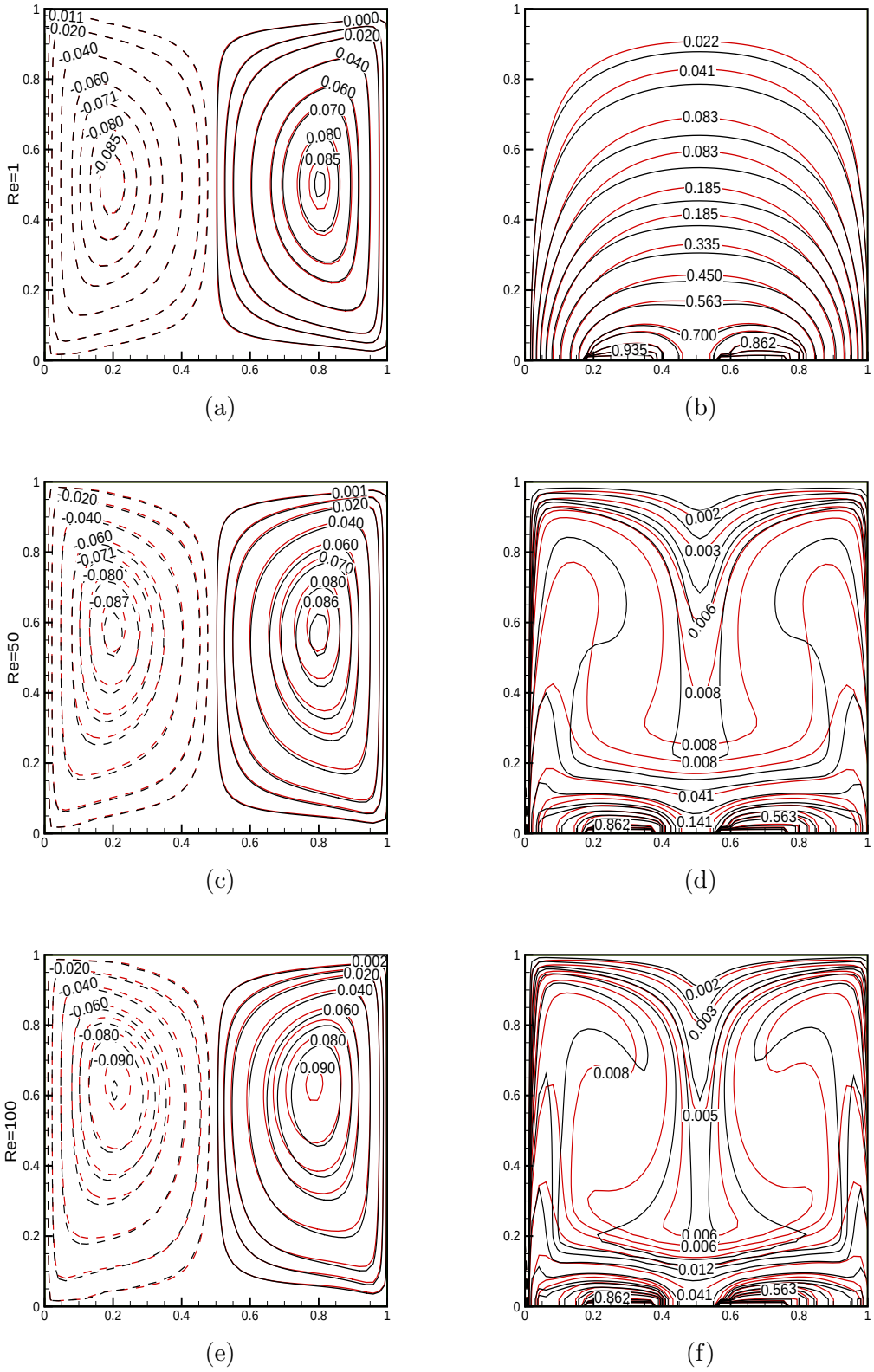

Figure 3.7: Streamlines and isotherm lines of clear fluid ($\phi = 0.0$, Black) and nanofluid ($\phi = 0.2$, Red) at Ri=0.1, $1 \leq Re \leq 100$ for case-III.

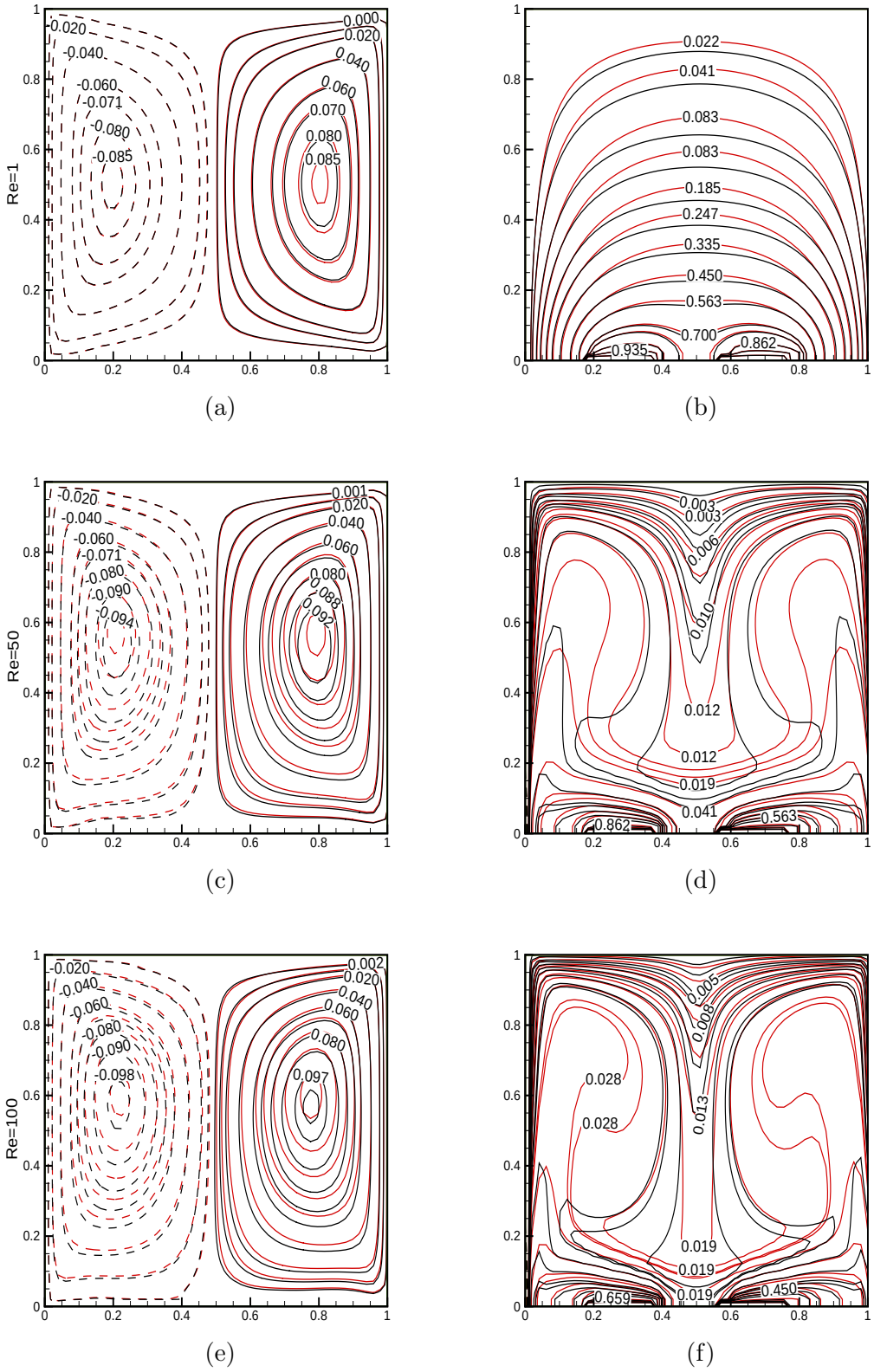

Figure 3.8: Streamlines and isotherm lines of clear fluid ($\phi = 0.0$, Black) and nanofluid ($\phi = 0.2$, Red) at Ri=10, $1 \leq Re \leq 100$ for case-III.

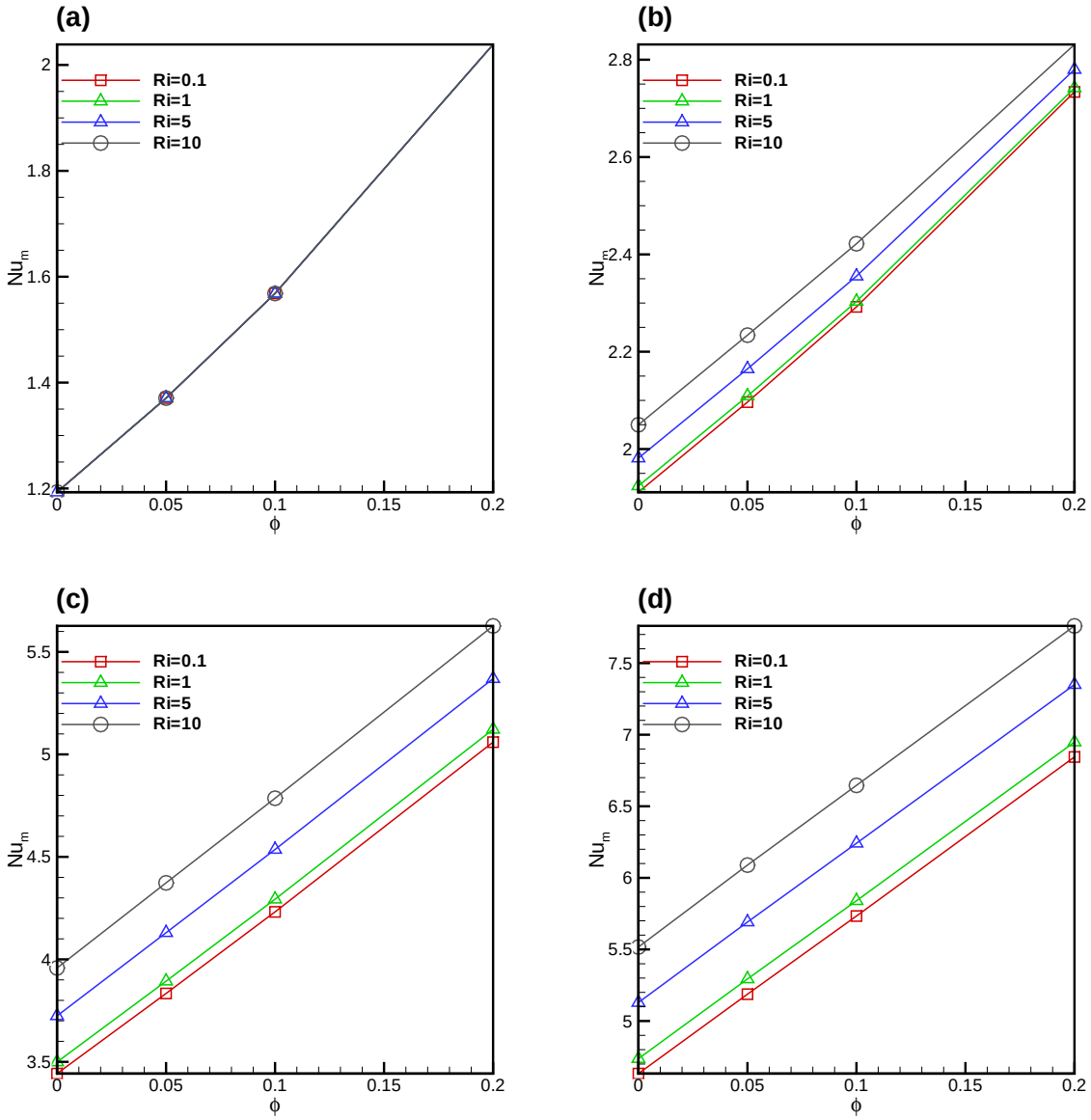

Figure 3.9: Variation of average Nusselt number with respect to solid volume fraction of nanoparticles and Richardson number for different values of Reynolds number ((a) $Re = 1$, (b) $Re = 10$, (c) $Re = 50$ and (d) $Re = 100$) for case-I.

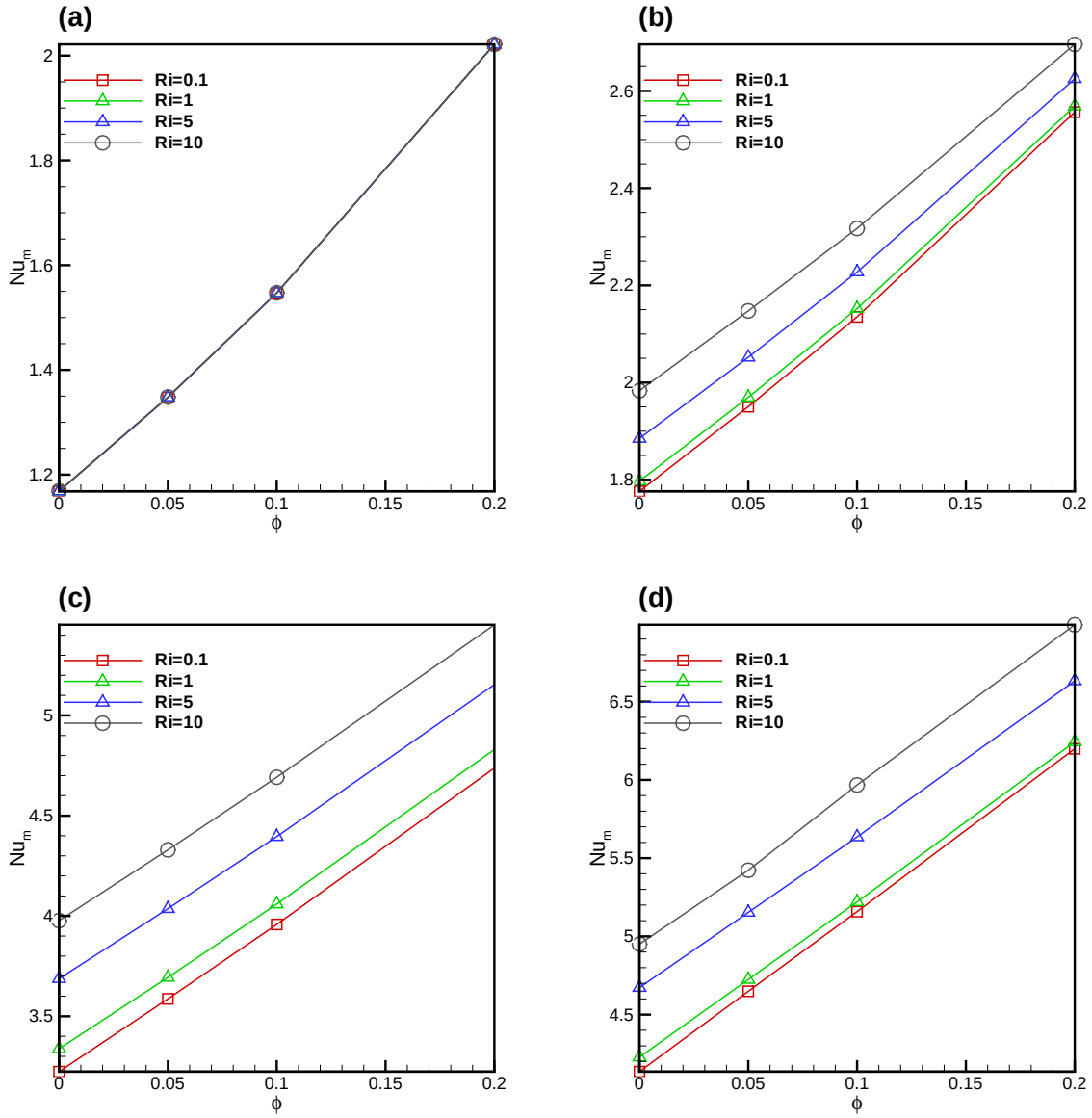

Figure 3.10: Variation of average Nusselt number with respect to solid volume fraction of nanoparticles and Richardson number for different values of Reynolds number ((a) $Re = 1$, (b) $Re = 10$, (c) $Re = 50$ and (d) $Re = 100$) for case-II.

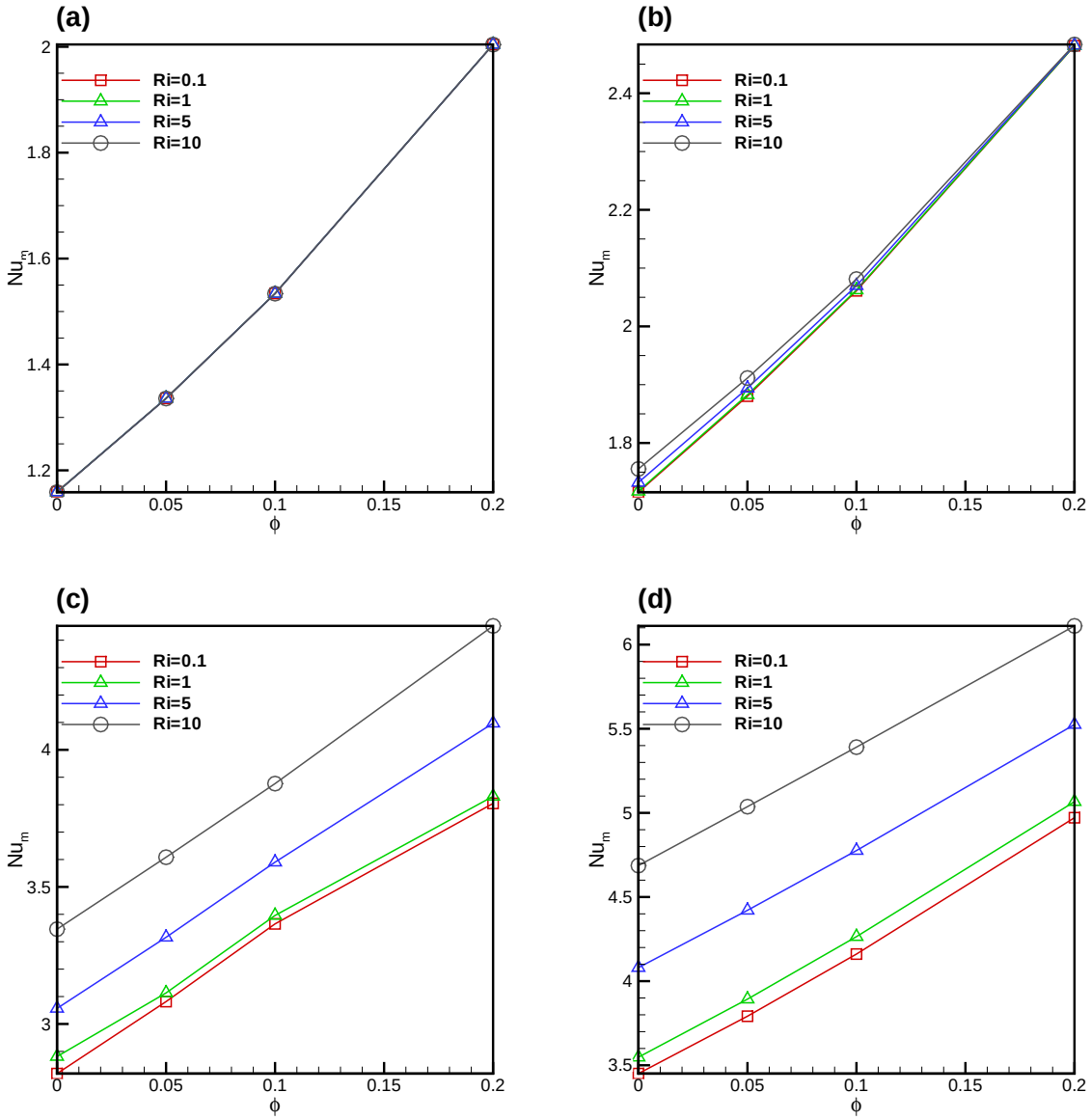

Figure 3.11: Variation of average Nusselt number with respect to solid volume fraction of nanoparticles and Richardson number for different values of Reynolds number ((a) $Re = 1$, (b) $Re = 10$, (c) $Re = 50$ and (d) $Re = 100$) for case-III.

Chapter 4

Magneto-convection and Its Effect on Partially Active Thermal Zones in a Porous Square Domain [1]

4.1 Introduction

Magneto-hydrodynamics (MHD) flow of an electrically-conducting fluid coupled with heat transfer has large scale applications in engineering problems such as magneto-hydrodynamic generators, nuclear reactors for nuclear waste repository, electrical equipment cooling, plasma physics, the migration of moisture in fibrous insulation, the spreading of chemical pollutants in saturated soil, geothermal energy extraction and the boundary layer control theory in the field of aerodynamics [28, 131].

Bejan and Khair [28] studied the natural convection flow effects in a fluid saturated medium with combined heat and mass transfer. They analyzed the convection near a vertical surface in a porous medium for various possible regimes based on the different values of buoyancy ratio and Lewis number. Lai and Kulacki [131] extended the problem of Bejan and Khair [28] to include wall fluid injection effects, since it has the application in migration of moisture in fibrous insulation, where it may exist an interfacial velocity at the wall due to injection.

Among the engineering activities, natural convection heat transfer in the porous layer has been applied to sensible heat storage using porous media, porous insulation materials, the oil separation technique of oil and sand by using steam [99]. Natural convective

[1] The contents of this chapter has been published in *International Journal of Heat and Mass Transfer, Elsevier, DOI:10.1016/j.ijheatmasstransfer.2015.12.037*

heat and mass transfer in an inclined porous layer was also studied experimentally by Inaba et al. [99]. Therein, two opposite walls of the tall rectangular cavity were thermally insulated, while the other walls are kept at different temperatures. In their study, they tried to obtain fundamental information related to the natural convection heat transfer rate through the inclined porous layer in wide ranges of parameters, such as, inclination angles, modified Rayleigh numbers, geometrical dimensions etc.

Chamkha and Khaled [46] considered magnetic field and wall mass transfer effects on coupled heat and mass transfer by natural convection from a vertical semi-infinite plate maintained at a constant heat flux. They have extended their problem to include a porous saturated medium which embeds the permeable surface in Chamkha and Khaled [47], where the parametric study indicates that increase in the ratio of concentration to thermal buoyancies results in the enhancement in the values of skin-friction parameter, Nusselt number and the Sherwood number for the studied thermal cases. Coupling of heat and mass transfer can find a great importance in natural phenomena such as currents in ocean driven by differentially heating and acting as a freight trains for salt as mentioned by Bejan [26] and also the role of factory waste gas diffusion in a differentially heated circulated air [46]. A significant number of studies has been done for the fluid flow and heat transfer in different geometries considering both porous and non-porous medium [115, 121, 144, 209, 234, 241]. Most of these studies include the Brinkman-extended Darcy equation of motion and flow governing parameters like Grashof number, Richardson number, Darcy number etc.

Recently, significant attention is focused on new applications of MHD flow and heat transfer effects in nanofluid using various domain ([4, 65, 66, 106, 203, 205]). Magnetohydrodynamic nanofluid hydrothermal treatment in a cubical enclosure heated from below is presented by Sheikholeslami and Ellahi [204]. They tried to find the significant effects of Brownian motion on the effective viscosity and thermal conductivity of nanofluid. A numerical study of non-Newtonian nanofluid is made by Ellahi [64] to study the effects of MHD and variable viscosities in a pipe flow. It is found that the magnetic field effects decrease down the fluid motion in the presence of variable viscosities. Magnetic effects and fluid flow under the influence of stream wise transverse magnetic fields in laminar regime is studied by Rashidia et al. [190]. They found that the effects of transverse

wise magnetic field on flow and heat transfer effects are more than that of stream wise magnetic field.

Sivasankaran et al. [220] studied the mixed convection in a lid driven square cavity in which the perpendicular boundaries are maintained with a time periodic temperature in the presence of a magnetic field. The horizontal walls are maintained with impermeable and adiabatic conditions. The fluid is considered to be a low Prandtl number liquid metal which is electrically conducting. They have discussed the heat transfer rate variation when the left and right walls are maintained with two different sinusoidal electric fields with different amplitude and phase differences. The flow behavior in the cavity is strongly affected due to the magnetic field.

Magnetohydrodynamics natural convection in a square cavity filled with a electrically conducting fluid is numerically investigated by Nityadevi et al. [172]. Some portion of the perpendicular walls are maintained with different temperatures, i.e. left portion of the wall is maintained with a time periodic heat source and the right portion is kept with constant heat sources. They have discussed the heat transfer rate by changing the locations of the heat source at left and right walls keeping all other boundaries or portion as adiabatic. For various values of flow parameters like Grashof number, amplitude, Hartmann number and Prandtl number. Nine different locations has been chosen to study the heat transfer rate and found that the heat transfer rate is optimum when the thermally activated zones are placed in the middle locations of the perpendicular walls.

From the industrial application point of view, mixed convection flow in fluid saturated porous medium has a wide range of applications in nuclear waste repository and electrical equipment cooling. The present work motivates to porous media research, since Darcys law or its modified forms are applied to describe the relation between the pressure drop and flow rate first [42, 238]. In an experimental investigation of fluid flow through a medium of variable porosity Vafai et al. [233] found that for a fixed pore diameter an increase in Reynolds number results in increase of Nusselt number. A time dependent oscillatory cavity driven flow with thermally activated walls in a fluid-saturated porous medium is studied by Jue [103]. He tried to find the effect of porous medium in fluid flow and heat transfer by using different flow parameters. The results indicate that the flow field is dominated by permeability of porous medium, and the flow strength becomes

weaker with decreasing permeability. Narayana and Sibanda [165] studied the mixed convection along permeable vertical wall in a non-Darcy porous medium in the presence of magnetic field. In their study it has been concluded that in aiding flow, the heat and mass transfer coefficients at the walls get reduced with increasing magnetic parameters. Al-Farhany and Turan [6] studied a steady double-diffusive natural convective heat and mass transfer in an inclined rectangular porous medium. They found that the average Nusselt number and Sherwood number decreases with an increase in the aspect ratio of enclosure.

Many industrial applications requires higher heat flux or higher thermal activated boundaries as compared to the fluid temperature, and chemical reactions which leads to a local thermal non-equilibrium condition [24, 57]. A local thermal non-equilibrium condition in fully developed laminar flows at constant wall-temperature inside a circular tube filled with saturated porous media is studied by Dehghan et al. [57]. The velocities and the temperature are computed using the perturbation and the successive approximation methods. A numerical study of forced convection, heat transfer and entropy generation in a channel, partially filled with a porous medium is discussed by Torabi et al. [232] using local thermal non-equilibrium model. Bifurcation phenomena are observed in the temperature field and rates of entropy generation using asymmetric boundary conditions. The model is extended by Torabi et al. [232] by using internal heat generation or consumption. They have analyzed and compared both local thermal equilibrium and local thermal non-equilibrium models.

A numerical study of laminar MHD mixed convection in an inclined lid-driven square cavity with opposing temperature gradients is studied by Ahmed et al. [3]. The vertical sidewalls are assumed to have non-uniform temperature variation while the top and bottom walls are kept insulated with the top surface moving at a constant speed. They have found that the heat transfer rate along the heated walls is enhanced on increasing either Hartmann number or inclination angle and the amplitude ratio for all values of the phase deviation. A combined study of MHD flow and heat transfer in a lid driven porous enclosure is done by Pekman and Tezer-Segen [181]. They discussed the time independent flow variation and heat transfer due to mixed convection by variation of permeability of porous medium and applied magnetic field. They found that the decrease in permeability

and increase of intensity in magnetic field slows down the fluid velocity. The heat transfer rate decreases with increase of Hartmann number and the magnetic potential rotates throughout the cavity with the high magnetic permeability of the fluid.

Large scale of studies have been made for the complete discussion of the convection dominated flow with heat transfer effects in enclosures equipped with differentially heated boundaries along with the magnetic field effects. Most of the related papers discussed above can be divided mostly into three categories based on either clear fluid flow or porous medium flow in enclosures. The first category deals with the mixed convection, the second category takes magneto-convection and the third category involves double diffusion flows. The boundaries of the above flow domains are classified either putting uniform or non-uniform thermal, solutal or magnetic fluxes and some studies are used sinusoidal temperature distributions either on one sidewall or on both sidewalls. In this chapter we investigated the heat transfer and fluid flow effects in a cavity filled with a fluid-saturated porous medium (i.e. a mixture of liquid metal and spherical particles or some kind of sand), since it has relevance in several industrial processes such as the oil separation technique of oil sand by using steam [107, 99]. We considered that the flow is governed by two mechanisms:

(i) a viscous electrically driven convective flow due to the presence of magnetic field and

(ii) natural convective flow due to thermally activated zones.

The work emphasizes to investigate the effects of the transient discrete heat sources at different locations of the perpendicular boundaries of the porous enclosure in the presence of magnetic field to probe the effect of porous medium in fluid flow and heat transfer. Since one of the recent study made by Ahmed et al. [3] found that the non-uniform heating is providing the higher heat transfer rate. In the present discussion we tried to establish the effect of magnetic field on the flow and heat transfer due to the variation of Hartmann number ($0 \leq Ha \leq 10$), Grashof number ($10^4 \leq Gr \leq 10^6$) and Prandtl number from ($0.0 \leq Pr \leq 10.0$) (Farhany and Turan [6]) with three different relative positions of the thermally active locations. In this discussion we have included low Prandtl number (0.054) liquid metal values, which is used for cooling process of nuclear reactors in thermodynamics systems [172].

4.2 Mathematical model and numerical method

4.2.1 Physical domain

The physical model considers a transient two dimensional flow within a closed square cavity of length L filled with an electrically conducting fluid saturated porous medium as shown in Fig. 4.1. A portion D (1/2 or 1/3 of the wall length) of the right vertical wall is maintained with constant wall temperature and the same length of the left vertical wall is maintained with a periodic temperature. The hot region of the wall is moving along top to bottom of the left wall and the cold region is moving along bottom to top of the opposite wall. The top, bottom and remaining parts of the boundaries of the cavity are thermally insulated. We want to investigate the heat transfer characteristics for three different combinations of the thermally active locations. Region (i) is for bottom-middle, region (ii) for middle-middle and region (iii) for upper-middle combination of heated and cooled wall. Initially, the fluid is considered to be at rest with a uniform temperature T_c.

The fluid is assumed to be Newtonian, incompressible and viscous and the flow is assumed to be laminar. The gravity acts vertically downwards. The fluid properties are assumed to be constant, except density [172]. Boussinesq's assumption is followed for density variation and the flow is driven by means of a constant applied pressure gradient and is permeated by a externally applied magnetic field of strength B_0 applied parallel to the gravity. A general Darcy-Brinkman-Forchheimer model is used to deal the flow in porous medium. The saturated porous medium is assumed to be thermally, hydrodynamically and electrically isotropic (neutral). In the present study, induced magnetic field is assumed to be negligible in comparison to the applied magnetic field and the Joule heating, viscous dissipation, pressure work and Hall effect are also assumed to be negligible. Variation of density are described by the Boussinesq approximation as,

$$\rho(T^*) = \rho_0[1 - \beta_T(T^* - T_c^*)], \tag{4.1}$$

ρ_0 is density of the undisturbed fluid. The volumetric thermal expansion coefficient is $\beta_T = -\frac{1}{\rho}\frac{\partial \rho}{\partial T^*} > 0$.

The governing equations for the two dimensional viscous incompressible fluid flow

for magneto natural convection in a porous square cavity can be represented as,

$$\frac{\partial u^*}{\partial x^*} + \frac{\partial v^*}{\partial y^*} = 0, \tag{4.2}$$

$$\frac{\partial u^*}{\partial t^*} + u^*\frac{\partial u^*}{\partial x^*} + v^*\frac{\partial u^*}{\partial y^*} = -\frac{1}{\rho_0}\frac{\partial p^*}{\partial x^*} + \nu\left(\frac{\partial^2 u^*}{\partial x^{*2}} + \frac{\partial^2 u^*}{\partial y^{*2}}\right) - \frac{\sigma B_0^2}{\rho_0}u^* - \frac{\nu}{K}u^*, \tag{4.3}$$

$$\frac{\partial v^*}{\partial t^*} + u^*\frac{\partial v^*}{\partial x^*} + v^*\frac{\partial v^*}{\partial y^*} = -\frac{1}{\rho_0}\frac{\partial p^*}{\partial y^*} + \nu\left(\frac{\partial^2 v^*}{\partial x^{*2}} + \frac{\partial^2 v^*}{\partial y^{*2}}\right) - \frac{\rho - \rho_0}{\rho_0}g - \frac{\nu}{K}v^*, \tag{4.4}$$

$$\frac{\partial T^*}{\partial t^*} + u^*\frac{\partial T^*}{\partial x^*} + v^*\frac{\partial T^*}{\partial y^*} = k\left(\frac{\partial^2 T^*}{\partial x^{*2}} + \frac{\partial^2 T^*}{\partial y^{*2}}\right), \tag{4.5}$$

along with the boundary conditions,

$$u^* = v^* = 0, \quad \frac{\partial T^*}{\partial y^*} = 0 \quad \text{at } y^* = 0 \text{ and } L, \quad 0 \le x^* \le L, \tag{4.6}$$

$$T^* = T_H(1 - asin(2\pi t^*/\hat{\omega})), \quad \text{on the hot portion (D)}, \quad \text{at } x^* = 0, \tag{4.7}$$

$$T^* = T_c, \quad \text{on the cold portion (D)}, \quad \text{at } x^* = L\ , \tag{4.8}$$

$$\frac{\partial T^*}{\partial x^*} = 0 \quad \text{at } x^* = 0 \text{ and } L, \quad 0 \le y^* \le L, \quad \text{except hot and cold part (D)}. \tag{4.9}$$

The dimensional variables as u^*, v^*, p^*, t^* and T^* for the velocity, pressure, time and temperature, respectively can be expressed in non-dimensional form as,

$$u = \frac{u^* L}{\nu},\ v = \frac{v^* L}{\nu},\ x = \frac{x^*}{L},\ y = \frac{y^*}{L},$$

$$t = \frac{t^* \nu}{L^2},\ T = \frac{T^* - T_c}{T_h - T_c},\ p = \frac{p^* L^2}{\rho_0 \nu^2}. \tag{4.10}$$

Using Boussinesq-fluid assumption, the governing flow equations and heat transport equation in non-dimensional form can be expressed as,

$$\frac{\partial u}{\partial x} + \frac{\partial v}{\partial y} = 0, \tag{4.11}$$

$$\frac{\partial u}{\partial t} + u\frac{\partial u}{\partial x} + v\frac{\partial u}{\partial y} = -\frac{\partial p}{\partial x} + \left(\frac{\partial^2 u}{\partial x^2} + \frac{\partial^2 u}{\partial y^2}\right) - \left(Ha^2 + \frac{1}{Da}\right)u, \tag{4.12}$$

$$\frac{\partial v}{\partial t} + u\frac{\partial v}{\partial x} + v\frac{\partial v}{\partial y} = -\frac{\partial p}{\partial y} + \left(\frac{\partial^2 v}{\partial x^2} + \frac{\partial^2 v}{\partial y^2}\right) + Gr\ T - \frac{1}{Da}v, \tag{4.13}$$

$$\frac{\partial T}{\partial t} + u\frac{\partial T}{\partial x} + v\frac{\partial T}{\partial y} = \frac{1}{Pr}\left(\frac{\partial^2 T}{\partial x^2} + \frac{\partial^2 T}{\partial y^2}\right). \tag{4.14}$$

It can be seen from the equations that the flow and heat transfer are characterized by four dimensionless parameters: (i) Hartmann number (Ha), (ii) Grashof number (Gr), (iii) Prandtl number (Pr) and (iv) Darcy number (Da) , which are given by

$$Ha = \frac{{B_0}^2 L^2 \sigma_e}{\mu}, \quad Gr = \frac{g\beta_T (T_h - T_c) L^3}{\nu^2}, \quad Pr = \frac{\nu}{k}, \quad Da = \frac{K}{L^2}. \tag{4.15}$$

The non dimensional heat sources along the boundaries are,

$$Q_h = 1 - Asin(\pi t/\delta), \quad Q_l = 0, \tag{4.16}$$

2δ is the period and A is the amplitude factor.

The initial conditions for time $t = 0$ are given by

$$u = v = 0, \quad T = T_c \quad \text{for } 0 \le x \le 1, \quad 0 \le y \le 1. \tag{4.17}$$

and the boundary conditions for time $t > 0$, for three different regions are,

$$u = v = 0, \quad \frac{\partial T}{\partial y} = 0 \quad \text{at } y = 0 \text{ and } 1, \quad 0 \le x \le 1,$$

$$T = Q_h, \quad \text{on the hot portion (D)}, \quad \text{at } x = 0$$

$$T = Q_l, \quad \text{on the cold portion (D)}, \quad \text{at } x = 1$$

$$\frac{\partial T}{\partial x} = 0 \quad \text{at } x = 0 \text{ and } 1, \quad 0 \le y \le 1, \quad \text{(except hot and cold part (D))}. \tag{4.18}$$

The heat flux at the left wall are written in non-dimensional terms by Nusselt number as

$$Nu = -\frac{\partial T}{\partial x}\Bigg]_{x=0}, \tag{4.19}$$

and average Nusselt number

$$Nu_m = \int_L Nu \; dy. \tag{4.20}$$

The bulk average temperature is calculated as [217],

$$\overline{T} = \int \frac{T dV}{V}, \tag{4.21}$$

where V is the enclosure volume.

4.2.2 Numerical method

In order to tackle the modeled nonlinear partial differential equations numerically, the method of Newton's linearization technique is applied, i.e. the values of n^{th} iteration of the dependent variables are known, the next iterated values of variables can be obtained by applying the Newton's linearization method as,

$$V_i^{n+1} = V_i^n + \Delta V_i^n. \tag{4.22}$$

where V stands for u, v, and T; ΔV_i^n represents the error at the n^{th} iteration and i is the grid-index.

In order to obtain the numerical solution of the governing flow equations along with the specified boundary conditions we opt a numerical method using control volume technique. In this approach the continuity, momentum and energy equations are integrated over a specified control volume using staggered grid. In the staggered grid process, the physical quantities like pressure and temperature are placed at the cell center and the velocity components are stored at the midpoints of the cell faces to which they are normal. The discretized form of the governing equations are obtained by integrating over each of the control volumes using the finite volume method [227].

Integrating the eq. (4.11) over the finite control volume around grid point (j, k) we obtain,

$$\int_{\Delta v} \frac{\partial u}{\partial x}\, dV + \int_{\Delta v} \frac{\partial v}{\partial y}\, dV = 0, \tag{4.23}$$

where Δv is the volume of the nodal point.

Eq. (4.12) is integrated over the finite volume around grid point (j, k) is,

$$\begin{aligned}\int_s^n \int_w^e \frac{\partial u}{\partial t} dxdy + \int_s^n \int_w^e \left(u\frac{\partial u}{\partial x}\right) dxdy + \int_w^e \int_n^s \left(v\frac{\partial u}{\partial y}\right) dydx = &- \int_s^n \int_w^e \left(\frac{\partial p}{\partial x}\right) dxdy \\ &+ \left[\int_s^n \int_w^e \frac{\partial}{\partial x}\left(\frac{\partial u}{\partial x}\right) dxdy + \int_w^e \int_s^n \frac{\partial}{\partial y}\left(\frac{\partial u}{\partial y}\right) dydx\right] \\ &- \left(Ha^2 + \frac{1}{Da}\right) \int_s^n \int_w^e u dxdy. \end{aligned} \tag{4.24}$$

The reduced form of u-momentum equation after the integration over u-control volume

is,

$$F_e u_e - F_w u_w + F_n u_n - F_s u_s = b, \tag{4.25}$$

here, F_e represents the non-linear coefficient of u_e and b contains the source terms and time derivative terms. At the interface the convective term is estimated by a quadratic interpolation of u. For example at the east face (Fig. 4.2) we have,

$$u_e = (\frac{3}{8}u_E + \frac{3}{4}u_P - \frac{1}{8}u_W) \quad \text{if} \quad F_e > 0, \tag{4.26}$$

$$u_e = (\frac{3}{4}u_E + \frac{3}{8}u_P - \frac{1}{8}u_{EE}) \quad \text{if} \quad F_e < 0, \tag{4.27}$$

which can be summarized as

$$F_e u_e = (\frac{3}{8}u_E + \frac{3}{4}u_P - \frac{1}{8}u_W)[[F_e, 0]] - (\frac{3}{4}u_E + \frac{3}{8}u_P - \frac{1}{8}u_{EE})[[-F_e, 0]]. \tag{4.28}$$

The v momentum and energy equation is also calculated in a similar manner. We have implemented a third-order QUICK (quadratic upstream interpolation for convective kinematics) [30] scheme (discussed above) to discretize the convective terms in the governing equations (described in Fig. 4.2). Time derivatives are discretized through implicit scheme. A finite volume based iterative algorithm SIMPLE (Semi Implicit Method for Pressure Linked Equations) based on pressure correction approach is used for solving the discretized equations.

The solution of the stated unsteady problem involves the process of solving a succession of steady state problems. For reasonable values of time step Δt, the known ϕ values at time t are used as a guess of the unknown ϕ values at time $t + \Delta t$ where ϕ denotes the dependent variables of the problem. The iterated computation at each time step keep on with till a divergence-free solution is obtained. A repeated time-independent numerical solution is obtained after large time steps which is convergent by advancing the flow field variables through a sequence of shorter time step $\Delta t = 0.001$. In all the numerical computations that has been carried out and presented in form of figures. We have adopted the steady state condition considering time $t = 10$, since the same values are repeated afterwards.

The solution for a single iteration consisting of pressure dependent terms follows the following sequential steps:

An implicit calculation of the momentum and energy equations are performed. The discretization of the governing Navier-Stokes equations and heat transfer equation results in a system of algebraic equations of the form

$$A^{\phi}\phi_{i-1,j}^{n+1} + B^{\phi}\phi_{i,j}^{n+1} + C^{\phi}\phi_{i+1,j}^{n+1} = D^{\phi}, \tag{4.29}$$

where ϕ denotes u, v and T; A^{ϕ}, B^{ϕ} and C^{ϕ} gives the coefficient matrix and D^{ϕ} gives the pressure and source terms for ϕ at time level n and time derivative terms. This system of algebraic equations can thus be written in matrix form with the coefficient matrix as a tridiagonal matrix. Due to coupling of energy equation with the momentum equations, the system of algebraic equations is solved through a block elimination method. The iteration process follows the following sequential steps:

1. The coupled form of energy equation and momentum equations represented in the form of system of algebraic equations and then solved through a block elimination method.

2. The associated pressure equation which is in the form of Poisson equation is solved through the successive under relaxation method.

3. The velocity field is updated at each cell using the pressure correction.

4. The convergence criteria employed for this calculation are as,

$$|\varepsilon_{i,j}^{n+1} - \varepsilon_{i,j}^{n}|_{max} < \delta, \quad |1.0 - \frac{Nu_{m_c}}{Nu_{m_h}}| < \alpha. \tag{4.30}$$

   The cell index are represented in i and j, n is the time level, ε is u, v, or T, and Nu_c and Nu_h are area-averaged Nusselt number on the walls with lower and higher temperature, respectively. The value of δ and α are considered to be 10^{-5} and 10^{-4} respectively.

The computation requires about $40,000$ time steps to give a repeated structure for time step Δt =0.001. To obtain the first convergence process the converged solution of the given set of parameters with smaller value is used as the initial guess.

To check the accuracy of our numerical scheme, a two dimensional lid driven cavity flow due to heating at the lower wall of the cavity without porosity is considered. The

non-dimensional governing equation includes the common flow parameters like Reynolds, Grashof, and Prandtl numbers for the computation. The grid independent tests are performed by varying the grids between 61×61 to 161×161. The grid size effects are presented in Fig. 4.3(a) for the average Nusselt number. The significant changes in the solution due to halving the grid size occur on the third decimal place and the optimal grid size is 81×81. In this figure also, we tried to show the comparison of local Nusselt number along the bottom (y=0) and top (y=1) walls for $Re = 500$ and $Gr = 10^5$. The maximum difference of our result with the result due to Moallemi and Jang [156] is obtained along the upper lid and is 5.5%.

A validation of local temperature flux profiles is made with the results due to Sathiyamoorthy et al. [195] and is presented in Fig. 4.3(b). They have considered a steady porous driven natural convection flow in a square cavity for linearly heated side walls. The results are presented for local Nusselt number due to the uniformly heated wall for $Pr = 0.7$ and $Da = 10^4$.

We have compared and validated our results for the case of a MHD flow without porous medium for the average Nusselt number with Nithyadevi et al. [172]. Their study represented the MHD convection in a square cavity filled with a electrically conducting fluid where the side walls are maintained with time periodic discrete temperatures. Nine different combinations of discrete heat sources have been considered to test the heat transfer characteristics. We have compared our result for average Nusselt number for Region (ii) and top bottom thermally active zones and presented in Fig.4.4(a) without any porosity. We found that our numerical result is validated with their result up to 98%. A comparison of our result with a recent study by Pekmen and Tezer [181] is made for average Nusselt number for different Ha values for two different Pr values. They have considered a lid driven cavity flow for a electrically conducting fluid in porous medium. We have presented our comparison in Fig. 4.4(b) for $Re = 100$, $Pr = 1.0$. The result is found to be optimum.

4.3 Results and discussion

In the present work, a numerical study has been carried out to investigate the MHD convection flow in a porous filled enclosure i.e. filled with an electrically conducting fluid. Vertical boundary walls are maintained with discrete time periodic heat sources. Mathematically, it is observed that mostly four major physical parameters are affecting the heat transfer process when a magnetic field is applied on the electrically conducting fluid. These physical parameters are Gr, Pr, Da and Ha. In the present study, pertaining to liquid metal with condensed vapored solutions, the value of the Prandtl number is varied from $0.054 - 10.0$ [99, 156].

The controlling parameters on the fluid flow for this investigation is Grashof number, which is varying from 10^4 to 10^6, measures the importance of thermal-buoyancy-driven natural convection relative to discrete heat sources. Different values of the magnetic field parameter i.e. Hartmann number (Ha) (= 1, 10 and 50) are chosen for the computation, which measures the relative importance of magnetic effects. Period of oscillation is varied from $\delta = 1$ to 5 and amplitude ratio $A = 0.2$ to 0.6 for the transient hot part of the wall. Other major parameter governing the flow is Da, which is varied from 0.001 to 1.0 [181]. For fixed value of Gr, the variation of Pr and Ha is due to the influence of magnetic field and thermal buoyancy force whilst porosity is kept constant and the variation of Gr is only due to the changes in thermal buoyancy force.

Fig. 4.5 represents the transient fluid flow and heat transfer profiles for $Gr = 10^4$, $Da = 10^{-2}$, $Ha = 10$, $A = 0.4$ and $\Omega = 3.0$ and $Pr = 0.71$ for Region (ii) hotcold active locations. In the beginning stage a small amount of fluid near the hot region is activated. For $t = 0.05$, a small clockwise rotating hot cell appears near the middle heating locations. They indicate conduction mode of heat transfer. At times 0.1 and 0.15 the clockwise rotating cell grows in size, moves slightly away from the boundary and expands and spreads to more than half of the cavity. When $t = 0.2$ and 0.25 the convective cell has moved to the center, elongated to elliptic shape and occupies the entire cavity. For $t = 0.3$ the second vortex started to form along the side of the wall. As t increases further up to 0.35 and 0.4 the inner cell splits into two and the streamlines are suppressed horizontally, and at $t = 0.45$ the second cell is well established showing the

development of the convective mode of heat transfer and at $t = 0.5$ two equal vortices formed. The isotherms for different time levels shows the corresponding increment of heat transfer rate as time increases. At the initial time level it is found that a vortex is formed close to the heated region due to thermal boundary layer effect. From the Fig. 4.5(lower) it is clearly shown that the movement of temperature lines value 0.0238 as time increases from $t = 0.05$ to $t = 0.10$. For further increase of time the thermal boundary layer shows convective mode of heat transfer and the secondary vortex started to appear along the right wall. At optimum level of time, it is observed that the heat transfer of the fluid particles near the right wall (cold location) is increased and the velocity and isotherms lines coincide each other respectively once the steady state is reached.

During the simulation it is observed that less dense fluid tends to rise and the more dense fluid tends to sink, which emerging in a tendency that the upper regions of the fluid to be composed of lower density material than the lower regions. Therefore the thermal buoyancy lead to the configuration of stable stratification. Our primary aim is to investigate the effect of flow velocities, temperature variation due to the combined effect of magnetic thermal buoyancy forces on the stable configuration.

Figures 4.6-4.9 depicts the effects of Grashof number and heat source length on the flow and temperature fields. The streamlines and isotherms lines are presented in these figures, where the upper row presents the flow lines and the lower row provides the temperature lines.

Fig. 4.6 presents the streamlines and temperature profiles for $Gr = 10^4$, $Da = 10^{-2}$, $Ha = 10$, $A = 0.4$, $\Omega = 3.0$, $D = L/3$ and $Pr = 0.71$ for different slot wise periodic magnetic fields. In Fig. 4.6(a) periodic hot source is kept at the lower section of the enclosure and cold slot is at the middle portion of the enclosure (Region I). As the bottom active location is at higher temperature the fluid particles closed to the temperature source or in contact with the hot region gets heated up and loses their densities and raise above their mean level, and moves towards the right active cold location. This movement of particles from hotter to colder regions produces a clockwise rotating eddy within which two smaller clockwise rotational eddies are appearing due to the same reason with a small stagnant region between them avoiding shear instability as shown in Fig. 4.6(a).

The hot cell closed to the left wall is small as compare to the cell generated closed

to the cold section of the right wall. As the heat location is moved to the middle position of the left wall, the hot cell is expanded and produce an elongated cell pattern (4.6(b)). It can be observed that at the middle heating position the initial single cell formation splits equally into dual cells within the larger flattened cell. The corresponding isotherms indicate convective mode of heat transfer at the active regions. The flow and the temperature field are symmetric with respect to the plane y= 0.5. Fig. 4.6(c) presents the streamlines and isotherms for the top heating position. The corresponding isotherms show that convective mode prevails everywhere inside the cavity with a thin thermal boundary layer at the top-middle active locations. In the top heating location (Fig. 4.6(c)), the flow pattern shows the reversal of the bottom hot and middle cold case with a thick thermal boundary layer formation.

Fig. 4.7 plots the streamlines and isotherms for $Gr = 10^5$, $Ha = 10$, $D = L/3$ and $A = 0.4$ at different hot source locations to asses further the accuracy of the physical concepts, with the increment of Gr values. The heat transfer is mostly conductive in the middle parts of the cavity and the size of the eddies are getting increased as Gr value is increasing as compared to earlier case. Fig. 4.7(a) shows that the lower-middle active locations contour lines are horizontal in the bulk of lower cavity region and slightly distorted near the hot or colder regions due to formation of primary eddy.

Fig. 4.7(b) shows that in the middle active locations contour lines are symmetrical closure to opposite walls, the flow rate exists with maximum value in the center of the circulation. Most of the fluid remains unperturbed in the bottom and top region of the cavity, since the density variation is very small due to weak porous media inertial, heat and magnetic effects. The flow is dominated by the impact of the heat transfer source length in the interior flow region of the cavity. Due to natural convection, hot fluid from the left side has the tendency to enter into the less heated region near the right side but feels opposing downward and upward action due to the hot and cold regions which placed opposite walls. This opposing action forms the above said eddies and much of the fluid remains stagnant in the top and bottom region. Fig. 4.7(c) presents the flow lines (Region (iii)) where the upper eddy is getting separated from the main flow stream. This is due to the combined effect of magnetic fields and heat source and it is evident from temperature contour lines (Fig. 4.7(c)).

The increasing rate of heat transfer within the cavity due to the increase of the internal Grashof Number leads to increase the flow rate in the secondary cell as well as increase in its size until it occupies half of the cavity. Fig. 4.8 depicts the streamlines and isotherms for high Grashof number at different heat source locations. Fig. 4.8(a) shows that at $Ha = 10$ with $Gr = 10^6$, the size of the primary eddy is increased and center of primary eddy move towards the center of the cavity with an increment to the lower corner which appears in the form of reduction in the size or position of the eddy of Fig. 4.7(a) due to the primary circulating fluid. This enlarged primary eddy distorted contour lines of temperature in the bulk of cavity (see Fig. 4.8(b)). The intensity of isotherms in the vicinity of the cavity's bottom wall increases as Grashof number increases. The heat transfer from the middle source is higher near the region where the primary eddy impinges on the hot middle wall is clearly pictured from Fig. 4.8(b). From Fig. 4.8(a) and (c), it is shown that the thermal buoyancy effect gain dominance over the initial fluid temperature and the fluid temperature transmitted slower.

Fig. 4.9 shows the streamlines and isotherms for $Ha = 10$, $A = 0.4$ with $Gr = 10^4$ by changing the source length ($D = L/2$) (both hot and cold). The size of the secondary eddies are increased due to the larger heat source as compared to earlier case and move towards the center of the cavity. The temperature are also increased as the source locations are changed from lower to upper. From the figure 4.9 it is observed that the strong thermal boundary layers form along both zones of the left and right walls. The isotherms are distributed besides the heated walls and takes more space in their distribution through the cavity as compared to the previous configuration (Fig. 4.8). From streamlines it can be observed that flow circulation is found in the entire region but the secondary flows are occurring near the source locations. This secondary flow slows down the movement of the fluid in the cavity due to the inertial effects and the applied magnetic field. The magnetic field has the tendency to slow down the movement of the fluid inside the cavity [3]. In this case, the heat source length is increased, causes more internal heat generation as compared to earlier case. This heat transfer rate assists the buoyancy effects to increase fluid flow by accelerating the fluid temperature as observed from Fig. 4.9(b). The left or right cell is not moving much upwards or downwards because of greater internal heat transfer. The fluid temperature increases significantly due to increase of the internal Prandtl number

which is shown in the isotherms.

When some portion of the vertical wall suddenly experiences a non-uniform temperature, the heat transfer to the surrounding fluid is initially by pure conduction. This is similar as the heat transfer into a semi infinite solid when its surface temperature is suddenly increased. We can conclude that the fluid far from the leading edge behaves as if the plate were infinite in length and the velocity in this range is independent of the horizontal direction and the heat transfer due to convection is zero. Fig. 4.10 shows that the average heat transfer rate along central region varies almost in the similar manner for all Grashof number. The rate of heat transfer increases subsequently when the Grashof number is increasing. From the comparison of different locations of the heat transfer it is evident from the figure that the rate of heat transfer varies more at middle-middle locations in comparison to top and bottom middle locations for both $D = L/3$ and $D = L/2$. The maximum rate of heat transfer is observed when the heat source length is larger. The minimum heat transfer rate is observed at top-middle combination (for both $D = L/3$ and $D = L/2$) and the heat transfer deviation is maximum for $D = L/3$ as observed from Fig. 4.10(a) and (b). The boundary layer growth due to heat transfer effect are varying in the horizontal direction, gradually propagates from the leading edge and begins to alter the flow configuration according to the time and position of the wall heat sources.

The change of average Nusselt number inside the enclosure for different combinations of heat source with the increase of Prandtl number values are shown in Fig. 4.11 for $Ha = 10$, $Gr = 10^5$ and $A = 0.4$. The rate of increase of heat transfer is very high in the range of $0.054 \leq Pr \leq 0.71$. It is also observed that in region (ii) active locations, the heat transfer rate is more than the other cases. The figure indicates a rapid increase of heat transfer up to $Pr = 1.0$ and then a smooth thermal rate increment in the cavity with an increase in Pr for both $D = L/3$ and $D = L/2$. This increment which is also a function of Re brings up the Nu_m up to 1.65 for $D = L/3$ (Fig. 4.11(a)) and 1.95 for $D = L/2$ (Fig. 4.11(b)).

Fig. 4.11(a) also represents the result of Sathiyamoorthy et al. ([195]), where they have considered the higher temperature along the whole left wall and lower values along the right wall. It is found that for low Pr, the effect is minimum but at higher Pr the difference is maximum. The Prandtl number influences more on the average Nusselt

number in the lower section of the hot wall for $D = L/3$ compared to $D = L/2$ than other parts but it reduces as move upwards (above middle portion). The variation of heat transfer rate for top middle active walls in case of $D = L/3$ is different from case of $D = L/2$, since the density of the isotherms are less and hence causes less movement of fluid. The improvement in Prandtl number causes the viscosity of the fluid in the porous cavity to augment and the fluid inclines to begin its movement from a lower place and nearer to the down side of the cavity. This concludes that, if the heat source length is increasing in the lower part of the cavity (bottom–middle: region (i)), the average heat transfer rate is decreasing as compared to upper heated part (top–middle: region (iii)).

The flow mechanisms and heat transfer characteristics are strongly influenced by the strength of the magnetic field in the core region of the cavity. The strong magnetic field generates a strong suppression of convective current inside the cavity. Influence of heat transfer due to the variation of magnetic field (Ha) and Darcy number (Da) is shown in Fig. 4.12 for fixed values of Grashof number at different locations of heat source. It is observed that the average Nusselt number decreases as Hartmann number increases for a fixed Darcy number $Da = 10^{-2}$. When the strength of the external magnetic field is changed, the same effect is observed in terms of Hartmann and side layers. That is, firstly the external magnetic field forces to separate the flow. Boundary layers now obey the rule that Hartmann layers are formed on the horizontal sides of the cavity, and side layers are on the top and bottom walls [181]. But as Grashof number increases, the rate of heat transfer also increases as shown in Fig. 4.12(b), which indicates that the variations of the average Nusselt number is significant due to the variation of Ha values. It is clearly observed from the figures 4.12(c) and (d) that the heat transfer characteristics inside the cavity are strongly affected by the presence of the porosity for fixed Ha. For figures 4.12(c) and (d) we have considered $Ha = 10,\ Gr = 10^4,\ 10^5$ and $10^{-3} \leq Da \leq 10^{-1}$. It is usually found that the porosity effects inhibit the fluid tendency to adjust to a steady state. This implies flow velocity decreases at which the porosity level decreases as well as the time required for steady state increases with the increase of magnetic field.

The overall effects upon the heat transfer rates are displayed for linearly heated vertical walls due to the variation of Da is shown in Fig. 4.13 for various values of Grashof numbers in different locations of heat source. We can observe that due to variation of

porosity, the velocity changes significantly. The variation of velocity strength causes high temperature difference. As Darcy number increases the heat transfer rate is increasing as observed from the figures 4.13(a, b, c) ([195]). It is interesting to note that the smoothly increasing trend breaks as we move towards higher Darcy's number with higher Grashof number due to the presence of strong secondary cells.

The bulk average temperature for different values of Grashof number is depicted in Fig. 4.14. It is found that bulk average temperature is lower for small Grashof number ($Gr = 10^2$), since the natural convection is dominated and bulk of the cavity remains at a lower temperature. For higher Grashof number, temperature distribution is more stratified when natural convection starts dominate. The flow profile remains almost constant up to $Gr = 10^4$ and then started increasing with the increment of Gr. Also,temperature gradient is higher in magnitude around this region as observed from the isothermal lines.

4.4 Conclusions

The flow and heat transfer in porous enclosure is encountered in industrial processes such as geothermal energy systems, and storage of nuclear waste. Inclusion of an external magnetic field and electrically conducting fluid in a porous media have also potential applications such as the fluid interaction in the geomagnetic field with the geothermal region, where the Earth's crust serves as a porous medium. Moreover, in metallurgical applications involving continuous casting, electromagnetic effect is used to obtain better mechanical properties of fine grained structure. Conducting fluids have additional properties for slowing down or accelerating the fluid motion through the external action of an electromagnetic field. Also, the external applied magnetic field determines the appearance of an induced magnetic field within the fluid [181].

A complete numerical study has been made to understand the combined heat and magnetic field effects in a fluid saturated porous square cavity in the presence of vertical time periodic temperature gradient. The following remarks can be concluded using the above study:

1. The flow is mostly dominated by the convection effects for fixed values of Gr and Ha. The buoyancy-induced activities are observed in the core region of the cavity,

fluids are well mixed and the temperature is well distributed in the bulk of cavity.

2. Under simultaneous thermal buoyancy forces along with the magnetic field effects, stably-stratified region becomes wider at the lower part of the cavity as the aspect ratio of the vertical temperature gradients gets increased.

3. Increase in Pr produces an increment in heat transfer for $Da < 1$.

4. It is observed that the average Nusselt number smoothly increases as the external Grashof number increases and average Nusselt number reduces as the strength of the applied magnetic field increases.

Figures

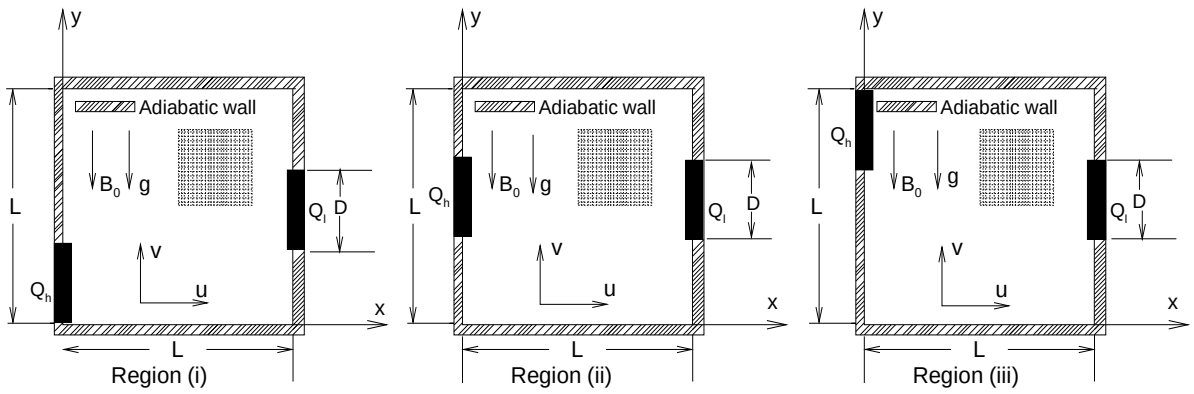

Figure 4.1: Flow configuration with three different hot and cold port locations

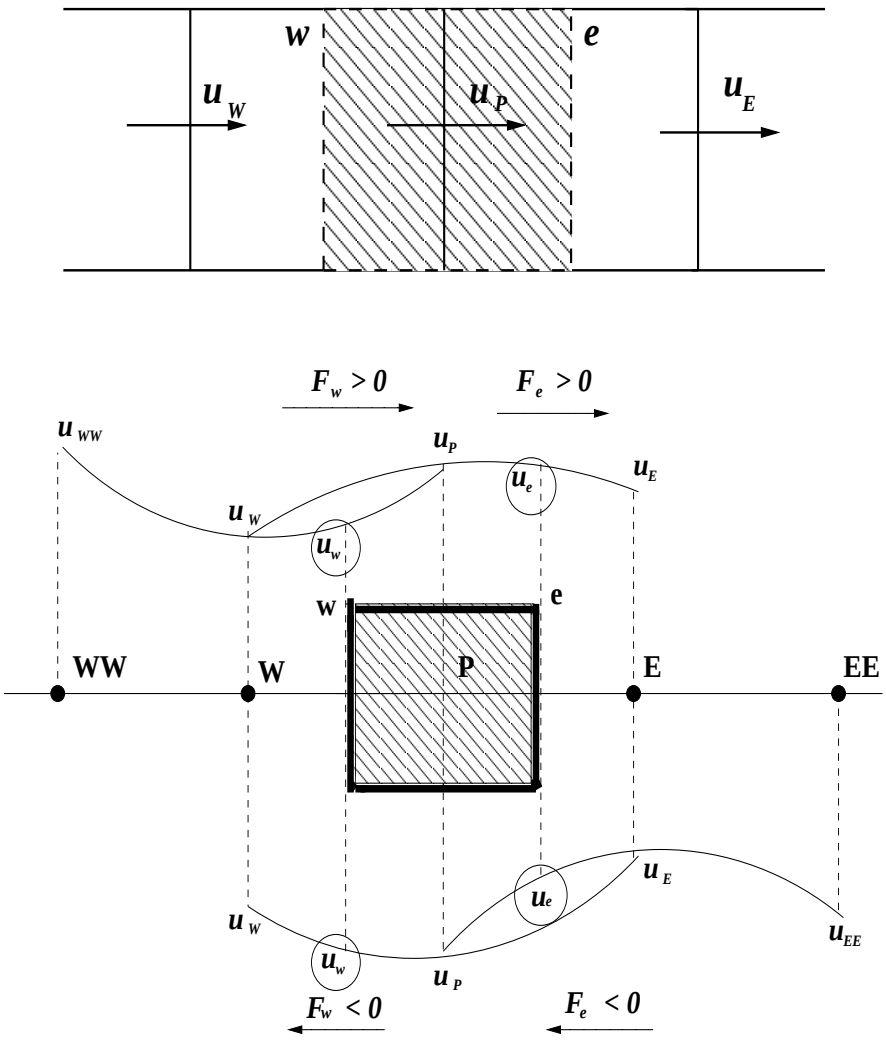

Figure 4.2: Schematic diagram of u control volume and quadratic upstream-based interpolation for u.

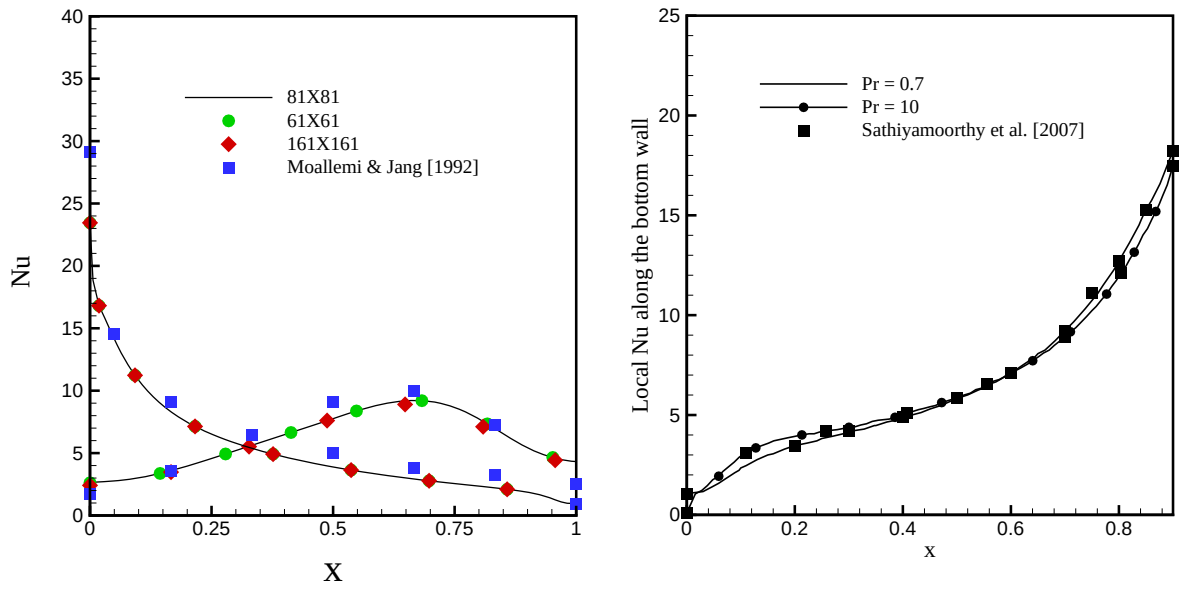

(a) (b)

Figure 4.3: (a) Influence of grid sizes on the average heat flux profile, at upper and lower lids with Moallemi and Jang [156] when $Pr = 1.0$, $B = 0.0$. Grashof number is 10^5, (b) Local heat flux comparison profiles for different Pr values with Sathiyamoorthy et al. [195].

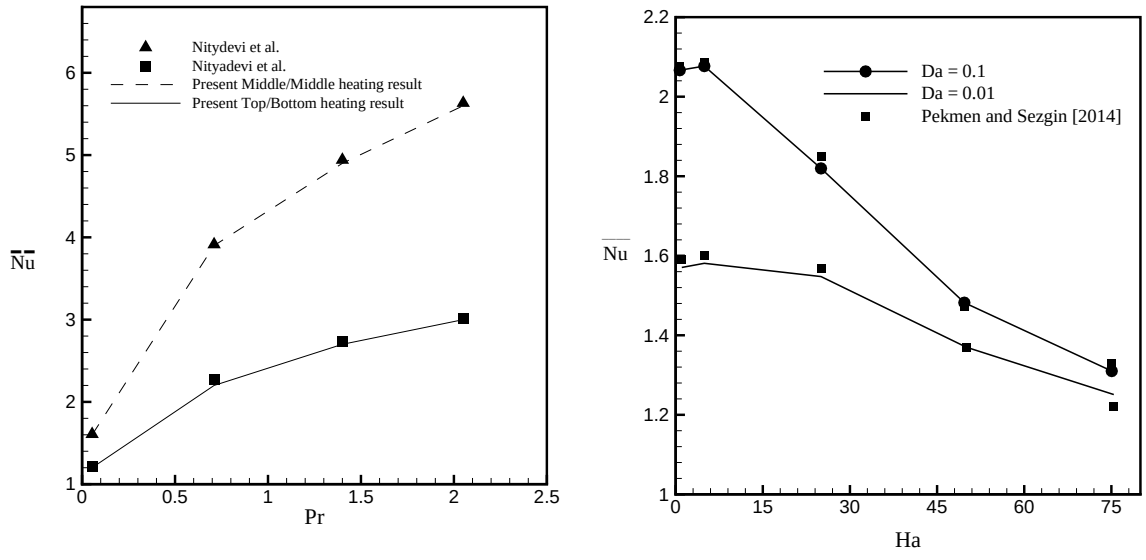

Figure 4.4: Comparison of present average Nusselt number (a) with Nityadevi et al. [172] (b) with Pekmen and Sezgin [181].

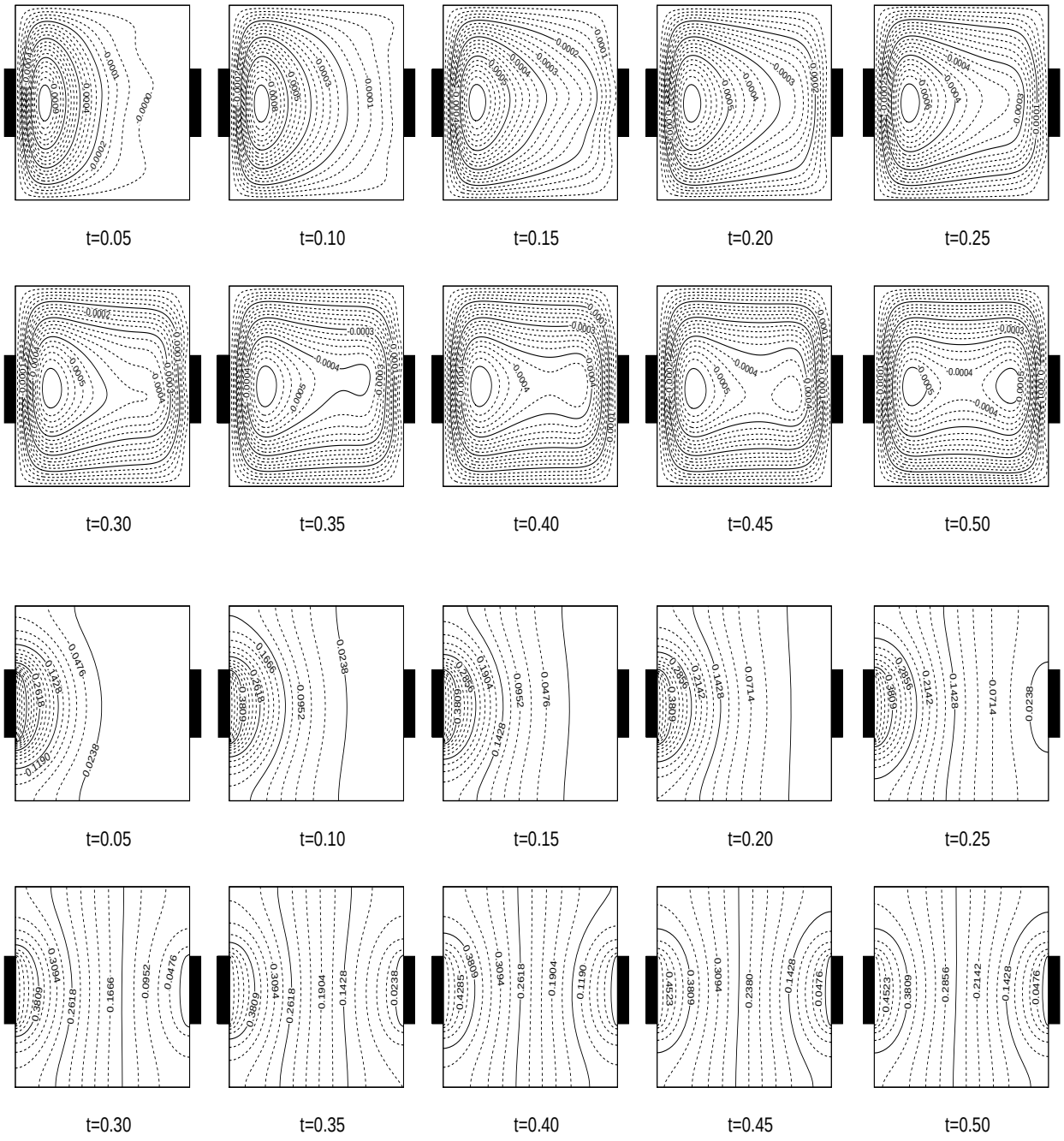

Figure 4.5: Time history contour plots of streamlines (upper) and isotherms (lower) for $Pr = 0.71$, $Ha = 10.0$, $\Omega = 3.0$, $Da = 10^{-2}$ with $\epsilon = 0.4$ of Region (ii) (Region (ii) active zones) for $Gr = 10^4$, when the heat source length is one third of the cavity height (i.e. $D = L/3$).

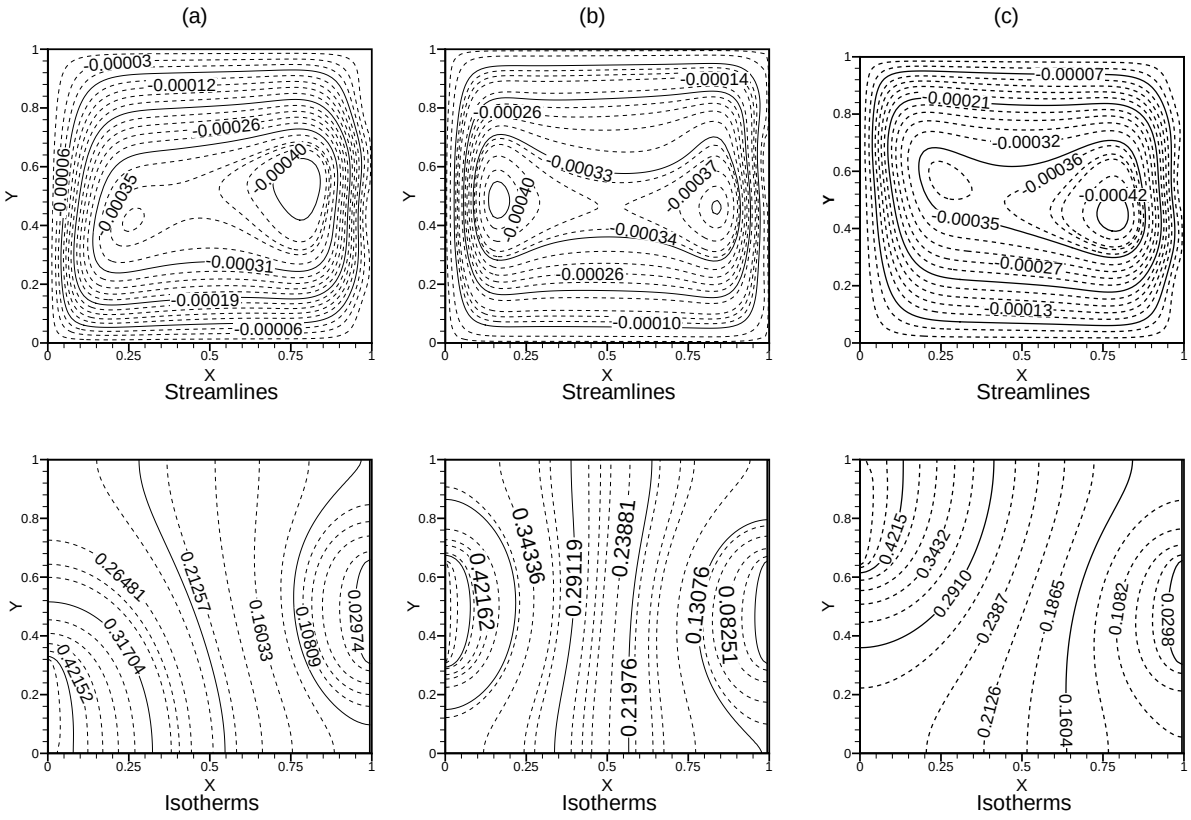

Figure 4.6: Contour plots of streamlines and temperature for $Pr = 0.71$, $Ha = 10.0$, $\Omega = 3.0$, $Da = 10^{-2}$ with $\epsilon = 0.4$ (a)Region (i), (b)Region (ii), (c)Region (iii), for $Gr = 10^4$, when the heat source length is one third of the cavity height (i.e., $D = L/3$).

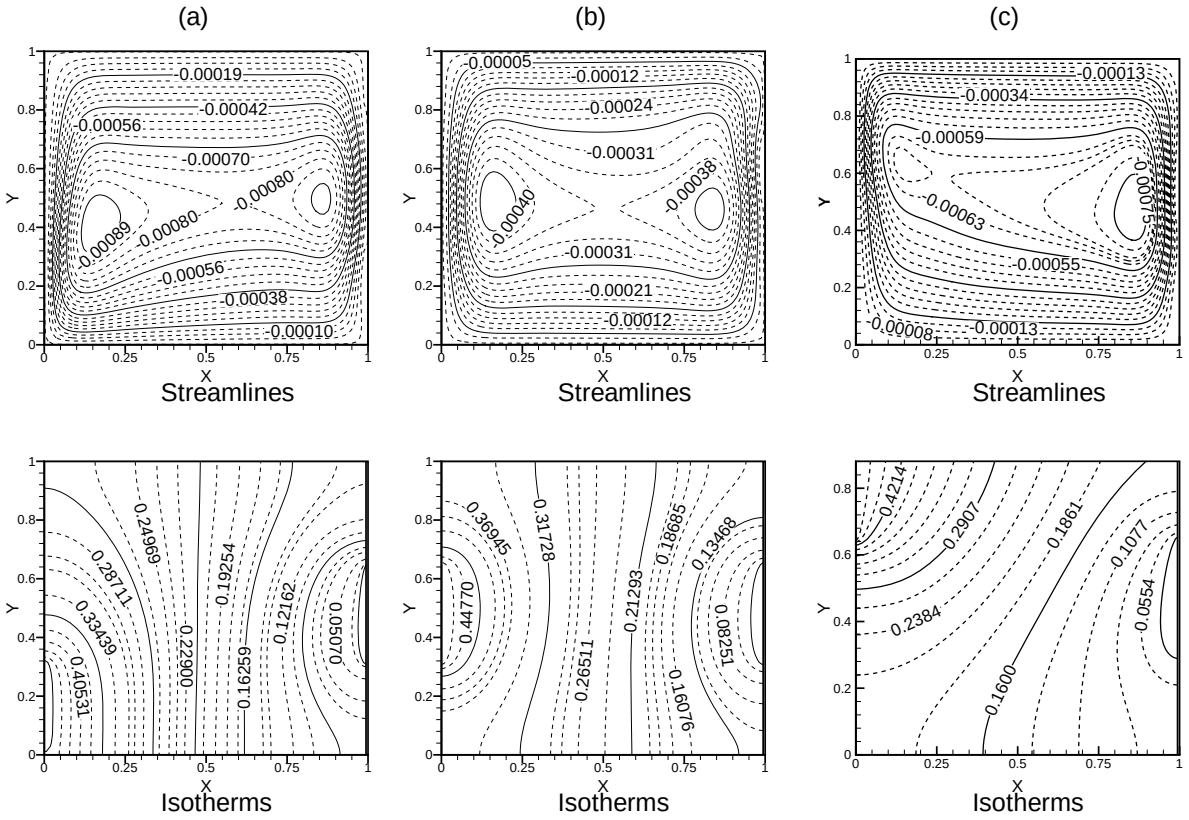

Figure 4.7: Contour plots of streamlines and temperature for $Pr = 0.71$, $Ha = 10.0$, $\Omega = 3.0$, $Da = 10^{-2}$ with $\epsilon = 0.4$ (a)Region (i), (b)Region (ii), (c)Region (iii), for $Gr = 10^5$, when the heat source length is one third of the cavity height (i.e. $D = L/3$) $Gr = 10^5$.

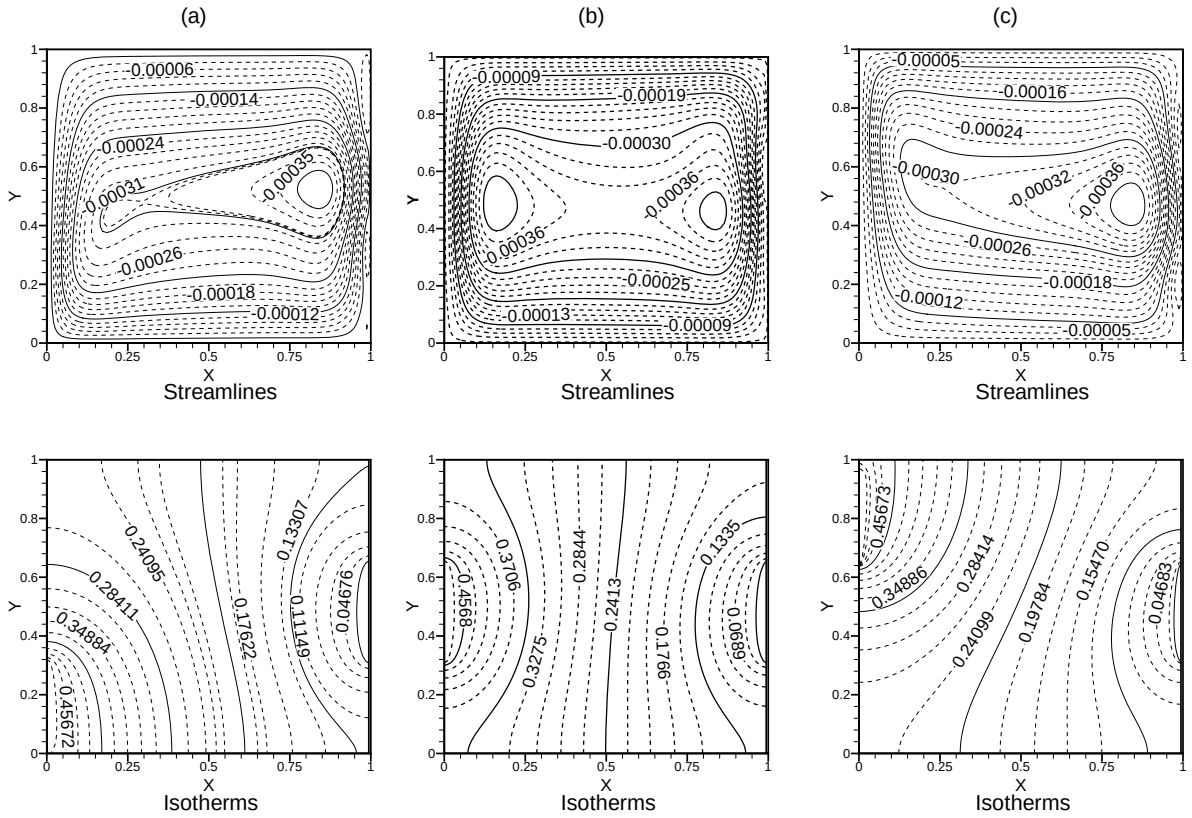

Figure 4.8: Contour plots of streamlines and temperature for $Pr = 0.71$, $Ha = 10.0$, $\Omega = 3.0$, $Da = 10^{-2}$ with $\epsilon = 0.4$ (a)Region (i), (b)Region (ii), (c)Region (iii), for $Gr = 10^6$, when the heat source length is one third of the cavity height (i.e., $D = L/3$).

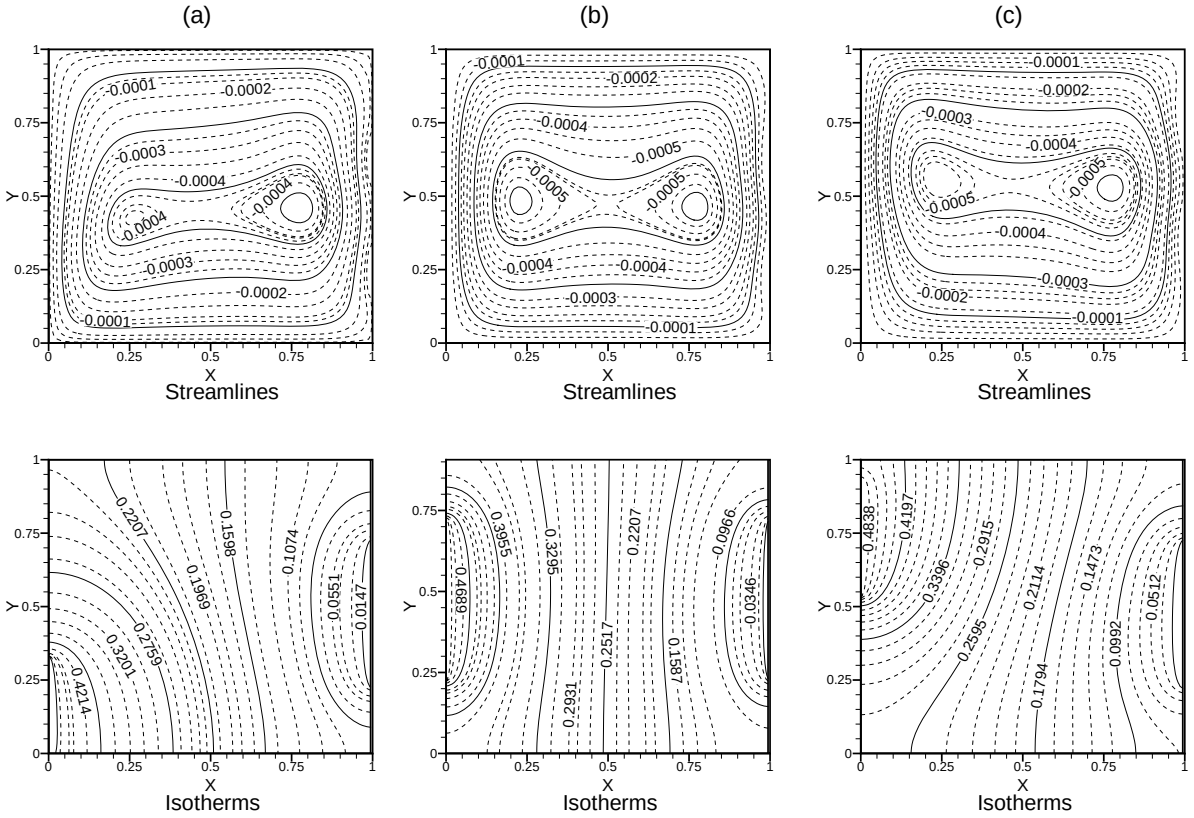

Figure 4.9: Contour plots of streamlines and temperature for $Pr = 0.71$, $Ha = 10.0$, $\Omega = 3.0$, $Da = 10^{-2}$ with $\epsilon = 0.4$, (a)Region (i), (b)Region (ii), (c)Region (iii), for $Gr = 10^4$, when the heat source length is half of the cavity height (i.e. $D = L/2$).

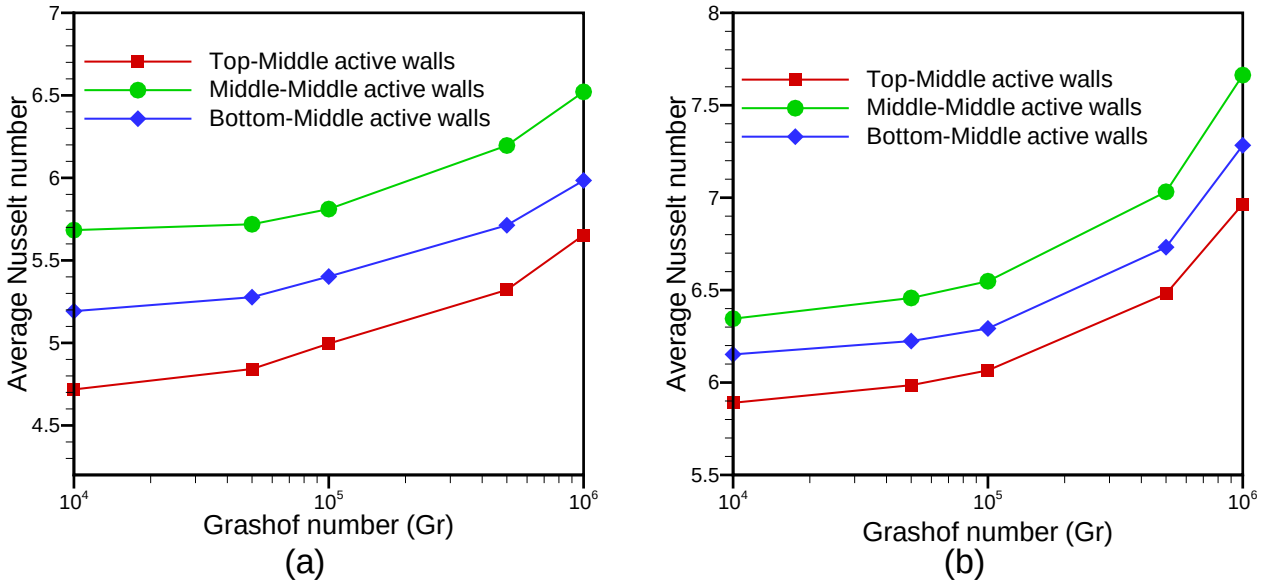

Figure 4.10: Average heat transfer due to the variation of Grashof number (a)$D = L/3$ (b)$D = L/2$ (heat source) when $Ha = 10.0$ and $Pr = 0.71$.

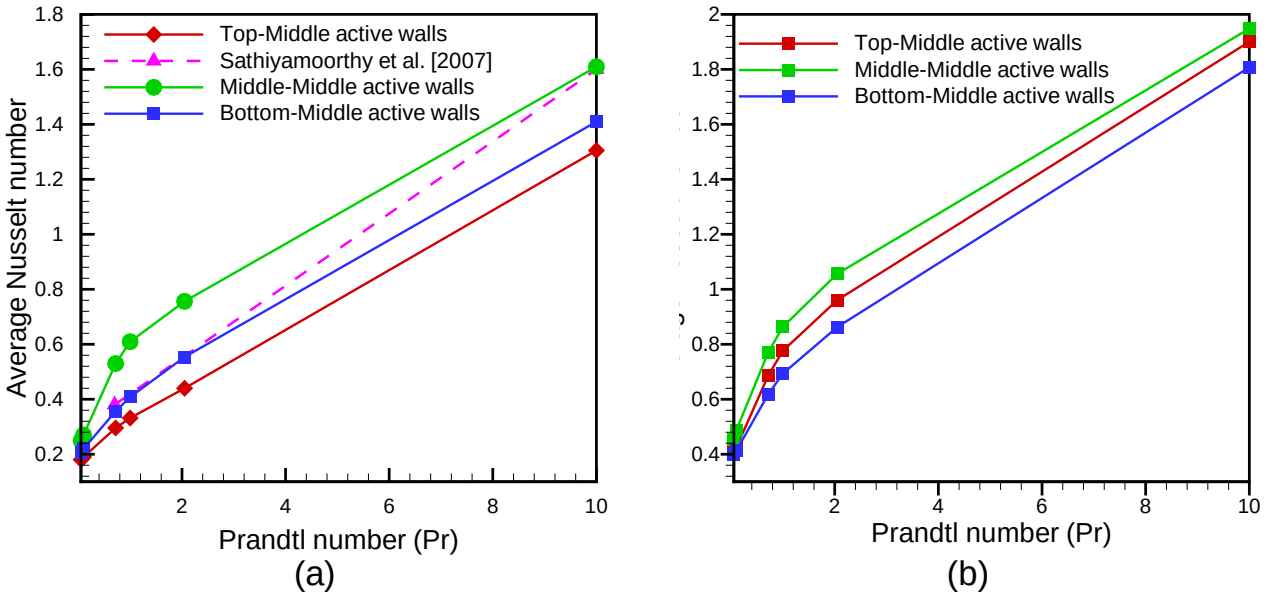

Figure 4.11: Average heat transfer due to the variation of Prandtl number, (a) $D = L/3$, (b) $D = L/2$ (heat source) when $Ha = 10$ and $Gr = 10^5$.

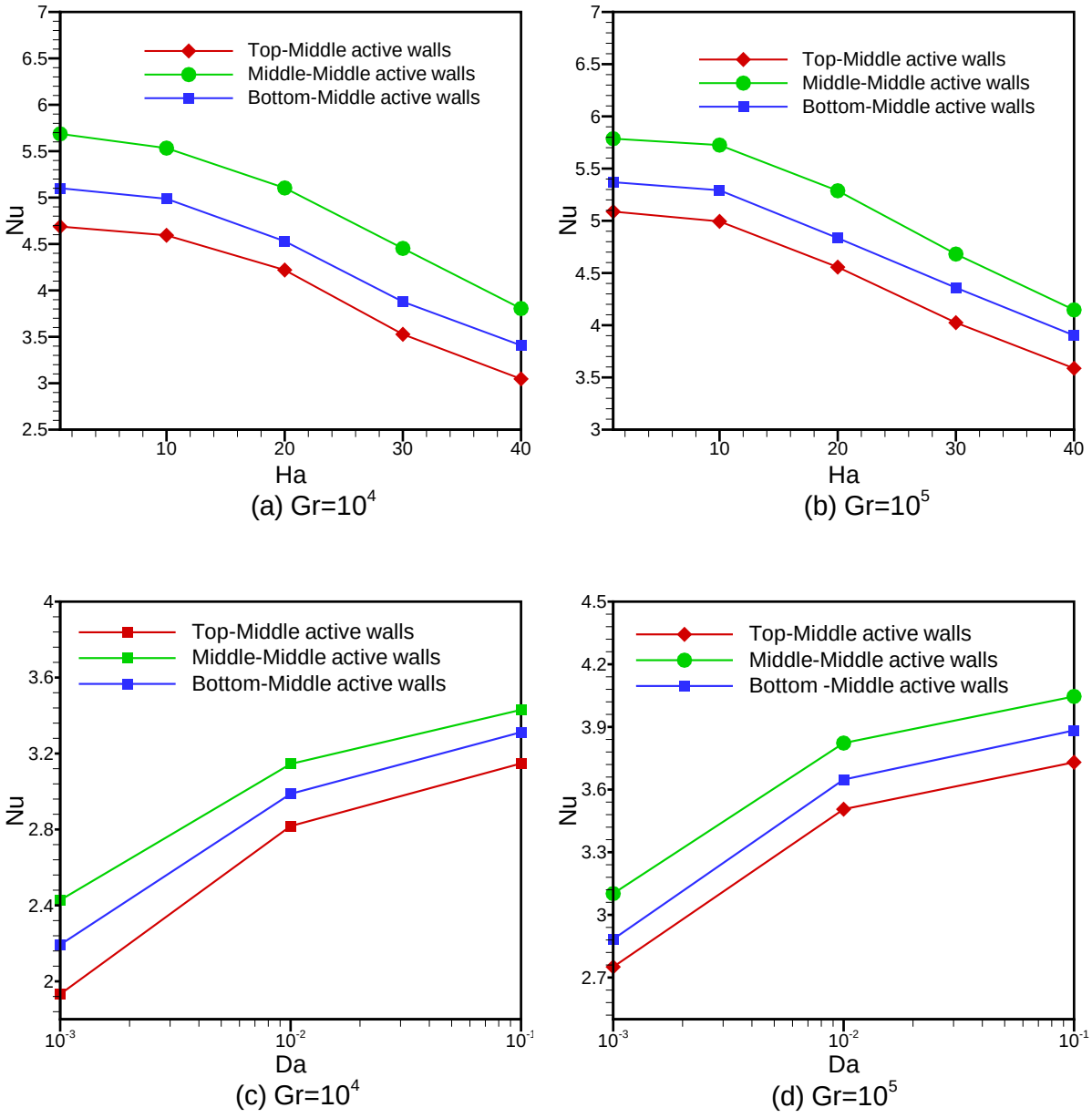

Figure 4.12: Effects of Hartman (a), (b) and Darcy's number (c), (d) on average heat transfer (Nu) from the middle plane when $Pr = 0.71$ and (a), (c) $Gr = 10^4$, (b), (d) $Gr = 10^5$.

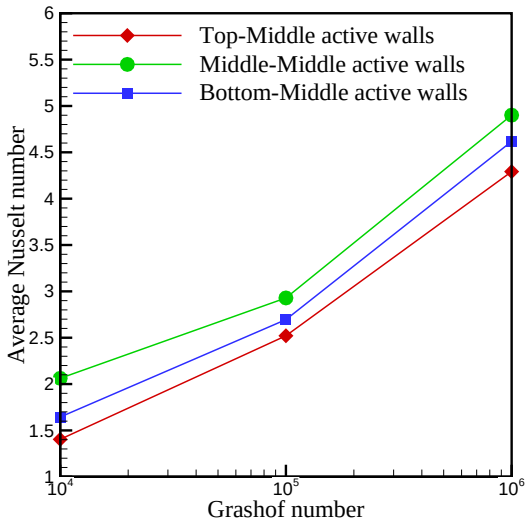

(a) Da=0.001

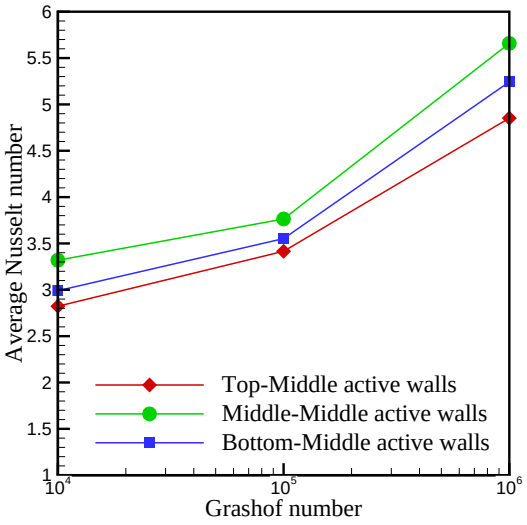

(b) Da=0.01

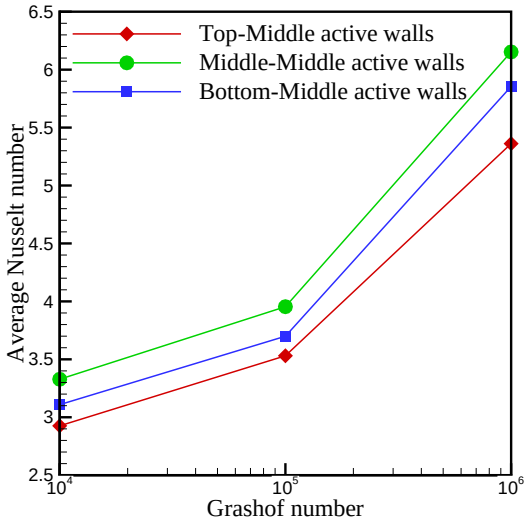

(c) Da=0.1

Figure 4.13: Effects of Darcy's number on average heat transfer (Nu) from the middle plane when $Pr = 0.71$, $Gr = 10^5$ and (a)$Pr = 0.001$, (b)$Pr = 0.01$, (c)$Pr = 0.1$.

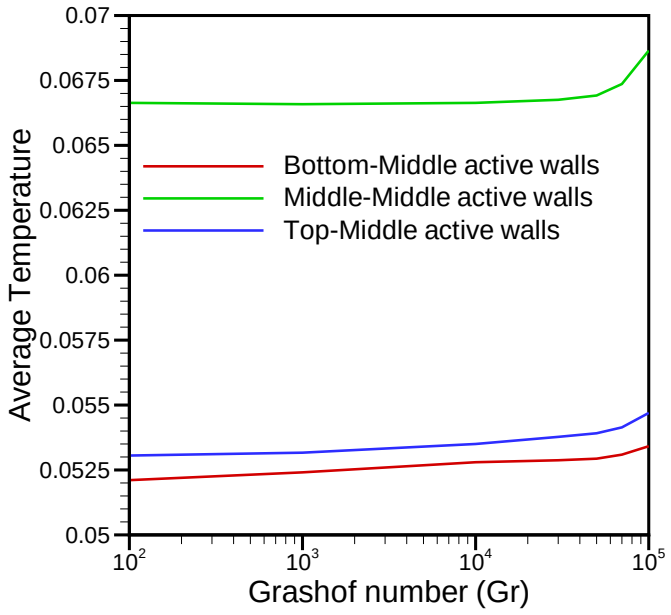

Figure 4.14: Bulk average temperature for different Gr values with heat source length $D = L/3$.

Chapter 5

Effect of Moving Walls on Heat Transfer and Entropy Generation in a Nanofluid Filled Enclosure [1]

5.1 Introduction

Mixed convection heat transfer inside the enclosures containing nanofluids has been studied extensively by several authors but very few studies have been conducted for the study of entropy generation inside the enclosure containing nanofluids. Many irreversible processes in a thermodynamical system leads to an increase in entropy which in turn results in degradation in the performance of thermodynamical system. For reversible processes the entropy generation is zero. In order to design an ideal system to achieve a better performance, a complete study of entropy generation minimization is required. In this chapter we have investigated the conditions under which a two-sided lid-driven nanofluid filled enclosure equipped with two discrete heat sources gives maximum heat transfer on the cost of minimum entropy generation.

In many industrial processes it is very essential to increase the heat transfer capability of the fluids. Conventional fluids such as water, ethylene glycol, oil etc. possess very low thermal conductivity which needs to be enhanced to optimize their heat transfer performance in various practical applications [104]. Heat transfer rates can be immensely enhanced by mixing dilute suspension of nano-sized particles (metallic or non-metallic) in the base fluid to form nanofluid. Various factors such as volume fraction, size, shape,

[1] The contents of this chapter has been published in *Journal of Engineering Mathematics, Springer, DOI:10.1007/s10665-017-9941-7*

thermophysical properties of base fluid and nanoparticles determine the heat transfer characteristics of the nanofluid [52].

The study of mixed convection heat transfer inside the enclosures are very frequently encountered in many industrial applications such as solar collectors, float glass production, drying technologies etc. [230]. These fields have received enormous attention from the researchers and hence substantial research efforts involving the experimental as well as numerical studies have been performed to obtain effective system performance through nanofluid. Fluid flow and heat transfer in square or rectangular cavities driven by shear and buoyancy effects have been studied extensively since it has large scale engineering applications in solar ponds, natural gas storage tanks, crystal manufacturing and solidification process [167].

A significant amount of efforts depending on empirical as well as theoretical observations is conducted to estimate the thermophysical properties of nanofluid and for application purposes it is crucial to correlate the numerical outcomes with empirical data. Maiga et al. [143] numerically analyzed the nanofluid flow in a uniformly heated tube and validated their results with the empirical data. They observed that increase of Reynolds number produces a higher heat transfer rate. The problem of differentially heated two-sided moving lid enclosure for clear fluid is first conducted by Oztop and Dagtekin [176] in which horizontal walls are considered as adiabatic. Three different directions of vertical wall movement were considered and it has been observed that the fluid flow and heat transfer properties are forced convection dominated when Richardson number is less than unity and are natural convection dominated when Richardson number is greater than unity. Same problem is extended by Tiwari and Das [230] for copper-water nanofluid and observed that heat transfer is more prominent when adjacent vertical walls move in opposite direction as compared to the same direction movement.

Rayleigh-Bénard convection refers to the convection in which the heat transfer takes place due to the rotation of fluids in closed convection cells [164]. Moumni et al. [159] studied the heat transfer effects of various water-based nanofluids in a two-sided lid-driven enclosure by placing discrete heat sources at different locations of the bottom wall of the enclosure. The Rayleigh-Bénard convection cells are found near the heat sources due to non-uniform temperature distribution from bottom part of the enclosure. Moreover, the

increment in Reynolds number, Richardson number and volume fraction of nanoparticles are found to be supporting factors for the heat transfer increment. The rate of heat transfer increment is found to be better in case of Cu-water and Ag-water nanofluids as compared to Al_2O_3-water and TiO_2-water nanofluids. Very complicated flow phenomena due to the movement of lids are represented by this type of fluid flow and heat transfer in spite of geometry being less complex. The flow variation involves forced convection as well as temperature differences resulting secondary buoyancy driven flow. A large number of such studies are conducted on the basis of first law of thermodynamics, however very few studies are available for nanofluid flow based on second law of thermodynamics.

According to K. Hooman [91], isotherms are not appropriate way to visualize the heat transfer in the field of convection. In fact, they have discussed the heat transfer visualization only in the conduction field as they are locally orthogonal to the true direction of energy flow. Hence, for better understanding of heat flow, one need to calculate the heatfunction. But, it is very difficult to solve the set of heatfunction equations when the boundary conditions or the geometry is complicated and also when closed form of the velocity distribution is not available. The only way to find the numerical solution is by using a numerical technique which may be computationally expensive. To overcome this difficulty, Hooman [91] introduced the concept of energy flux vectors which are locally tangent to the heatlines. Hence, the proper visualization of heat flow can be shown using energy flux vectors.

In a recent study, a numerical investigation of skewed enclosure filled with copper-water nanofluid with differentially heated side walls is made by Nayak et al. [169], considering the nanoparticle volume fraction variation upto 20% with variation of Richardson number. They concluded that increment in skew angle leads to a higher heat transfer rate. In extension of the earlier study, Nayak et al. [170] considered a lid-driven square enclosure to study the effect of heat transfer by increasing nanoparticle volume fraction with variation of Reynolds number and Richardson number and reported that addition of more nanoparticles decreases the buoyancy effects and the heat transfer rate is dominated by forced convection effect.

Buongiorno [40] considered various slip mechanisms, like thermophoresis, Brownian diffusion, inertia, fluid drainage, diffusiophoresis, magnus effect and gravity which are

responsible for relative velocity among base fluid and nanoparticles but thermophoresis and Brownian motion are considered as the most important factor for flow behavior inside the nanofluid [40, 140, 242, 243]. Recently, Garoosi et al. [74, 75] found that for the nanoparticle having high thermal conductivity like Cu the thermophoresis effects are negligible. In such cases, the single phase models are valid. In another recent study, Garoosi et al. [76] indicated that the particle distribution in nanofluids remains almost uniform for low Richardson number and the effect of drag, gravity and buoyancy forces have negligible effect on the distribution of nanoparticles.

Together with the heat transfer capability the performance of any mechanical system is dependent on the entropy generation inside the system. Entropy generation analysis is used to provide the information about the performance of thermodynamic system [48]. According to Anandalakshmi and Basak [12] the prediction of entropy generation during natural convection is helpful in improving the performance of system by minimizing the total entropy generation. In the present study two major factors are responsible for the entropy generation inside the enclosure namely; fluid friction irreversibility and heat transfer irreversibility. The prediction of entropy generation due to these factors enables to design the most energy efficient mechanical systems, which in turn improves the performance of mechanical systems.

Bejan [25] initially analyzed the idea of entropy and showed the heat transfer and fluid flow control through entropy generation. The entropy generation inside the cavities in different physical situations are studied by various authors [23, 98, 136, 235]. Recently, Khorasanizadeh et al. [123] analyzed the mixed convection and entropy generation in a differentially heated square enclosure. The results show that the use of nanofluid in place of pure fluid causes the increment in Nusselt number and increase in Reynolds and Rayleigh number increases the total entropy generation. The problem of heat transfer increment and entropy generation minimization is studied by many authors but the higher heat transfer rate on the cost of minimum entropy generation is still a challenge for the better performance of the mechanical systems.

In this chapter, a homogeneous model for the flow of nanofluid in a moving lid enclosure without the boundary layer assumption is considered. Based on the industrial

applications the higher heat transfer and entropy generation minimization plays a vital role in the improvement of system performance, which is the main objective in the proposed study.

The numerical investigation of mixed convection and entropy generation has been carried out in a two-sided lid-driven enclosure filled with copper-water nanofluid. Three different cases have been discussed depending on the direction of moving vertical walls to analyze the behavior of fluid flow and heat transfer in nanofluid. The buoyancy effects are incorporated with two discrete heat sources placed on the bottom wall maintaining a fixed distance from both side walls. Remaining sections of the bottom wall is kept insulated while other walls are maintained at constant low temperature. A two-dimensional computational visualization technique has been employed to demonstrate the main findings of the presented work. The effect of higher nanoparticle volume fraction (upto 20%) with variation of Reynolds number and Richardson number is studied to find the rate of heat transfer. The results are presented using streamlines, isotherms and energy flux vectors. The performance evaluation criteria of the system is analyzed through Nusselt number and entropy generation.

5.2 Problem formulation and governing equations

In this chapter we have considered a two-sided lid-driven square enclosure of length L, filled with Cu-water nanofluid. Two heat sources (T_h) of equal length (L/4) are attached along the lower wall and rest part of the wall is kept insulated all other walls are maintained with relatively lower temperature (T_c). A three-dimensional visualization of the physical domain is presented in Fig.5.1 . Three different flow domains are considered based on the movement of vertical walls as:

Case-I: left wall is sliding downwards and the right wall is sliding upwards,

Case-II: both vertical walls are sliding in downward direction and

Case-III: both vertical walls are sliding in upward direction.

A steady and laminar flow of Newtonian incompressible nanofluid is considered inside the enclosure in which the nanofluid is assumed to be in thermal equilibrium with no slip condition between two phases. The thermophysical properties except density are

assumed to be constant. The density variation due to temperature difference is based on Boussinesq approximation. Further, the nanoparticles are assumed to be spherical in shape with diameter 100nm. The thermophysical properties of copper and clear water at reference temperature are given in Table 5.1.

The unsteady two dimensional flow governing equations are expressed as,

$$\frac{\partial u^*}{\partial x^*} + \frac{\partial v^*}{\partial y^*} = 0,$$

$$\frac{\partial u^*}{\partial t^*} + \frac{\partial (u^* u^*)}{\partial x^*} + \frac{\partial (u^* v^*)}{\partial y^*} = \frac{-1}{\rho_{nf}} \frac{\partial p^*}{\partial x^*} + \frac{\mu_{nf}}{\rho_{nf}} \Big(\frac{\partial^2 u^*}{\partial {x^*}^2} + \frac{\partial^2 u^*}{\partial {y^*}^2} \Big),$$

$$\frac{\partial v^*}{\partial t^*} + \frac{\partial (u^* v^*)}{\partial x^*} + \frac{\partial (v^* v^*)}{\partial y^*} = \frac{-1}{\rho_{nf}} \frac{\partial p^*}{\partial y^*} + \frac{\mu_{nf}}{\rho_{nf}} \Big(\frac{\partial^2 v^*}{\partial {x^*}^2} + \frac{\partial^2 v^*}{\partial {y^*}^2} \Big) + \frac{(\rho\beta)_{nf}}{\rho_{nf}} g(T^* - T_c),$$

$$\frac{\partial T^*}{\partial t^*} + \frac{\partial (u^* T^*)}{\partial x^*} + \frac{\partial (v^* T^*)}{\partial y^*} = \alpha_{nf} \Big(\frac{\partial^2 T^*}{\partial {x^*}^2} + \frac{\partial^2 T^*}{\partial {y^*}^2} \Big)$$

where, $\alpha_{nf} = k_{nf}/(\rho C_p)_{nf}$ is the thermal diffusivity , $\rho_{nf} = (1-\phi)\rho_f + \phi\rho_s$ is the effective density of nanofluid at reference temperature, $(\rho C_p)_{nf} = (1-\phi)(\rho C_p)_f + \phi(\rho C_p)_s$ is the heat capacitance of nanofluid and $(\rho\beta)_{nf} = (1-\phi)(\rho\beta)_f + \phi(\rho\beta)_s$ is the thermal expansion coefficient. For two-component entity of spherical-particle suspension, the Maxwell model [153] is given by,

$$\frac{k_{nf}}{k_f} = \frac{k_s + 2k_f - 2\phi(k_f - k_s)}{k_s + 2k_f + \phi(k_f - k_s)}$$

and the effective viscosity of nanofluid proposed by Brinkmann [39] as $\mu_{nf} = \mu_f/(1-\phi)^{2.5}$.

For better understanding of convective heat transfer the equations of heatfunction (h^*) are given by [91],

$$\frac{\partial h^*}{\partial y^*} = (\rho C_p)_{nf} u^* (T^* - T_c) - k_{nf} \frac{\partial T^*}{\partial x^*}, \tag{5.1}$$

$$\frac{\partial h^*}{\partial x^*} = -(\rho C_p)_{nf} v^* (T^* - T_c) - k_{nf} \frac{\partial T^*}{\partial y^*}. \tag{5.2}$$

The dimensionless form of the above mentioned equations is obtained by adopting the following non-dimensional variables,

$$(x, y) = \frac{(x^*, y^*)}{L};\ (u, v) = \frac{(u^*, v^*)}{U_0};\ T = \frac{T^* - T_c}{T_h - T_c};\ h = \frac{h^*}{k_f(T_h - T_c)};$$

$$t = \frac{t^* U_0}{L}; p = \frac{p^*}{\rho_{nf} U_0^2};\ Re = \frac{U_0 L}{\nu_f};\ Pr = \frac{\nu_f}{\alpha_f};\ Ri = \frac{g\beta L(T_h - T_c)}{U_0^2};$$

Using these variables, the flow governing equations in dimensionless form are given by,

$$\frac{\partial u}{\partial x}+\frac{\partial v}{\partial y}=0, \tag{5.3}$$

$$\frac{\partial u}{\partial t}+\frac{\partial (uu)}{\partial x}+\frac{\partial (vu)}{\partial y}=\frac{-\partial p}{\partial x}+\Gamma\left(\frac{\partial^2 u}{\partial x^2}+\frac{\partial^2 u}{\partial y^2}\right), \tag{5.4}$$

$$\frac{\partial v}{\partial t}+\frac{\partial (uv)}{\partial x}+\frac{\partial (vv)}{\partial y}=\frac{-\partial p}{\partial y}+\Gamma\left(\frac{\partial^2 v}{\partial x^2}+\frac{\partial^2 v}{\partial y^2}\right)+\gamma T, \tag{5.5}$$

$$\frac{\partial T}{\partial t}+\frac{\partial (uT)}{\partial x}+\frac{\partial (vT)}{\partial y}=\Lambda\left(\frac{\partial^2 T}{\partial x^2}+\frac{\partial^2 T}{\partial y^2}\right) \tag{5.6}$$

where,

$$\Gamma=\frac{\rho_f}{Re\rho_{nf}}\frac{1}{(1-\phi)^{2.5}},\ \ \gamma=\frac{\rho_f}{\rho_{nf}}Ri\left(1-\phi+\phi\frac{\rho_s\beta_s}{\rho_f\beta_f}\right)\ \text{ and }\ \Lambda=\frac{1}{RePr}\frac{k_{nf}}{k_f}\frac{(\rho C_p)_f}{(\rho C_p)_{nf}}.$$

The relevant boundary conditions in the computational domain are given by,

$$\begin{aligned}
&u=0, v=v_l,\ T=0 \quad \text{if } x=0,\ y\in[0,1];\\
&u=0, v=v_r,\ T=0 \quad \text{if } x=1,\ y\in[0,1];\\
&u=0, v=0, T=T_b \quad \text{if } x\in[0,1],\ y=0;\\
&u=0, v=0,\ T=0 \quad \text{if } x\in[0,1],\ y=1.
\end{aligned} \tag{5.7}$$

where, $T_b=\begin{cases} T=1 & \text{if } x\in(1/8,3/8]\cup(5/8,7/8]\\ \frac{\partial T}{\partial y}=0 & \text{elsewhere}\end{cases}$

The flow velocities along the vertical walls are considered as,

$$\begin{aligned}
&\text{Case-I: } v_l=-1,\ v_r=1,\\
&\text{Case-II: } v_l=-1,\ v_r=-1,\\
&\text{Case-III: } v_l=1,\ v_r=1.
\end{aligned}$$

The average heat transfer enhancement is computed in the form of Nu (Nusselt number) and Nu_m (average Nusselt number) along the heated surfaces as,

$$Nu(X)=-\frac{k_{nf}}{k_f}\left(\frac{\partial T}{\partial x}\right)_{hot\ wall}, \tag{5.8}$$

$$Nu_{m_i}=\frac{\int_{hot\ wall} Nu(X)dX}{\int_{hot\ wall} dX} \tag{5.9}$$

and

$$Nu_m = \frac{Nu_{m_1} + Nu_{m_2}}{2} \tag{5.10}$$

where, the suffixes m_1 and m_2 represents the hot portions of lower wall. The non-dimensional representation of heatfunction equations given in eq. (5.1) and (5.2) can be written as,

$$\frac{\partial h}{\partial y} = RePr\frac{(\rho C_p)_{nf}}{(\rho C_p)_f}uT - \frac{k_{nf}}{k_f}\frac{\partial T}{\partial x}, \tag{5.11}$$

$$\frac{\partial h}{\partial x} = -RePr\frac{(\rho C_p)_{nf}}{(\rho C_p)_f}vT + \frac{k_{nf}}{k_f}\frac{\partial T}{\partial y} \tag{5.12}$$

where, h represents the non-dimensional form of heatfunction. But, it is very difficult to find the expression of heatfunction from the above relation, hence the proper visualization of heat flow can be found out by using energy flux vectors as,

$$E = \frac{\partial h}{\partial y}\hat{i} - \frac{\partial h}{\partial x}\hat{j} \tag{5.13}$$

The non-dimensional local entropy generation for heat and fluid flow in two-dimensional cartesian co-ordinates are,

$$S_h = \left(\frac{k_{nf}}{k_f}\right)\left[\left(\frac{\partial T}{\partial x}\right)^2 + \left(\frac{\partial T}{\partial y}\right)^2\right], \tag{5.14}$$

$$S_f = \chi\left(\frac{\mu_{nf}}{\mu_f}\right)\left[2\left(\left(\frac{\partial u}{\partial x}\right)^2 + \left(\frac{\partial v}{\partial y}\right)^2\right) + \left(\frac{\partial u}{\partial y} + \frac{\partial v}{\partial x}\right)^2\right] \tag{5.15}$$

and

$$S_{gen} = S_h + S_f. \tag{5.16}$$

S_h and S_f are the local entropy generation due to heat transfer and fluid friction irreversibility. In eq. (5.15), χ denotes the irreversibility distribution ratio. For the present study χ is considered as 10^{-4} [170]. The average entropy generation (S_m) is given by,

$$S_m = \frac{1}{V}\int_V S_{gen}dV \tag{5.17}$$

where, V denotes the volume of enclosure. The dominance effect of entropy generation due to heat transfer irreversibility over fluid friction irreversibility is given by Bejan number (Be) is,

$$Be = \frac{S_h}{S_{gen}} \tag{5.18}$$

and the average Bejan number (Be_m) is given by,

$$Be_m = \frac{1}{V}\int_V Be dV. \tag{5.19}$$

$Be_m > 0.5$ implies dominance of S_h, $Be_m < 0.5$ implies dominance of S_f and $Be = 0.5$ shows the equal contribution of S_h and S_f to the entropy generation [12].

5.3 Numerical procedure and code validation

The set of flow governing equations along with its boundary conditions are solved through the finite volume method based algorithm which satisfy the conservation of mass, momentum, energy and flux continuity in a coupled form. Discretization of these equations is made in staggered grid approach over each control volume and the convective terms are discretized by employing the QUICK scheme [30]. A first order implicit approach is adopted for time derivative. A pressure correction based approach, SIMPLE, is adopted for the solution of discretized flow governing equations. The resulting algebraic equations are solved iteratively by tridiagonal matrix algorithm.

At each time step, the nonlinear terms are approximated as

$$\left(u\frac{\partial u}{\partial x}\right)^{n+1} = u^n\left(\frac{\partial u}{\partial x}\right)^{n+1},$$

with $n \geq 0$, where n is the iteration index. The discretization of non-linear flow governing equations is made in the similar fashion as discussed in section 2.3 (eq. 2.16 to 2.19). The successive over relaxation (SOR) method is employed for the solution of resulting equations. The convergence criterion used for the calculation of velocities, temperature and pressure correction is given by,

$$\varepsilon = \left|\epsilon_{i,j}^{n+1} - \epsilon_{i,j}^{n}\right| \leq 10^{-5}$$

where, ε is the error of tolerance in a particular time step and ϵ represents the flow variables.

On advancing the flow field variables, a transient solution is achieved through a sequence of small time levels of discretization $\delta t = 0.001$. No significant differences in the results are observed on further decrement in δt. At the initial time level, the fluid is

considered to be static and after a transient phase, a steady solution is obtained for the prescribed parametric values.

The test for grid independent solution is performed by comparing the outcome of vertical velocity profile using grid size 61×61, 81×81, and 121×121 with Muthtamilselvan et al. [162] and represented in Fig. 5.2(a). Muthtamilselvan et al. [162] studied the mixed convection effect of a lid-driven enclosure filled with a Cu-water nanofluid in which the upper wall, maintained with higher temperature and is moving with a constant velocity. A comparatively lower temperature is maintained along the bottom wall and all other walls are kept adiabatic. The result due to Muthtamilselvan et al. [162] for $Ri = 1,\ Ra = 100$ and $\phi = 2\%$ found a good agreement with our results for 81×81 grid size. Hence, 81×81 is found to be optimum grid size and is chosen for all of our computations.

Another validation of numerical simulation is conducted for average Nusselt number comparison with the results due to Moumni et al. [159]. The work of Moumni et al. [159] is based on the study of mixed convective flow of a Cu-water nanofluid in a two-sided lid driven square enclosure. Two discrete heat sources are placed along the bottom wall and rest part of the bottom wall is kept insulated and all other walls are kept at a lower temperature. Fig. 5.2(b) shows the comparison of average Nusselt number for the present solution with different volume fraction of nanoparticles at $Ri = 10,\ Re = 100$ and $\phi = 0.2$. It is found that maximum average Nusselt number differs by 0.7% from the result due to Moumni et al. [159].

5.4 Results and discussion

Mixed convective flow and entropy generation in a two-sided lid driven enclosure filled with Cu-water nanofluid are studied for the heat transfer effect. Two discrete heat sources of length $L/4$ are placed along the bottom wall at a distance of $L/8$ and $7L/8$ from the left wall, respectively. The flow governing parameters are Richardson number, Rayleigh number and nanoparticle volume fraction which varies in the ranges of $0.1 \leq Ri \leq 10,\ 1 \leq Re \leq 100,\ 0 \leq \phi \leq 0.2$. Three different configurations are chosen based on the direction of moving lids. In the plots of streamlines and isotherms, dashed lines represent the flow lines for clear fluid whereas the solid lines show the flow lines for nanofluid.

Although, many researchers [159, 162, 176, 196, 230] worked on similar geometry with clear fluid as well as nanofluid but they restricted their studies only for obtaining the higher heat transfer rate. In order to improve the performance of any mechanical system the total energy loss within the system is also needs to be minimized. Moreover, whenever the heat transfer in the system increases, the entropy of the system also increases, hence it is not always a good move to stuck only with heat transfer increment of the system. A proper balance between heat transfer and entropy generation can improve the overall performance of the system. The present work focuses on improving the performance of the mechanical system by obtaining the higher heat transfer rate on the cost of least entropy generation.

5.4.1 Streamlines and isotherms

Figs. 5.3 to 5.6 represents the streamlines and isotherms of case-I to case-III respectively for $0.1 \leq \text{Ri} \leq 10$ at Re=100 with $\phi = 0.0$ (clear fluid, dashed lines) and $\phi = 0.2$ (nanofluid, solid lines). Increasing Richardson number for fixed Reynolds number and Prandtl number leads to an increase in convective heat transfer in all the cases. The temperature difference near the bottom heated portion increases with increasing Richardson number. The temperature profiles in Figs. 5.3 to 5.6 show that heat plums developed above each heat source. Buoyancy forces drive the heated fluid towards the upper cold surface from the heat source and upper cold fluid move downwards. The temperature along the cold fluid region again increases due to the heat source and the fluid move upwards which repeats the flow pattern. The closest layer of fluid makes a stable recirculation zone centered along the edges of heat sources. In all the cases, the pattern of isotherms corresponding to clear fluid is much different than that of nanofluid and this difference is clearly visible at the core of the enclosure.

In case-I (Fig. 5.3(a, c, e)), the right wall is sliding in upward direction and left wall is sliding in downward direction resulting the fluid flow in anticlockwise direction. Increase in nanoparticle volume fraction increases the viscosity in the fluid and the effect can be clearly seen in the core of the cavity where the streamlines due to clear fluid overlaps the streamlines due to nanofluid. The streamlines in the core of the enclosure for the clear

fluid appear to be oval-shaped, whereas, for the nanofluid, they appear to be circular-shaped due to larger viscous forces. However, as the Richardson number increases, the streamlines of nanofluid at the innermost region overlap the streamlines of the clear fluid. The effect of forced convection due to the sliding walls can be clearly observed from the isotherms presented in Fig. 5.3(b, d, f). As soon as the cold fluid comes near the hot wall, it gets heated and starts to move in the upward direction. Due to the combined effect of forced convection and buoyancy, the heated fluid move upwards along the right wall. The isotherms corresponding to the clear fluid are mostly found near the walls of cavity whereas they are well distributed throughout the cavity in case of nanofluid.

The effect of nanoparticle volume fraction increment on streamlines and isotherms is observed more clearly in Fig. 5.4(a, b) for case-I at $Re = 100$ with $Ri = 10$. The dashed lines represents the clear fluid($\phi = 0.0$) case whereas the solid lines represent the flow lines for nanofluid($\phi = 0.2$) case. The streamlines and isotherms are plotted at the horizontal mid-section (y=0.5) of enclosure with respect to x-axis. The effect of increased nanoparticle volume fraction on the streamlines is clearly visible when x values are between 0.2 to 0.8. Similarly, the effect of increased nanoparticle volume fraction on the isotherms can be observed for x values between 0.1 to 0.9.

For case-II, both vertical walls are moving in the downward direction, and, as a result, the shear force acts downwards and opposes the buoyancy force. The streamlines presented in Fig. 5.5(a, c, e) show the development of Rayleigh-Bénard convection cells above each heat source. The fluid on the left portion of the enclosure moves in anticlockwise direction whereas on the right moves in clockwise direction. Due to the downward movement of both vertical walls and the bottom heat sources, the eddies become oval-shaped for higher Richardson number. The plots of the isotherms in Fig. 5.5(b, d, f) show that the lids drag the cold fluid towards the hot surface of the lower wall which leads to a sharp paraboloid profile. This signifies that the hot fluid passes towards vertical mid-section of the center and upper cold region of the enclosure, where shear force effect is minimum.

For case-III, both walls slide in the upward direction, and buoyancy is supported by shear and the streamlines are presented in Fig. 5.6(a, c, e). The fluid starts moving in the upward direction due to shear effect and with increment of Richardson number,

the eddies move in the upward direction. The eddies corresponding to the clear fluid are positioned at lower heights as compared to the eddies corresponding to the nanofluid, which clearly shows that the nanofluid gets heated quickly and moves in upward direction with a velocity greater than that of the clear fluid. The isotherms in Fig. 5.6(b, d, f) are clustered near the moving wall, forming vortices along the upper section of the enclosure. The density of the cold fluid decreases as it gets heated from the bottom, and tries to move upwards along vertical walls because of the forced convection effect. The hot fluid enters the upper part of the cavity and the cold fluid deviates downwards from the middle portion of the cavity.

5.4.2 Energy Flux Vectors

Fig. 5.7 shows the energy flux vectors which are tangent to heatlines at $Ri = 10$ and $Re = 100$ for clear fluid ($\phi = 0.0$, Fig. 5.7(a, c, e)) and nanofluid ($\phi = 0.2$, Fig. 5.7(b, d, f)) for all the three cases. The total energy passing through unit area per unit time is represented by the magnitude of the energy flux vector. The energy flux vectors originate from the bottom heated portion and moves in the enclosure due to the shear effect caused by vertical wall movement. Similar patterns are followed by the energy flux vectors as that of streamlines ensuring high thermal mixing because of dominating convection effect in this region.

For case-I, the energy flux vectors originating from the left hot portion follow longer paths than those originating from the right portion, as shown in Fig. 5.7(a, b), which results from the combined effect of bottom heating and forced convection. The energy transfer from the left heated portion starts due the downward moving left wall and the bottom heated portion. The upward movement of the right wall supports energy flow in the upward direction. The energy flux vectors become weaker as they move from right upper portion to the left of the enclosure, which signifies that the convective heat transfer is getting lower in the upper right portion of the cavity. Over all, the convective heat transfer is found to be higher in the lower half portion of the enclosure and becomes weaker in the upper half of the enclosure.

In Fig. 5.7(c, d), the dominating effect of forced convection can be clearly seen as the energy transfer is completely determined by the movement of downward moving walls.

The fluid near the vertical walls move in the downward direction due to the shear effect and passes through the hot bottom portions. The energy flux vectors generated from the heated portions of the bottom wall and move towards the center of enclosure. As a result, Rayleigh-Bénard convection cells are formed. The convective heat transfer occurs near the bottom heated portions and reaches the upper portion of enclosure through the center. Finally, the heated fluid in the upper section of the cavity moves in both sides of the cavity and get in touch with the side walls due to the downward movement of the walls.

In case-III (Fig. 5.7(e, f)), both the vertical walls are moving in upward direction, the shear force favors the buoyancy effects. Hence, the maximum energy transfer from bottom to top is analyzed via side walls. The energy flux vectors originates from the bottom portion and travels in upward direction through the side walls and gets weaker as they move in upward direction due to which a comparatively lesser amount of convective heat transfer is found.

Finally, most of the energy flow inside the enclosure is found to be highly influenced by the direction of moving walls. From the Figs. 5.7(a to f) it is evident that the convective heat transfer is found to be highest in case-II as the energy flux vectors are more stronger in this case. In all three cases, energy is input from the bottom heat sources and is distributed in different directions due to the forced convection effect of moving walls. In case-I and III, the flow of energy occurs mostly around the sidewalls whereas in case-II the energy flow takes place in the middle section. In case-II, energy passes through the mid-section of the enclosure and directly influences the top portion of the enclosure, whereas in case-III, the energy distribution is higher along the sidewalls and as a result the sidewalls are mostly affected by flow of energy than the heat of top wall.

5.4.3 Nusselt number

The average Nusselt number (Nu_m) in each case is computed with the variation of Richardson numbers and the outcomes are presented in Fig. 5.8 to Fig. 5.10 using eq. (5.10). It is observed in Fig. 5.8 that heat transfer efficiency increases with ϕ. A sharp variation in Nu_m is observed when Re is increased from 1 to 50 and 50 to 100. It can be seen that Nu_m at $Re = 50$ is higher when ϕ is increased from 0.1 to 0.2 compared

to $Re = 100$ with $\phi = 0.0$. This implies that ϕ is one of the important factors for fluid flow, and heat transfer and is capable of changing the flow features. Fig. 5.9 and Fig. 5.10 shows the average Nusselt number for case-II and case-III respectively, which increases with Ri and ϕ. For each case, it is found that Nu_m is almost constant for $Re = 1$ with variation of Ri and ϕ. In case-II (Fig. 5.9), Nu_m is increasing with ϕ and Ri and the increment is not linear in case of $Re = 50$ and $Re = 100$.

From the above observations, it can be concluded that average Nusselt number along the cavity surface is maximum in case-I as compared to other cases for all Ri and ϕ values. Increment in volume fraction of nanoparticles increases the heat transfer rate in nanofluid very efficiently. In case-I, increment in heat transfer rate is found to be 47.73% with $Ri = 0.1$ and 40.65% with $Ri = 10$ for $Re = 100$ in Cu-water nanofluid, where the nanoparticle volume fraction is changing from 0.0% to 20%. Similarly, in case-II, the variation is found to be 49.82% for $Ri = 0.1$ and 39.12% for $Ri = 10$ and in case-III, it is found to be 44.07% and 30.39% for $Ri = 0.1$ and 10 respectively. The maximum value of average Nusselt number in case-I to III are found to be 7.7599, 6.9914 and 6.1112 respectively at $Ri = 10$, $Re = 100$ and $\phi = 0.2$. According to the analysis of average Nusselt number, the maximum heat transfer is found in case-I as the average Nusselt number values corresponding to all parameters are higher as compared to the other cases. The minimum heat transfer rate is observed in case-III corresponding to all parameters.

5.4.4 Entropy generation and Bejan number

Fig.5.11 and 5.12 depicts the local entropy generation due to fluid friction and heat transfer irreversibility for each case at $Re = 100$, $Ri = 10$ with $\phi = 0.0$ (dashed lines) and 0.2 (solid lines). The local entropy generation due to fluid friction irreversibility is mostly distributed near the moving walls. From Fig. 5.11(a), it is observed that the entropy generation is found near the moving lid and also an effect is found at the lower left and upper right corner of the enclosure. This is because of the fluid friction caused by the movement of lid in the corner of the enclosure. Similar effect can also be seen in other two cases. It is evident from Fig. 5.11 that addition of nanoparticles play a key role in the increment of entropy generation due to the increment of the viscosity of the fluid which results in an increment in values.

Fig. 5.12 shows the heat transfer irreversibility for $Re = 100$, $Ri = 10$ with $\phi = 0.0$ and 0.2. The local entropy generation due to heat transfer is mostly observed near the heat sources. In case-I (Fig. 5.12(a)), the entropy generation near the isothermal region is due to the higher temperature gradient which is depicted from the heavily compressed isotherms, represented by Fig. 5.3(f), in that region. The downward movement of left wall repels the heated fluid towards the right side of the enclosure resulting in the increment of entropy generation since heat transfer is occurring along the right portion of the enclosure. Another supporting factor due to which most of the heat transfer irreversibility is found in the proximity of the right vertical wall due to the upward movement of the wall.

The heat transfer entropy generation in case-II is mostly noticed in the lower middle portion of the vertical wall near the heat source. This effect can also be observed in the form of isotherm lines in Fig. 5.5(f) where the isotherms are highly compressed. A small amount of entropy is also found on the upper mid portion of the enclosure due to the compressed isotherms. In case-III, the heat transfer entropy generation is mostly found in both the lower corners of the enclosure but a small amount is observed near the vertical boundary. The entropy generation is also increased with the increase of volume fraction of nanoparticles in the fluid in all three cases as represented in Fig. 5.12. The solid lines and dashed lines represents the heat transfer entropy generation due to nanofluid and clear fluid respectively.

Fig. 5.13 depicts the variation of average entropy generation at $Re = 100$ with the variation of ϕ and Ri in all the three cases. Our results depict that S_m is increasing with increase in Ri due to the increment of buoyancy effect. The figure ensures that S_m is increasing linearly with the increment of ϕ. The increase in S_m is caused due the increment in the thermal conductivity and viscosity of the fluid on increasing the nanoparticle volume fraction which results in the augmentation of fluid friction and heat transfer irreversibility. S_m is found to be minimum in case-II and maximum in case-I. The average entropy generation for $Ri = 10$, at $\phi = 0.2$ is 34.7417, 24.7387 and 29.8688 in case-I, II and III respectively. In case-I, the average entropy generation is increased by 43.1% for the value of $Ri = 10$ when the nanoparticle volume fraction is increased from 0.0 to 0.2. Similarly, in case-II and III, the entropy generation increment is found to be 32.8% and 29.1% respectively. It is noticeable that the increment in entropy generation

due to increment of nanoparticle volume fraction is minimum in case-III.

Fig. 5.14 depicts the variation of S_m at fixed Ri (=10) with varying ϕ and Re in all the cases. It is observed that the increment of Re for the fixed Ri increases S_m. For low Reynolds number, the variation in nanoparticle volume fraction has no significant contribution in the average entropy generation. But, for higher Reynolds number average entropy generation increases significantly with increase in the nanoparticle volume fraction. This effect is maximum in case-I and minimum in case-II. Hence, the direction of moving walls and the Reynolds number plays a vital role for entropy generation in the fluid flow.

The ratio of irreversibility due to heat transfer to the total irreversibility is termed as Bejan number. The variation of average Bejan number with Ri=0.1, 1, 5 and 10 and ϕ = 0.0, 0.05, 0.1 and 0.2 at Re=100 is shown in Fig. 5.15. In all three cases the value of average Bejan number is greater than 0.65, hence, the fluid friction irreversibility is dominated by the heat transfer irreversibility. Moreover, Be_m increases with the increase in ϕ for a fixed Re. For fixed Re, Be_m decreases with the increase of values Ri, in case-I and II, but increases in case-III as the heat transfer is diminished by the buoyancy forces, and hence the heat transfer entropy generation decreases. In case-III, both vertical walls slide upwards, with high Reynolds number and the flow is dominated by forced convection and hence, the Bejan number increases with Richardson number.

5.4.5 Thermodynamic Optimization

The analysis made in the previous sections leads to the conclusion that the heat transfer is an increasing function of Re, Ri and ϕ but at the same time the entropy generation is also increasing in a similar manner. Hence, the performance evaluation criteria of the system is analyzed by using the ratio of average Nusselt number to the average entropy generation. Fig. 5.16(a) represents the Nu_m/S_m variation with the corresponding ϕ values at Re=100 and Ri=0.1, 1, 5 and 10. In case-I, the highest heat transfer rate on the cost of least entropy generation is found for $\phi = 0.0$ (clear fluid) with Ri=10. In case-II, the highest rate of heat transfer with minimum entropy generation is found when $Ri = 0.1$ with $\phi = 0.2$. Case-III represents the variation in performance evaluation criteria due to the upward movement of side walls and the highest heat transfer rate is obtained on the

cost of least entropy generation when Ri=0.1 with $\phi = 0.2$.

The best test case for performance evaluation criteria is case-II where the ratio $Nu_m/S_m = 0.2957$, which is the highest recorded value at $Re = 100$ in all the three cases. Fig. 5.16(b) represents the relative variation of Nu_m/S_m with respect to ϕ for different Re at $Ri = 10$. In all cases, the variation in Nu_m/S_m with ϕ is almost constant for smaller Re(=1) but for $Re = 10$ and 50, Nu_m/S_m is increasing and a mixed behavior is observed at $Re = 100$. Case-II is found to be the most suitable configuration as compared to other two cases for least entropy generation with highest heat transfer rate for all Reynolds number. The maximum value of Nu_m/S_m is observed at $Re = 1$ with $\phi = 0.2$, however a minute increment in Nu_m/S_m is observed with the increment of ϕ from 0.0($Nu_m/S_m = 0.3988$) to 0.2($Nu_m/S_m = 0.4002$).

5.5 Conclusion

A comparative study of mixed convection flow and entropy generation in a two-dimensional lid-driven square enclosure filled with Cu-water nanofluid is presented in this chapter. Two discrete heat sources are used to study the partial heating effect of nanofluid from the bottom wall. The effect of nanoparticle volume fraction, Reynolds number, Richardson number and the direction of lid movement on the fluid flow and heat transfer is investigated numerically. The fluid flow and thermal field effects are analyzed using streamlines, isotherms and energy flux vectors. The heat transfer rate is analyzed by illustrating the average Nusselt number, entropy generation due to various flow parameters and Bejan number. The results indicates that best performance from the system can be attained by using the configuration used for case-II in which the values of Nu_m/S_m are found to be higher as compared to other two configurations. The main findings from the above study are summarized as follows:

1. In the present study, it is found that the direction of movement of vertical walls is an important factor for the entropy generation inside the cavity filled with nanofluid.

2. The heat transfer is maximum in case of oppositely moving lids as compared to the same direction moving lids. For constant values of ϕ, it is found that heat transfer increases irrespective of the direction of moving walls with increase in Re and Ri.

3. Though the heat transfer is found to be best in case-I, the entropy generation is also highest in case-I.

4. When $Re = 100$ is fixed, the maximum rate of heat transfer on the cost of minimum entropy generation is found in case-II at $Ri = 0.1$ and $\phi = 0.2$.

5. When $Ri = 10$ is fixed, the maximum rate of heat transfer on the cost of minimum entropy generation is found in case-II at $Re = 1$ and $\phi = 0.2$.

6. The average rate of heat transfer has a sharp variation in case-III for large Ri and Re as the strength of the circulation is decreasing by the opposite lid movement.

7. An increase in Reynolds number, Richardson number and volume fraction of nanoparticles leads to the increase in heat transfer.

8. The addition of nanoparticles increases the entropy generation and also, the average entropy generation increases with increase in Richardson number and Reynolds number.

9. The analysis of average Bejan number shows that the irreversibility due to heat transfer is the main contributing factor in entropy generation. Bejan number is an increasing function of nanoparticle volume fraction. The value of Be is found to be maximum in case-II.

10. The physical flow parameter Ri is mostly affecting the heat transfer rate. When $Ri < 1$, the results predicts that the flow is dominated by forced convection effect and when $Ri > 1$ the flow and heat transfer is dominated by the natural convection effect.

Table and figures

Table 5.1: Thermophysical properties of copper and water [142].

Property	Copper	Water
C_p	383	4179
ρ	8954	997.1
k	400	0.6
β	1.67×10^{-5}	2.1×10^{-4}

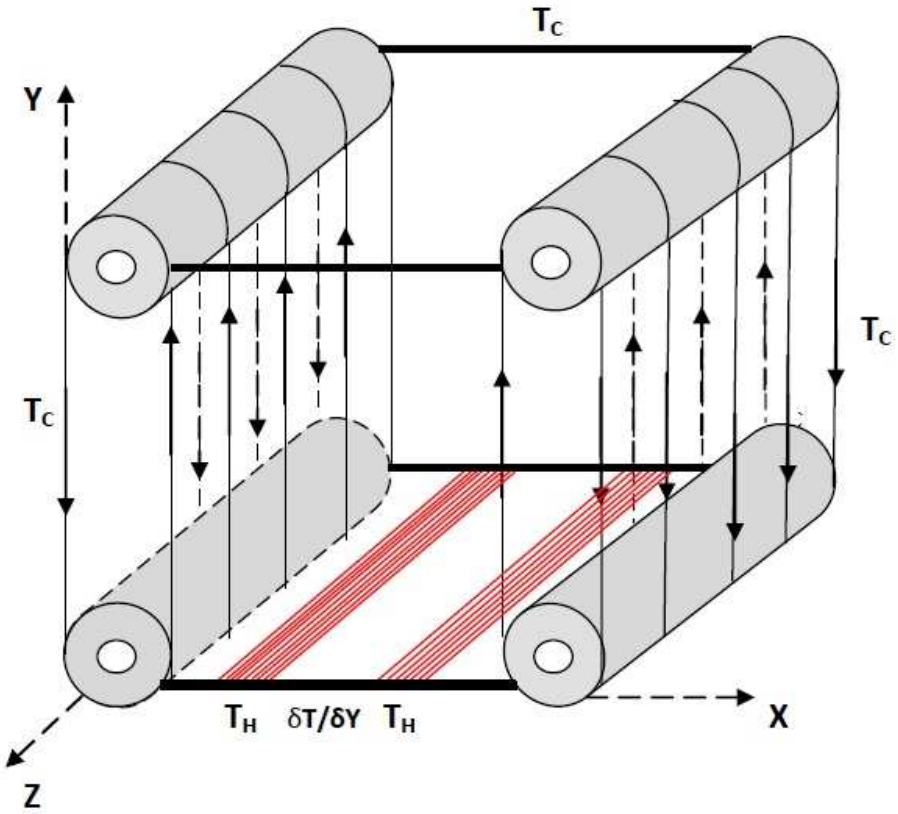

Figure 5.1: Three dimensional view of the problem geometry

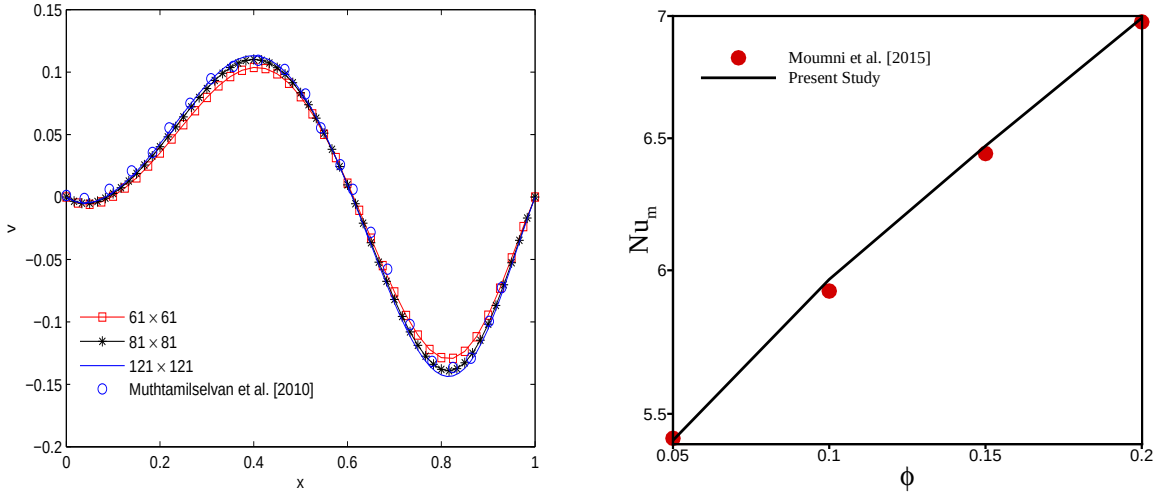

(a) (b)

Figure 5.2: Comparison of (a) vertical component of velocity at mid-section of cavity due to Muthtamilselvan et al. [162] for $Ri = 1, Ra = 100$, $\phi = 2\%$, for various grid size from 61×61 to 121×121, (b) average Nusselt number with results due to [159] with $Pr = 6.2,\ Ri = 10,\ Re = 100$ and $0.05 \leq \phi \leq 0.2$.

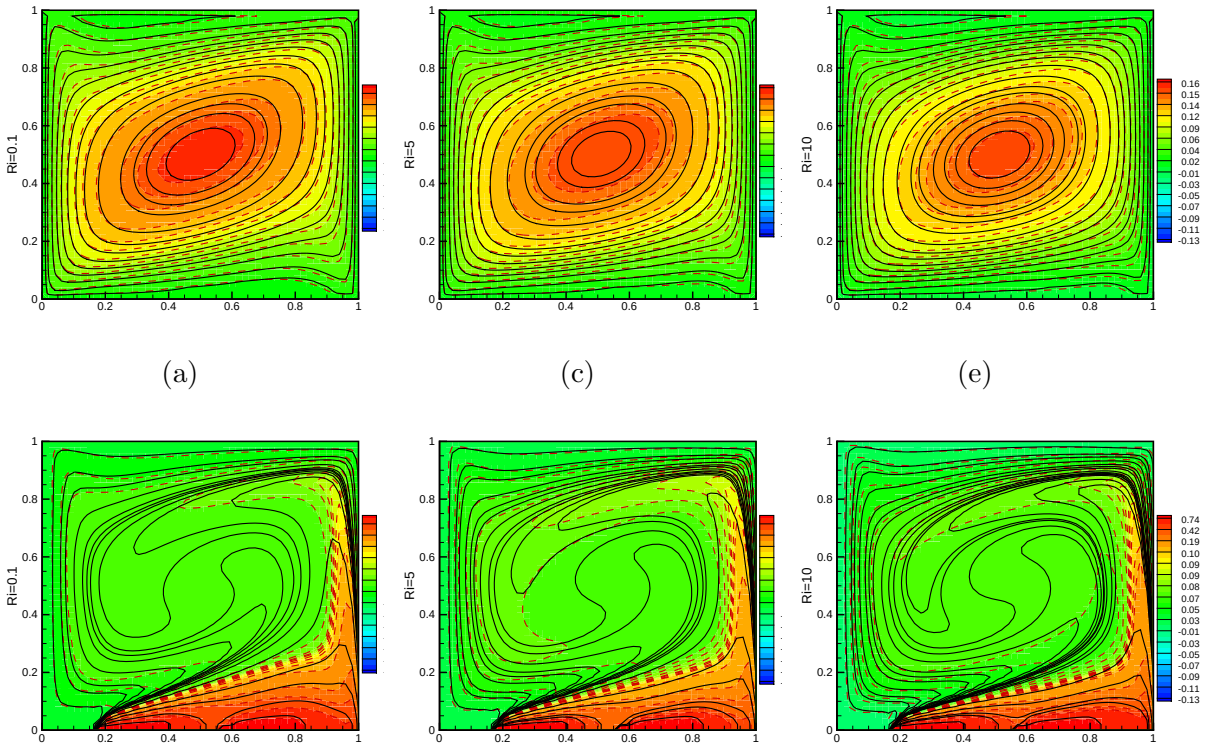

(a) (c) (e)

(b) (d) (f)

Figure 5.3: Streamlines(a, c, e) and isotherms(b, d, f) for $Re = 100$, $0.1 \leq Ri \leq 10$ with $\phi = 0.0$ (dashed lines) and $\phi = 0.2$ (solid lines) for case-I.

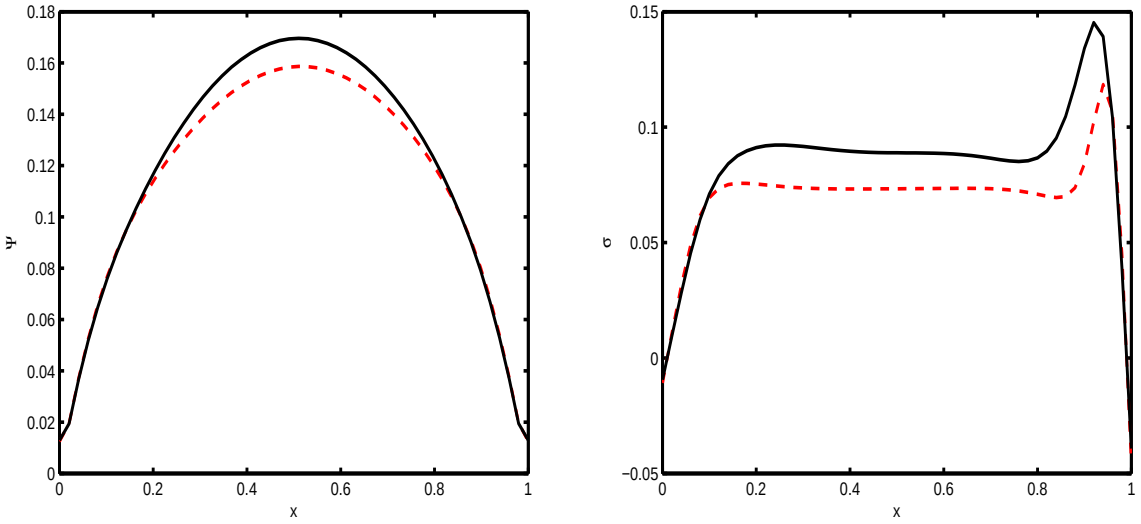

(a) (b)

Figure 5.4: Streamlines(a) and isotherms(b) for $Re = 100$, $Ri = 10$ with $\phi = 0.0$ (dashed lines) and $\phi = 0.2$ (solid lines) for case-I at the horizontal mid-section of enclosure.

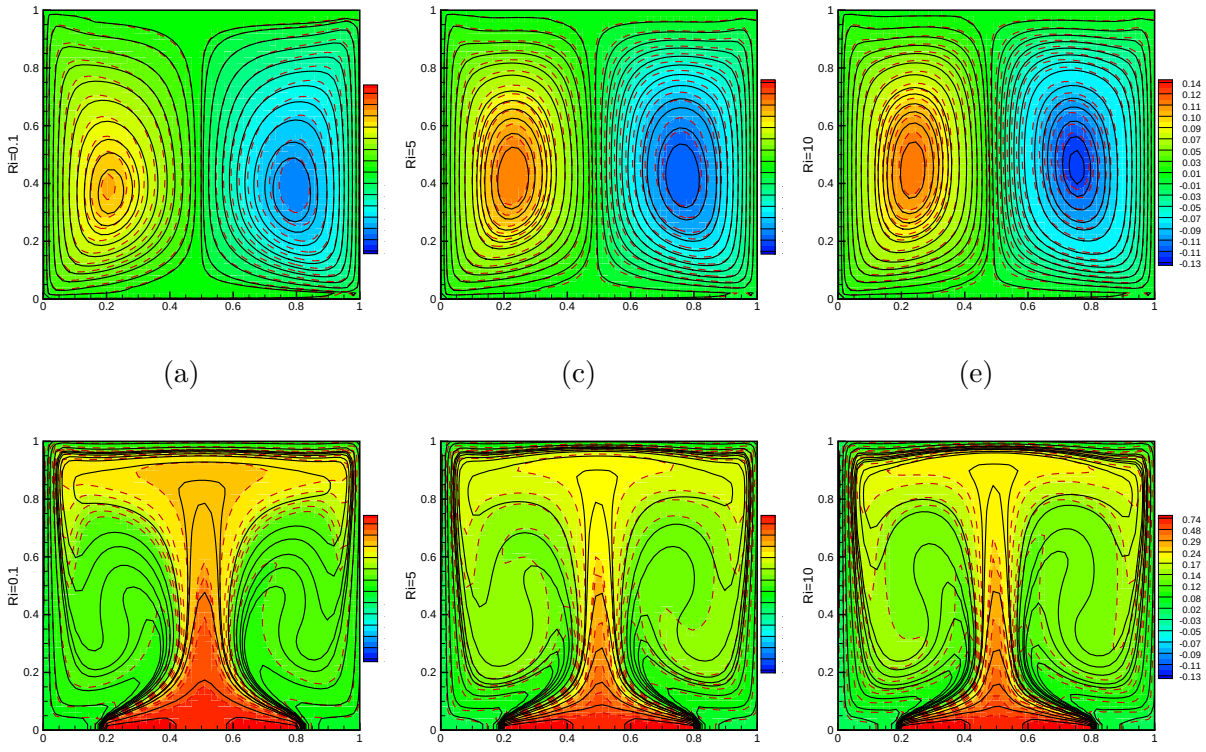

(a) (c) (e)

(b) (d) (f)

Figure 5.5: Streamlines(a, c, e) and isotherms(b, d, f) for $Re = 100$, $0.1 \leq Ri \leq 10$ with $\phi = 0.0$ (dashed lines) and $\phi = 0.2$ (solid lines) for case-II.

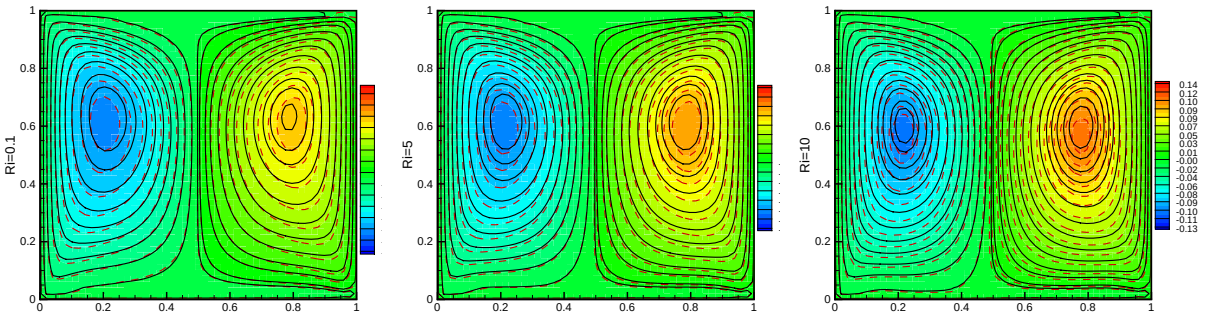

(a) (c) (e)

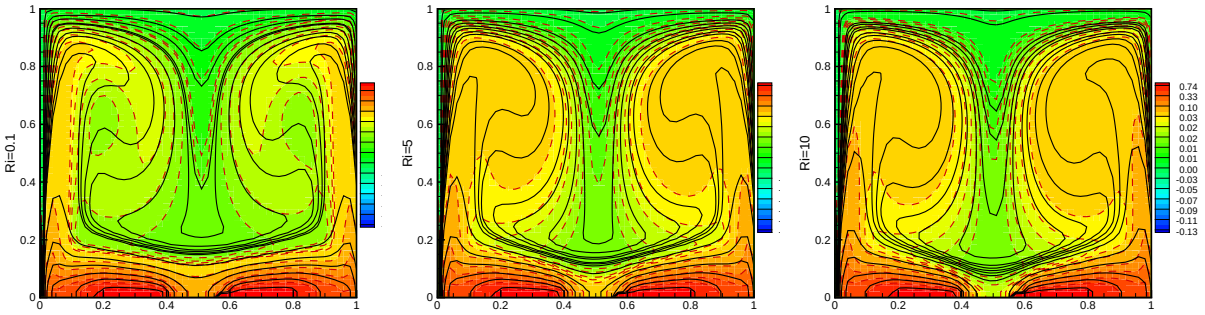

(b) (d) (f)

Figure 5.6: Streamlines(a, c, e) and isotherms(b, d, f) for $Re = 100$, $0.1 \leq Ri \leq 10$ with $\phi = 0.0$ (dashed lines) and $\phi = 0.2$ (solid lines) for case-III.

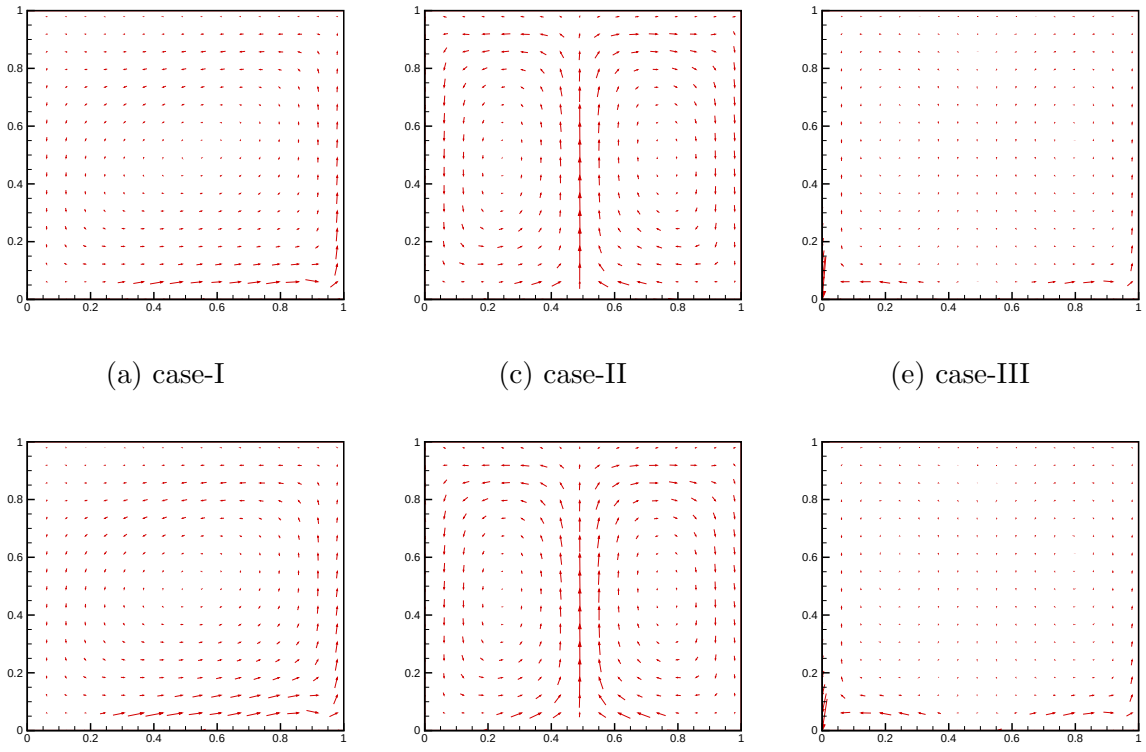

(a) case-I (c) case-II (e) case-III

(b) case-I (d) case-II (f) case-III

Figure 5.7: Energy flux vectors at $Ri = 10$, $Re = 100$ with $\phi = 0.0$ (upper) and $\phi = 0.2$ (lower) for (a, b) case-I, (c, d) case-II and (e, f) case-III.

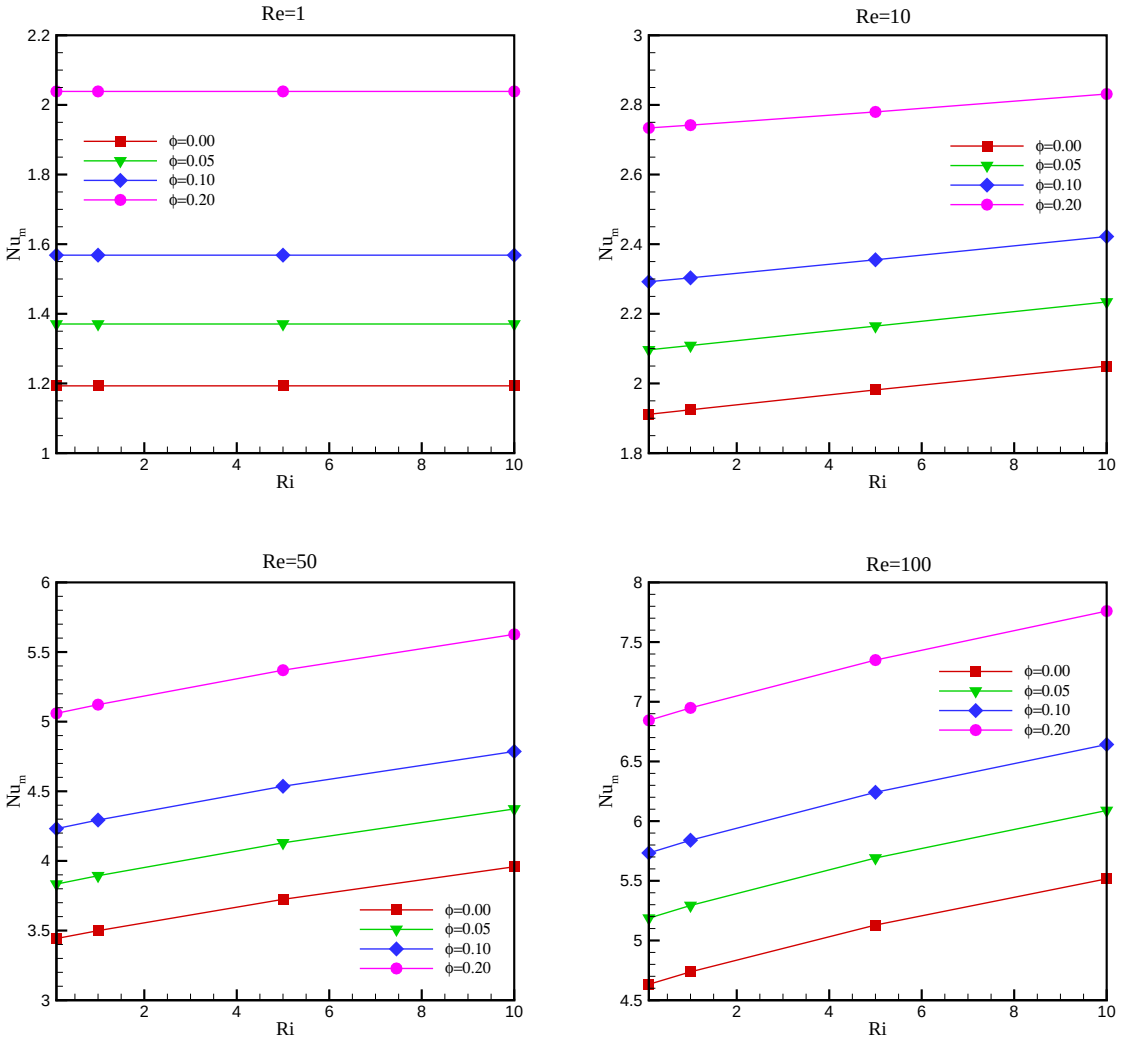

Figure 5.8: Variation in Nu_m with respect to Ri and ϕ at different values of Re for case-I.

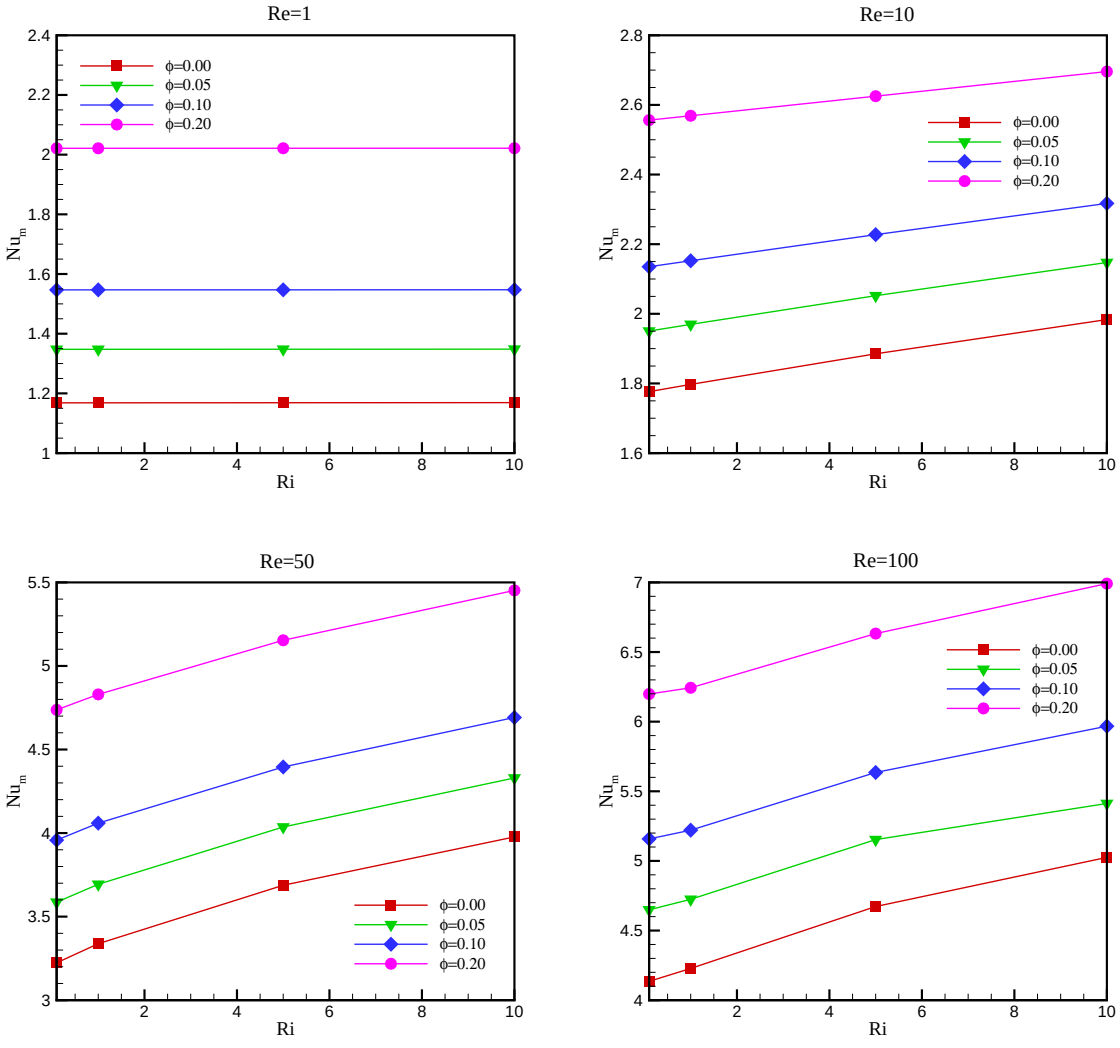

Figure 5.9: Variation in Nu_m with respect to Ri and ϕ at different values of Re for case-II.

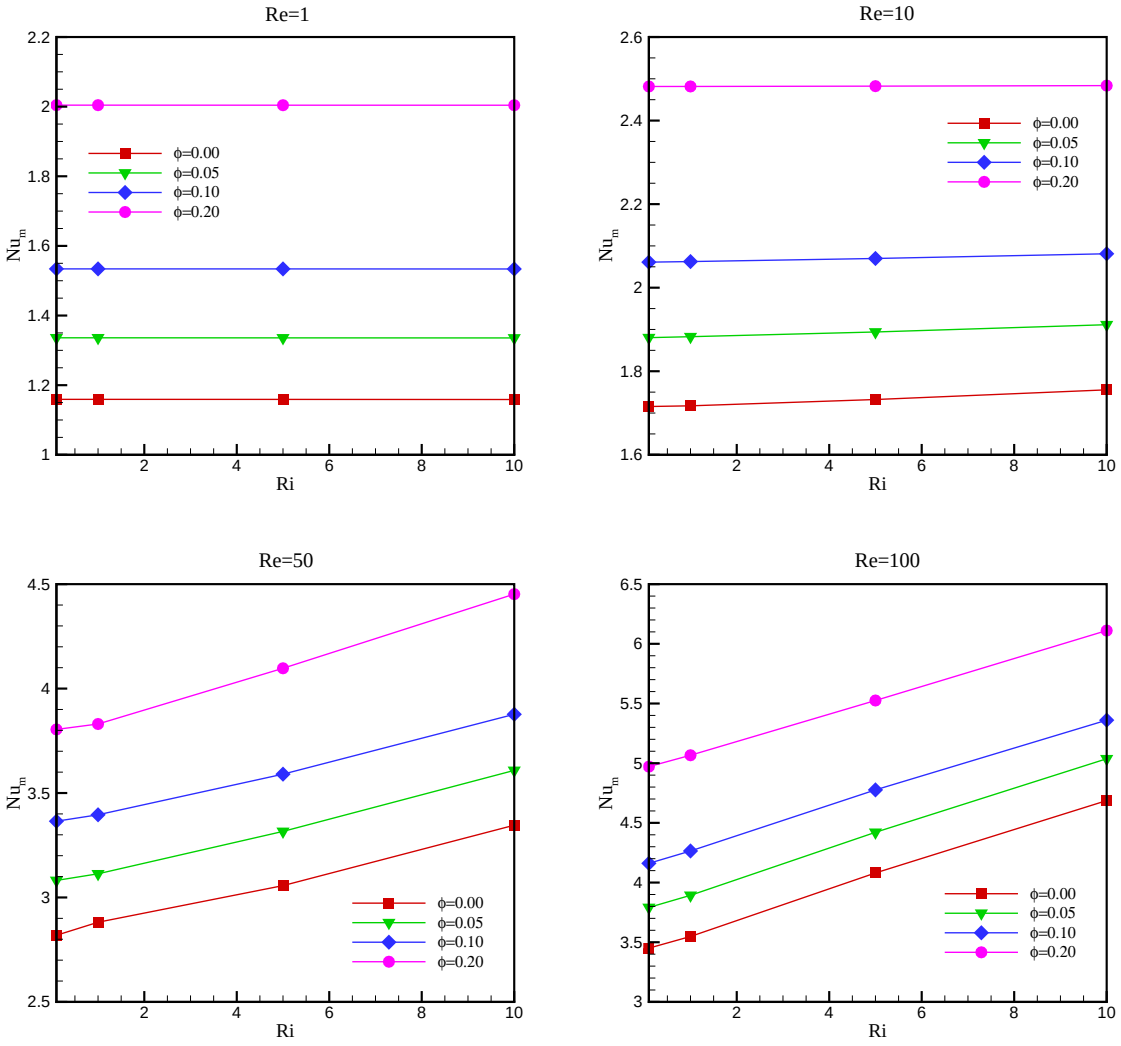

Figure 5.10: Variation in Nu_m with respect to Ri and ϕ at different values of Re for case-III.

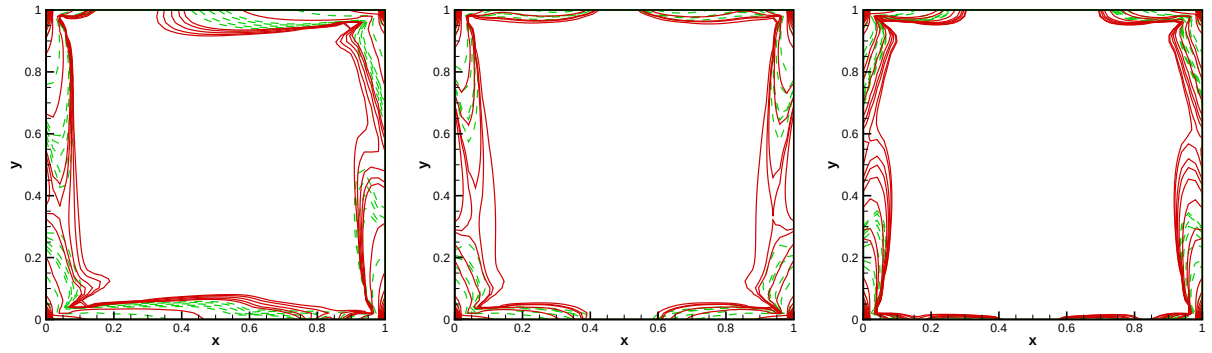

(a) case-I (b) case-II (c) case-III

Figure 5.11: Local entropy generation due to fluid friction for Re=100, Ri=10 at $\phi = 0$ (dashed lines) and $\phi = 0.2$ (solid lines) for (a) case-I, (b) case-II, (c) case-III.

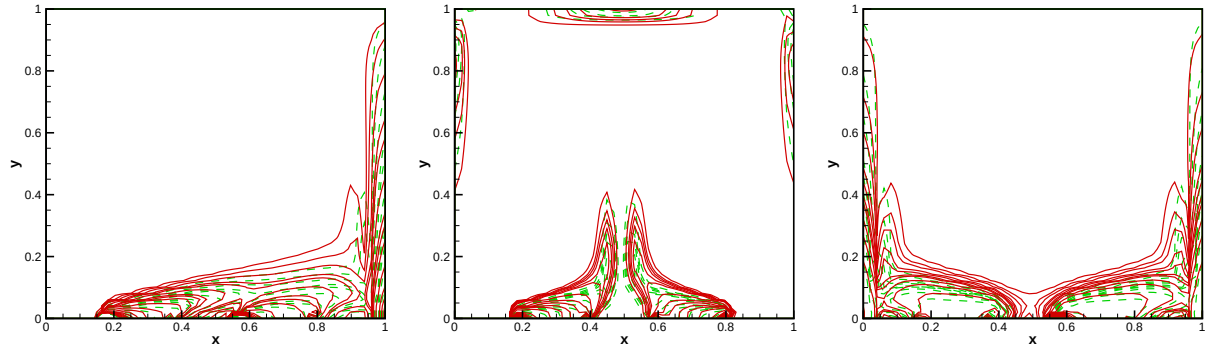

(a) case-I (b) case-II (c) case-III

Figure 5.12: Local entropy generation due to heat transfer with $Re = 100$, $Ri = 10$ at $\phi = 0$ (dashed lines) and $\phi = 0.2$ (solid lines) for (a) case-I, (b) case-II, (c) case-III.

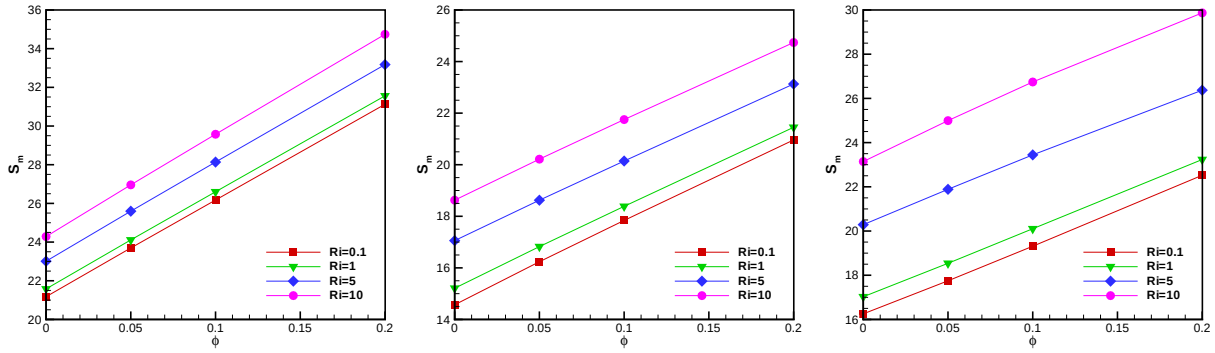

(a) case-I (b) case-II (c) case-III

Figure 5.13: Variation of S_m with ϕ at $Re = 100$ with $0.1 \leq Ri \leq 10$ for (a) case-I, (b) case-II, (c) case-III.

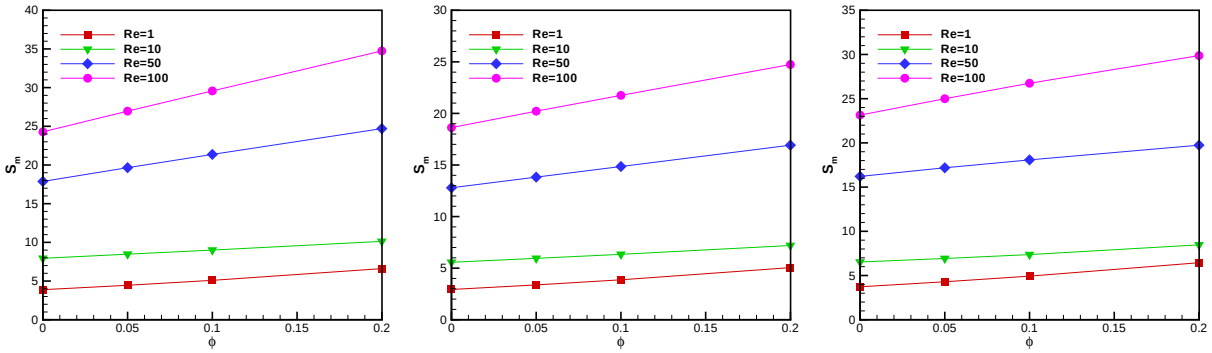

(a) case-I (b) case-II (c) case-III

Figure 5.14: Variation of S_m with ϕ at $Ri = 10$ with $1 \leq Re \leq 100$ for (a) case-I, (b) case-II, (c) case-III.

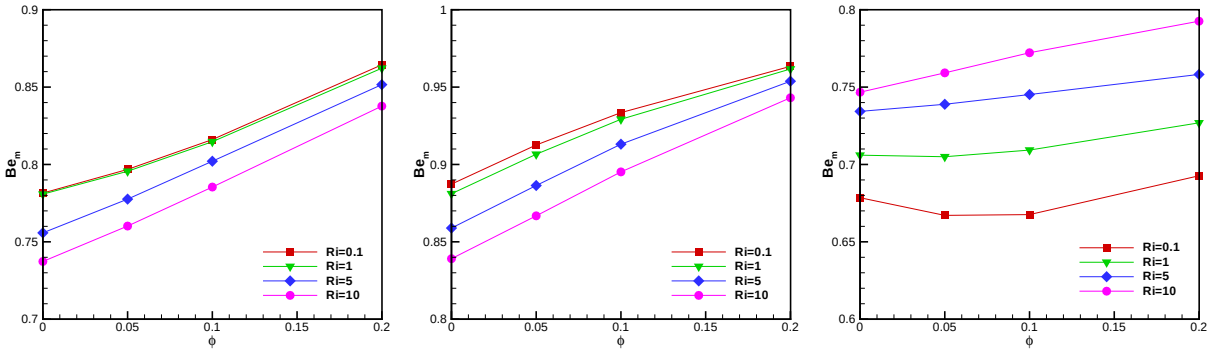

(a) case-I (b) case-II (c) case-III

Figure 5.15: Variation of average Bejan number with solid volume fraction for $Re = 100$ with $0.1 \leq Ri \leq 10$.

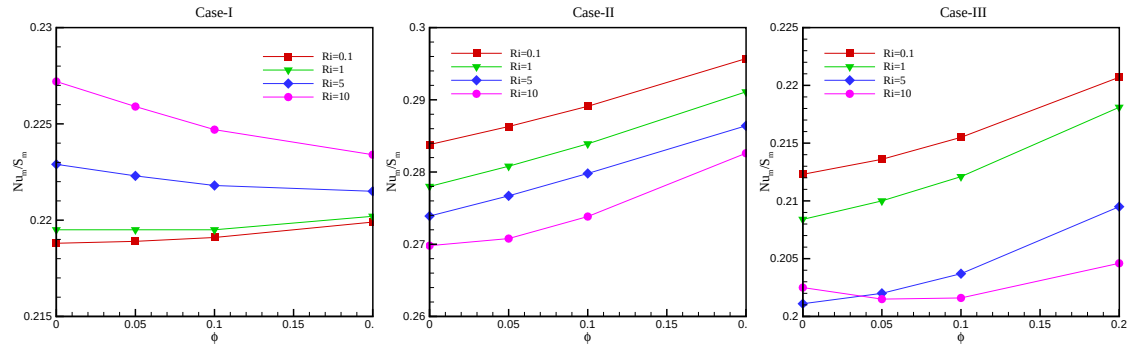

(a) Re=100

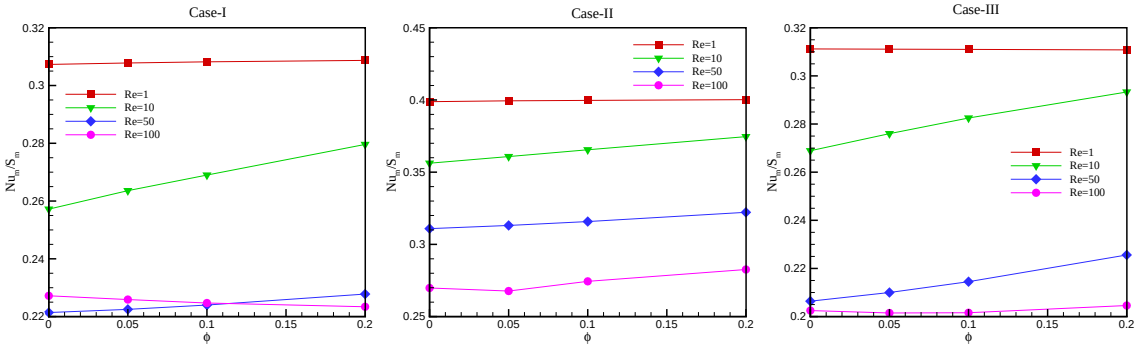

(b) Ri=10

Figure 5.16: Variation of Nu_m/S_m with ϕ at (a) fixed $Re = 100$ and varying Ri, (b) fixed $Ri = 10$ and varying Re.

Chapter 6

MHD Convection and Entropy Generation of Nanofluid in a Porous Enclosure With Sinusoidal Heating [1]

6.1 Introduction

Large scale applications such as magneto-hydrodynamic generators, electrical equipment cooling, plasma physics, geothermal energy extraction, the chemical pollutants spreading in saturate soil and boundary layer control theory in the field of mechanics requires a better understanding of Magneto-hydrodynamic flow of an electrically-conducting fluid coupled with heat transfer [208]. Many engineering applications deal with the heat transfer by natural convection in enclosures such as cooling of electronic devices, solar energy, heat exchanger design, continuous strips or filaments etc. [38, 118].

In practical applications, the process of heating and cooling of fluid is very sensitive and sometimes requires very quick response of heating as well as cooling. Clear fluid like water, ethylene glycol etc. fails this quick response property to heating and cooling due to which the nanoparticles with relatively high thermal conductivity such as Cu, Al_2O_3, TiO_2 etc. are required to be suspended into the base fluid. Convective flow through porous media is gaining interest from researchers of fluid mechanics and heat transfer due to its broad range of engineering applications in petroleum and geothermal processes, high performance insulation in buildings packed bed chemical reactors and transpiration cooling [161, 127]. Now a days, the MHD flow inside a porous medium has drawn the interest

[1] The contents of this chapter has been published in *International Journal of Heat and Mass Transfer, Elsevier, DOI:10.1016/j.ijheatmasstransfer.2017.03.123*

of several researchers because of its importance in many industrial applications such as MHD power generator designing, control of chemical waste and pollutants dissemination, optimization of solidification processes of metals and alloys. The relative problem also appear in the operation of microelectronic devices and electronic packages [70]. Horton and Rogers [92] and Lapwood [132] were the first to study the effects of fluid flow and heat transfer in porous media [56]. Kumar et al. [128] carried out the numerical study of mixed convection flow in a non-Darcian fluid-saturated homogeneous porous medium.

The effect of MHD convection in an electrically conducting fluid inside a differentially heated rectangular enclosure is investigated by Rudraiah et al. [193]. They found that the convective heat transfer decreases with increment of Hartmann number. Oztop et al. [177] studied a square cavity with two semicircular heaters placed at the lower wall considering adiabatic horizontal walls and isothermal boundary conditions on vertical walls in the presence of magnetic field. They concluded that the flow strength as well as convective heat transfer decreases with increasing magnetic field effect.

Sivasankaran et al. [222] used finite volume method to study the effect of sinusoidal boundary temperatures at the vertical walls in a lid-driven square cavity having adiabatic horizontal walls. They concluded that the amplitude ratio increases the heat transfer rate. The work is further extended in the presence of magnetic field and found that increment in Hartmann number decreases the total heat transfer rate in Buoyancy-driven convection [220]. Subsequently, Sivasankaran and Pan [221] used saturated porous medium with same boundary conditions to investigate the effect of amplitude ratio on the heat transfer rate. The temperature difference is found to be increasing with increase of amplitude ratio, Darcy number and porosity.

Mostly, nanofluids are used to obtain higher heat transfer rate in industry as compared to low conductivity clear fluids. The term 'nanofluid' was coined by Choi and Eastman [52] and a number of experimental as well as numerical studies have been conducted by considering the thermal conductivity of nanofluids till date. Experimentally, Eastman et al. [61] used 0.3% volume fraction of copper nanoparticles of size <10nm in ethylene glycol and the effective thermal conductivity is found to be increased upto 40% as compared to pure ethylene glycol. The study of externally applied magnetic field and convective heat transfer over a linearly stretching sheet has been conducted by Shit et al.

[210] and found that the average Nusselt number increases with increase in magnetic field strength. Recently, Ghodsinezhad et al. [78] performed an experimental study to find the optimum fraction of nanoparticles in natural convection of Al_2O_3-water nanofluids. In natural convection, it is predicted that heat transfer rate is increasing upto 15%, if the volume fraction is changed from 0 to 0.1% and further increment of nanoparticle fraction descends the rate of heat transfer.

The effect of magnetic field on heat and fluid flow in a CuO-water nanofluid filled enclosure heated from below is studied by Sheikholeslami et al. [203]. They found that heat transfer rate is increasing with the increment of heat source length and Hartmann number, and decreases with increment in Rayleigh number. Ghasemi et al. [77] studied the natural convection of Al_2O_3-water nanofluid inside a differentially heated square enclosure in presence of magnetic field. The results show that the increment of nanoparticle volume fraction results in the variation of heat transfer depending on the increment of Hartmann number and increment of Rayleigh number respectively.

MHD flow in nanofluid filled domain is an important aspect of study as it is beneficial for energy optimization and designing of heat removal devices of MHD power generator [97, 194]. In a recent study, Elshehabey and Ahmed [67] presented a numerical study of MHD mixed convection of nanofluid inside a square enclosure with sinusoidal temperature and nanoparticle volume fraction on both vertical walls. The results show that the flow variation inside the cavity decreases with increasing buoyancy ratio.

Pekmen and Tezer-Sezgin [181] numerically studied the mixed convection flow inside a lid-driven square enclosure filled with porous medium activated by magnetic field using local thermal equilibrium(LTE) approach. They have concluded that the fluid flow becomes slower with the increase of the magnetic field intensity and decrease in porosity. In LTE approach the fluid temperature is considered to be equal to the solid temperature, whereas in local thermal non-equilibrium (LTNE) approach different temperature of fluid and solid medium is considered. LTE approach is used by many authors for transport phenomena in porous media, Al-Nimr and Haddad [7], Rees and Vafai [192], Kim and Vafai [124] and Mohamad [157]. Haddad et al. [81] developed an analytical technique for the validation of LTE assumption of a natural convective flow in a porous media along a vertical flat plate. A lot more high quality research are also performed on the local

thermal non-equilibrium (LTNE) approach in nanofluids which is also an advanced model for the flow of nanofluid in porous medium [5, 17, 228, 229, 244].

The analysis of entropy generation in magnetohydrodynamic porous channel is made by Ibáñez [96] analytically. Their results show that the total entropy generated during the process, increases with slip flow due to decrease in the temperature of the system. Khalili et al. [117] investigated the unsteady MHD flow and heat transfer over a stretching/shrinking sheet in a nanofluid filled porous medium and reported that increase in nanoparticle volume fraction results an increase of skin friction and heat transfer coefficient. Recently, Kefayati [110] discussed the effect of non-Newtonian nanofluids on heat transfer and entropy generation in a porous cavity and concluded that increment in Rayleigh number increases the heat transfer and entropy generation. In another recent study Kefayati and Sidik [114] studied the non-Newtonian nanofluid in an inclined cavity for the effect of entropy generation. The result shows enhancement in fluid friction and heat transfer irreversibility due to Rayleigh number. Fersadou et al. [69] made a numerical study to analyze the effect of magnetic field on entropy generation inside a vertical porous channel filled with Cu-water nanofluid. Results show that nanoparticle addition increases the entropy generation of the system. The entropy generation in a partially heated two sided lid-driven cavity under magnetic field effect filled with Al_2O_3-water nanofluid is studied by Hussain et al. [94]. The augmentation of total entropy generation due to increment in Reynolds number and solid volume fraction is analyzed. Recently, Shit et al. [211] conducted the study of heat transfer and entropy generation on MHD nanofluid flow in porous medium. A strong impact of applied magnetic field as well as thermal radiation on the entropy generation has been observed.

In the present study, the convective heat transfer is analyzed through energy flux vectors. The conductive heat transfer is easily visualized using the isotherms whereas convective mode of heat transfer can be understood by using heatlines. It is also reported that visualization of heat transfer rate due to heatlines as compared to isotherms are better in case of convective mode of transfer rate [27]. Kaluri and Basak [105] presented the heatline analysis of natural convection due to discrete heating in porous cavities for a wide range of Prandtl number, Rayleigh number and Darcy number. The study of heatlines is found to be very useful in the analysis of heat transfer in discretely heated

enclosures filled with porous medium. For small Darcy numbers, a conduction dominated heat transfer is reported whereas heat transfer is found to be convection dominated for higher Darcy number. Heatline analysis of convective heat transfer in a differentially heated square enclosure filled with nanofluid is made by Basak and Chamkha [21]. The heat transfer due to convection is found to be dominant in nanofluids. Recently, Hooman [91] suggested that instead of solving a difficult form of heat function equations, it is comparatively easy to use the concept of energy flux vectors, which are locally tangent to the heatlines. The heat transfer lines are not sufficient enough to visualize energy transfer effect in case of a transient flow and hence in the present study energy flux vectors are used to visualize the flow of energy. Moreover, the energy flux vectors can also serve the purpose of reducing extra efforts of formulating and solving the additional differential equations without implementing the boundary conditions as in heatlines [138].

Nithyadevi et al. [172] considered the natural convective flow inside a square enclosure with partially active thermal zones applied along the vertical walls in which one is considered to be time periodic and the other being isothermal. The rate of heat transfer is found to be highest for the middle-middle thermally activated zones. In the present chapter, we tried to find the optimum heat transfer and entropy generation for natural convection of nanofluid flow in enclosure containing saturated porous media in the presence of magnetic field. The effect of various flow governing parameters such as Grashof number, Hartmann number, Darcy number and nanoparticle volume fraction over the fluid flow is studied. The study focuses on the optimum heat transfer and entropy generation analysis by variations of above mentioned parameters. The fluid flow and heat transfer behavior inside the enclosure and convective heat transfer analysis is made with the help of energy flux vectors. The time history analysis is investigated to visualize the flow enhancement during the initial time level and the flow phase variation with respect to time.

6.2 Problem formulation and governing equations

The physical domain as represented in Fig.6.1 considers a two-dimensional closed square enclosure of length L, filled with a saturated porous medium containing an electrically

conducting Cu-water nanofluid. Constant temperature has been maintained at the mid-portion of right vertical walls of length $L/3$ and its left counterpart of the same length is maintained with a time-periodic heat transfer of oscillating nature. The remaining sections of the boundaries are assumed to be thermally insulated. The fluid is considered to be Newtonian and is assumed to be incompressible and laminar which is in thermal equilibrium with negligible slip effect between two phases. Boussinesq assumption is followed for variation of density.

The shape of nanoparticles is assumed to be spherical with 100nm diameter. The magnetic Reynolds number ($Re_m = \mu_f \sigma_{e_f} u_m L \ll 1$) is assumed to be small which enables the induced magnetic effect to be trivial as compared to the external magnetic field [154]. The thermophysical properties of copper and water are tabulated in table 6.1. The flow in the porous medium is dealt with Darcy-Brinkman-Forchheimer model. The saturated porous medium is assumed to be isotropic thermally, electrically and hydrodynamically. The Hall effect, viscous dissipation, radiation effect, Joule heating and pressure work are also assumed to be negligible [111, 168]. Two dimensional flow field equation along with the above mentioned assumptions are given by [8, 147],

continuity equation

$$\frac{\partial u^*}{\partial x^*} + \frac{\partial v^*}{\partial y^*} = 0, \tag{6.1}$$

momentum equations

$$\frac{\partial u^*}{\partial t^*} + u^* \frac{\partial u^*}{\partial x^*} + v^* \frac{\partial u^*}{\partial y^*} = \frac{1}{\rho_{nf}} \left[- \frac{\partial p^*}{\partial x^*} + \mu_{nf} \left(\frac{\partial^2 u^*}{\partial x^{*2}} + \frac{\partial^2 u^*}{\partial y^{*2}} \right) - \sigma_{e_{nf}} B_0^2 u^* - \frac{\mu_{nf} u^*}{K} \right], \tag{6.2}$$

$$\frac{\partial v^*}{\partial t^*} + u^* \frac{\partial v^*}{\partial x^*} + v^* \frac{\partial v^*}{\partial y^*} = \frac{1}{\rho_{nf}} \left[- \frac{\partial p^*}{\partial y^*} + \mu_{nf} \left(\frac{\partial^2 v^*}{\partial x^{*2}} + \frac{\partial^2 v^*}{\partial y^{*2}} \right) + (\rho\beta)_{nf} g (T^* - T_c^*) - \frac{\mu_{nf} v^*}{K} \right], \tag{6.3}$$

and *energy equation*

$$\frac{\partial T^*}{\partial t^*} + u^* \frac{\partial T^*}{\partial x^*} + v^* \frac{\partial T^*}{\partial y^*} = \alpha_{nf} \left(\frac{\partial^2 T^*}{\partial x^{*2}} + \frac{\partial^2 T^*}{\partial y^{*2}} \right). \tag{6.4}$$

The associated boundary conditions are,

$$u^* = v^* = \frac{\partial T^*}{\partial y^*} = 0 \quad \text{at } y^* = 0 \text{ and } L, \quad 0 \leqslant x^* \leqslant L$$

$$u^* = v^* = 0 \quad \text{at } x^* = 0 \text{ and } L, \quad 0 \leqslant y^* \leqslant L$$

with

$$T^* = \begin{cases} T_h^*(1 - asin(2\pi t^*/\omega)) & \text{at } x^* = 0, \\ T_c^* & \text{at } x^* = L \end{cases} \qquad L/3 \leqslant y^* \leqslant 2L/3$$

and

$$\frac{\partial T^*}{\partial x^*} = 0 \quad \text{elasewhere on } x^* = 0 \text{ and } x^* = L \tag{6.5}$$

where, the effective density and dynamic viscosity are defined by [112, 113, 169],

$$\rho_{nf} = \phi\rho_s + (1-\phi)\rho_f, \tag{6.6}$$

$$\mu_{nf} = \frac{\mu_f}{(1-\phi)^{2.5}}, \tag{6.7}$$

and the thermal diffusivity, heat capacitance and thermal expansion coefficient are given by,

$$\alpha_{nf} = \frac{k_{nf}}{(\rho C_p)_{nf}}, \tag{6.8}$$

$$(\rho C_p)_{nf} = \phi(\rho C_p)_s + (1-\phi)(\rho C_p)_f, \tag{6.9}$$

$$(\rho\beta)_{nf} = \phi(\rho\beta)_s + (1-\phi)(\rho\beta)_f. \tag{6.10}$$

The effective thermal conductivity and electrical conductivity for uniformly distributed spherical shaped nanoparticles are calculated by using Maxwell model [152] as,

$$\frac{k_{nf}}{k_f} = \frac{k_s + 2k_f - 2\phi(k_f - k_s)}{k_s + 2k_f + \phi(k_f - k_s)}, \tag{6.11}$$

$$\frac{\sigma_{e_{nf}}}{\sigma_{e_f}} = 1 + \frac{3(\frac{\sigma_{e_s}}{\sigma_{e_f}} - 1)\phi}{(\frac{\sigma_{e_s}}{\sigma_{e_f}} + 2) - (\frac{\sigma_{e_s}}{\sigma_{e_f}} - 1)\phi}. \tag{6.12}$$

The performance of the system is reduced by various factors that creates irreversibility in the system. There are three sources of entropy generation in our system: the heat transfer, viscous effects and the magnetic field. Hence, the total entropy generation rate is given by [8, 9, 37],

$$S_{gen}^* = S_{ht}^* + S_{ff}^* + S_{mf}^* \tag{6.13}$$

where,

$$S_{ht}^* = \frac{k_{nf}}{T_0^{*2}}\left[\left(\frac{\partial T^*}{\partial x^*}\right)^2 + \left(\frac{\partial T^*}{\partial y^*}\right)^2\right], \tag{6.14}$$

$$S_{ff}^* = \frac{\mu_{nf}}{T_0^*}\left[(u^{*2} + v^{*2}) + \frac{K\rho_{nf}}{\mu_{nf}}\left\{2\left(\frac{\partial u^*}{\partial x^*}\right)^2 + 2\left(\frac{\partial v^*}{\partial y^*}\right)^2 + \left(\frac{\partial u^*}{\partial y^*} + \frac{\partial v^*}{\partial x^*}\right)^2\right\}\right] \tag{6.15}$$

and

$$S^*_{mf} = \frac{\sigma_{e_{nf}} B_0^2}{T_0^*} u^{*2} \tag{6.16}$$

with $T_0^* = \frac{T_h^* + T_c^*}{2}$.

Using the non-dimensional variables [8, 146, 147]

$$u = \frac{u^* L}{\alpha_f}, \quad v = \frac{v^* L}{\alpha_f}, \quad x = \frac{x^*}{L}, \quad y = \frac{y^*}{L}, \quad p = \frac{p^* L^2}{\rho_{nf} \alpha_f^2}, \quad t = \frac{t^* \alpha_f}{L^2}, \quad T = \frac{T^* - T_c^*}{(T_h^* - T_c^*) L} k_f,$$

$$Gr = \frac{g \beta_f (T_h - T_c) L^3 \rho_f^2}{\mu_f^2}, \quad Pr = \frac{\mu_f}{\rho_f \alpha_f}, \quad Ha = B_0 L \sqrt{\frac{\sigma_{e_f}}{\mu_f}} \text{ and } Da = \frac{K}{L^2}, \tag{6.17}$$

the dimensionless form of the governing equations are written as,

$$\frac{\partial u}{\partial x} + \frac{\partial v}{\partial y} = 0, \tag{6.18}$$

$$\frac{\partial u}{\partial t} + u\frac{\partial u}{\partial x} + v\frac{\partial u}{\partial y} = -\frac{\partial p}{\partial x} + \frac{\mu_{nf}}{\rho_{nf}\alpha_f}\left(\frac{\partial^2 u}{\partial x^2} + \frac{\partial^2 u}{\partial y^2}\right) - \frac{\sigma_{e_{nf}}\beta_f}{\sigma_{e_f}\rho_{e_{nf}}} u Ha^2 Pr - \frac{\mu_{nf} u}{\rho_{nf}\alpha_f Da}, \tag{6.19}$$

$$\frac{\partial v}{\partial t} + u\frac{\partial v}{\partial x} + v\frac{\partial v}{\partial y} = -\frac{\partial p}{\partial y} + \frac{\mu_{nf}}{\rho_{nf}\alpha_f}\left(\frac{\partial^2 v}{\partial x^2} + \frac{\partial^2 v}{\partial y^2}\right) + \frac{(\rho\beta)_{nf}}{\rho_{nf}\beta_f} Gr Pr^2 T - \frac{\mu_{nf} v}{\rho_{nf}\alpha_f Da}, \tag{6.20}$$

$$\frac{\partial T}{\partial t} + u\frac{\partial T}{\partial x} + v\frac{\partial T}{\partial y} = \frac{\alpha_{nf}}{\alpha_f}\left(\frac{\partial^2 T}{\partial x^2} + \frac{\partial^2 T}{\partial y^2}\right). \tag{6.21}$$

The dimensionless form of boundary conditions are given by,

$$u = v = \frac{\partial T}{\partial y} = 0 \quad \text{at } y = 0 \text{ and } 1, \quad 0 \leqslant x \leqslant 1,$$

$$u = v = 0 \quad \text{at } x = 0 \text{ and } 1, \quad 0 \leqslant y \leqslant 1$$

with

$$T = \begin{cases} 1 - A sin(2\pi t/\delta) & \text{at } x = 0, \\ 0 & \text{at } x = 1 \end{cases} \qquad 1/3 \leqslant y \leqslant 2/3,$$

and

$$\frac{\partial T}{\partial x} = 0 \quad \text{elasewhere on } x = 0 \text{ and } x = 1 \tag{6.22}$$

where, A and 2δ denotes the amplitude factor and the period respectively.

For time $t = 0$, the initial conditions are taken as follows,

$$u = v = T = 0 \quad \text{for } \ 0 \leqslant x \leqslant 1, \quad 0 \leqslant y \leqslant 1. \tag{6.23}$$

The non-dimensional form of entropy generation is given by

$$S_{gen} = S_{ht} + S_{ff} + S_{mf}, \tag{6.24}$$

where,

$$S_{ht} = \frac{k_{nf}}{k_f}\left[\left(\frac{\partial T}{\partial x}\right)^2 + \left(\frac{\partial T}{\partial y}\right)^2\right], \tag{6.25}$$

$$S_{ff} = \chi\frac{\mu_{nf}}{\mu_f}\left[(u^2+v^2) + Da\left\{2\left(\frac{\partial u}{\partial x}\right)^2 + 2\left(\frac{\partial v}{\partial y}\right)^2 + \left(\frac{\partial u}{\partial y} + \frac{\partial v}{\partial x}\right)^2\right\}\right], \tag{6.26}$$

$$S_{mf} = \chi\frac{\sigma_{e_{nf}} Ha^2}{\sigma_{e_f}} u^2 \tag{6.27}$$

and

$$\chi = \frac{\mu_f T_0}{k_f}\left(\frac{\alpha_f^2}{K(T_h - T_c)^2}\right), \tag{6.28}$$

where, χ is called as irreversibility distribution ratio. The value of χ is considered to be 0.01, in all of our computations [20, 93, 236]. The volume averaged entropy generation is calculated as,

$$S_m = \frac{1}{V}\int_V S_{gen} dV, \tag{6.29}$$

where, V is the total nanofluid volume. The relative dominance of heat transfer irreversibility is analyzed through Bejan number which is calculated as the ratio of heat transfer entropy generation to the total entropy generation and is written as,

$$Be = \frac{S_{ht}}{S_{gen}}. \tag{6.30}$$

The heat transfer rate is characterized by local (Nu) and average Nusselt number (Nu_m) and are represented as,

$$Nu(x=0) = -\frac{k_{nf}}{k_f}\left(\frac{\partial T}{\partial y}\right), \tag{6.31}$$

$$Nu_m(x=0) = \frac{\int Nu(x=0)dy}{\int dy}. \tag{6.32}$$

The heat flow inside the enclosure is visualized through the energy flux vectors which are represented by,

$$E = \frac{\partial H'}{\partial y}\hat{i} - \frac{\partial H'}{\partial x}\hat{j}, \tag{6.33}$$

where, H' is calculated from conductive heat fluxes $(-\frac{\partial T}{\partial x}, -\frac{\partial T}{\partial y})$ and convective heat fluxes (uT, vT), which satisfies the steady energy balance equations,

$$\frac{\partial H'}{\partial y} = uT - \frac{\alpha_{nf}}{\alpha_f}\frac{\partial T}{\partial x}, \quad \frac{\partial H'}{\partial x} = -vT + \frac{\alpha_{nf}}{\alpha_f}\frac{\partial T}{\partial y}. \tag{6.34}$$

6.3 Numerical approach

6.3.1 Methodology

All the computations are performed using finite volume method based on SIMPLE algorithm [32]. The system of non-dimensional governing equations (6.18) to (6.21) is integrated over the stated control volume as,

$$\int_{\Delta V} \frac{\partial u}{\partial x} dV + \int_{\Delta V} \frac{\partial v}{\partial y} dV = 0, \tag{6.35}$$

where ΔV denotes the volume of the nodal point. The momentum equation can be represented as defined in section 4.2.2, and the representation in case of nanofluid is,

$$\begin{aligned} \int_s^n \int_w^e \frac{\partial u}{\partial t} dxdy + \int_s^n \int_w^e u \frac{\partial u}{\partial x} dxdy + \int_w^e \int_s^n v \frac{\partial u}{\partial y} dydx = &- \int_s^n \int_w^e \frac{\partial p}{\partial x} dxdy \\ &+ \frac{\mu_{nf}}{\rho_{nf}\alpha_f} \left[\int_s^n \int_w^e \frac{\partial^2 u}{\partial x^2} dxdy + \int_w^e \int_s^n \frac{\partial^2 u}{\partial y^2} dydx \right] \\ &- \left[Ha^2 Pr \frac{\sigma_{e_{nf}} \beta_f}{\sigma_{e_f} \rho_{nf}} + \frac{\mu_{nf}}{\rho_{nf}\alpha_f Da} \right] \int_s^n \int_w^e u dxdy. \end{aligned} \tag{6.36}$$

The reduced form of the equation can be represented as,

$$F_e u_e - F_w u_w + F_n u_n - F_s u_s = b \tag{6.37}$$

where, F denotes the non-linear coefficients of u and b contains the source and time derivative terms.

A QUICK (quadratic upstream interpolation for convective kinematics) third-order accurate scheme is used for the discretization of convective terms of the governing equations. For instance, at interface the approximation due to quadratic interpolation for u is,

$$u_e = \frac{1}{8}(3u_E + 6u_P - u_W) \quad \text{if} \quad F_e > 0, \tag{6.38}$$

$$u_e = \frac{1}{8}(6u_E + 3u_P - u_W) \quad \text{if} \quad F_e < 0, \tag{6.39}$$

and hence,

$$F_e u_e = \frac{1}{8}(3u_E + 6u_P - u_W)[[F_e, 0]] - \frac{1}{8}(6u_E + 3u_P - u_W)[[-F_e, 0]]. \tag{6.40}$$

Similar procedure is followed for the computations at west, north and south faces and time derivatives are discretized using a third-order implicit scheme. The resultant discretized

system of equations is dealt with the iterative Semi Implicit Method for Pressure Linked Equation (SIMPLE algorithm) based on the pressure correction approach.

The procedure for finding the solutions of successive steady state problems is the initial step, that gradually pave the way for the solution of current unsteady problem. For any reasonable value of Δt, the values of the unknown dependent variable Φ at time $t + \Delta t$ can be approximated using the values of Φ at time t taken as initial guess. This iterative procedure is carried out until a convergent solution is obtained. The flow field variables are required to move through a progression of smaller time-steps $\Delta t = 0.001$ to ultimately obtain a repeated time independent and convergent solution. The steady state condition considering $t = 10$ has been adopted to compute all the numerical results which have been presented in the form of figures, as the values are repeated. The following sequence has been followed to obtain the solution of a particular iteration that consists of pressure dependent terms:

1. The discretized form of flow governing and heat transfer equations provides an algebraic system of equations that can be written as follows:

$$A_\Phi \Phi_{i-1,j}^{n+1} + B_\Phi \Phi_{i,j}^{n+1} + C_\Phi \Phi_{i+1,j}^{n+1} = D_\Phi \tag{6.41}$$

   where, Φ is used for $u,\ v$ and T and $A_\Phi,\ B_\Phi$, and C_Φ together forms the coefficient matrix and D_Φ represents the pressure and source terms for Φ at n^{th} time step. This system of equations in turn can be written in the form of matrices in which the coefficient matrix is in tri-diagonal form.

2. As the energy and momentum equations can be coupled, a block elimination procedure has been employed to deal with this system of equations.

3. The successive under relaxation method is employed to solve the associated pressure equation that is an analogue of Poisson equation.

4. The pressure correction is used to update the velocity field at each cell.

The following convergence criteria is employed throughout the computations,

$$|\varepsilon_{i,j}^{n+1} - \varepsilon_{i,j}^{n}| < \epsilon \tag{6.42}$$

where, ε is used for $u,\ v$ or T, n is the time level, i, j represent the cell index and ϵ is the tolerance which is taken as 10^{-5}.

6.3.2 Grid independency & Code validation

The code validation and grid independency test is presented in Fig. 6.2(a) by considering the grid size between 81×81 to 121×121 and compared with the results of Ghasemi et al. [77]. The results show the variation of average Nusselt number with varying Hartmann number from 0 to 60 for $Ra = 10^5$, $\phi = 0.03$ and $Pr = 6.2$ in natural convection flow of nanofluids in the presence of magnetic field. The results did not change for grid size of 101×101 and higher. Hence, for the present study the grid size of 101×101 is chosen for all the computations.

Another code validation test is conducted and compared with the outcomes of Sathiyamoorthy et al. [195] for average Nusselt number with varying Rayleigh number from 10^3 to 10^6 for $Da = 10^3$ and $Pr = 0.7$ and represented in Fig. 6.2(b). The results show the variation of average Nusselt number with Rayleigh number for clear fluid in porous domain. Our results found to be in excellent agreement with those of Sathiyamoorthy et al. [195].

Ho et al. [90] made an experimental study on Al_2O_3-water nanofluid, the results are presented in the form of average Nusselt number at varying Rayleigh numbers for different nanoparticle volume fractions. Fig. 6.2(c) shows the comparison of average Nusselt number at different Rayleigh numbers with $\phi = 0.001$. The results are found to be in good agreement with the experimental results by Ho et al. [90]. The comparison for the validation of entropy generation is made with the results of Basak et al. [20]. The study of entropy generation in a porous cavity is made by considering five different cases of natural convection in square cavity. The presented comparison in Fig.6.2(d) is made with case 5 of the study and the results are found to be in a good agreement with the results of Basak et al. [20].

6.4 Results and discussion

The MHD study of electrically conducting nanofluid flow in a porous medium is presented with discrete time periodic heat source along the left vertical wall whereas the opposite wall (right) is maintained at a constant but lower temperature. The results are presented with the variation of Grashof number ($10^4 \leq Gr \leq 10^6$, to measure the thermal buoyancy effects in natural convection), Hartmann number ($1 \leq Ha \leq 50$, to measure the magnetic field effects), Darcy number ($0.001 \leq Da \leq 1.0$, measuring the effect of porosity) and ϕ ($0.0 \leq \phi \leq 0.2$, to measure the effect of nanoparticle volume fraction on heat transfer) to obtain the effective heat transfer with a fixed Prandtl number ($Pr = 6.2$). The outcomes are discussed using streamlines, isotherms, energy flux vectors, Nu_m (to measure the average heat transfer near the heat source), S_m (to measure the total entropy release) and Be (measuring the dominance of irreversibility due to heat transfer over the irreversibility due to fluid friction and magnetic field).

The transient behavior of fluid flow and heat transfer enhancement due to natural convection at various time levels is presented in the form of streamlines and isotherms in Fig. 6.3 for $Gr = 10^4$, $Ha = 10$, $Da = 0.001$ and $\phi = 0.0$. As the process starts the fluid adjacent to the time periodic heated zone on left vertical wall gets activated. A small clockwise rotating circulation zone is formed near the heat source due to conduction effect. With the increase of time the circulation zone move towards the right section of the enclosure and stacked at the cold part of the enclosure. It is observed that, as time proceeds the heat transfer increases resulting the increment of flow velocity. At $t = 0.05$, the stream vortex formed a vertical oval shape adjacent to the hot wall and move towards the right section as time increases. The vortex becomes stronger as time increases to $t = 0.30$ representing a circular shape along the central part of the enclosure defines a shift of heat transfer mode from conduction to convection. For higher time levels the shape deformed to a elliptical shape, representing a fully convection dominated mode of heat transfer.

The isotherms at varying time spans represent the corresponding growth of heat transfer rate with increase in time. At small time levels, it is observed that a semi-elliptical thermal zone is formed near the thermally activated region due to the effect of thermal

boundary layer. From Fig. 6.3, the movement of heat transfer lines value at 0.20 is clearly observed as time increases from $t = 0.10$ to $t = 0.15$. For further increment of time the isotherms expand and move towards the central zone and the thermal boundary layer has less influence on heat transfer shows a convection mode of heat transfer rate. A secondary vortex starts to appear along the right cold wall at $t = 0.25$ and the heat transfer of fluid is getting stronger and achieved a steady state when the isotherms coincides with each other. No further improvement of heat transfer is observed around the right vertical wall after $t = 0.50$, i.e., always represents the same value closed to the right wall.

Fig. 6.4 represents the streamlines, isotherms and energy flux vectors for $Gr = 10^4,\ 10^5$ and 10^6 at $Ha = 50,\ Da = 0.001$ and $\phi = 0.2$ (dashed lines) when length of heat source is $L/3$. Solid lines in the streamlines and isotherm curves corresponds to $\phi = 0.0$ (clear fluid). As the temperature of the mid active location is higher as compared to the other sections of the wall, the fluid close to the hot region gets heated and loose its density. Weak dense fluid rises above its mean level and forced towards the cold locations of the right vertical wall resulting a faster movement of fluid particles. This movement from hot region to cold region of fluid particles forms a large recirculating clockwise rotating eddy inside the enclosure within which a smaller clockwise eddy is formed with a small stagnant region to avoid the shear instability as represented in Fig. 6.4(a to d).

In Fig. 6.4(a), the streamlines corresponding to $\phi = 0.2$ appears inside the streamlines due to $\phi = 0.0$, i.e., most of the clear fluid occupies outer region of the cavity but with the increase in nanoparticle volume fraction, the shear force increases due to which the fluid lies in the core of enclosure. The isotherms lines corresponding to $\phi = 0.0$ are limited to low values of streamlines as compared to that of $\phi = 0.2$, which shows higher heat transfer rate in case of nanofluids as compared to clear fluid. As Gr increases to 10^5 the streamlines corresponding to clear fluid in the core of the enclosure forms an oval shape, and appears closer to heated region as compared to the streamlines of nanofluid, which is due to the higher effect of buoyancy forces on nanofluid. With further increase of Gr values, it is found that two small eddies rotating clockwise are formed with a small stagnant fluid (Fig. 6.4(g)). The stagnant fluid region started to form a circular shape for $Gr = 10^4$, elongated to elliptical shape for $Gr = 10^5$ and splits into two for $Gr = 10^6$ representing the buoyancy dominated effect as compared to a natural convection effects.

Fig. 6.4(b, e, h) shows that heat transfer lines have maximum variation for the case of $Gr = 10^6$, and the isotherms at mid section becomes almost parallel to the horizontal walls of the enclosure showing the convection dominated flow in the corresponding region. When the heater located on the left wall is switched on, left wall attains the maximum temperature of the mid-plane. A major convection effect is indicated by the energy flux vectors towards the right wall from left part of the enclosure Fig. (6.4(c, f, i)). This is different from steady state outcomes where most of the energy flux vectors are released from the left heated portion. With peak shifts of Grashof number from 10^4 to 10^6, the output pattern of heat transfer lines increasingly changes close to the heater to overcome the sinusoidal variation. The complex non-linear features increases with the increase of Gr because of higher convective fluid flow. The interaction of two different fluids (cold and hot) creates a complex flow pattern as observed in Fig. 6.4(g). The energy flux vectors are weaker for low Gr values and getting stronger, and showing a clear flow of energy flux from left heated portion to the right cold portion through the upper region of enclosure for increasing Gr values.

Fig. 6.5 shows the streamlines, isotherms and energy flux vectors for $Gr = 10^4$, 10^5 and 10^6 at $Ha = 50$, $Da = 0.001$, $\phi = 0.2$ (dashed lines) when heat source length is $L/2$. The solid lines in the streamlines and isotherms represent the lines corresponding to $\phi = 0.0$. The streamline values are found to be slightly increased at the central region of the enclosure in Fig. 6.5 as compared to Fig. 6.4 for smaller Grashof number ($Gr = 10^4$ and 10^5) but, a significant increase is observed when $Gr = 10^6$ due to higher heat transfer rate in case of clear fluid as well as nanofluid. At $Gr = 10^4$, no density variation is found within the enclosure that predominates a single cellular flow pattern where heated fluid accelerates along the left wall and cold fluid moves down along the right wall represented in Fig. 6.5(a).

The streamlines corresponding to nanofluid shows higher deviation into the opposite direction of heat source as compared to the clear fluid, this effect is almost negligible at $Gr = 10^4$ when heat source length is $L/3$. With the increase of Gr, a density inversion is observed inside the enclosure resulting a dual cell pattern. At this stage, the conductive mode of heat transfer is transferred to convective mode. At $Gr = 10^6$, a pair of center rotating cells appeared with maximum density variations and energy transfer along the

center of the enclosure due to expansion of anomalous density of water represented in Fig. 6.5(g and i). The thermal boundary layers near the heated portion appeared to be larger with larger heat source length. The isotherms are distributed in vertically upward direction for small Gr and as Gr increases the hot fluid moves in upward direction due to buoyancy effect and drives the cold fluid in opposite direction, which give rise to the convection force. The central region of the energy flux vectors at $Gr = 10^5$ and 10^6 is more dense as compared to the previous case (Fig.6.4) where heat source length is $L/3$. The energy flux vectors moves from hot to cold region as the density variation is maximum for $L/2$.

In Fig. 6.6, the steady state streamlines, isotherms and energy flux vectors are presented to show the effect of Darcy number for $Gr = 10^5$, $Ha = 50$ and $\phi = 0.20$ when length of heat source is $L/3$. The intensity of the primary flow is increased due to the increase in Da. Low Da number represents an elliptic shape of streamlines in the core of the enclosure for $Da = 0.001$. Since the flow is dominated by porosity hence, with the increase of Da number from 0.001 to 0.01, the streamline value along the core is increased from 0.005 to 0.012. With an increase in Darcy number, the cellular pattern shifts to form multicellular and the dual cells separated from the flow at the core as depicted in Fig. 6.6(g) and 6.6(j). The flow represents a major conductive cell with a minor inner cell for small Darcy number and develops a convective regime as the heated fluid confines to the boundary layer retarded by the applied magnetic field.

The isotherms are almost parallel, straight and horizontal reflecting a convective mode of heat transfer for all Da values as shown in Fig. 6.6(b, e, h and k). The heat transfer is found to be maximum when Da canges from 0.001 to 0.01. Since the clockwise rotating cell expands and moves away from hot boundaries. The convective heat transfer can be clearly observed from energy flux vector plots. The energy flux vectors for $Da = 0.001$ are less dense representing lower convection effects but with the increase in Da values the energy flux vectors becomes stronger and forms circular movement of vectors in the core of enclosure. The energy flux vectors originated from the left active region, pass through upper region and eliminates from the right cold portion of enclosure. For higher Da values, the upper region of the enclosure is mostly occupied by the energy flux vectors, representing the existence of higher convective forces.

The average heat transfer on the left wall is calculated in terms of average Nusselt number. Total entropy generation by the combined effect of irreversibilities due to heat transfer, fluid friction and magnetic field is calculated using entropy generation. The analysis for the optimum heat transfer on the cost of least entropy generation is discussed using the ratio of average Nusselt number with total entropy generation. The dominating characteristics of irreversibility due to heat transfer over irreversibility due to fluid friction and magnetic field is analyzed through Bejan number.

The comparison of average heat transfer and entropy generation with different combination of heat source locations on the vertical walls including Middle-Middle, Top-Top, Bottom-Bottom, Bottom-Top and Top-Bottom combinations for $Gr = 10^6$, $Ha = 50$, $Da = 0.001$ and $0.0 \leq \phi \leq 0.2$ are presented in Fig. 6.7. The heat transfer is found to be increasing with nanoparticle volume fractions for all combinations, but, in the case of Top-Top combination, the increment is lower as compared to other combinations as shown in Fig. 6.7(a). The heat transfer is maximum in case of Bottom-Top combination and is minimum in Top-Bottom combination. The entropy generation for different combinations is represented in Fig.6.7(b) and is found to be maximum when both the sources are placed at Middle-Middle locations and minimum in case of Top-Bottom combination. The increment in entropy generation with nanoparticle volume fraction is found to be minimum in case of Bottom-Bottom combination.

Fig. 6.8 shows the local entropy generation due to (a) heat transfer, (b) fluid friction, (c) magnetic field and (d) total entropy generation due to combined effect of heat transfer, fluid friction and magnetic field irreversibilities for $Gr = 10^5$, $Ha = 10$, $Da = 0.001$ with $\phi = 0.0$ (solid lines) and $\phi = 0.2$ (dashed lines). The irreversibility due to heat transfer is found to be the most dominating factor in the entropy generation inside the system as compared to the irreversibility due to fluid friction and magnetic field. Major contribution of heat transfer irreversibility is found in the middle horizontal part of the enclosure and is maximum near the heat source locations as shown in Fig. 6.8(a). Minimum contribution of the local entropy generation in the system is found to be of fluid friction irreversibility, and maximum values are found near the side walls of the enclosure as shown in Fig. 6.8(b).

The local entropy generation due to magnetic field irreversibility is shown in Fig.

6.8(c). The irreversibility due to magnetic field mostly occurred along the lower and upper part of the enclosure. But the contribution of entropy generation due to magnetic field to the total entropy generation in the enclosure is much smaller as compared to the entropy generation due to heat transfer. From Fig. 6.8(d), it is clearly observed that the total entropy generation inside the enclosure is almost similar to the entropy generation due to heat transfer which shows that the contribution of heat transfer entropy generation is much higher as compared to other factors of entropy generation. Also, it is evident from Fig. 6.8(a to d) that the entropy generation in case of clear fluid ($\phi = 0.0$) is less distributed as compared to that of nanofluid ($\phi = 0.2$), which reveals that the entropy generation at higher nanoparticle volume fraction is more as compared to clear fluid.

Increasing Gr values leads to a considerable change in the heat transfer and entropy generation. Fig. 6.9 represents the variation in average heat transfer, entropy generation and Bejan number for different values of Grashof number and nanoparticle volume fraction at $Ha = 50$ with $Da = 0.001$. Both the volume fraction and Grashof number show a positive impact on the average heat transfer. From Fig. 6.9(a), the absolute increase in average Nusselt number is found to be 0.2128 for $Gr = 10^4$, 0.1196 for $Gr = 10^5$ and 0.5313 for $Gr = 10^6$ on increasing the nanoparticle volume fraction by 20%. The increment of volume fraction in nanofluids depicts an increment of the thermal conductivity and viscosity of nanofluid resulting a combined variation of heat transfer and fluid friction. Similarly, from Fig. 6.9(b), the absolute increase in average entropy generation in the enclosure is found to be 0.1138, 0.0475, 0.2541 for $Gr = 10^4$, $Gr = 10^5$ and $Gr = 10^6$ respectively on 20% increment of volume fraction.

With the change in Grashof number together with nanoparticle volume fraction we tried to obtain the ratio of heat transfer to entropy generation. The maximum heat transfer on the cost of minimum entropy generation is found to be at $Gr = 10^4$ with $\phi = 0.0$ when $Ha = 50$ and $Da = 0.001$ as shown in Fig. 6.9(c). Fig. 6.9(d) represents the Bejan number variation with Gr and ϕ at $Ha = 50$ and $Da = 0.001$ and the value of Bejan number is found to be greater than 0.5 for all values of Gr and ϕ which shows the entropy generation dominance due to heat transfer over entropy generation due to magnetic field and fluid flow. Although, the maximum heat transfer is obtained at higher

values of Grashof number but at the same time the entropy generation attains its maximum values for these parameters. In a recent study Torabi et al. [231] discussed the performance evaluation criteria as a factor for higher heat transfer rate with minimum entropy generation. A similar performance evaluation criteria (PEC=Nu_m/S_m) is used in the present study for obtaining higher heat transfer rate on the cost of low entropy generation and is shown in Fig. 6.9(c), where the maximum performance is observed at $Gr = 10^4$ with $\phi = 0.0$.

The average Nusselt number for various Ha and ϕ at $Gr = 10^6$ and $Da = 0.001$ is shown in Fig. 6.10(a). The effect of variation in Ha is found to be almost negligible on Nu_m for all ϕ values, but a considerable increase in average Nusselt number is found on increasing nanoparticle volume fraction. Nu_m is found to be maximum at $Ha = 1.0$ with $\phi = 0.20$ with $Nu_m = 2.2279$. The absolute decrease in Nu_m on increasing Ha from 1 to 50 is 0.0059. But Nu_m is increased upto 0.5313 when ϕ is increased from 0.0 to 0.20, at $Ha = 50$. The average entropy generation is found to be maximum when $Ha = 50$ and $\phi = 0.20$ as shown in Fig. 6.10(b). The change in S_m is observed to be almost negligible on increasing Ha from 1 to 10, whereas on increasing the Ha value from 10 to 50 a noticeable change is found in S_m. S_m is increased by 0.2265 at $\phi = 0.0$ and 0.2541 at $\phi = 0.2$ when $Ha = 50$.

From Fig. 6.10(c), maximum heat transfer at the cost of minimum entropy generation is found at $Ha = 1$ with $\phi = 0.20$ as the value of Nu_m/S_m is maximum. The values of Nu_m/S_m at $Ha = 1$ are almost same as that of $Ha = 10$. The variation of Bejan number with variation of Ha and ϕ values are shown in Fig. 6.10(d). Be values are greater than 0.5 for all Ha and ϕ, which signifies that irreversibility due to heat transfer is dominant over irreversibility due to magnetic field and fluid flow. Be is maximum when $Ha = 1$, and the entropy generation due to heat transfer is maximum when $Ha = 1$. It can be observed from Fig. 6.10(c) and 6.10(d) that the Nu_m/S_m values at $Ha = 1$ and 10 are almost same but a noticeable difference is found in Be values at $Ha = 1$ and 10. Hence, it can be concluded that heat transfer entropy generation is more when $Ha = 1$ as compared to $Ha = 10$ (from Fig. 6.10(d)), whereas the total entropy generation is almost same for these values. Finally, from Fig. 6.10(c) it can be concluded that maximum performance of system can be obtained at $Ha = 1$ with $\phi = 0.20$ when $Gr = 10^6$ and $Da = 0.001$, as

the higher values of Ha leads to higher entropy generation in the system and decreases the performance level.

Fig. 6.11(a) shows the variation of Nu_m with corresponding Da and ϕ values. The effect of increasing Da is clearly seen on Nu_m when Da values are increased from 0.001 to 0.1, but increase in Nu_m becomes almost negligible when Da is increased from 0.1 to 1.0. Also, it is clear from the figure that for higher values of Da the difference between various values of Nu_m decreases (Fig. 6.11(a)) but the difference between S_m is clearly visible for higher values of Da. The absolute increase in Nu_m on increasing Da from 0.001 to 1 is found to be 0.3872, 0.4692, 0.5621 and 0.7873 for ϕ =0.0, 0.05, 0.1 and 0.2 respectively. Similarly, the increment in S_m in absolute form on increasing Da from 0.001 to 1 is found to be 0.4064, 0.4867, 0.5805 and 0.8227 for ϕ =0.0, 0.05, 0.1 and 0.2 respectively.

The optimum value for maximum heat transfer and minimum entropy generation is obtained at $Da = 0.001$ and $\phi = 0.2$ for $Gr = 10^6$ and $Ha = 50$, where Nu_m/S_m is 1.3286 as shown in Fig. 6.11(c). Fig. 6.11(d) shows the variation of Be with Da and ϕ at $Gr = 10^6$ and $Ha = 50$. The heat transfer irreversibility is dominant over irreversibility due to magnetic field and fluid friction for $Da \geq 0.1$ for all values of ϕ except when $\phi = 0.2$. When $Da = 1$, the heat transfer irreversibility is dominant in case of clear fluid, but with the involvement of nanoparticles in the fluid the combined effect of magnetic field and fluid friction irreversibility is dominant over heat transfer irreversibility. The least value of Be is found for $\phi = 0.2$ with $Da = 1$.

6.5 Conclusion

Heat transfer and entropy generation inside a closed chamber is encountered in various industrial applications, such as geothermal energy extraction, nuclear waste storage, solidification process of metals and alloys etc. A finite volume simulation has been carried out for the numerical study of heat transfer and entropy generation of a MHD flow inside a porous medium. Time periodic boundary conditions are used for temperature distribution on the mid portion of left wall and the adjacent side wall is maintained at comparatively cold temperature. Time history analysis has been presented for $Gr = 10^4$, $Ha = 10$, $Da = 0.001$ and $\phi = 0.0$. Further, for the discussion of PEC the results are calculated

for $10^4 \leq Gr \leq 10^6$, $1 \leq Ha \leq 50$, $0.001 \leq Da \leq 1$ and $0.0 \leq \phi \leq 0.2$. The important results of the conducted study have been listed as follows:

1. The flow is dominated by convection effects when Gr values shifts from 10^4 to 10^5. For higher values of Grashof number the fluid is well mixed and more entropy is generated.

2. Higher heat transfer and entropy generation is found for higher Grashof number. But the ratio of average Nusselt number to average entropy is large when $Gr = 10^4$, which shows the higher heat transfer on the cost of least entropy generation.

3. Based on the results obtained, it can be concluded that for $Gr = 10^6$ and $Ha = 50$, the maximum heat transfer on the cost of least entropy can be obtained when $Da = 0.001$ with $\phi = 0.2$.

4. It is found that when $Gr = 10^6$ and $Da = 0.001$, the rate of heat transfer is almost constant for varying Ha, but the entropy generation is higher when Ha is increased from 10 to 50. The heat transfer irreversibility is found to be dominant over magnetic field and fluid friction irreversibility. The total entropy generation is almost equal at $Ha = 1$ and 10, but the entropy generation due to heat transfer is more when $Ha = 1$ as compared to $Ha = 10$.

5. The average heat transfer rate increases with increase in Da, but it become constant for $Da > 0.1$. Total entropy generation in the system increases with increase in Da. The heat transfer irreversibility is dominant over irreversibility due to magnetic field and fluid friction when $Da > 0.1$. For $Da = 0.1$, the irreversibility due to heat transfer is dominant for $\phi \leq 0.1$ and for $Da = 1$ heat transfer irreversibility is found to be dominant for clear fluid (i.e. $\phi = 0.0$).

6. The fractional increment of Cu nanoparticles in water increases the heat transfer rate very effectively.

Table and Figures

Table 6.1: Thermophysical properties of water and copper [142].

Property	Water	Copper
C_p	4179	383
ρ	997.1	8954
k	0.6	400
β	2.1×10^{-4}	1.67×10^{-5}
σ_e	0.05	5.96×10^{7}

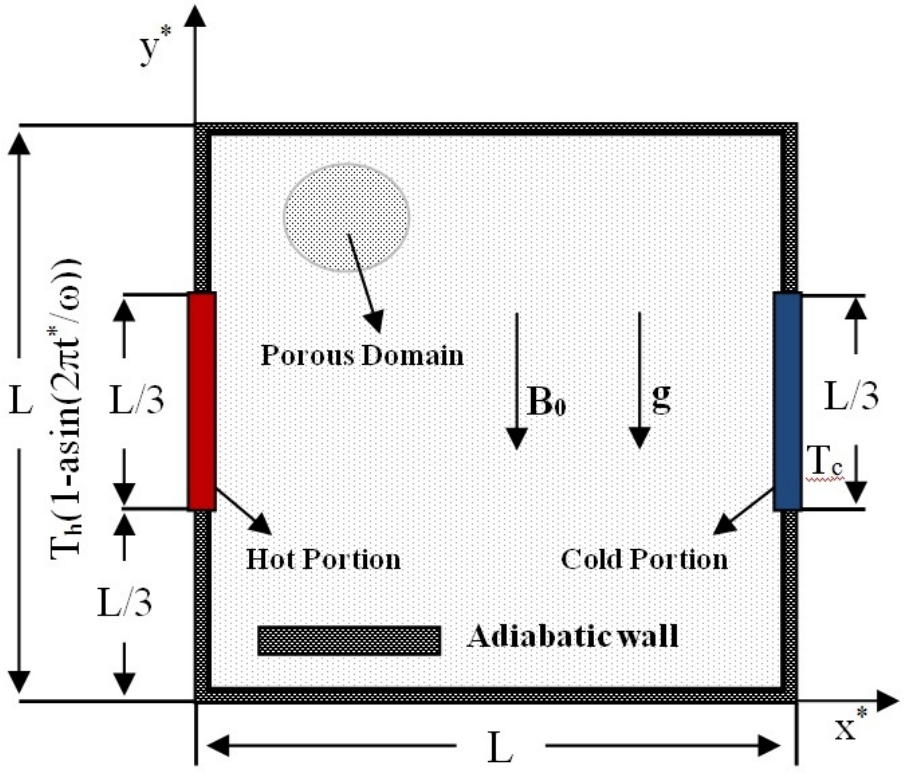

Figure 6.1: Physical Configuration.

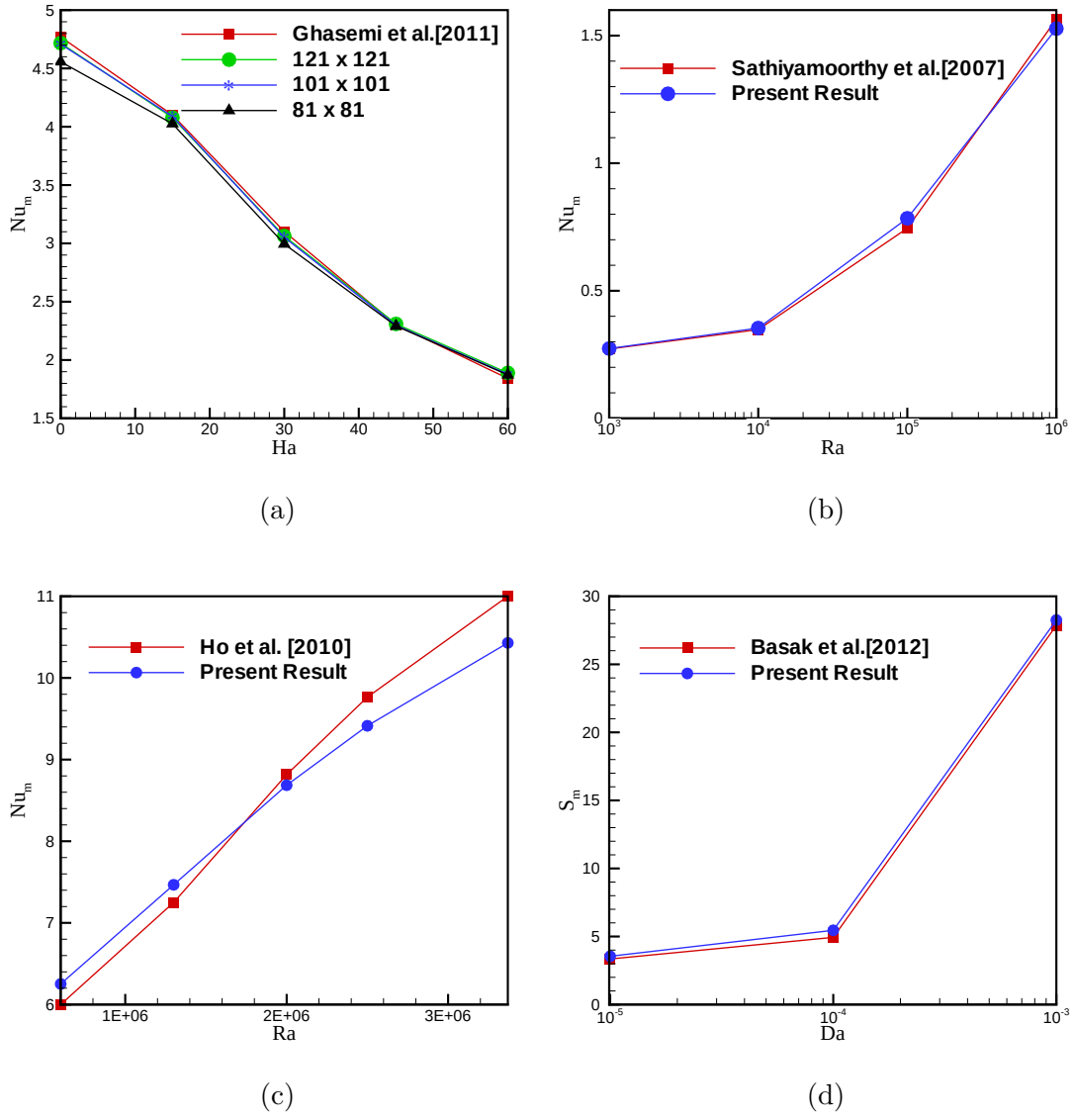

Figure 6.2: Comparison of average Nusselt number with (a) the results of [77] for $Ra = 10^5$, $\phi = 0.03$, $Pr = 6.2$ and $0 \leq Ha \leq 60$ for various grid size from 81×81 to 121×121, (b) the results of [195] for $Da = 10^3$, $Pr = 0.7$ and $10^3 \leq Ra \leq 10^6$, (c) the results of [90] for $6 \times 10^5 \leq Ra \leq 3.37 \times 10^6$ at $\phi = 0.001$, (d) the results of [20] for $Ra = 5 \times 10^5$ with $10^{-5} \leq Da \leq 10^{-3}$ at $Pr = 10$.

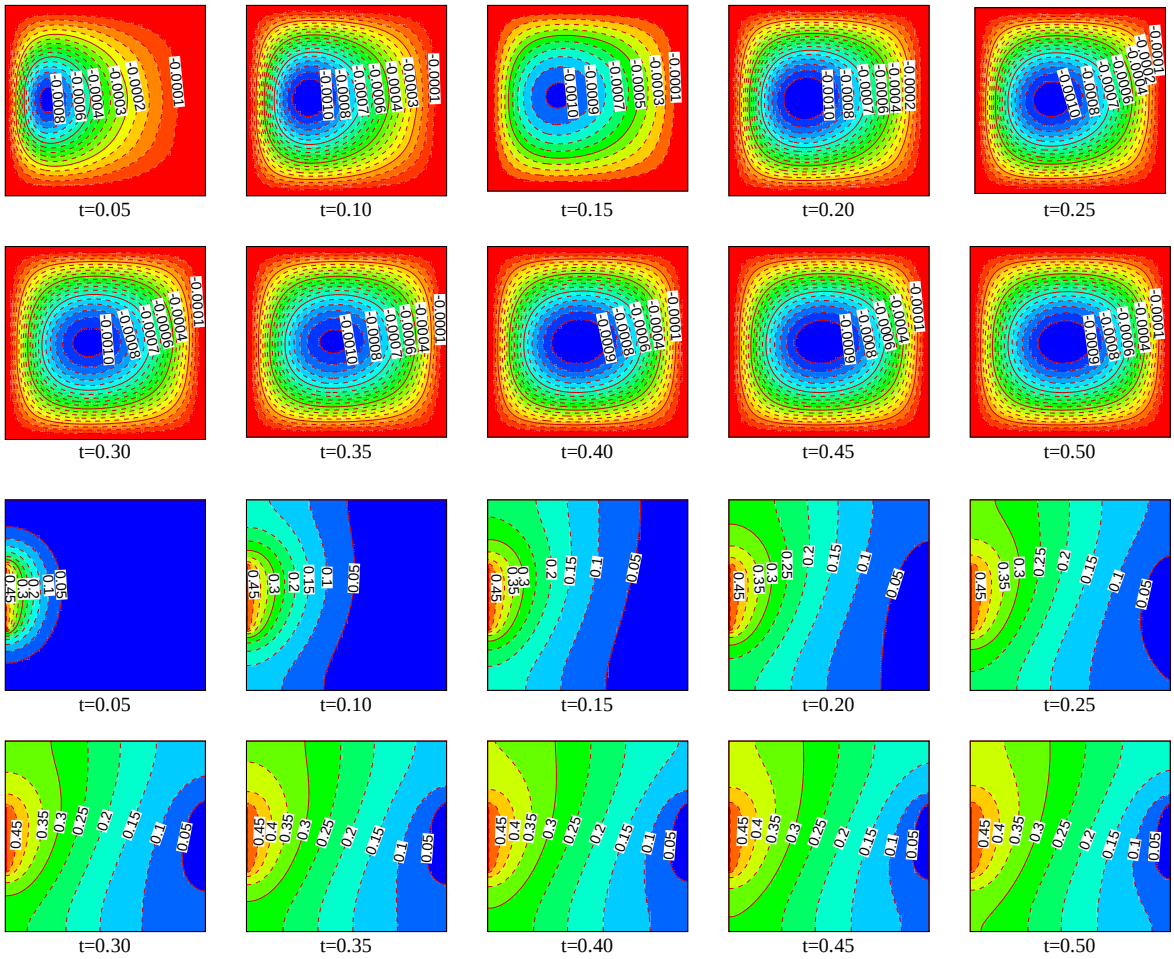

Figure 6.3: Development of streamlines and isotherms at different time levels with improvement of time for $Gr = 10^4$, $Ha = 10$, $Da = 0.001$ and $\phi = 0.0$

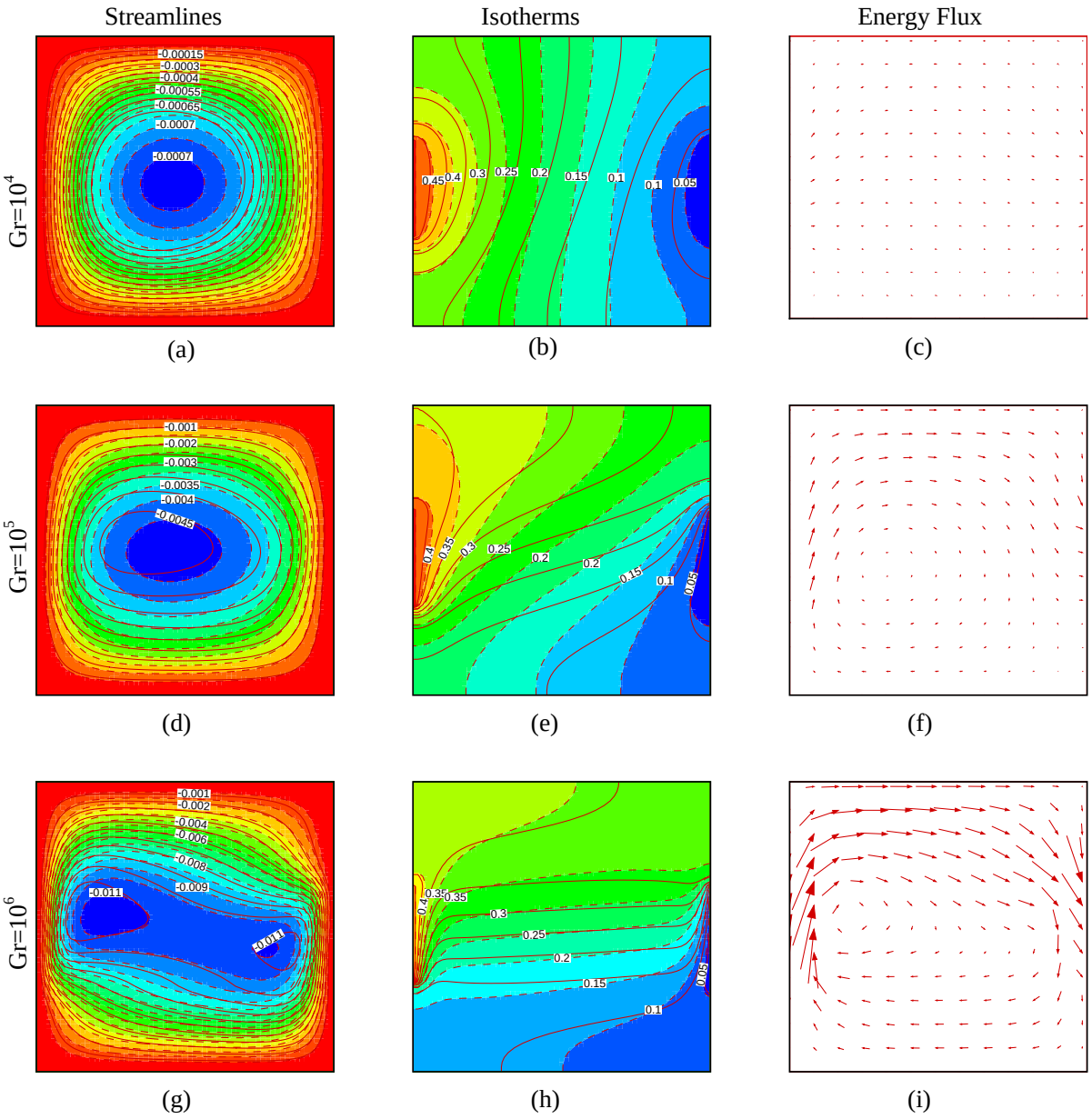

Figure 6.4: Streamline, isotherm and energy flux vector plots at $Ha = 50$, $Da = 0.001$ with $\phi = 0.0$ (solid lines) and $\phi = 0.20$ (dashed lines) for $10^4 \leq Gr \leq 10^6$ when heat source length is $L/3$.

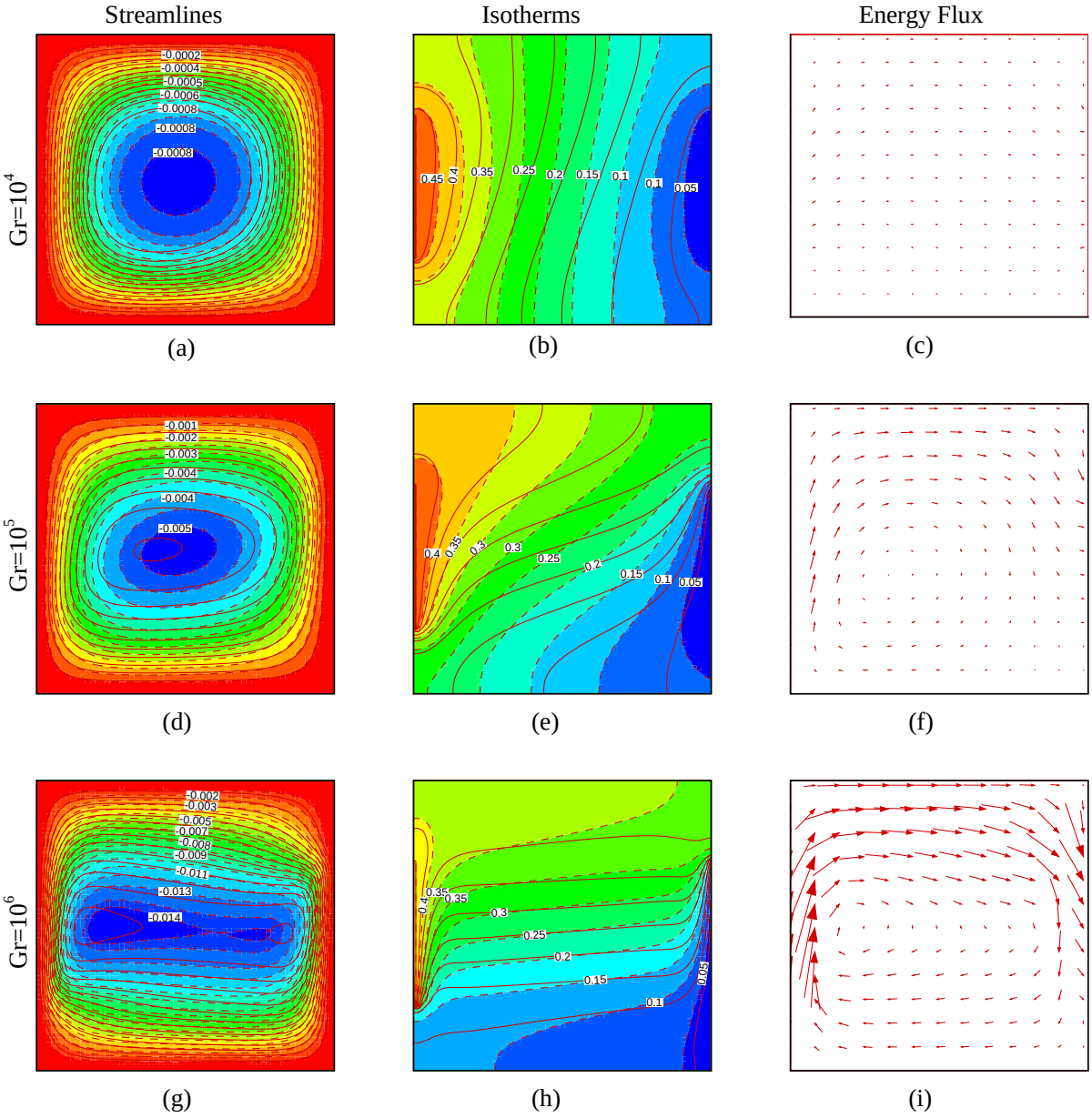

Figure 6.5: Streamline, isotherm and energy flux vector plots at $Ha = 50$, $Da = 0.001$ with $\phi = 0.0$ (solid lines) and $\phi = 0.20$ (dashed lines) for $10^4 \leq Gr \leq 10^6$ when heat source length $L/2$.

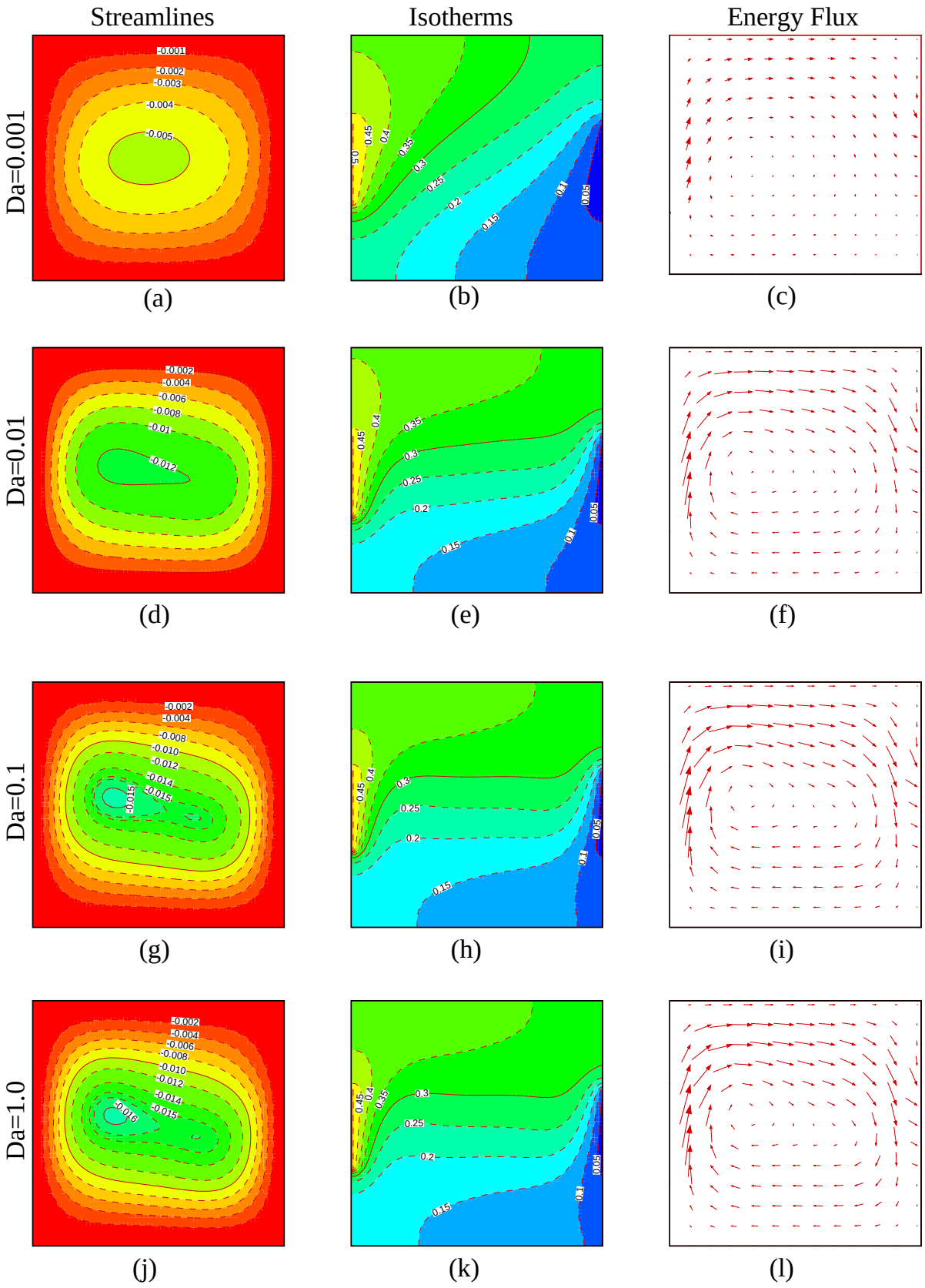

Figure 6.6: Streamline, isotherm and energy flux vector plots at $Gr = 10^5$, $Ha = 50$ and $\phi = 0.20$ for $0.001 \leq Da \leq 1.0$.

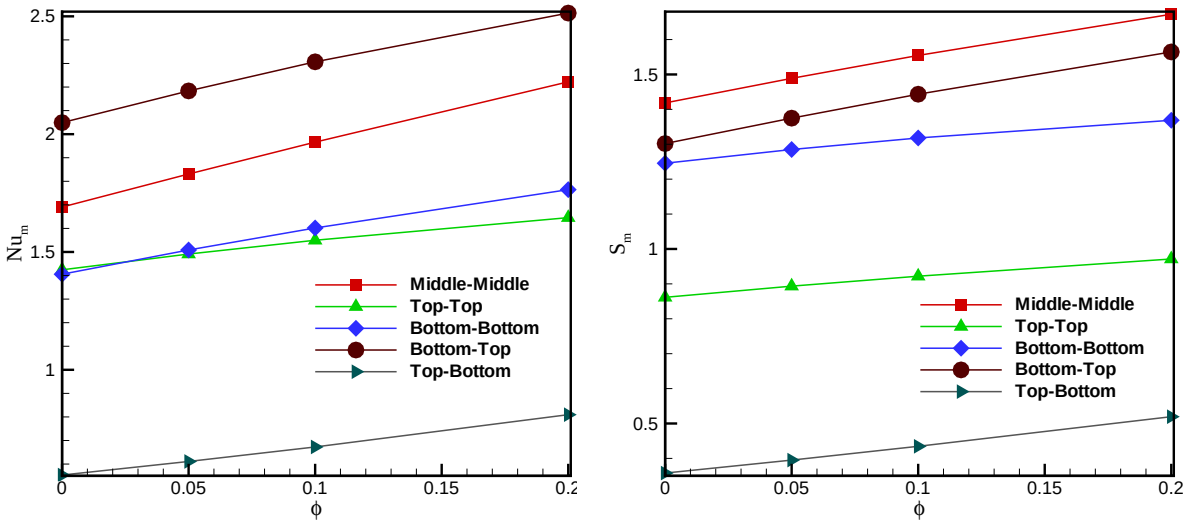

(a) (b)

Figure 6.7: Comparison of (a) average heat transfer and (b) entropy generation with different heat source locations at $Gr = 10^6$, $Ha = 50$, $Da = 0.001$ and $0.0 \leq \phi \leq 0.2$.

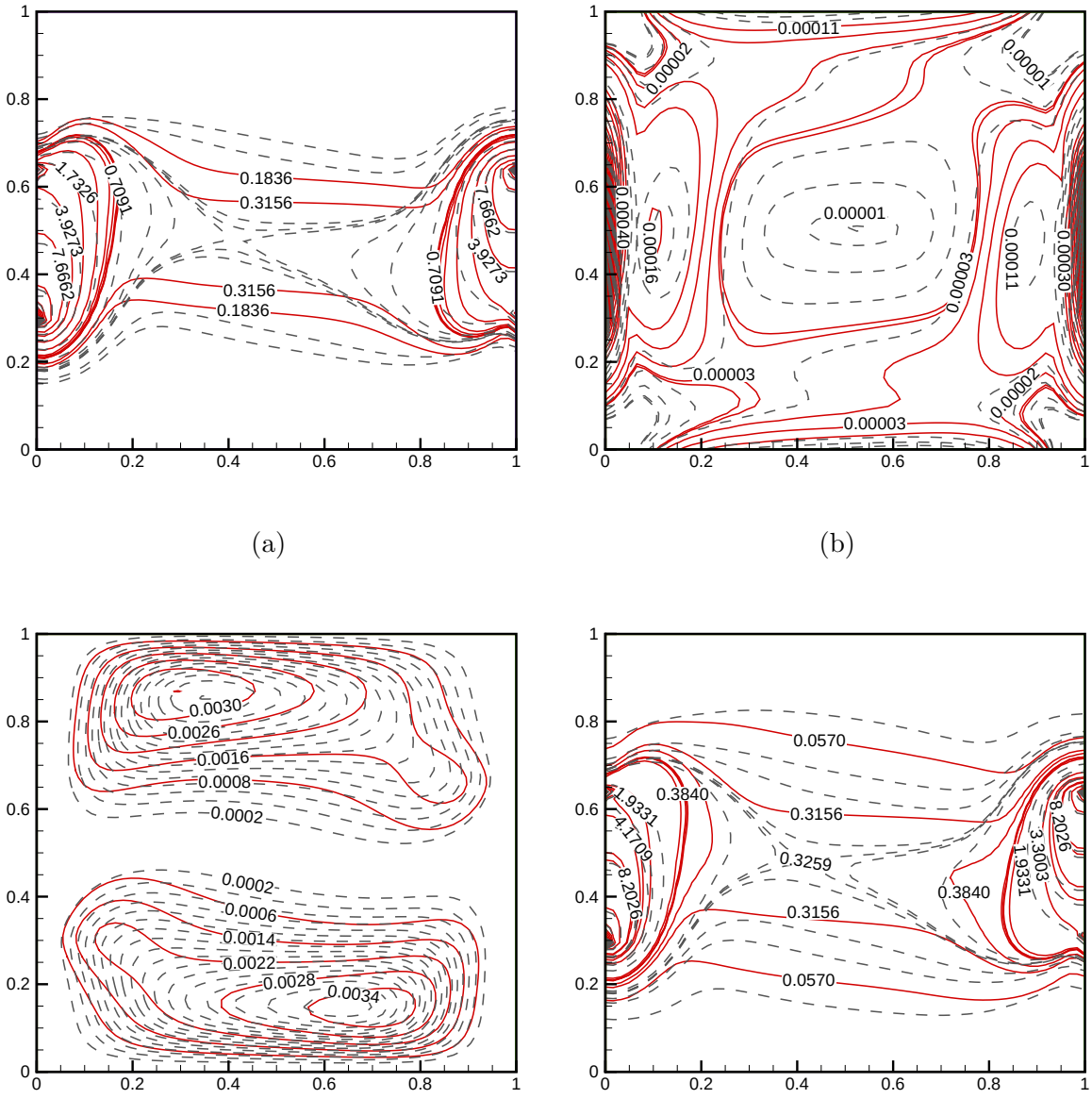

Figure 6.8: (a) Local entropy generation due to heat transfer, (b) local entropy generation due to fluid friction, (c) local entropy generation due to magnetic field and (d) Total entropy generation at $Gr = 10^5$, $Ha = 10$ $Da = 0.01$ with $\phi = 0.0$ (solid lines) and $\phi = 0.2$ (dashed lines).

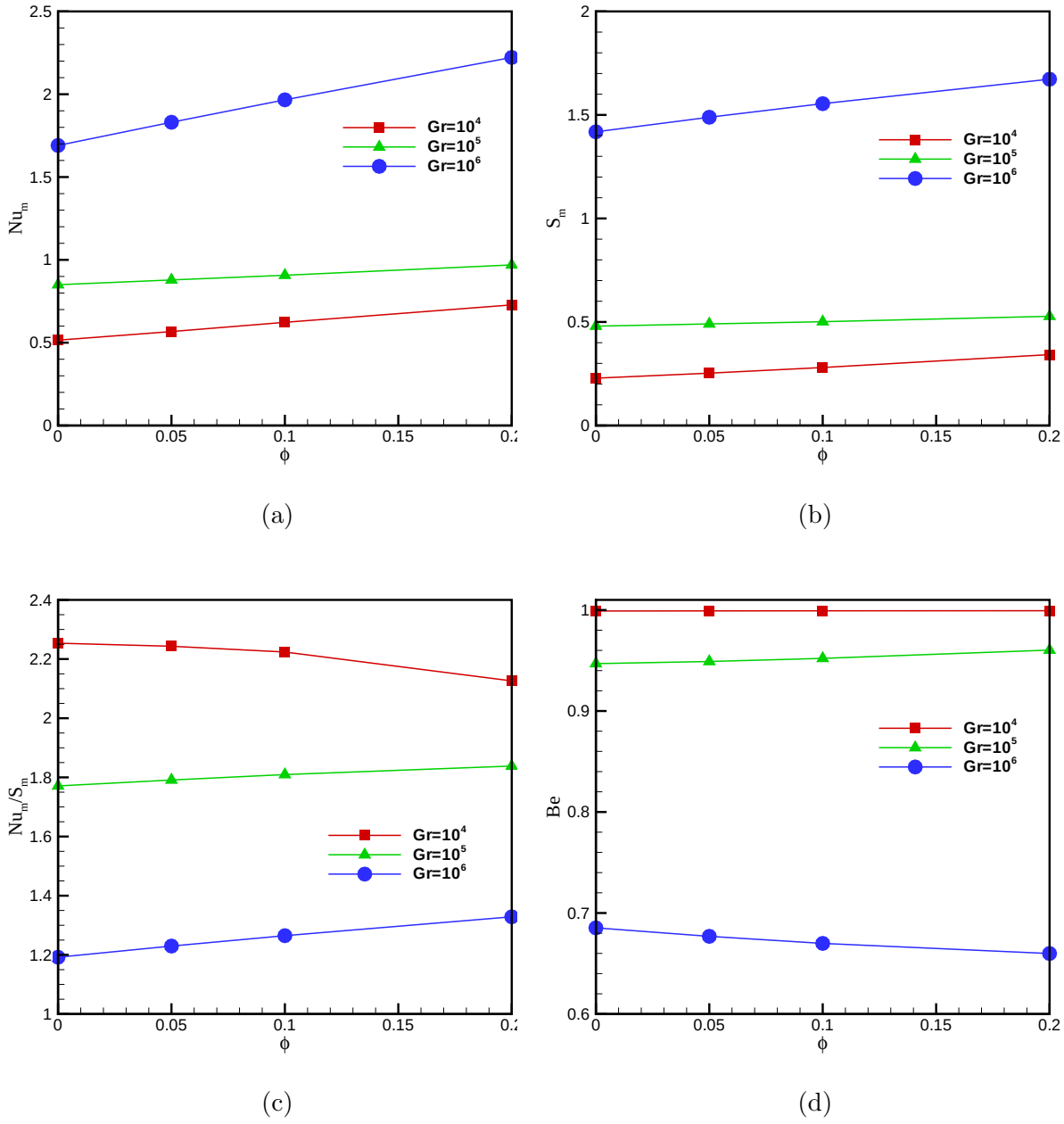

Figure 6.9: (a) Average heat transfer, (b) entropy generation, (c) PEC (Nu_m/S_m) and (d) Bejan number with variation of ϕ and Gr at Ha=50, Da=0.001.

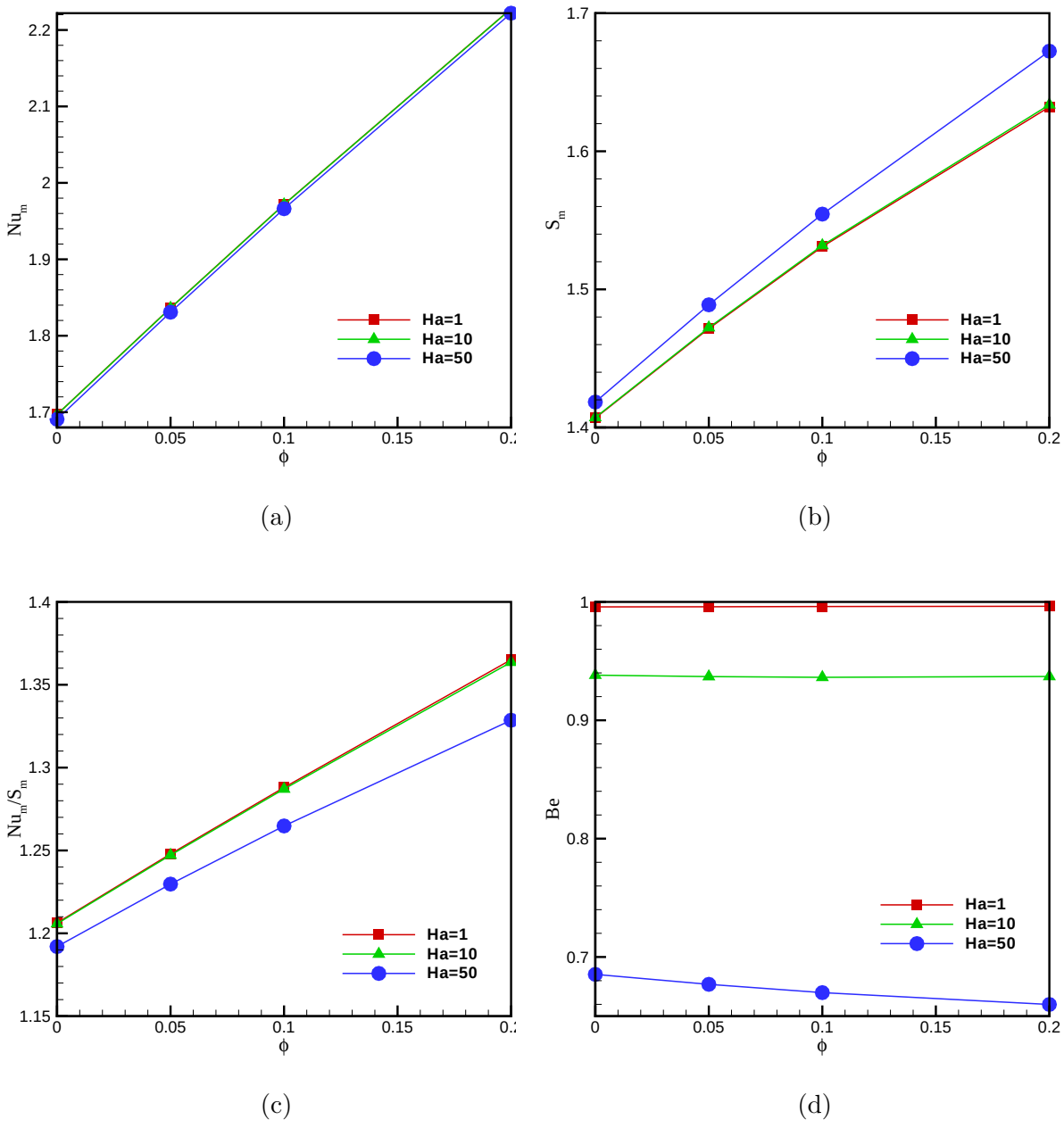

Figure 6.10: (a) Average heat transfer, (b) entropy generation, (c) PEC (Nu_m/S_m) and (d) Bejan number with variation of ϕ and Ha at $Gr = 10^6$, $Da = 0.001$.

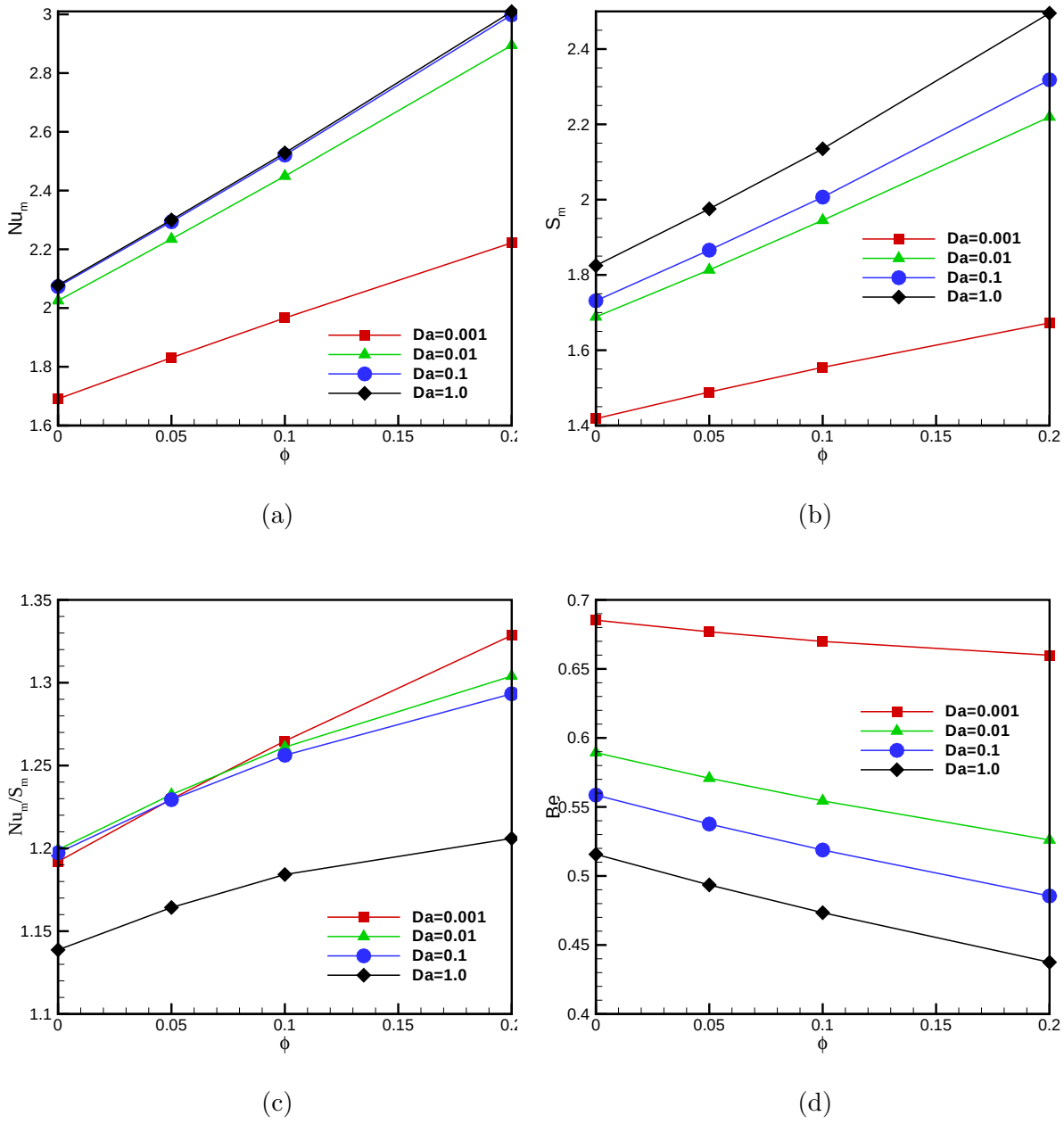

Figure 6.11: (a) Average heat transfer, (b) entropy generation, (c) PEC (Nu_m/S_m) and (d) Bejan number with variation of ϕ and Da at $Gr = 10^6$, $Ha = 50$.

Chapter 7

Future Scope

The work of the thesis can be extended in various directions. Some of the future works to be carried out are listed follows.

- Numerical investigation of nanofluid flows in open channels with porous obstacle.
- Entropy generation of nanofluid flows in microchannels.
- Entropy generation analysis of MHD nanofluid flow in a porous enclosure.
- Two phase dynamics of nanofluid flows can be studied and the following problems can be formulated.
- Analysis of various kinds of nanofluids and their applicability in different domains.
- Phase analysis and surface interaction of nanofluids.
- Mathematical modeling of Interface effect and fluid friction activities in nanofluid flows.

Appendix A

Appendix A: Alternating-Direction Implicit Method

The ADI method, due to Peaceman and Rachford (1955), is a very popular iterative method for solving the Laplace equation based on line-by-line iteration. The advantage of this particular technique is that, in the SOR method, the number of iterations required for convergence increases with the size of mesh, while in ADI technique, it is almost independent of the size of the mesh (Roache (1985)). ADI method is, therefore, preferable, particularly for a large size of mesh.

This section is concerned with the numerical solution of the equation

$$\frac{\partial u}{\partial t} = K\left(\frac{\partial^2 u}{\partial x^2} + \frac{\partial^2 u}{\partial y^2}\right), \tag{A.1}$$

over the rectangular region $0 < x < a, 0 < y < b$, where u is known initially at all points within and on the boundary of the rectangle, and is known subsequently at all points on the boundary. Define the co-ordinates (x_i, y_i, t_n), of the mesh points of the solution domain by

$$x_i = i\delta x, \quad y_j = j\delta y, \quad t_n = n\delta t$$

where i, j, n are positive integers, and denote the values of u at these mesh points by

$$u(i\delta x, j\delta y, n\delta t) = u^n_{i,j}.$$

The explicit finite-difference representation of equation A.1

$$\frac{u^{n+1}_{i,j} - u^n_{i,j}}{\delta t} = \frac{K}{(\delta x)^2}\left(u^n_{i-1,j} - 2u^n_{i,j} + u^n_{i+1,j}\right) + \frac{K}{(\delta y)^2}\left(u^n_{i,j-1} - 2u^n_{i,j} + u^n_{i,j+1}\right)$$

appears attractively simple but is computationally laborious because the condition for its validity, which is

$$K\left(\frac{1}{(\delta x)^2} + \frac{1}{(\delta y)^2}\right) \leq \frac{1}{2}$$

necessitates extremely small values for δt. For most problems it is an impractical method.

The Crank-Nicolson method, namely

$$\frac{u_{i,j}^{n+1} - u_{i,j}^{n}}{\delta t} = \frac{K}{2}\left[\left(\frac{\partial^2 u}{\partial x^2} + \frac{\partial^2 u}{\partial y^2}\right)_{i,j}^{n} + \left(\frac{\partial^2 u}{\partial x^2} + \frac{\partial^2 u}{\partial y^2}\right)_{i,j}^{n+1}\right]$$

is valid for all values of $\delta x, \delta y$ and δt, but requires the solution of $(N-1)\times(M-1)$ simultaneous algebraic equations for each step forward in time, where $N\delta x = a$, $M\delta y = b$. Unlike the one dimensional case they cannot be solved by a simple recursive process. For large value of N and M they would often be solved iteratively.

Peaceman and Rachford (1955) put forward the following method and showed, for a typical problem with a rectangular region in the xy plane, that it involved about twenty five time less work than the explicit method and about seven times less work than the Crank-Nicolson method.

Assume the solution is known for time $t_n = n\delta t$. Their method consists of replacing only one of the second-order derivatives, $\partial^2 u/\partial x^2$ say, by an implicit difference approximation in terms of unknown pivotal values of u from the $(n+1/2)^{th}$ time level, the other second order derivative, $\partial^2 u/\partial y^2$, being replaced by an explicit finite difference approximation. The advantage of the solution to the $(n+1)^{th}$ time level is then achieved by replacing $\partial^2 u/\partial y^2$ by implicit difference approximation and $\partial^2 u/\partial x^2$ by an explicit one. The time interval $(\delta t)/2$ must be the same for each advancement.

Provided the solution for successive time steps is derived by alternating between rows and columns as described above the method is valid for all ratios of $\delta/(\delta x)^2$ and $\delta/(\delta y)^2$. Each step on its own is unstable and unilateral repetition leads to an unacceptable growth of errors.

The detail is as follows (Fig. A.1). The equation

$$\frac{u_{i,j}^{n+1/2} - u_{i,j}^{n}}{K(\delta t)/2} = \frac{\left(u_{i-1,j}^{n+1/2} - 2u_{i,j}^{n+1/2} + u_{i+1,j}^{n+1/2}\right)}{(\delta x)^2} + \frac{\left(u_{i,j-1}^{n} - 2u_{i,j}^{n} + u_{i,j+1}^{n}\right)}{(\delta y)^2}$$

is used to advance the solution from the n^{th} to the $(n+1/2)^{th}$ time step, and the equation

$$\frac{u_{i,j}^{n+1} - u_{i,j}^{n+1/2}}{K(\delta t)/2} = \frac{\left(u_{i-1,j}^{n+1/2} - 2u_{i,j}^{n+1/2} + u_{i+1,j}^{n+1/2}\right)}{(\delta x)^2} + \frac{\left(u_{i,j-1}^{n+1} - 2u_{i,j}^{n+1} + u_{i,j+1}^{n+1}\right)}{(\delta y)^2}$$

for advancement from the $(n+1/2)^{th}$ to the $(n+1)^{th}$ time step.

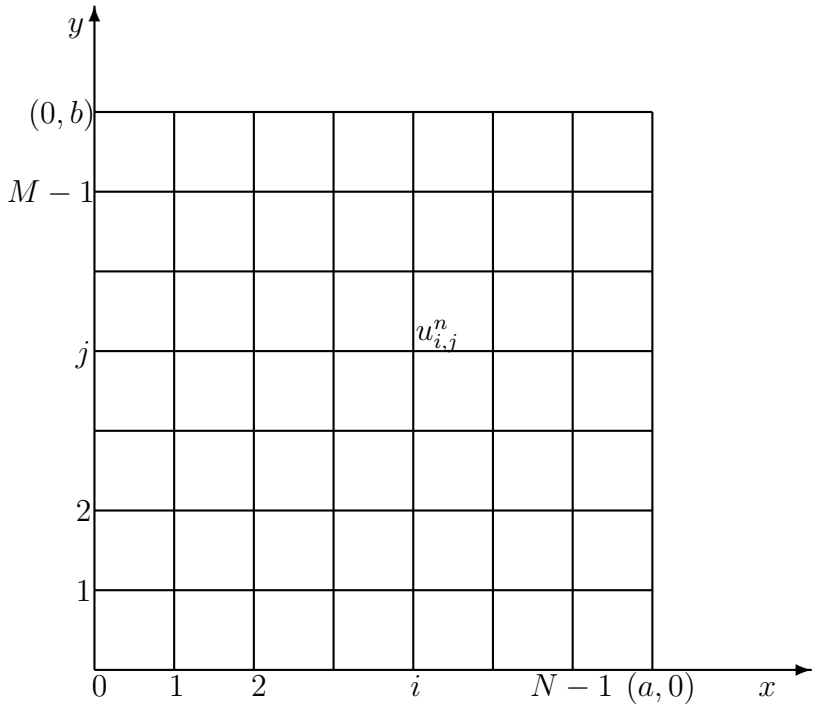

Fig. A.1 Mesh points of the solution domain.

Appendix B

Appendix B: Successive Over Relaxation

The relaxation technique is a finite-difference method particularly suited for the solution of elliptic partial differential equations. Successive over-relaxation (SOR) is a technique which can be used in an attempt to accelerate any iteration procedure but we will propose it here primarily as a refinement to the Gauss-Seidel method. As we apply Gauss-Seidel iteration to a system of simultaneous algebraic equation, we expect to make several recalculations or iterations before convergence to an acceptable level is achieved. A major disadvantage of the otherwise attractive Gauss-Seidel method is that its convergence is too slow, especially when a large number of grid points are involved. The reason for the slowness is easy to understand; the method transmits the boundary condition information at a rate of one grid interval per iteration.

In the iterative solution of the algebraic equation or in the overall iterative scheme employed for handing nonlinearity, it is often desirable to speed up or to slow down the changes. This process is called over-relaxation or under-relaxation depending on whether the variable changes are accelerated or slowed down. An arbitrary correction to the intermediate values of the unknowns from any iteration procedure according to the form

$$u_{i,j}^{k+1'} = wu_{i,j}^{k+1} + (1-w)u_{i,j}^{k'}$$

is known as over-relaxation or successive over-relaxation (SOR).

Here, k denotes iteration level and $u_{i,j}^{k+1}$ is the most recent value of $u_{i,j}$ calculated from the Gauss-Seidel procedure, $u_{i,j}^{k'}$ is the value from the previous iteration as a adjusted by previous application of this formula if the over-relaxation is being applied successively and $u_{i,j}^{k+1'}$ is newly adjusted for $u_{i,j}$ at the $k+1$ iteration level. w is the relaxation parameter whose value is usually found by trail-and-error experimentation for a given

problem. For over-relaxation, generally the value of w is bounded by $1 < w < 2$ and for under-relaxation, w is bounded by $0 < w < 1$.

Appendix C

Appendix C: Thomas Algorithm

Suppose we have to solve a linear system of algebraic equations

$$AV = D \tag{C.1}$$

where

$$A = \begin{bmatrix} b_1 & c_1 & & & & & \\ a_2 & b_2 & c_2 & & & & \\ & . & . & . & & & \\ & & a_i & b_i & c_i & & \\ & & & . & . & . & \\ & & & & a_{N-1} & b_{N-1} & c_{N-1} \\ & & & & & a_N & b_N \end{bmatrix}$$

is a $N \times N$ tri-diagonal matrix,

$$V = \begin{bmatrix} v_1 \\ v_2 \\ . \\ v_i \\ . \\ v_{N-1} \\ v_N \end{bmatrix}$$

is the vector of unknowns and

$$D = \begin{bmatrix} d_1 \\ d_2 \\ . \\ d_i \\ . \\ d_{N-1} \\ d_N \end{bmatrix}$$

is the known vector. All elements in A, other than those shown, are zero.

The Thomas algorithm for solving (C.1) consists of two parts. First (C.1) is manipulated into the form

$$\begin{bmatrix} 1 & c_1^1 & & & & & \\ & 1 & c_2^1 & & & & \\ & & . & . & & & \\ & & & 1 & c_i^1 & & \\ & & & & . & . & \\ & & & & & 1 & c_{N-1}^1 \\ & & & & & & 1 \end{bmatrix} \begin{bmatrix} v_1 \\ v_2 \\ . \\ v_i \\ . \\ v_{N-1} \\ v_N \end{bmatrix} = \begin{bmatrix} d_1^1 \\ d_2^1 \\ . \\ d_i^1 \\ . \\ d_{N-1}^1 \\ d_N^1 \end{bmatrix}$$

i.e., the a_i coefficients have been eliminated and the b_i coefficients normalized to unity. For the first equation

$$c_1^1 = \frac{c_1}{b_1}, d_1^1 = \frac{d_1}{b_1}$$

and for the general equation

$$c_i^1 = \frac{c_i}{b_i - a_i c_{i-1}^1}, d_i^1 = \frac{d_i - a_i d_{i-1}^1}{b_i - a_i c_{i-1}^1}. \tag{C.2}$$

The equation are modified as in (C.2). The second stage consists of a back substitution

$$v_N = d_N^1, v_i = d_i^1 - v_{i+1} c_i^1.$$

The Thomas algorithm is particularly economical, it requires only $5N - 4$ operations (multiplications and divisions). But to present ill conditioning, it is necessary that

$$| b_i | > | a_i | + | c_i |$$

Bibliography

[1] Abu-Nada, E., Masoud, Z., Oztop, H. F. and Campo, A.: 2010, Effect of nanofluid variable properties on natural convection in enclosures, *International Journal of Thermal Sciences* **49**(3), 479–491.

[2] Adamu, G. and Sinha, P.: 2012, Thermal and roughness effects in a tilted pad slider bearing considering heat conduction through the pad and slider, *Proceedings of the National Academy of Sciences, India Section A: Physical Sciences* **82**(4), 323–333.

[3] Ahmed, S. E., Mansour, M. and Mahdy, A.: 2013, MHD mixed convection in an inclined lid-driven cavity with opposing thermal buoyancy force: effect of non-uniform heating on both side walls, *Nuclear Engineering and Design* **265**, 938–948.

[4] Akbar, N. S., Raza, M. and Ellahi, R.: 2014, Interaction of nanoparticles for the peristaltic flow in an asymmetric channel with the induced magnetic field, *The European Physical Journal Plus* **129**(7), 155.

[5] Al-Amiri, A. M.: 2002, Natural convection in porous enclosures: the application of the two-energy equation model, *Numerical Heat Transfer: Part A: Applications* **41**(8), 817–834.

[6] Al-Farhany, K. and Turan, A.: 2012, Numerical study of double diffusive natural convective heat and mass transfer in an inclined rectangular cavity filled with porous medium, *International Communications in Heat and Mass Transfer* **39**(2), 174–181.

[7] Al-Nimr, M. and Haddad, O.: 1999, Fully developed free convection in open-ended vertical channels partially filled with porous material, *J. Porous Media* **2**(2), 179–189.

[8] Al-Zamily, A. and Amin, M. R.: 2015, Natural convection and entropy generation

in a cavity filled with two horizontal layers of nanofluid and porous medium in presence of a magnetic field, *Proceedings of the ASME 2015 International Mechanical Engineering Congress and Exposition* **8B**, 913–926.

[9] Al-Zamily, A. M. J.: 2017, Analysis of natural convection and entropy generation in a cavity filled with multi-layers of porous medium and nanofluid with a heat generation, *International Journal of Heat and Mass Transfer* **106**, 1218–1231.

[10] Aminossadati, S. and Ghasemi, B.: 2009, Natural convection cooling of a localised heat source at the bottom of a nanofluid-filled enclosure, *European Journal of Mechanics-B/Fluids* **28**(5), 630–640.

[11] Amsden, A. A. and Harlow, F. H.: 1970, A simplified mac technique for incompressible fluid flow calculations, *Journal of computational physics* **6**(2), 322–325.

[12] Anandalakshmi, R. and Basak, T.: 2015, Natural convection in rhombic enclosures with isothermally heated side or bottom wall: entropy generation analysis, *European Journal of Mechanics-B/Fluids* **54**, 27–44.

[13] Anderson, D. A., Tannehill, J. C. and Pletcher, R. H.: 1984, *Computational fluid dynamics and heat transfer*, Hemisphere, Washington.

[14] Anderson, J.: 1995, *Computational fluid dynamics: the basics with applications*, McGrawhill Inc, New York.

[15] Anjorin, V. and Barton, I.: 2001, Removal of temporal and under-relaxation terms from the pressure-correction equation of the simple algorithm, *International Journal of Fluid Dynamics* **5**(5), 59–75.

[16] Arani, A. A., Sebdani, S. M., Mahmoodi, M., Ardeshiri, A. and Aliakbari, M.: 2012, Numerical study of mixed convection flow in a lid-driven cavity with sinusoidal heating on sidewalls using nanofluid, *Superlattices and Microstructures* **51**(6), 893–911.

[17] Armaghani, T., Chamkha, A. J., Maghrebi, M. and Nazari, M.: 2014, Numerical

analysis of a nanofluid forced convection in a porous channel: a new heat flux model in ltne condition, *Journal of Porous Media* **17**(7).

[18] Azizian, M. R.: 2009, Evaluation of thermo-physical properties of nanofluids, *Eastern Mediterranean University* .

[19] Baker, A. J.: 1983, *Finite element computational fluid mechanics*, Hemisphere, Washington, D. C.

[20] Basak, T. and Chamkha, A. J.: 2012a, Heatline analysis on natural convection for nanofluids confined within square cavities with various thermal boundary conditions, *International Journal of Heat and Mass Transfer* **55**(2122), 5526 – 5543.

[21] Basak, T. and Chamkha, A. J.: 2012b, Heatline analysis on natural convection for nanofluids confined within square cavities with various thermal boundary conditions, *International Journal of Heat and Mass Transfer* **55**(2122), 5526 – 5543.

[22] Batchelor, G.: 1977, The effect of brownian motion on the bulk stress in a suspension of spherical particles, *Journal of fluid mechanics* **83**(1), 97–117.

[23] Baytaş, A.: 2000, Entropy generation for natural convection in an inclined porous cavity, *International Journal of Heat and Mass Transfer* **43**(12), 2089–2099.

[24] Baytas, A.: 2003, Thermal non-equilibrium natural convection in a square enclosure filled with a heat-generating solid phase, non-darcy porous medium, *International journal of energy research* **27**(10), 975–988.

[25] Bejan, A.: 1979, A study of entropy generation in fundamental convective heat transfer, *J. Heat Transfer* **101**(4), 718–725.

[26] Bejan, A.: 1993, *Convection heat transfer*, Wiley, New York, NY.

[27] Bejan, A.: 2013, *Convection heat transfer*, John wiley & sons.

[28] Bejan, A. and Khair, K. R.: 1985, Heat and mass transfer by natural convection in a porous medium, *International Journal of Heat and Mass Transfer* **28**(5), 909–918.

[29] Bhattacharya, P., Saha, S., Yadav, A., Phelan, P. and Prasher, R.: 2004, Brownian dynamics simulation to determine the effective thermal conductivity of nanofluids, *Journal of Applied Physics* **95**(11), 6492–6494.

[30] Bhattacharyya, S., Maiti, D. and Dhinakaran, S.: 2006, Influence of buoyancy on vortex shedding and heat transfer from a square cylinder in proximity to a wall, *Numerical Heat Transfer, Part A: Applications* **50**(6), 585–606.

[31] Bhattacharyya, S. and Singh, A.: 2009, Augmentation of heat transfer from a solid cylinder wrapped with a porous layer, *International Journal of Heat and Mass Transfer* **52**(7), 1991–2001.

[32] Bhattacharyya, S. and Singh, A.: 2010, Vortex shedding and heat transfer dependence on effective reynolds number for mixed convection around a cylinder in cross flow, *International Journal of Heat and Mass Transfer* **53**(1516), 3202 – 3212.

[33] Bhattacharyya, S. and Singh, A.: 2011, Reduction in drag and vortex shedding frequency through porous sheath around a circular cylinder, *International Journal for Numerical Methods in Fluids* **65**(6), 683–698.

[34] Bicerano, J., Douglas, J. F. and BRUNE, D. A.: 1999, Model for the viscosity of particle dispersions.

[35] Biegger, C., Sotgiu, C. and Weigand, B.: 2015, Numerical investigation of flow and heat transfer in a swirl tube, *International Journal of Thermal Sciences* **96**, 319–330.

[36] Biegger, C. and Weigand, B.: 2015, Flow and heat transfer measurements in a swirl chamber with different outlet geometries, *Experiments in Fluids* **56**(4), 78.

[37] Biswal, P., Nag, A. and Basak, T.: 2016, Analysis of thermal management during natural convection within porous tilted square cavities via heatline and entropy generation, *International Journal of Mechanical Sciences* **115116**, 596 – 615.

[38] Bondareva, N. S., Sheremet, M. A., Oztop, H. F. and Abu-Hamdeh, N.: 2016, Heatline visualization of MHD natural convection in an inclined wavy open porous cavity

filled with a nanofluid with a local heater, *International Journal of Heat and Mass Transfer* **99**, 872 – 881.

[39] Brinkman, H.: 1952, The viscosity of concentrated suspensions and solutions, *The Journal of Chemical Physics* **20**(4), 571–571.

[40] Buongiorno, J.: 2006, Convective transport in nanofluids, *Journal of Heat Transfer* **128**(3), 240–250.

[41] Buongiorno, J., Hu, L.-W., Kim, S. J., Hannink, R., Truong, B. and Forrest, E.: 2008, Nanofluids for enhanced economics and safety of nuclear reactors: an evaluation of the potential features, issues, and research gaps, *Nuclear Technology* **162**(1), 80–91.

[42] Burns, P., Chow, L. and Tien, C.: 1977, Convection in a vertical slot filled with porous insulation, *International Journal of Heat and Mass Transfer* **20**(9), 919–926.

[43] C. Wan, BSV Patnaik, G. W. D.: 2001, A new benchmark quality solution for the buoyancy-driven cavity by discrete singular convolution, *Numerical Heat Transfer: Part B: Fundamentals* **40**(3), 199–228.

[44] *Cavity flows driven by buoyancy and shear*: n.d., **51**.

[45] Chamkha, A. J. and Abu-Nada, E.: 2012, Mixed convection flow in single-and double-lid driven square cavities filled with water-Al_2O_3 nanofluid: effect of viscosity models, *European Journal of Mechanics-B/Fluids* **36**, 82–96.

[46] Chamkha, A. J. and Khaled, A.: 2000a, Hydromagnetic coupled heat and mass transfer by natural convection from a permeable constant heat flux surface in porous media, *Journal of Porous Media* **3**(3).

[47] Chamkha, A. J. and Khaled, A.-R. A.: 2000b, Hydromagnetic combined heat and mass transfer by natural convection from a permeable surface embedded in a fluid-saturated porous medium, *International Journal of Numerical Methods for Heat & Fluid Flow* **10**(5), 455–477.

[48] Chamkha, A., Rashad, A., Mansour, M., Armaghani, T. and Ghalambaz, M.: 2017, Effects of heat sink and source and entropy generation on MHD mixed convection

of a Cu-water nanofluid in a lid-driven square porous enclosure with partial slip, *Physics of Fluids* **29**(5), 052001.

[49] Chao, Z., Zhang, Y., Wang, Y., Jakobsen, J. P. and Jakobsen, H. A.: 2017, Modelling of binary fluidized bed reactors for the sorption-enhanced steam methane reforming process, *The Canadian Journal of Chemical Engineering* **95**(1), 157–169.

[50] Chattopadhyay, A., Pandit, S. K., Sarma, S. S. and Pop, I.: 2016, Mixed convection in a double lid-driven sinusoidally heated porous cavity, *International Journal of Heat and Mass Transfer* **93**, 361–378.

[51] Chen, H., Ding, Y. and Tan, C.: 2007, Rheological behaviour of nanofluids, *New journal of physics* **9**(10), 367.

[52] Chol, S. et al.: 1995, Enhancing thermal conductivity of fluids with nanoparticles, *ASME-Publications-Fed* **231**, 99–106.

[53] Chorin, A. J.: 1967, A numerical method for solving incompressible viscous flow problems, *Journal of Computational Physics* **2**(1), 12 – 26.

[54] Chung, T.: 1978, *Finite element analysis in fluid dynamics*, McGraw-Hill, New York.

[55] de Vahl Davis, G.: 1983, Natural convection of air in a square cavity: a bench mark numerical solution, *International Journal for numerical methods in fluids* **3**(3), 249–264.

[56] Deepika, N., Narayana, P. and Hill, A. A.: 2017, Onset of darcy-brinkman convection with a uniform internal heat source and vertical throughflow, *International Journal of Thermal Sciences* **117**, 136–144.

[57] Dehghan, M., Jamal-Abad, M. T. and Rashidi, S.: 2014, Analytical interpretation of the local thermal non-equilibrium condition of porous media imbedded in tube heat exchangers, *Energy Conversion and Management* **85**, 264–271.

[58] Demirbas, M. F.: 2006, Thermal energy storage and phase change materials: an overview, *Energy Sources, Part B: Economics, Planning, and Policy* **1**(1), 85–95.

[59] Deresse, G. A. and Sinha, P.: 2011, Thd analysis for finite slider bearing with roughness: special reference to load generation in parallel sliders, *Acta Mechanica* **222**(1-2), 1–15.

[60] Doormaal, J. P. V. and Raithby, G. D.: 1984, Enhancements of the simple method for predicting incompressible fluid flows, *Numerical Heat Transfer* **7**(2), 147–163.

[61] Eastman, J. A., Choi, S., Li, S., Yu, W. and Thompson, L.: 2001, Anomalously increased effective thermal conductivities of ethylene glycol-based nanofluids containing copper nanoparticles, *Applied physics letters* **78**(6), 718–720.

[62] Einstein, A.: 1956, *Investigations on the Theory of the Brownian Movement*, Courier Corporation.

[63] el malik Bouchoucha, A., Bessah, R., Oztop, H. F., Al-Salem, K. and Bayrak, F.: 2017, Natural convection and entropy generation in a nanofluid filled cavity with thick bottom wall: Effects of non-isothermal heating, *International Journal of Mechanical Sciences* **126**(Supplement C), 95 – 105.

[64] Ellahi, R.: 2013, The effects of MHD and temperature dependent viscosity on the flow of non-newtonian nanofluid in a pipe: analytical solutions, *Applied Mathematical Modelling* **37**(3), 1451–1467.

[65] Ellahi, R., Aziz, S. and Zeeshan, A.: 2013, Non-newtonian nanofluid flow through a porous medium between two coaxial cylinders with heat transfer and variable viscosity, *Journal of Porous Media* **16**(3).

[66] Ellahi, R., Hassan, M. and Zeeshan, A.: 2015, Study of natural convection MHD nanofluid by means of single and multi-walled carbon nanotubes suspended in a salt-water solution, *IEEE Transactions on Nanotechnology* **14**(4), 726–734.

[67] Elshehabey, H. M. and Ahmed, S. E.: 2015, MHD mixed convection in a lid-driven cavity filled by a nanofluid with sinusoidal temperature distribution on the both vertical walls using buongiornos nanofluid model, *International Journal of Heat and Mass Transfer* **88**, 181 – 202.

[68] Fereidoon, A., Saedodin, S., Hemmat Esfe, M. and Noroozi, M.: 2013, Evaluation of mixed convection in inclined square lid-driven cavity filled with Al_2O_3-water nanofluid, *Engineering Applications of Computational Fluid Mechanics* **7**(1), 55–65.

[69] Fersadou, I., Kahalerras, H. and El Ganaoui, M.: 2015, MHD mixed convection and entropy generation of a nanofluid in a vertical porous channel, *Computers & Fluids* **121**, 164–179.

[70] Fersadou, I., Kahalerras, H. and Ganaoui, M. E.: 2015, MHD mixed convection and entropy generation of a nanofluid in a vertical porous channel, *Computers & Fluids* **121**, 164 – 179.

[71] Ferziger, J. H. and Peric, M.: 1996, *Computational methods for fluid dynamics*, Springer-Verlag, New York.

[72] Fletcher, C.: 1991, *Computational techniques for fluid dynamics-I & II*, Springer-Verlag, Berlin Heidelberg.

[73] Frankel, N. and Acrivos, A.: 1967, On the viscosity of a concentrated suspension of solid spheres, *Chemical Engineering Science* **22**(6), 847–853.

[74] Garoosi, F., Bagheri, G. and Rashidi, M. M.: 2015, Two phase simulation of natural convection and mixed convection of the nanofluid in a square cavity, *Powder Technology* **275**, 239–256.

[75] Garoosi, F., Jahanshaloo, L. and Garoosi, S.: 2015, Numerical simulation of mixed convection of the nanofluid in heat exchangers using a buongiorno model, *Powder Technology* **269**, 296–311.

[76] Garoosi, F., Rohani, B. and Rashidi, M. M.: 2015, Two-phase mixture modeling of mixed convection of nanofluids in a square cavity with internal and external heating, *Powder Technology* **275**, 304–321.

[77] Ghasemi, B., Aminossadati, S. and Raisi, A.: 2011, Magnetic field effect on natural convection in a nanofluid-filled square enclosure, *International Journal of Thermal Sciences* **50**(9), 1748–1756.

[78] Ghodsinezhad, H., Sharifpur, M. and Meyer, J. P.: 2016, Experimental investigation on cavity flow natural convection of Al_2O_3-water nanofluids, *International Communications in Heat and Mass Transfer* **76**, 316–324.

[79] Graham, A. L.: 1981, On the viscosity of suspensions of solid spheres, *Applied Scientific Research* **37**(3), 275–286.

[80] Guta, L. and Sundar, S.: 2010, Navier-stokes-brinkman system for interaction of viscous waves with a submerged porous structure, *Tamkang Journal of Mathematics* **41**(3), 217–243.

[81] Haddad, O., Al-Nimr, M. and Al-Khateeb, A.: 2004, Validation of the local thermal equilibrium assumption in natural convection from a vertical plate embedded in porous medium: non-darcian model, *International Journal of Heat and Mass Transfer* **47**(89), 2037 – 2042.

[82] Hajialigol, N., Sheikhzadeh, G., Ebrahim Qomi, M. and Fattahi, A.: 2011, Laminar mixed convection of Cu-water nanofluid in two-sided lid-driven enclosures, *Journal of Nanostructures* **1**(1), 44–53.

[83] Hamilton, R. and Crosser, O.: 1962, Thermal conductivity of heterogeneous two-component systems, *Industrial & Engineering chemistry fundamentals* **1**(3), 187–191.

[84] Han, T., Humphrey, J. and Launder, B.: 1981, A comparison of hybrid and quadratic-upstream differencing in high reynolds number elliptic flows, *Computer Methods in Applied Mechanics and Engineering* **29**(1), 81–95.

[85] Harlow, F. H. and Welch, J. E.: 1965, Numerical calculation of time-dependent viscous incompressible flow of fluid with free surface, *The physics of fluids* **8**(12), 2182–2189.

[86] Hayase, T., Humphrey, J. and Greif, R.: 1992, A consistently formulated quick scheme for fast and stable convergence using finite-volume iterative calculation procedures, *Journal of Computational Physics* **98**(1), 108–118.

[87] Henze, M., Von Wolfersdorf, J., Weigand, B., Dietz, C. and Neumann, S.: 2011, Flow and heat transfer characteristics behind vortex generators–a benchmark dataset, *International Journal of Heat and Fluid Flow* **32**(1), 318–328.

[88] Hirt, C., Nichols, B. and Romero, N.: 1975, Sola: A numerical solution algorithm for transient fluid flows, *Technical report*, Los Alamos Scientific Lab., N. Mex.(USA).

[89] Ho, C.-J., Chen, M. and Li, Z.: 2008, Numerical simulation of natural convection of nanofluid in a square enclosure: effects due to uncertainties of viscosity and thermal conductivity, *International Journal of Heat and Mass Transfer* **51**(17), 4506–4516.

[90] Ho, C., Liu, W., Chang, Y. and Lin, C.: 2010, Natural convection heat transfer of alumina-water nanofluid in vertical square enclosures: an experimental study, *International Journal of Thermal Sciences* **49**(8), 1345–1353.

[91] Hooman, K.: 2010, Energy flux vectors as a new tool for convection visualization, *International Journal of Numerical Methods for Heat & Fluid Flow* **20**(2), 240–249.

[92] Horton, C. and Rogers Jr, F.: 1945, Convection currents in a porous medium, *Journal of Applied Physics* **16**(6), 367–370.

[93] Hoseinpour, B., Ashorynejad, H. R. and Javaherdeh, K.: 2016, Entropy generation of nanofluid in a porous cavity by lattice boltzmann method, *Journal of Thermophysics and Heat Transfer* pp. 1–8.

[94] Hussain, S., Mehmood, K. and Sagheer, M.: 2016, MHD mixed convection and entropy generation of wateralumina nanofluid flow in a double lid driven cavity with discrete heating, *Journal of Magnetism and Magnetic Materials* **419**, 140 – 155.

[95] Hwang, K. S., Lee, J.-H. and Jang, S. P.: 2007, Buoyancy-driven heat transfer of water-based Al_2O_3 nanofluids in a rectangular cavity, *International Journal of Heat and Mass Transfer* **50**(19), 4003–4010.

[96] Ibáñez, G.: 2015, Entropy generation in MHD porous channel with hydrodynamic slip and convective boundary conditions, *International Journal of Heat and Mass Transfer* **80**, 274–280.

[97] Ibáñez, G., López, A., Pantoja, J. and Moreira, J.: 2016, Entropy generation analysis of a nanofluid flow in MHD porous microchannel with hydrodynamic slip and thermal radiation, *International Journal of Heat and Mass Transfer* **100**, 89–97.

[98] Ilis, G. G., Mobedi, M. and Sunden, B.: 2008, Effect of aspect ratio on entropy generation in a rectangular cavity with differentially heated vertical walls, *International Communications in Heat and Mass Transfer* **35**(6), 696–703.

[99] Inaba, H., Sugawara, M. and Blumenberg, J.: 1988, Natural convection heat transfer in an inclined porous layer, *International journal of heat and mass transfer* **31**(7), 1365–1374.

[100] Issa, R. I.: 1986, Solution of the implicitly discretised fluid flow equations by operator-splitting, *Journal of computational physics* **62**(1), 40–65.

[101] Iwatsu, R., Hyun, J. M. and Kuwahara, K.: 1993, Mixed convection in a driven cavity with a stable vertical temperature gradient, *International Journal of Heat and Mass Transfer* **36**(6), 1601–1608.

[102] Jang, S. P. and Choi, S. U.: 2004, Role of brownian motion in the enhanced thermal conductivity of nanofluids, *Applied physics letters* **84**(21), 4316–4318.

[103] Jue, T.-C.: 2002, Analysis of flows driven by a torsionally–oscillatory lid in a fluid-saturated porous enclosure with thermal stable stratification, *International journal of thermal sciences* **41**(8), 795–804.

[104] Kakaç, S. and Pramuanjaroenkij, A.: 2016, Single-phase and two-phase treatments of convective heat transfer enhancement with nanofluids–a state-of-the-art review, *International Journal of Thermal Sciences* **100**, 75–97.

[105] Kaluri, R. S. and Basak, T.: 2010, Heatline analysis of thermal mixing due to natural convection in discretely heated porous cavities filled with various fluids, *Chemical Engineering Science* **65**(6), 2132 – 2152.

[106] Kandelousi, M. S. and Ellahi, R.: 2015, Simulation of ferrofluid flow for magnetic

drug targeting using the lattice boltzmann method, *Zeitschrift für Naturforschung A* **70**(2), 115–124.

[107] Kaneko, T., Mohtadi, M. and Aziz, K.: 1974, An experimental study of natural convection in inclined porous media, *International Journal of Heat and Mass Transfer* **17**(4), 485–496.

[108] Kashani, S., Ranjbar, A., Mastiani, M. and Mirzaei, H.: 2014, Entropy generation and natural convection of nanoparticle-water mixture (nanofluid) near water density inversion in an enclosure with various patterns of vertical wavy walls, *Applied Mathematics and Computation* **226**, 180–193.

[109] Keblinski, P., Phillpot, S., Choi, S. and Eastman, J.: 2002, Mechanisms of heat flow in suspensions of nano-sized particles (nanofluids), *International journal of heat and mass transfer* **45**(4), 855–863.

[110] Kefayati, G.: 2016a, Heat transfer and entropy generation of natural convection on non-newtonian nanofluids in a porous cavity, *Powder Technology* **299**, 127–149.

[111] Kefayati, G.: 2016b, Simulation of heat transfer and entropy generation of {MHD} natural convection of non-newtonian nanofluid in an enclosure, *International Journal of Heat and Mass Transfer* **92**, 1066 – 1089.

[112] Kefayati, G. R.: 2015a, {FDLBM} simulation of magnetic field effect on mixed convection in a two sided lid-driven cavity filled with non-newtonian nanofluid, *Powder Technology* **280**, 135 – 153.

[113] Kefayati, G. R.: 2015b, Mesoscopic simulation of mixed convection on non-newtonian nanofluids in a two sided lid-driven enclosure, *Advanced Powder Technology* **26**(2), 576–588.

[114] Kefayati, G. and Sidik, N. A. C.: 2017, Simulation of natural convection and entropy generation of non-newtonian nanofluid in an inclined cavity using buongiorno's mathematical model (part ii, entropy generation), *Powder Technology* **305**, 679 – 703.

[115] Khaled, A.-R. and Vafai, K.: 2003, The role of porous media in modeling flow and heat transfer in biological tissues, *International Journal of Heat and Mass Transfer* **46**(26), 4989–5003.

[116] Khaled, A.-R. and Vafai, K.: 2005, Heat transfer enhancement through control of thermal dispersion effects, *International Journal of Heat and Mass Transfer* **48**(11), 2172–2185.

[117] Khalili, S., Dinarvand, S., Hosseini, R., Tamim, H. and Pop, I.: 2014, Unsteady MHD flow and heat transfer near stagnation point over a stretching/shrinking sheet in porous medium filled with a nanofluid, *Chinese Physics B* **23**(4), 048203.

[118] Khalili, S., Tamim, H., Khalili, A. and Rashidi, M. M.: 2015, Unsteady convective heat and mass transfer in pseudoplastic nanofluid over a stretching wall, *Advanced Powder Technology* **26**(5), 1319–1326.

[119] Khanafer, K. M., Al-Amiri, A. M. and Pop, I.: 2007, Numerical simulation of unsteady mixed convection in a driven cavity using an externally excited sliding lid, *European Journal of Mechanics-B/Fluids* **26**(5), 669–687.

[120] Khanafer, K. M. and Chamkha, A. J.: 1999, Mixed convection flow in a lid-driven enclosure filled with a fluid-saturated porous medium, *International Journal of Heat and Mass Transfer* **42**(13), 2465–2481.

[121] Khanafer, K. and Vafai, K.: 2002, Double-diffusive mixed convection in a lid-driven enclosure filled with a fluid-saturated porous medium, *Numerical Heat Transfer: Part A: Applications* **42**(5), 465–486.

[122] Khanafer, K., Vafai, K. and Lightstone, M.: 2003, Buoyancy-driven heat transfer enhancement in a two-dimensional enclosure utilizing nanofluids, *International journal of heat and mass transfer* **46**(19), 3639–3653.

[123] Khorasanizadeh, H., Nikfar, M. and Amani, J.: 2013, Entropy generation of Cu–water nanofluid mixed convection in a cavity, *European Journal of Mechanics-B/Fluids* **37**, 143–152.

[124] Kim, S. and Vafai, K.: 1989, Analysis of natural convection about a vertical plate embedded in a porous medium, *International journal of Heat and Mass transfer* **32**(4), 665–677.

[125] Koo, J. and Kleinstreuer, C.: 2004, A new thermal conductivity model for nanofluids, *Journal of Nanoparticle Research* **6**(6), 577–588.

[126] Kulkarni, D. P., Das, D. K. and Chukwu, G. A.: 2006, Temperature dependent rheological property of copper oxide nanoparticles suspension (nanofluid), *Journal of nanoscience and nanotechnology* **6**(4), 1150–1154.

[127] Kumar, B., Belouettar, S., Murthy, S., Rees, D. and Chandra, P.: 2010, Soret and dufour effect on double diffusive natural convection in a wavy porous enclosure, *Porous Media: Heat And Mass Transfer, Transport And Mechanics* **85**.

[128] Kumar, B. R., Murthy, S. V. K., Sangwan, V., Nigam, M. and Chandra, P.: 2010, Non-darcy mixed convection in a fluid-saturated square porous enclosure under suction effect: part i, *Journal of Porous Media* **13**(6).

[129] Kumar, D. H., Patel, H. E., Kumar, V. R., Sundararajan, T., Pradeep, T. and Das, S. K.: 2004, Model for heat conduction in nanofluids, *Physical Review Letters* **93**(14), 144301.

[130] Kumar, S., Prasad, S. K. and Banerjee, J.: 2010, Analysis of flow and thermal field in nanofluid using a single phase thermal dispersion model, *Applied Mathematical Modelling* **34**(3), 573–592.

[131] Lai, F. and Kulacki, F.: 1991, Non-darcy mixed convection along a vertical wall in a saturated porous medium, *Journal of Heat Transfer (Transcations of the ASME (American Society of Mechanical Engineers), Series C);(United States)* **113**(1).

[132] Lapwood, E.: 1948, Convection of a fluid in a porous medium, *Mathematical Proceedings of the Cambridge Philosophical Society*, Vol. 44, Cambridge University Press, pp. 508–521.

[133] Leonard, B. P.: 1979, A stable and accurate convective modelling procedure based on quadratic upstream interpolation, *Computer Methods in Applied Mechanics and Engineering* **19**(1), 59–98.

[134] Li, S. and Eastman, J.: 1999, Measuring thermal conductivity of fluids containing oxide nanoparticles, *J. Heat Transf* **121**(2), 280–9.

[135] Lomax, H., Pulliam, T. H. and Zingg, D. W.: 2013, *Fundamentals of computational fluid dynamics*, Springer-Verlag, New York.

[136] Magherbi, M., Abbassi, H. and Brahim, A. B.: 2003, Entropy generation at the onset of natural convection, *International journal of Heat and Mass transfer* **46**(18), 3441–3450.

[137] Mahapatra, P. S., De, S., Ghosh, K., Manna, N. K. and Mukhopadhyay, A.: 2013, Heat transfer enhancement and entropy generation in a square enclosure in the presence of adiabatic and isothermal blocks, *Numerical Heat Transfer, Part A: Applications* **64**(7), 577–596.

[138] Mahapatra, P. S., Manna, N. K., Ghosh, K. and Mukhopadhyay, A.: 2015, Heat transfer assessment of an alternately active bi-heater undergoing transient natural convection, *International Journal of Heat and Mass Transfer* **83**, 450–464.

[139] Mahdavi, M., Saffar-Avval, M., Tiari, S. and Mansoori, Z.: 2014, Entropy generation and heat transfer numerical analysis in pipes partially filled with porous medium, *International Journal of Heat and Mass Transfer* **79**, 496–506.

[140] Mahian, O., Kianifar, A., Kalogirou, S. A., Pop, I. and Wongwises, S.: 2013, A review of the applications of nanofluids in solar energy, *International Journal of Heat and Mass Transfer* **57**(2), 582–594.

[141] Mahmoudi, A. H., Shahi, M., Raouf, A. H. and Ghasemian, A.: 2010, Numerical study of natural convection cooling of horizontal heat source mounted in a square cavity filled with nanofluid, *International Communications in Heat and Mass Transfer* **37**(8), 1135–1141.

[142] Mahmoudi, A. H., Shahi, M. and Talebi, F.: 2010, Effect of inlet and outlet location on the mixed convective cooling inside the ventilated cavity subjected to an external nanofluid, *International Communications in Heat and Mass Transfer* **37**(8), 1158–1173.

[143] Maiga, S. E. B., Palm, S. J., Nguyen, C. T., Roy, G. and Galanis, N.: 2005, Heat transfer enhancement by using nanofluids in forced convection flows, *International journal of heat and fluid flow* **26**(4), 530–546.

[144] Maiti, D. K.: 2011, Numerical study on heat/mass transfer by shear/thermal/solutal-convection in a cavity under counteracting buoyancies, *Heat and mass transfer* **47**(3), 245–257.

[145] Maiti, D. K., Bhatt, R. and Alam, M. M.: 2016, Aerodynamic forces on square cylinder due to secondary flow by rectangular vortex generator in offset tandem: Comparison with inline, *Computers & Fluids* **134**, 157–176.

[146] Mansour, M. and Ahmed, S. E.: 2015, A numerical study on natural convection in porous media-filled an inclined triangular enclosure with heat sources using nanofluid in the presence of heat generation effect, *Engineering Science and Technology, an International Journal* **18**(3), 485–495.

[147] Mansour, M. and Bakier, M.: 2015, Influence of thermal boundary conditions on MHD natural convection in square enclosure using Cu–water nanofluid, *Energy Reports* **1**, 134–144.

[148] Manzari, M.: 1999, An explicit finite element algorithm for convection heat transfer problems, *International Journal of Numerical Methods for Heat & Fluid Flow* **9**(8), 860–877.

[149] Matle, S. and Sundar, S.: 2012a, A 2d finite element study on the flow pattern and temperature distribution for an isothermal spherical furnace with the aperture, *Open Journal of Applied Sciences* **2**(04), 319.

[150] Matle, S. and Sundar, S.: 2012b, Axi symmetric 2d simulation and numerical heat transfer characteristics for the calibration furnace in a rectangular enclosure, *Applied Mathematical Modelling* **36**(3), 878–893.

[151] Maxwell, J.: n.d., *A treatise on electricity and magnetism*, number v. 1-2 in *A Treatise on Electricity and Magnetism*.

[152] Maxwell, J. C.: 1881, *A treatise on electricity and magnetism*, Vol. 1, Clarendon press.

[153] Maxwell, J. C.: 1904, A treatise on electricity and magnetism, vol. ii. clarendon.

[154] Mehrez, Z., Cafsi, A. E., Belghith, A. and Qur, P. L.: 2015, {MHD} effects on heat transfer and entropy generation of nanofluid flow in an open cavity, *Journal of Magnetism and Magnetic Materials* **374**, 214 – 224.

[155] Mintsa, H. A., Roy, G., Nguyen, C. T. and Doucet, D.: 2009, New temperature dependent thermal conductivity data for water-based nanofluids, *International Journal of Thermal Sciences* **48**(2), 363–371.

[156] Moallemi, M. and Jang, K.: 1992, Prandtl number effects on laminar mixed convection heat transfer in a lid-driven cavity, *International Journal of Heat and Mass Transfer* **35**(8), 1881–1892.

[157] Mohamad, A.: 2001, Natural convection from a vertical plate in a saturated porous medium: nonequilibrium theory, *Journal of Porous Media* **4**(2), 181–186.

[158] Mooney, M.: 1951, The viscosity of a concentrated suspension of spherical particles, *Journal of colloid science* **6**(2), 162–170.

[159] Moumni, H., Welhezi, H., Djebali, R. and Sediki, E.: 2015, Accurate finite volume investigation of nanofluid mixed convection in two-sided lid driven cavity including discrete heat sources, *Applied Mathematical Modelling* **39**(14), 4164–4179.

[160] Mukhopadhyay, A.: 2010, Analysis of entropy generation due to natural convection in square enclosures with multiple discrete heat sources, *International Communications in Heat and Mass Transfer* **37**(7), 867–872.

[161] Murthy, S. K., Kumar, B. R., Chandra, P., Sangwan, V. and Nigam, M.: 2011, A study of double diffusive free convection from a corrugated vertical surface in a darcy porous medium under soret and dufour effects, *Journal of Heat Transfer* **133**(9), 092601.

[162] Muthtamilselvan, M., Kandaswamy, P. and Lee, J.: 2010, Heat transfer enhancement of copper-water nanofluids in a lid-driven enclosure, *Communications in Nonlinear Science and Numerical Simulation* **15**(6), 1501–1510.

[163] Nandkeolyar, R., Kameswaran, P. K., Shaw, S. and Sibanda, P.: 2014, Heat transfer on nanofluid flow with homogeneous–heterogeneous reactions and internal heat generation, *Journal of Heat Transfer* **136**(12), 122001.

[164] Narayana, M., Sibanda, P., Motsa, S. and Lakshmi-Narayana, P.: 2012, Linear and nonlinear stability analysis of binary maxwell fluid convection in a porous medium, *Heat and Mass Transfer* **48**(5), 863–874.

[165] Narayana, P. L. and Sibanda, P.: 2011, Influence of the soret effect and double dispersion on MHD mixed convection along a vertical flat plate in non-darcy porous medium, *Int. J. Nonlinear Sci* **12**, 352–364.

[166] Nasrin, R., Alim, M. and J. Chamkha, A.: 2013, Modeling of mixed convective heat transfer utilizing nanofluid in a double lid-driven chamber with internal heat generation, *International Journal of Numerical Methods for Heat & Fluid Flow* **24**(1), 36–57.

[167] Nayak, A. and Bhattacharyya, S.: 2012, Double-diffusive convection in a cubical lid-driven cavity with opposing temperature and concentration gradients, *Theoretical and Computational Fluid Dynamics* **26**(6), 565–581.

[168] Nayak, A., Malik, S., Venkateshwarlu, K. and Jena, P.: 2016, Magneto-convection and its effect on partially active thermal zones in a porous square domain, *International Journal of Heat and Mass Transfer* **95**, 913–926.

[169] Nayak, R., Bhattacharyya, S. and Pop, I.: 2015, Numerical study on mixed convection and entropy generation of Cu–water nanofluid in a differentially heated skewed enclosure, *International Journal of Heat and Mass Transfer* **85**, 620–634.

[170] Nayak, R., Bhattacharyya, S. and Pop, I.: 2016, Numerical study on mixed convection and entropy generation of a nanofluid in a lid-driven square enclosure, *Journal of Heat Transfer* **138**(1), 012503.

[171] Nguyen, C., Desgranges, F., Roy, G., Galanis, N., Maré, T., Boucher, S. and Mintsa, H. A.: 2007, Temperature and particle-size dependent viscosity data for water-based nanofluids–hysteresis phenomenon, *International Journal of Heat and Fluid Flow* **28**(6), 1492–1506.

[172] Nithyadevi, N., Kandaswamy, P. and Sundari, S. M.: 2009, Magnetoconvection in a square cavity with partially active vertical walls: Time periodic boundary condition, *International Journal of Heat and Mass Transfer* **52**(7), 1945–1953.

[173] Oden, J. T.: 1992, *Finite elements of nonlinear continua*, McGraw-Hill, New York.

[174] Otanicar, T. P., Phelan, P. E., Prasher, R. S., Rosengarten, G. and Taylor, R. A.: 2010, Nanofluid-based direct absorption solar collector, *Journal of renewable and sustainable energy* **2**(3), 033102.

[175] Oztop, H. F. and Abu-Nada, E.: 2008, Numerical study of natural convection in partially heated rectangular enclosures filled with nanofluids, *International Journal of Heat and Fluid Flow* **29**(5), 1326 – 1336.

[176] Oztop, H. F. and Dagtekin, I.: 2004, Mixed convection in two-sided lid-driven differentially heated square cavity, *International journal of heat and mass transfer* **47**(8), 1761–1769.

[177] Oztop, H. F., Rahman, M., Ahsan, A., Hasanuzzaman, M., Saidur, R., Al-Salem, K. and Rahim, N.: 2012, MHD natural convection in an enclosure from two semi-circular heaters on the bottom wall, *International Journal of Heat and Mass Transfer* **55**(78), 1844 – 1854.

[178] Patankar, S.: 1980, *Numerical heat transfer and fluid flow*, Hemisphere, Washington, DC.

[179] Patankar, S. and Spalding, D.: 1972, A calculation procedure for heat, mass and momentum transfer in three-dimensional parabolic flows, *International Journal of Heat and Mass Transfer* **15**(10), 1787 – 1806.

[180] Patel, H. E., Anoop, K., Sundararajan, T. and Das, S. K.: 2006, A micro-convection model for thermal conductivity of nanofluids, *International Heat Transfer Conference 13*, Begel House Inc.

[181] Pekmen, B. and Tezer-Sezgin, M.: 2014, MHD flow and heat transfer in a lid-driven porous enclosure, *Computers & Fluids* **89**, 191–199.

[182] Peyret, R. and Taylor, T. D.: 1983a, *Computational methods for fluid flow*, Springer-Verlag, New York/Berlin.

[183] Peyret, R. and Taylor, T. D.: 1983b, Computational methods for fluid flow.

[184] Pollard, A. and Siu, A. L. W.: 1982, The calculation of some laminar flows using various discretisation schemes, *Computer Methods in Applied Mechanics and Engineering* **35**(3), 293–313.

[185] Prasher, R., Bhattacharya, P. and Phelan, P. E.: 2006, Brownian-motion-based convective-conductive model for the effective thermal conductivity of nanofluids, *Journal of heat transfer* **128**(6), 588–595.

[186] Putra, N., Thiesen, P., Roetzel, W. et al.: 2003, Temperature dependence of thermal conductivity enhancement for nanofluids, *Journal of heat transfer* **125**, 567–574.

[187] Raithby, G. and Schneider, G.: 1979, Numerical solution of problems in incompressible fluid flow: treatment of the velocity-pressure coupling, *Numerical Heat Transfer, Part A: Applications* **2**(4), 417–440.

[188] Ramshaw, J. D. and Mesina, G. L.: 1991, A hybrid penalty—pseudocompressibility method for transient incompressible fluid flow, *Comput. Fluids* **20**(2), 165–175.

[189] Ramshaw, J. and Mousseau, V.: 1990, Accelerated artificial compressibility method for steady-state incompressible flow calculations, *Computers & fluids* **18**(4), 361–367.

[190] Rashidi, S., Dehghan, M., Ellahi, R., Riaz, M. and Jamal-Abad, M.: 2015, Study of stream wise transverse magnetic fluid flow with heat transfer around an obstacle embedded in a porous medium, *Journal of Magnetism and Magnetic Materials* **378**, 128–137.

[191] Ravnik, J., Škerget, L. and Hriberšek, M.: 2010, Analysis of three-dimensional natural convection of nanofluids by bem, *Engineering Analysis with Boundary Elements* **34**(12), 1018–1030.

[192] Rees, D. A. S.: 1999, Darcy-brinkman free convection from a heated horizontal surface, *Numerical Heat Transfer: Part A: Applications* **35**(2), 191–204.

[193] Rudraiah, N., Barron, R., Venkatachalappa, M. and Subbaraya, C.: 1995, Effect of a magnetic field on free convection in a rectangular enclosure, *International Journal of Engineering Science* **33**(8), 1075 – 1084.

[194] Saidi, M. H. and Tamim, H.: 2016, Heat transfer and pressure drop characteristics of nanofluid in unsteady squeezing flow between rotating porous disks considering the effects of thermophoresis and brownian motion, *Advanced Powder Technology* **27**(2), 564 – 574.

[195] Sathiyamoorthy, M., Basak, T., Roy, S. and Pop, I.: 2007, Steady natural convection flow in a square cavity filled with a porous medium for linearly heated side wall(s), *International Journal of Heat and Mass Transfer* **50**(910), 1892 – 1901.

[196] Sebdani, S. M., Mahmoodi, M. and Hashemi, S. M.: 2012, Effect of nanofluid variable properties on mixed convection in a square cavity, *International Journal of Thermal Sciences* **52**, 112–126.

[197] Selimefendigil, F. and Öztop, H. F.: 2015, Natural convection and entropy generation of nanofluid filled cavity having different shaped obstacles under the influence of magnetic field and internal heat generation, *Journal of the Taiwan Institute of Chemical Engineers* **56**, 42–56.

[198] Selimefendigil, F., Öztop, H. F. and Al-Salem, K.: 2014, Natural convection of ferrofluids in partially heated square enclosures, *Journal of Magnetism and Magnetic Materials* **372**, 122–133.

[199] Shahi, M., Mahmoudi, A. H. and Raouf, A. H.: 2011, Entropy generation due to natural convection cooling of a nanofluid, *International Communications in Heat and Mass Transfer* **38**(7), 972–983.

[200] Sharma, T., Reddy, A. L. M., Chandra, T. and Ramaprabhu, S.: 2008, Development of carbon nanotubes and nanofluids based microbial fuel cell, *International journal of hydrogen energy* **33**(22), 6749–6754.

[201] Shaw, S., Ganguly, S., Sibanda, P. and Chakraborty, S.: 2014, Dispersion characteristics of blood during nanoparticle assisted drug delivery process through a permeable microvessel, *Microvascular research* **92**, 25–33.

[202] Shaw, S., Sibanda, P., Sutradhar, A. and Murthy, P.: 2014, Magnetohydrodynamics and soret effects on bioconvection in a porous medium saturated with a nanofluid containing gyrotactic microorganisms, *Journal of Heat Transfer* **136**(5), 052601.

[203] Sheikholeslami, M., Bandpy, M. G., Ellahi, R. and Zeeshan, A.: 2014, Simulation of MHD cuo–water nanofluid flow and convective heat transfer considering lorentz forces, *Journal of Magnetism and Magnetic Materials* **369**, 69–80.

[204] Sheikholeslami, M. and Ellahi, R.: 2015, Three dimensional mesoscopic simulation of magnetic field effect on natural convection of nanofluid, *International Journal of Heat and Mass Transfer* **89**, 799–808.

[205] Sheikholeslami, M., Ellahi, R., Ashorynejad, H., Domairry, G. and Hayat, T.: 2014, Effects of heat transfer in flow of nanofluids over a permeable stretching wall in a porous medium, *Journal of Computational and Theoretical Nanoscience* **11**(2), 486–496.

[206] Sheremet, M. A. and Pop, I.: 2014, Conjugate natural convection in a square porous cavity filled by a nanofluid using buongiornos mathematical model, *International Journal of Heat and Mass Transfer* **79**, 137–145.

[207] Sheremet, M. A. and Pop, I.: 2015, Mixed convection in a lid-driven square cavity filled by a nanofluid: Buongiorno's mathematical model, *Applied Mathematics and Computation* **266**, 792–808.

[208] Sheremet, M. A., Pop, I. and Roca, N. C.: 2016, Magnetic field effect on the unsteady natural convection in a wavy-walled cavity filled with a nanofluid: Buongiorno's mathematical model, *Journal of the Taiwan Institute of Chemical Engineers* **61**, 211 – 222.

[209] Shit, G. and Haldar, R.: 2011, Effects of thermal radiation on MHD viscous fluid flow and heat transfer over nonlinear shrinking porous sheet, *Applied Mathematics and Mechanics* **32**(6), 677–688.

[210] Shit, G., Haldar, R. and Ghosh, S.: 2016, Convective heat transfer and MHD viscoelastic nanofluid flow induced by a stretching sheet, *International Journal of Applied and Computational Mathematics* **2**(4), 593–608.

[211] Shit, G., Haldar, R. and Mandal, S.: 2017, Entropy generation on MHD flow and convective heat transfer in a porous medium of exponentially stretching surface saturated by nanofluids, *Advanced Powder Technology* **28**(6), 1519–1530.

[212] Shyy, W.: 1985, A study of finite difference approximations to steady-state, convection-dominated flow problems, *Journal of Computational Physics* **57**(3), 415–438.

[213] Shyy, W., Thakur, S. and Wright, J.: 1992, Second-order upwind and central difference schemes for recirculatingflow computation, *AIAA journal* **30**(4), 923–932.

[214] Singh, A. K., Basak, T., Nag, A. and Roy, S.: 2015, Role of entropy generation on thermal management during natural convection in tilted porous square cavities, *Journal of the Taiwan Institute of Chemical Engineers* **50**, 153–172.

[215] Singh, A. K., Roy, S., Basak, T. and Momoniat, E.: 2014, Role of entropy generation on thermal management during natural convection in a tilted square cavity with isothermal and non-isothermal hot walls, *Numerical Heat Transfer, Part A: Applications* **66**(11), 1243–1267.

[216] Singh, D., Toutbort, J., Chen, G. et al.: 2006, Heavy vehicle systems optimization merit review and peer evaluation, *Annual Report, Argonne National Laboratory* **23**, 405–411.

[217] Singh, S. and Sharif, M.: 2003, Mixed convective cooling of a rectangular cavity with inlet and exit openings on differentially heated side walls, *Numerical Heat Transfer: Part A: Applications* **44**(3), 233–253.

[218] Sinha, P. and Adamu, G.: 2013, Analysis of thermal deformation of a rough slider and its asperities and its impact on load generation in parallel sliders, *Proceedings of World Academy of Science, Engineering and Technology*, pp. 137–145.

[219] Sitprasert, C., Dechaumphai, P. and Juntasaro, V.: 2009, A thermal conductivity model for nanofluids including effect of the temperature-dependent interfacial layer, *Journal of Nanoparticle Research* **11**(6), 1465–1476.

[220] Sivasankaran, S., Malleswaran, A., Lee, J. and Sundar, P.: 2011, Hydro-magnetic combined convection in a lid-driven cavity with sinusoidal boundary conditions on both sidewalls, *International Journal of Heat and Mass Transfer* **54**(13), 512 – 525.

[221] Sivasankaran, S. and Pan, K.: 2012, Numerical simulation on mixed convection in a porous lid-driven cavity with nonuniform heating on both side walls, *Numerical Heat Transfer, Part A: Applications* **61**(2), 101–121.

[222] Sivasankaran, S., Sivakumar, V. and Prakash, P.: 2010, Numerical study on mixed convection in a lid-driven cavity with non-uniform heating on both sidewalls, *International Journal of Heat and Mass Transfer* **53**(1920), 4304 – 4315.

[223] Smith, G. D.: 1985, *Numerical solution of partial differential equations: finite difference methods*, Oxford university press.

[224] Solsvik, J., Becker, P. J., Sheibat-Othman, N. and Jakobsen, H. A.: 2016, Numerical solution of the drop population balance equation using weighted residual and finite volume methods, *Journal of Dispersion Science and Technology* **37**(1), 80–88.

[225] Sun, X., Liu, Z., Welsher, K., Robinson, J. T., Goodwin, A., Zaric, S. and Dai, H.: 2008, Nano-graphene oxide for cellular imaging and drug delivery, *Nano research* **1**(3), 203–212.

[226] Talebi, F., Mahmoudi, A. H. and Shahi, M.: 2010, Numerical study of mixed convection flows in a square lid-driven cavity utilizing nanofluid, *International Communications in Heat and Mass Transfer* **37**(1), 79–90.

[227] Thakur, S. and Shyy, W.: 1993, Some implementational issues of convection schemes for finite-volume formulations, *Numerical Heat Transfer, Part B Fundamentals* **24**(1), 31–55.

[228] Ting, T. W., Hung, Y. M. and Guo, N.: 2014, Viscous dissipative forced convection in thermal non-equilibrium nanofluid-saturated porous media embedded in microchannels, *International Communications in Heat and Mass Transfer* **57**, 309–318.

[229] Ting, T. W., Hung, Y. M. and Guo, N.: 2015, Entropy generation of viscous dissipative nanofluid flow in thermal non-equilibrium porous media embedded in microchannels, *International Journal of Heat and Mass Transfer* **81**, 862–877.

[230] Tiwari, R. K. and Das, M. K.: 2007, Heat transfer augmentation in a two-sided lid-driven differentially heated square cavity utilizing nanofluids, *International Journal of Heat and Mass Transfer* **50**(9), 2002–2018.

[231] Torabi, M., Peterson, G., Torabi, M. and Karimi, N.: 2016, A thermodynamic analysis of forced convection through porous media using pore scale modeling, *International Journal of Heat and Mass Transfer* **99**, 303–316.

[232] Torabi, M., Zhang, K., Yang, G., Wang, J. and Wu, P.: 2015, Heat transfer and entropy generation analyses in a channel partially filled with porous media using local thermal non-equilibrium model, *Energy* **82**, 922–938.

[233] Vafai, K., Alkire, R. and Tien, C.: 1985, An experimental investigation of heat transfer in variable porosity media, *Journal of Heat Transfer* **107**(3), 642–647.

[234] Vafai, K. and Tien, C.: 1981, Boundary and inertia effects on flow and heat transfer in porous media, *International Journal of Heat and Mass Transfer* **24**(2), 195–203.

[235] Varol, Y., Oztop, H. F. and Koca, A.: 2008, Entropy generation due to conjugate natural convection in enclosures bounded by vertical solid walls with different thicknesses, *International Communications in Heat and Mass Transfer* **35**(5), 648–656.

[236] Varol, Y., Oztop, H. F. and Pop, I.: 2009, Entropy generation due to natural convection in non-uniformly heated porous isosceles triangular enclosures at different positions, *International Journal of Heat and Mass Transfer* **52**(5), 1193–1205.

[237] Vassallo, P., Kumar, R. and DAmico, S.: 2004, Pool boiling heat transfer experiments in silica-water nanofluids, *International Journal of Heat and Mass Transfer* **47**(2), 407–411.

[238] Vasseur, P., Wang, C. and Sen, M.: 1990, Natural convection in an inclined rectangular porous slot: the brinkman-extended darcy model, *Journal of Heat Transfer* **112**(2), 507–511.

[239] Vékás, L., Bica, D. and Avdeev, M. V.: 2007, Magnetic nanoparticles and concentrated magnetic nanofluids: synthesis, properties and some applications, *China Particuology* **5**(1), 43–49.

[240] Versteeg, H. K. and Malalasekera, W.: 1995, *An introduction to computational fluid dynamics: the finite volume method*, McGraw-Hill, Loughborough University.

[241] Vishnuvardhanarao, E. and Das, M. K.: 2009, Mixed convection in a buoyancy-assisted two-sided lid-driven cavity filled with a porous medium, *International Journal of Numerical Methods for Heat & Fluid Flow* **19**(3/4), 329–351.

[242] Wen, D., Lin, G., Vafaei, S. and Zhang, K.: 2009, Review of nanofluids for heat transfer applications, *Particuology* **7**(2), 141–150.

[243] Wong, K. V. and De Leon, O.: 2010, Applications of nanofluids: current and future, *Advances in Mechanical Engineering* **2**, 519659.

[244] Wu, F., Wang, G. and Zhou, W.: 2014, Natural convection in a cavity filled with porous medium with partially thermal active sidewalls under local thermal nonequilibrium conditions, *Journal of Porous Media* **17**(11).

[245] Xie, H., Wang, J., Xi, T., Liu, Y. and Ai, F.: 2002, Dependence of the thermal conductivity of nanoparticle-fluid mixture on the base fluid, *Journal of Materials Science Letters* **21**(19), 1469–1471.

[246] Xu, J., Yu, B., Zou, M. and Xu, P.: 2006, A new model for heat conduction of nanofluids based on fractal distributions of nanoparticles, *Journal of Physics D: Applied Physics* **39**(20), 4486.

[247] Xuan, Y. and Li, Q.: 2000, Heat transfer enhancement of nanofluids, *International Journal of heat and fluid flow* **21**(1), 58–64.

[248] Xuan, Y., Li, Q. and Hu, W.: 2003, Aggregation structure and thermal conductivity of nanofluids, *AIChE Journal* **49**(4), 1038–1043.

[249] You, S., Kim, J. and Kim, K.: 2003, Effect of nanoparticles on critical heat flux of water in pool boiling heat transfer, *Applied Physics Letters* **83**(16), 3374–3376.

[250] Yu, W. and Choi, S.: 2003, The role of interfacial layers in the enhanced thermal conductivity of nanofluids: a renovated maxwell model, *Journal of Nanoparticle Research* **5**(1-2), 167–171.

[251] Zhang, L., Jiang, Y., Ding, Y., Povey, M. and York, D.: 2007, Investigation into the antibacterial behaviour of suspensions of zno nanoparticles (zno nanofluids), *Journal of Nanoparticle Research* **9**(3), 479–489.

[252] Zhang, Y., Chao, Z. and Jakobsen, H. A.: 2017, Modelling and simulation of hydrodynamics in double loop circulating fluidizedbed reactor for chemical looping combustion process, *Powder Technology* **310**, 35–45.

[253] Zhou, J., Wu, Z., Zhang, Z., Liu, W. and Xue, Q.: 2000, Tribological behavior and lubricating mechanism of cu nanoparticles in oil, *Tribology Letters* **8**(4), 213–218.